



## 저작자표시-비영리-변경금지 2.0 대한민국

이용자는 아래의 조건을 따르는 경우에 한하여 자유롭게

- 이 저작물을 복제, 배포, 전송, 전시, 공연 및 방송할 수 있습니다.

다음과 같은 조건을 따라야 합니다:



저작자표시. 귀하는 원저작자를 표시하여야 합니다.



비영리. 귀하는 이 저작물을 영리 목적으로 이용할 수 없습니다.



변경금지. 귀하는 이 저작물을 개작, 변형 또는 가공할 수 없습니다.

- 귀하는, 이 저작물의 재이용이나 배포의 경우, 이 저작물에 적용된 이용허락조건을 명확하게 나타내어야 합니다.
- 저작권자로부터 별도의 허가를 받으면 이러한 조건들은 적용되지 않습니다.

저작권법에 따른 이용자의 권리는 위의 내용에 의하여 영향을 받지 않습니다.

이것은 [이용허락규약\(Legal Code\)](#)을 이해하기 쉽게 요약한 것입니다.

[Disclaimer](#)

공학박사학위논문

**NANOENGINEERED BIOMIMETIC  
PLATFORMS FOR CONTROLLING CELL  
FUNCTION AND TISSUE REGENERATION**

**세포기능 조절 및 조직 재생을 위한  
생체모방형 나노구조 플랫폼 개발**

2014년 8월

서울대학교 대학원

바이오시스템·소재학부 바이오시스템공학전공

김 장 호

# NANOENGINEERED BIOMIMETIC PLATFORMS FOR CONTROLLING CELL FUNCTION AND TISSUE REGENERATION

## 세포기능 조절 및 조직 재생을 위한 생체모방형 나노구조 플랫폼 개발

지도교수: 정 종 훈

이 논문을 공학박사 학위논문으로 제출함

2014년 7월

서울대학교 대학원  
바이오시스템·소재학부 바이오시스템공학 전공  
김 장 호

김장호의 공학박사 학위논문을 인준함  
2014년 7월

위 원 장      전 누 리      (인)

부위원장      정 종 훈      (인)

위      원      김 학 진      (인)

위      원      홍 지 향      (인)

위      원      정 연 훈      (인)

# **Nanoengineered Biomimetic Platforms for Controlling Cell Function and Tissue Regeneration**

by

**Jangho Kim**

Submitted to the Department of Biosystems & Biomaterials Science and Engineering in Partial Fulfillment of the Requirements for the Degree of

**Doctor of Philosophy in Biosystems Engineering**

at the  
**Seoul National University**

July 2014

**Jong Hoon Chung, Ph.D.** \_\_\_\_\_

Dissertation Advisor

Professor of Department of Biosystems & Biomaterials Science and Engineering  
Seoul National University

**Noo Li Jeon, Ph.D.** \_\_\_\_\_

Professor of School of Mechanical and Aerospace Engineering  
Seoul National University

**Hak-Jin Kim, Ph.D.** \_\_\_\_\_

Professor of Department of Biosystems & Biomaterials Science and Engineering  
Seoul National University

**Ji Hyang Hong, Ph.D.** \_\_\_\_\_

Senior Researcher of Research Institute of Agriculture Life Sciences  
Seoul National University

**Yun-Hoon Choung, M.D., D.D.S., Ph.D.** \_\_\_\_\_

Professor of Department of Otolaryngology  
Ajou University School of Medicine



For the Glory of the LORD  
I always believe the LORD's covenant to me.

&

To My Family and Genie

## Abstract

Living cells are exposed to complex and functional microenvironment including soluble macromolecules, biophysical cues, and interactions between cell-cell and cell-extracellular matrix (ECM), suggesting that the design and manipulation of engineered cellular microenvironments is of great important in a wide variety of biological applications such as fundamental biology, therapeutic and diagnostic research, stem cells and regenerative medicine, and developing *in vitro* disease models. Compared with the effects of soluble macromolecules and biophysical cues, the extent and importance of architecture of ECMs in defining cellular function is currently poorly understood in spite of the essential fact that living cells display high sensitivity to the ECM composed of complex and well-defined topographies in protein fibers such as fibrillar collagens and elastins with feature sizes ranging from tens to several hundreds of nanometers *in vivo*. Namely, the architecture effects of ECMs are mainly neglected or minimized as a considering factor for most *in vitro* and *in vivo* experimentation.

In this dissertation, we developed a series of advanced nanopatterned platforms inspired by the unique architectures of native tissues and ECMs in a detailed and comprehensive fashion using nanofabrication technologies such as capillary force lithography (CFL) to provide cells the *in vivo*-like topographical cell environment. Using the nanoengineered biomimetic platforms, the roles of nanotopography in regulation of cellular and multicellular structure and function were investigated. We also utilized the biomimetic systems composed of a nanoengineered substrate, specific soluble macromolecules, and cells to achieve desired phenotypic responses toward tissue regeneration. The specific aims of my thesis are as follows are: (1) to design and manipulate nanotopographically defined platforms with precisely controlled topographical architectures as a synthetic ECM for regulating structure and function of cells in single (i.e., single adherent cells) and multi-cellular (i.e., cohesive groups of cells) levels, (2) to investigate the detailed role of nanotopography in cellular behavior for developing a methodology for promoting cell function and modeling biological processing such as stem cell differentiation and wound repair, and (3) to develop a strategy for tissue regeneration such as bone and tympanic membrane using nanoengineered biomimetic systems. The working hypothesis underlying my research is that nanoengineered biomimetic platforms can (i) provide cells *in vivo*-like topographical cues that control cellular and multicellular structure and function, and (ii) allow appropriate environments

for repair or regeneration of damaged tissues without surgical treatments.

The main results of my dissertation research can be summarized as follows. First, inspired by the architectures of native ECMs in various tissues, nanotopographically defined ridge/groove patterned substrata with precisely controlled sizes were developed using CFL. Using these platforms, it was found that nanotopographical density can control the morphology, focal adhesion formation, migration, ECM molecule production of fibroblast cells, and would healing as well as the adhesion, migration, and differentiation of mesenchymal stem cells (MSCs). Second, nanopatterned hierarchical platforms (i.e., multiscale topography) were developed for better mimicking architectures of ECMs using CFL in combination with micro wrinkling technique and nanomaterials. Using anisotropically multiscale patterned substrata with precisely defined micro- and nanotopography, the potential role of nanotopography in ECMs were investigated; the nanotopography can regulate the cell-substrate or cell-cell interactions, which may eventually promote the function of cells including NIH3T3 fibroblast cells, MG-63 cells, and MSCs. Furthermore, it was found that graphene-matrix nanotopography hybrid substrata with nano and sub-nanopatterned hierarchical features can promote the functions of cells including differentiation of MSCs, enhanced mineralization of MC-3T3 cells, and capillary tube formation of HUVEC. Finally, nanoengineered biomimetic systems composed of the ECM-like topographical substrate, chemical molecules, and cells were proposed as a strategy for repair or regeneration of damaged tissues. Inspired by the aligned nanostructures and co-existence of vascular cells and stem cells in bone tissues, the systems comprised of nanotopography and co-culture platforms were developed, showing that the osteogenesis of MSCs was further enhanced by the two factors in combination whereas both nanotopography and co-culture independently enhanced the osteogenesis. In addition, a stem cell patch that integrates MSCs into the nanopatterned hierarchical substrate was developed using a Food and Drug Administration (FDA)-approved poly(lacticco-glycolic acid) (PLGA) polymer. It was demonstrated that the nanopatterned stem cell patches can guide the bone regeneration and the nanofibrillar patch synthesized from bacterial cellulose can promote the tympanic membrane regeneration without complex surgical treatments or tissue transplantation.

**Keywords:** Nanofabrication, Biomimetic, Biomaterials, Cell mechanics, Tissue regeneration

**Student Number:** 2012-30997

# Table of Contents

<b>Abstract</b>	<b>i</b>
<b>Table of Contents</b>	<b>iii</b>
<b>List of Table</b>	<b>vi</b>
<b>List of Figures</b>	<b>vii</b>
<b>Scope and Format of Dissertation</b>	<b>x</b>
<b>1 Introduction</b>	<b>1</b>
1.1 General introduction	2
1.2 Objectives	
<b>2 Micro- and nanoengineered biomimetic platforms for modeling biological processing and tissue regeneration</b>	<b>4</b>
2.1 Summary	4
2.2 Histological background	4
2.3 Micro- and nanofabrication technology for biomimetic microenvironment	5
2.4 Microfluidics for physiologically relevant microenvironment	8
2.5 Discussion	9
2.6 References	10
<b>Part I Designing and manipulating nanopatterned platforms with precisely controlled topographical architectures and sizes</b>	<b>15</b>
<b>3 Nanotopographic pattern arrays with variable local sizes for engineering adhesion and migration of fibroblast cells</b>	<b>17</b>
3.1 Summary	17
3.2 Introduction	18
3.3 Materials and methods	19
3.4 Results	22
3.5 Discussion	29
3.6 References	30
<b>4 Designing nanotopographical density of extracellular matrix for controlled morphology and function of mesenchymal stem cells</b>	<b>40</b>
4.1 Summary	40
4.2 Introduction	41
4.3 Materials and methods	43
4.4 Results	49
4.5 Discussion	57

4.6	References .....	63
<b>Part II</b>	<b>Designing and manipulating nanopatterned hierarchical platforms with precisely controlled topographical architectures and sizes .....</b>	<b>82</b>
<b>5</b>	<b>Bioinspired configurable hierarchical micro- and nanostructure with precisely controlled sizes for functional alignment and guided orientation of cells .....</b>	<b>84</b>
5.1	Summary .....	84
5.2	Introduction .....	85
5.3	Materials and methods .....	86
5.4	Results .....	91
5.5	Discussion .....	96
5.6	References .....	98
<b>6</b>	<b>Nano- and sub-nanopatterned hierarchical platforms composed of graphene and matrix nanotopography for promoting cellular function .....</b>	<b>110</b>
7.1	Summary .....	110
7.2	Introduction .....	111
7.3	Materials and methods .....	112
7.4	Results .....	116
7.5	Discussion .....	121
7.6	References .....	122
<b>Part III</b>	<b>Development of nanoengineered biomimetic systems for tissue regeneration .....</b>	<b>135</b>
<b>7</b>	<b>Synergistic effects of nanotopography and co-culture with endothelial cells on osteogenesis of mesenchymal stem cells .....</b>	<b>136</b>
7.1	Summary .....	136
7.2	Introduction .....	137
7.3	Materials and methods .....	138
7.4	Results .....	144
7.5	Discussion .....	151
7.6	References .....	156
<b>8</b>	<b>Multiscale patterned transplantable stem cell patches for bone tissue regeneration .....</b>	<b>170</b>
8.1	Summary .....	170
8.2	Introduction .....	170
8.3	Materials and methods .....	173
8.4	Results .....	179
8.5	Discussion .....	185
8.6	References .....	189
<b>9</b>	<b>Bacterial cellulose nanofibrillar patch as a wound healing platform of tympanic membrane perforation .....</b>	<b>199</b>

9.1	Summary .....	199
9.2	Introduction .....	199
9.3	Materials and methods .....	201
9.4	Results .....	205
9.5	Discussion .....	211
9.6	References .....	211
<b>10</b>	<b>Concluding remarks .....</b>	<b>223</b>
10.1	Introduction .....	223
10.2	Summary of dissertation work .....	224
10.3	Broad implications of this dissertation work for biological engineering .....	230
	<b>Abstract (Korean) .....</b>	<b>232</b>
	<b>Curriculum Vitae .....</b>	<b>235</b>

## List of Table

Table 6.1	Topographical characteristics of the graphene-matrix nanotopography, showing the nano- and sub-nanopatterned hierarchical topography	126
Table 9.1	Characteristics of the BC nanofibrillar patch fabricated in this study	214

## List of Figures

Figure 1.1	A schematic representation of the complexity of the native cellular microenvironment	3
Figure 2.1	Timelines of major historic events in engineering systems for cell and tissue culture platforms	14
Figure 3.1	Fabrication of anisotropic nanotopographic pattern arrays with variable local sizes in the form of uniformly-spaced ridge/grooved nanosurfaces as model systems of ECM architectures	32
Figure 3.2	Morphological responses of fibroblast cells to the local density of nanotopographic pattern arrays with variable local sizes in the form of uniformly-spaced ridge/grooved nanosurfaces	33
Figure 3.3	Effects of the local density of nanotopographic pattern arrays on cell alignment and migration	34
Figure 3.4	Effects of the local density of nanotopographic pattern arrays on the organization of focal adhesions	35
Figure 3.5	Morphological responses and organizations of produced fibronectin (FN) fibers of fibroblast cells to the local density of nanotopographic pattern arrays with variable local sizes in the form of uniformly-spaced ridge/grooved nanosurfaces in multi cell level	36
Figure 3.6	<i>In vitro</i> wound healing study with nanotopographic pattern arrays	37
Figure 3.7	A proposed model of the role of nanotopographical density during wound healing	38
Figure 4.1	Rational design and fabrication of bio-inspired anisotropic nanotopography with various nanogroove sizes	70
Figure 4.2	Effect of nanotopographical density on the cell morphology	71
Figure 4.3	Representative SEM images of cellular morphologies on various nanopatterned surfaces	72
Figure 4.4	Effect of nanotopographical density on the organization of focal adhesions	73
Figure 4.5	Osteogenesis of hMSCs on various nanopatterned surfaces	74
Figure 4.6	Neurogenesis of hMSCs on various nanopatterned surfaces	75
Figure 4.7	Quantification of biochemical soluble factors and proteins according to nanotopographical density	76
Figure 4.8	Relative trends of morphological factors, intracellular protein levels and cell functions with respect to the nanotopographical densities	77
Figure 5.1	Fabrication of micro- and nanopatterned hierarchical ECM-like platforms	101
Figure 5.2	Morphological responses of fibroblast cells to the micro- and nanopatterned topography with variable local sizes in the form of uniformly-spaced ridge/grooved surfaces	102
Figure 5.3	Morphological responses of osteoblast-like cells, endothelial cells, and stem cells	103
Figure 5.4	Representative SEM images of morphologies of (a) fibroblast cells, (b) osteoblast-like cells, and (c) endothelial cells on micro- and nanopatterned surfaces	104
Figure 5.5	Mechanosensitivity of cell alignment and elongation to nanotopography in multiscale surfaces	105



Figure 5.6	Analysis of cell-substrate and cell-cell interaction in fibroblast cells on micro- and nanopatterned substrates	106
Figure 5.7	Analysis of proliferation, cell organization, and produced fibronectin (FN) fibers of fibroblast cells in multi cell level on the micropatterned and the micro- and nanopatterned substrates	107
Figure 5.8	A proposed model for mechanosensitivity of fibroblast cells to nanotopography in micro- and nanopatterned substrates	108
Figure 6.1	Rational design and fabrication of nano and sub-nanopatterned hierarchical platforms with matrix nanotopography as a biomimetic ECM	127
Figure 6.2	Effects of graphene-matrix nanotopography hybrid platforms on adhesion and structure of hMSCs	128
Figure 6.3	Enhanced differentiation of hMSCs on the graphene-matrix nanotopography hybrid platforms	129
Figure 6.4	Effects of graphene-matrix nanotopography hybrid platforms on cell-substrate and cell-cell interaction	130
Figure 6.5	Enhanced cellular function of osteoblast and endothelial cells on graphene-matrix nanotopography hybrid platforms	131
Figure 7.1	Rational design and fabrication of bone tissue-like nanopatterned matrix with various groove sizes	161
Figure 7.2	Effects of nanopatterned matrix on the morphology and orientation of hMSCs and HUVECs	162
Figure 7.3	Time-dependent morphology and orientation of hMSCs and HUVECs guided by nanopatterned matrix	163
Figure 7.4	Proliferation of cells on nanopatterned matrix in co-culture systems for 7 days	164
Figure 7.5	Osteogenesis of hMSCs on nanopatterned matrix in co-culture with HUVECs	165
Figure 7.6	Synergistically enhanced osteogenesis of hMSCs on nanopatterned matrix in co-culture with HUVECs	166
Figure 7.7	Synergistically enhanced osteogenesis of hMSCs on nanopatterned matrix in co-culture with HUVECs	167
Figure 7.8	A model for the synergistically enhanced osteogenesis of hMSCs on nanopatterned matrix in co-culture with HUVECs	168
Figure 8.1	Fabrication of the nanopatterned hierarchical PLGA substrates	192
Figure 8.2	Surface characteristics of multiscale hierarchical PLGA patch	193
Figure 8.3	Normal and shear adhesion forces of the multiscale hierarchical PLGA patch	194
Figure 8.4	Adhesion of hMSCs with controlled macroscopic alignment and orientation on the multiscale hierarchical topography	195
Figure 8.5	Bone regeneration using multiscale patterned stem cell patches	196
Figure 9.1	Basic concept of this study for TM regeneration using BC nanofibrillar patch	215
Figure 9.2	Representative (a) digital camera image and (b) SEM image of the BC nanofibrillar patch	216
Figure 9.3	Time-dependent cell viability of the TM cells on the BC nanofibrillar patch and TCPS as a control at 6 h, 3, 5, and 7 days after seeding of cells, showing a similar time-dependent cell viability of TM cells between the BC nanofibrillar patch and the TCPS group	217
Figure 9.4	<i>In vitro</i> wound healing study for growth and migration of the TM cells under guidance of the BC nanofibrillar patch	218

- Figure 9.5 *In vivo* animal study of regeneration of traumatic TM perforation using (a) the 219  
BC nanofibrillar patch
- Figure 9.6 ABR results of the normal TMs, the perforated TMs, and the regenerated TMs 220  
with the BC nanofibrillar patch, indicating that the hearing ability of the TM rats  
regenerated with the patches was recovered
- Figure 9.7 Representative H&E image of (a) the regenerated TM spontaneously and (b) the 221  
regenerated TM with the BC nanofibrillar patch
- Figure 9.8 Representative TEM images of the (a) normal TMs, (b) the regenerated TM 222  
with the BC nanofibrillar patch, and (c) the regenerated TM spontaneously

## Scope and Format of Dissertation

Nanoengineering approaches were applied to develop the *in vivo*-like topographical cell environment for controlling cellular function. The objectives of this dissertation were to design and manipulate nanoengineered biomimetic systems for regulating and promoting cell function, and modeling biological processing such as stem cell differentiation, wound repair, and bone regeneration.

The dissertation is divided into three parts (excluding introduction, literature review, and conclusion) comprised of six research chapters. Each chapter is written as a ‘complete story’ in a specific aspect of the *in vivo*-like topographical cell environments with focus on the nanoscale architectures. Each three parts develops nanoengineered biomimetic systems and approaches to control and improve cellular function. **Chapter 1** provides the background of this thesis work and introduces the detailed objectives. **Chapter 2** describes the current micro- and nanoengineered biomimetic platforms for modeling biological processing and tissue regeneration as a literature review on this work. The next two chapters provide the contents for Part I. **Part I** developed a series of nanofabricated platforms with defined ridge/groove patterns with precisely controlled sizes using capillary force lithography (CFL) to control the nanotopographical density, implying an existence of potentially optimized nanotopographical density for functions of cells. **Chapter 3** shows that the matrix nanotopography with local density of ridge/groove patterns can direct the adhesion, migration, and production of extracellular matrix (ECM) molecules of fibroblast cells. **Chapter 4** describes that the matrix nanotopography with controlled density of groove spacing ratio can also control the adhesion, migration, and differentiation of mesenchymal stem cells (MSCs). **Part II** is comprised of the next two chapters and develops a series of nanopatterned hierarchical platforms. **Chapter 5** provides the methodology to fabricate the micro- and nanopatterned hierarchical structures using CFL in combination with micro wrinkling technique while **Chapter 6** describes the platforms with nano and sub-nanopatterned hierarchical topographies fabricated by using graphene and matrix nanotopography. These platforms demonstrate that the multiscale topography can promote the function of various types of cells. **Part III** shows a strategy to regenerate the damaged tissues using nanoengineered biomimetic systems composed of ECM-like topographical substrates, chemical molecules, and cells. **Chapter 7** shows the importance of biomimetic system comprised of nanotopography and

co-culture platform, promoting the osteogenesis of stem cells by the two factors in combination. **Chapter 8** describes that the nanoengineered biomimetic systems can be used as an efficient strategy for bone tissue regeneration without complex surgical treatments or tissue transplantation. It is shown that the stem cell patch that integrates MSCs into the nanopatterned substrate can guide the bone regeneration. **Chapter 9** demonstrates that the nanofibrillar patch synthesized from *Gluconacetobacter xylinus*, one of types of bacterial celluloses, can promote the tympanic membrane regeneration without complex surgical treatments. **Chapter 10** provides an outline of the conclusion and suggests the broad implications of this dissertation work toward biological engineering.

## Chapter 1. Introduction

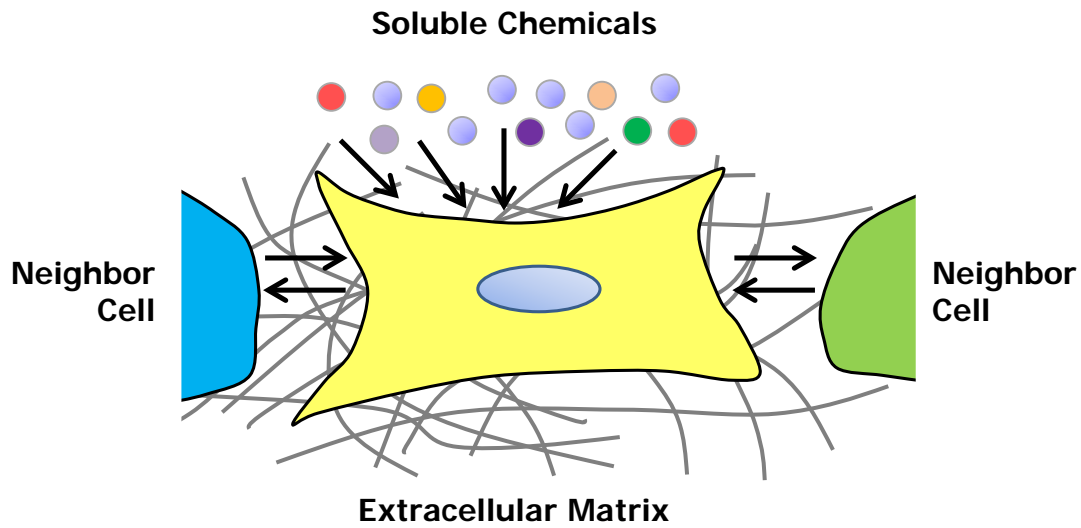
### 1.1. General introduction

Living cells are exposed to biochemically and physically complex microenvironments that enable them to maintain appropriate biological functions as well as adapt to dynamic changes in the physiological environments (Fig. 1.1.). The native cellular microenvironments in which cells reside *in vivo* comprise soluble chemical factors (e.g., growth factors, cytokines), biomechanical factors (e.g., shear stress, hydrostatic pressure), neighbor cells (e.g., cell-cell junction), and extracellular matrix (ECM), which can eventually be converted into biological signals to regulate the function of cells in health and disease states. In particular, many biochemical and physical cues are provided by the ECM which typically consists of a complex and well-defined micro- and nanoscale topographic structures and acts as a physical framework supporting cell attachment and growth. However, compared with the effects of other biochemical factors or physical factors, the extent and the importance of nanotopography of the ECM on cell behaviors and function is currently poorly understood. For example, most *in vitro* cell studies neglect this factor for elucidating fundamental principles in cell biology; biologists usually examine cells cultured on flat 2D rigid substrates (e.g., Petri dish). Moreover, the precisely defined nanotopography is usually neglected or minimized for the design and fabrication of cell culture platforms or scaffolds. The general goal of my doctoral dissertation is therefore to apply advanced nanofabrication techniques for manipulation of nanoengineering systems to mimic *in vivo*-like topographical architectures in the cellular microenvironments, and for their applications such as fundamental biology platforms, mechanobiology, therapeutic tool, and cell and tissue engineering.

## 1.2. Objectives

The working hypothesis underlying my dissertation research is that (i) nanoengineered biomimetic platforms can provide cells *in vivo*-like topographical cues that control cellular and multicellular structure and function; (ii) nanoengineered biomimetic systems composed of nanopatterned substrates, chemical molecules, and cells can provide appropriate environments for repair or regeneration of damaged tissues without surgical treatments. To address these hypotheses, we developed a series of nanofabricated platforms inspired by the ultrastructural analysis of *ex vivo* tissue organization. Using these platforms in combination with traditional cell biology approaches, we investigated the structure and function of cells in cellular (i.e., single adherent cells) and multicellular (i.e., cohesive groups of cells) level under the nanotopographic stimulation. Finally, nanoengineered biomimetic systems were proposed as a strategy for repair or regeneration of damaged tissues in a more clinically relevant setting. The specific aims of my dissertation work are as follows:

- Aim 1. To design and manipulate nanotopographically defined platforms with precisely controlled topographical architectures as a synthetic ECM for regulation of cellular and multicellular structure and function
- Aim 2. To investigate a detailed role of nanotopography in cellular behavior for developing a methodology for promoting cell function and modeling biological processing such as stem cell differentiation and would repair
- Aim 3. To develop strategies for regeneration of tissues such as bone and tympanic membrane using biomimetic systems composed of nanoengineered platforms, specific soluble macromolecules, and stem cells



**Soluble chemicals:** growth factor, cytokine, hormone

**Neighbor cells:** cadherin, connexin

**Extracellular matrix:** topography, composition, stiffness

**Figure 1.1. A schematic representation of the complexity of the native cellular microenvironment.** Living cells can be profoundly affected by complex microenvironments such as both soluble and insoluble macromolecules that comprise the extracellular matrix or mediate extracellular communication via direct or indirect cell-cell communication as well as mechanical, electrical, and optical signals.

## **Chapter 2. Micro- and Nanoengineered Biomimetic Platforms for Modeling Biological Processing and Tissue Regeneration**

### **2.1. Summary**

Biologically inspired approaches employing micro- and nanoengineering techniques have been influential in the progress of cell and tissue engineering as well as fundamental biology. Here, we describe the current micro- and nanofabrication technologies that have contributed to major advances in cell and tissue culture platforms for modeling biological processing and engineering complex tissues. We also discuss opinion on the principal challenges and future prospects in biologically inspired micro- and nanoengineering systems for understanding and regeneration of functional and complex tissues.

### **2.2. Histological background**

Living tissues are intricate ensembles of various cell types that can maintain and regulate the important function in living systems such as humans and animals [1-4]. The introduction of *in vitro* cell culture in 1907 dramatically changed the study of cell biology due to the ability to observe cellular behavior clearly under the microscope in a real-time manner [5] (Fig. 2.1). This revolution enabled observation of systematic cell behaviors in response to various factors such as *in vivo*-like chemical, mechanical and electrical cues [6–10]. One century later, cell science and engineering have combined again through the pioneering concept named ‘tissue engineering’ from the work of Robert Langer and Joseph Vacanti [3], which was an interdisciplinary fabrication method combining principles from both the life sciences and engineering such as soft lithography, polymer engineering, and microfluidics for tissue and organ regeneration (Fig. 2.1) [1, 4]. These early works demonstrated the potential of sophisticated control of cell behaviors to



repair the damaged tissues or partially regenerate new tissues. Two decades later, cell and tissue engineers can utilize more sophisticated micro- and nanoengineering techniques to engineer more functional and complex tissues and organs (Fig. 2.1).

The development of technologies to engineer tissues for the regeneration of damaged tissues and organs associated with congenital defects, injury, or disease is becoming increasingly urgent [1, 2]. To meet these global clinical needs, tissue engineering has rapidly grown and has been recognized as a pioneering methodology to overcome current complex surgical treatments or tissue/organ transplantation [1–3]. Traditional tissue engineering approaches simply transplanted biocompatible scaffolds containing cells and growth factors into the targeted area [3]. More recently, those in the tissue engineering and regenerative medicine field are starting to recognize the importance of micro- and nano-scale biological complexity, and its influence on cellular and multicellular behaviors [2, 4]. Manipulation of biological engineering systems to resemble the *in vivo* microenvironment is now emphasized as a key factor not only to engineer more complex and functional tissues but also to better understand fundamental biology at the cell and tissue levels. Recent works on micro- and nanoengineering systems to mimic *in vivo*-like microenvironments mainly include two topics: (i) micro- and nanofabrication for extracellular matrix (ECM)-like microenvironment and (ii) microfluidics for organ-on-a-chip (Fig. 1).

### **2.3. Micro- and nanofabrication technology for biomimetic microenvironment**

The micro- and nanostructuring techniques include a variety of fabrication methods to construct two- or three-dimensional (3D) structures that resemble natural ECM in tissues by using various fabrication methods such as photolithography, rapid prototyping, electrospinning, and soft lithography [4, 11]. The engineering of synthetic ECM is important as cell functions such as

proliferation, migration and proliferation *in vivo* are significantly affected by the alignment, size and density of ECM [1]. As a representative example of synthetic ECM engineering, Kim *et al.* described an approach to engineer the topography of ECMs to control the structure and function of cardiomyocytes, in addition to myocardial regeneration [12]. Inspired by the highly aligned nanoscale ECM fibres in the native heart, they developed polyethylene glycol (PEG) scaffolds using capillary force lithography with nanogrooves. Cardiomyocytes cultured on these platforms showed highly elongated and aligned structure, as well as anisotropic contractions and action potential propagation, which is similar to that of the structure and function of cardiomyocytes *in vivo*.

Polymer-based micro- and nanoengineering including collagen, fibrin, alginate, poly(lactide-co-glycolide) (PLG), and PEG scaffolds are another approach for physiologically relevant ECM-like microenvironments [13]. The design of such scaffolds to mimic the mechanical and chemical properties of a native tissue can be engineered with control over parameters such as the morphology, the elastic modulus, and the chemical concentration of the ECM [13]. These polymer-based scaffolds are especially useful when mimicking 3D environments (i.e., dense nanofibrous matrices with controlled porosity). For example, Mooney and colleagues proposed bioactive materials-incorporated PLG matrices as 3D engineering tissues that mimic the mechanical and chemical properties of the native tissues [14]. Furthermore, a fibrin hydrogel-laden microfluidics system seeded with human umbilical endothelial cells (HUVEC) demonstrated spontaneous 3D morphogenesis such as angiogenesis and vasculogenesis, showing collective cellular penetration into the hydrogel network [15]. The porous polymer-based engineering systems also have the potential to make headway into the understanding of invasion-based cell behaviors such as cancer metastasis [16].

More recently, micro- and nanofabrication-based engineering systems have been focused to mimic the complex environmental cues such as multiple or active stimulation to generate more physiological functionality and complexity (e.g. anisotropic mechanical properties and electrical pathways), which allows us to systemically investigate the functional and complex tissues as well as their regeneration [17-23]. For example, cells exposed to unique topographical and biophysical stimuli related to specific tissues will be directed towards organ-specific functions such as protection (skin), mechanical maintenance (bone), transmission of force (ligament and tendons), conduction of electrical signal (neuron), blood circulation (heart and vessels), or force generation (skeletal muscle) [4]. To this end, recent efforts include: an accordion-like geometry of cardiac scaffold that realized not only the anisotropic elastic modulus depending on the stretching orientation, but also alignment of cardiomyocyte [17]; a gold nanowire-embedded scaffold [18] and a carbon nanotube-embedded scaffold [19] that showed synchronized cellular contraction and electrical conduction.

Micro- and nanofabrication technology can allow us to fabricate more complex engineering systems that can help to mimic the characteristic of native ECM microenvironments, especially in terms of feature size, density, and mechanical properties. These systems thus offer more advanced tools for better understanding and precise manipulation of the functions of living cells and tissues, showing new insights into tissue engineering. Nevertheless, these engineering systems still have many limitations and large gaps in order to fully use for their clinical trials in tissue regeneration. From a clinical perspective, for example, current micro- and nanofabrication technologies are still complex, time consuming, expensive, and in the boundary of laboratory levels. In addition, the further development of the advanced micro- and nanofabrication technology on developing more biomimetic and complex ECM-like are important challenge.

## 2.4. Microfluidics for physiologically relevant microenvironment

Microfluidics can offer a controlled microenvironment in terms of mechanical shear stress, and chemical concentration gradients. The fluidic shear stress is critically important to tissues circulating fluids such as the lung, blood vessel and kidney. According to the recent studies, the cells exposed to ‘fluidic’ and ‘static’ environment respectively demonstrated different cell behaviors such as intracellular reorganization and differentiation [24]. A recently reported biomimetic microsystem of the human alveolar–capillary interface of lung showed the usefulness of microfluidics in the understanding tissue function and potential applications for tissue engineering [25]. In this lung-on-a-chip system, following the geometry of alveoli–capillary interface, two types of cells were cultured in a multilayered form facing each other with a sandwiched flexible porous membrane in between cell layers. The top layer consists of human alveolar epithelial cells, and the bottom layer consists of human lung capillary endothelial cells. According to the toxicity test of nanoparticle, cells showed higher toxicity when cyclically stretched due to the damaged cell-cell junctions upon stretching. Interestingly, the results were also demonstrated by the *in vivo* animal study on the toxicity of nanoparticles upon breathing [26]. More recently, a field effect transistor (FET)-embedded scaffold seeded with smooth muscle cells *in vitro* can sensitively detect change of pH in a real-time manner without leakage of fluid [20].

Microfluidics-based engineering systems can provide us new opportunities to create tissue or organ-like environments in a physiologically relevant and tissue/organ-specific context. Especially, the microfluidics-based organ chips can offer fluidic shear stress with digital equipment, three-dimensional environment with porous membranes and hydrogels, and cost-efficiency due to the small processing volume. Thus microfluidics-based organ chips allow us to

understand the cell and tissue functions (e.g., cell-cell, cell-mechanical cues, and tissue-tissue interaction) *in vitro*, although efforts to develop integrated tissue or organ platforms mimicking complex whole body physiology in a single platform (e.g., body-on-a-chip) are still important challenges. Furthermore, incorporation of various cues such as electrically active and mechanically dynamic environment is challengeable.

## **2.5. Discussion**

Although the present tissue engineering strategies have presented bridges in between the *in vivo* and *in vitro*, it seems that several limitations in terms of fabrication technique exist. First of all, the resolution of fabrication technique is still of primary challenge in tissue engineering. Especially, the utilization of fabrication methods requiring high resolution photolithography (few hundreds of nanometers or below) is still limited due to the high processing cost (e.g. preparation of nanoscale mold in soft lithography technique). Second, the functional materials with moderate processability are still in demand. Since the various tissues in human body have various electrical, mechanical properties as well as topology, the mechanically and electrically tunable biocompatible materials can enlighten the field of biomedical engineering. Third, the 3D organization with controlled porosity and orientation is required. Although the hydrogel engineering has partly resolved such demand on 3D environment, it still cannot recapitulate aligned fibrous morphologies which are frequently observed in tissues such as brain, ligament, and heart.

As well as the limitations in fabrication techniques, we believe that there is still further room for more physiologically and functionally similar native tissues. In this context, biologically inspired design principles must be emphasized more in micro- and nanoengineering

strategies (Fig. 2.1). For example, multiscale topographical engineered platforms with highly controlled size closely resembling the *in vivo*-like ECM or tissue topography, in combination with other engineered systems mentioned above [i.e. multiscale structures + multiple cues (mechanical, electrical, chemical, and biological)], would regulate cellular structure and function with more precision to enable functional tissue assembly. As an alternative aspect, the ‘scaled-up’ platforms of micro- and nanoengineering systems (e.g. large scaffolds with *in vivo*-like nanotopographies) are also crucial since most of the studies reported recently focus on proof-of-concept with miniaturized system. In addition, we believe that future strategies will involve monitoring the state of tissues under regeneration in a real-time manner, and dynamically responding to the tissue state by secreting growth factors or drugs in timely fashion, or by irradiating light to the light-sensitive tissues for micro-stimulation [27, 28]. We envisage that biologically inspired micro- and nanoengineering systems may encourage the next revolution to shed light on the path to advanced cell and tissue engineering.

## 2.7. References

- [1] Johnson, P.C., Mikos, A.G., Fisher, J.P., and Jansen, J.A. Strategic directions in tissue engineering. *Tissue Engineering* **13**(12), 2827–2837, 2007
- [2] Atala, A., Kasper, F.K., and Mikos, A.G. Engineering complex tissues. *Science Translational Medicine* **4**(160), 160rv12, 2012.
- [3] Langer, R., and Vacanti, J.P. Tissue engineering. *Science* **260**, 920–926, 1993.
- [4] Kim, H.N., Jiao, A. Hwang, N.S. Kim, M.S. Kang, D.H. Kim, D.H., et al. Nanotopography-guided tissue engineering and regenerative medicine. *Advanced Drug Delivery Reviews* **65**, 536–558, 2013.

- [5] Harrison, R.G. On the stereotropism of embryonic cells. *Science* **34**, 279-281, 1911
- [6] Lo, C. M. Wang, H. B. Dembo, M., and Wang, M.L. Cell movement is guided by the rigidity of the substrate. *Biophysical Journal* **79**, 144–152, 2000.
- [7] Carter, S.B. Principles of cell motility: the direction of cell movement and cancer invasion. *Nature* **208**, 1183–1187, 1965.
- [8] Zhao, M. Song, B. Pu, J., Wada, T., Reid, B., Tai, G., et al. Electrical signals control wound healing through phosphatidylinositol-3-OH kinase-gamma and PTEN. *Nature* **442**, 457–460, 2006.
- [9] Petrie, R.J., Doyle, A.D., and Yamada, K.M. Random versus directionally persistent cell migration. *Nature Reviews Molecular Cell Biology* **10**, 538–549, 2009.
- [10] Zigmond, S.H., and Hirsch, J.G. Leukocyte locomotion and chemotaxis – new methods for evaluation and demonstration of a cell-derived chemotactic factor. *Journal of Experimental Medicine* **137**, 387–410, 1973.
- [11] Kim, H.N., Kang D.H., Kim, M.S., Jiao, A., Kim, D.-H., and Suh, K.Y. Patterning methods for polymers in cell and tissue engineering. *Annals of Biomedical Engineering* **40**, 1339–1355, 2012.
- [12] Kim, D.H., Lipke, E.A., Kim, P., Cheong, R., Thompson, S., Delannoy, M., et al. Nanoscale cues regulate the structure and function of macroscopic cardiac tissue constructs. *Proceedings of the National Academy of Sciences of the United States of America* **107**, 565–570, 2010.
- [13] Zorlutuna, P., Annabi, N., Camci-Unal, G., Nikkhah, M., Cha, J. M., Nichol, J. W., et al. Microfabricated biomaterials for engineering 3D tissues. *Advanced Materials* **24**, 1782–1804, 2012.
- [14] Shea, L.D., Smiley, E., Bonadio, J., and Mooney, D.J. DNA delivery from polymer matrices

for tissue engineering. *Nature Biotechnology* **17**, 551–554, 1999.

[15] Kim, S., Lee, H., Chung, M. and Jeon, N.L. Engineering of functional, perfusable 3D microvascular networks on a chip. *Lab on a Chip* **13**, 1489–1500, 2013.

[16] Griffith, L.G. and Swartz, M.A. Capturing complex 3D tissue physiology *in vitro*. *Nature Reviews Molecular Cell Biology* **7**, 211–224, 2006.

[17] Engelmayer, G.C., Cheng, M.Y., Bettinger, C.J., Borenstein, J.T., Langer, R., and Freed, L.E. Accordion-like honeycombs for tissue engineering of cardiac anisotropy. *Nature Materials* **7**, 1003–1110, 2008.

[18] Dvir, T., Timko, B.P., Brigham, M.D., Naik, S.R., Karajanagi, S.S., Levy, O., et al. Nanowired three-dimensional cardiac patches. *Nature Nanotechnology* **6**, 720–725, 2011.

[19] Shin, S.R., Jung, S.M., Zalabany, M., Kim, K., Zorlutuna, P., Kim, S.B., et al. Carbon-nanotube-embedded hydrogel sheets for engineering cardiac constructs and bioactuators. *ACS Nano* **7**, 2369–2380, 2013.

[20] Tian, B.Z., Liu, J., Dvir, T., Jin, L.H., Tsui, J.H., Qing, Q., et al. Macroporous nanowire nanoelectronic scaffolds for synthetic tissues. *Nature Materials* **11**, 986–994, 2012.

[21] Kim, J.H., Kim, D.H., Lim, K.T., Seonwoo, H., Park, S.H., Kim, Y.R., Kim, Y., Choung, Y.H., Choung, P.H., and Chung J.H. Charged nanomatrices as efficient platforms for modulating cell adhesion and shape. *Tissue Engineering Part C: Methods* **18**, 913–912, 2012.

[22] Kim, J., Kim, H.N., Lim, K.T., Kim, Y., Pandey, S., Garg, P., Choung, Y.H., Choung, P.H., Suh, K.P., and Chung J.H. Synergistic effects of nanotopography and co-culture with endothelial cells on osteogenesis of mesenchymal stem cells. *Biomaterials* **34**, 7257–7268, 2013.

[23] Kim, J., Kim H.N., Lim, K.T., Kim, Y., Seonwoo, H., Park, S.H., Lim, H.J., Kim, D.H., Suh, K.P., Choung, P.H., Choung, Y.H., and Chung J.H. Designing nanotopographical density of



extracellular matrix for controlled morphology and function of human mesenchymal stem cells. *Scientific Reports* **3**:3552, 2013

[24] Huh, D., Hamilton, G.A., and Ingber, D.E. From 3D cell culture to organs-on-chips. *Trends in Cell Biology* **21**, 745–754, 2011.

[25] Huh, D., Matthews, B.D., Mammoto, A., Montoya-Zavala, M., Hsin, H.Y., and Ingber, D.E. Reconstituting organ-level lung functions on a chip. *Science* **328**, 1662–1668, 2010.

[26] Huh, D., Leslie D.C., Matthews, B.D., Fraser J.P., Jurek, S., Hamilton, G.A., Thorne, K.S., McAlexander, M.A., and Ingber, D.E. A human disease model of drug toxicity–induced pulmonary edema in a lung-on-a-chip microdevice. *Science Translational Medicine* **4**, 159ra147, 2012.

[27] Kim, T.I., McCall, J.G., Jung, Y.H., Huang, X., Siuda, E.R., Li, Y.H., et al. Injectable, cellular-scale optoelectronics with applications for wireless optogenetics. *Science* **340**, 211–216, 2013.

[28] Hwang, S.W., Tao, H., Kim, D.H., Cheng, H.Y., Song, J.K., Rill, E., et al. A physically transient form of silicon electronics. *Science* **337**, 1640–1644, 2012.

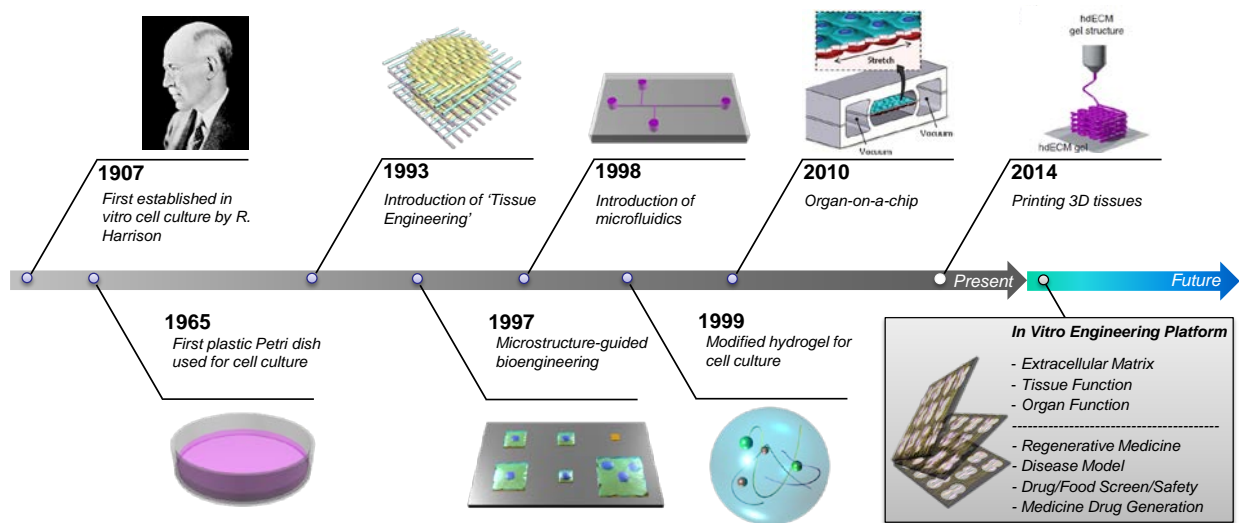


**Figure 2.1. Timelines of major historic events in engineering systems for cell and tissue culture platforms.** Recently, biologically inspired micro- and nanoengineering systems have been proposed as a pioneering approach in the progress of cell and tissue engineering.

## PART I: DESIGNING AND MANIPULATING NANOPATTERNED PLATFORMS WITH PRECISELY CONTROLLED TOPOGRAPHICAL ARCHITECTURES AND SIZES

---

### Overview

From the concept of a ‘cell microenvironment,’ designing nanotopographical platforms is of great important in a wide variety of biological applications such as fundamental biology, therapeutic and diagnostic research, regenerative medicine, and developing *in vitro* disease models. In Part I, inspired from the topographical features of extracellular matrix (ECM), we developed a series of nanofabricated platforms with defined ridge/groove patterns with precisely controlled sizes using capillary force lithography (CFL) to control the nanotopographical density, which no attempts have been made yet in detail. In addition, we used these new platforms as a tool for quantitative analysis of cell behaviors, implying an existence of potentially optimized nanotopographical density for functions of cells. Chapter 3 showed that the matrix nanotopography with local density of ridge/groove patterns (i.e., ridge = groove = 300, 400, 500, 600, 700, 800 nm, respectively) can direct the adhesion, migration, and production of ECM molecules of fibroblast cells. In particular, *In vitro* wound healing study suggested that the nanotopographical local density of platforms greatly influenced the repaired tissue matrix during dermis wound healing through the controlled cell migration and synthesized fibronectin fibers by topographical cues, showing that the dense nanotopography repaired the dense tissue matrix whereas the sparse nanotopography repaired the sparse tissue matrix. In Chapter 4, we designed and manipulated the matrix nanotopography with controlled density of groove spacing ratio (i.e., matrix nanogrooves with 1:1, 1:3, and 1:5 spacing ratio (width:spacing, width = 550 nm)) using CFL. We investigated the detailed stem cell-substrate interaction in terms of cell adhesion and

function. In response to the nanotopographical density, the adhesion, migration, and differentiation of stem cells were sensitively controlled. Importantly, it was found that the osteo- or neurogenesis of stem cells were enhanced at the 1:3 spacing ratio rather than 1:1 or 1:5 spacing ratio, implying an existence of potentially optimized nanotopographical density for stem cell function. Furthermore, the potential mechanisms of such phenomena were explored. Our findings in Part I propose that nanotopographical density greatly influenced the structure and function of cells, which may be a key parameter for the design and manipulation of functional cell culture platforms or scaffolds.

## **Chapter 3. Nanotopographic Pattern Arrays with Variable Local Sizes for Engineering Adhesion and Migration of Fibroblast Cells**

### **3.1. Summary**

Anisotropic nanotopographic pattern arrays with variable local sizes in the form of uniformly-spaced ridge/grooved nanosurfaces were designed and fabricated as synthetic extracellular matrixs (ECMs) for the analysis of cell-architectures of ECM interactions. The nanopatterned platforms with the variable ridge width and groove widths (ranged from 300 nm to 800 nm; defined as dense nanotopography (300 - 400 nm), intermediate nanotopography (500 - 600 nm), and sparse nanotopography (700 - 800 nm)) allowed us to characterize the effect topographical cues of ECM architectures on cellular responses including cell shape, orientation, migration, and function. The morphology and focal adhesion of NIH 3T3 fibroblast cells were quite sensitive to the defined nanoengineered platforms, showing that the maximal speeds of cells were observed on the dense nanotopography (i.e., 300 - 400 nm patterned platforms) whereas the maximal synthesized fibronectin fibers from cells were observed on the intermediate nanotopography (i.e., 500 - 600 nm patterned platforms). *In vitro* wound healing study suggested that the nanotopographical sizes of platforms greatly influenced the repaired tissue matrix in the processing dermis wound healing through the controlled cell migration and synthesized fibronectin fibers by topographical cues, showing that the dense, intermediate, and sparse nanotopography repaired the dense, intermediate, and sparse tissue matrix, respectively. The described experimental platform could be used not only for further understanding of biomechanical regulation of cell–matrix interactions, but also for contribution to bioengineering of devices with the optimally structured design of cell–material interface.

### 3.2. Introduction

Living cells display high sensitivity to the local architectures of complex and well-defined structures of extracellular matrix (ECM) that can regulate the fate and function of cells [1-3]. The structure of the natural ECM frequently reveals hierarchical structures with many protein fibers such as fibrillar collagens and elastins with feature sizes ranging from tens of nanometers to several hundred microns [3]. For example, connective tissues are commonly composed of bundles of micro- and nanoscale fibrils in parallel to each other and attached various cells to them [6], suggesting that topographic features of the surrounding ECM might play a crucial role in regulation of the physiologically relevant cellular function *in vivo*. Inspired by such ultrastructural observations, it has been studied that surface topography which models features encountered in the native ECM can profoundly affect various cell behaviors such as morphology [7,8], migration [9-11], proliferation [12,13], and differentiation [14-16]. In this context, ongoing research has provided important insights into the use of topographically defined patterns as an enabling tool to a wide variety of biological applications such as fundamental biology, therapeutic and diagnostic research, regenerative medicine, and developing *in vitro* disease models.

Despite the significant findings mentioned above, current efforts in designing and manipulating synthetic ECMs still have large gap and limitation in several aspects, in order to fully understand the cellular response to topographical cues. First, most studies have dealt with a simple topographical design, especially in nanoscale features, because of the limited nanofabrication techniques such as complex, time consuming, and expensive with less control over feature size. Second, a systematic analysis on the fate and functions of cells in response to nanotopographical cues (e.g., various local densities in nanoscale) has not been largely

performed. For example, it has been reported that cellular behavior such as cell shape, orientation, and migration was greatly influenced by the variable micro-topographic pattern densities; fibroblast cells adhering to the denser pattern areas aligned and elongated more strongly along the direction of micro-ridges, vs. those on the sparser areas, exhibiting a biphasic dependence of the migration speed on the micro-pattern density [17]. However, cell responses to a nanotopographical local density are still unexplored even though the density of ECM is known as a critical mediator in maintaining integrity, homeostasis and remodeling of mechano-sensitive tissues [18,19].

Here we describe the design and manipulation of matrix nanotopography with variable local pattern density using ultraviolet (UV)-assisted capillary force lithography (CFL) as a model platform of ECM for investigating the relationship between nanotopographical local density and cellular behavior. It is hypothesized that the defined nanotopographical density would be an important factor for controlling morphology and function of cells as well as fundamental biological processes such as wound healing. We investigated whether the cytoskeletal organization, focal adhesion, migration, and function of fibroblast cells were regulated by the nanotopographical local density. Furthermore, inspired from the various densities of tension lines in dermis, the crucial role of nanotopographical local density in dermal wound healing processing was proposed.

### **3.3. Materials and methods**

#### **3.3.1. Fabrication of poly(urethane acrylate) (PUA) mold**

Silicon wafers were spin-coated with a photoresist (Shipley, Marlborough, MA) and then patterned via electron-beam lithography (JBX-9300FS, JEOL). After photoresist development

(MF320, Shipley), exposed silicon was deep reactive ion etched (STS ICP Etcher) to form arrays. The remaining photoresist on silicon wafers was removed using ashing process (BMR ICP PR Asher) and then diced into silicon masters for subsequent replica molding.

To fabricate topographic nanopattern arrays, poly(urethane acrylate) (PUA) was used as a mold material from the silicon master. Briefly, a UV-curable PUA precursor (Minuta Tech., South Korea) was drop-dispensed onto the master and brought into contact with a 100  $\mu\text{m}$ -thick polyethylene terephthalate (PET) film (SKC Inc., South Korea) as a backing plane. After subsequent irradiation of UV for few tens of seconds, a negative PUA replica was formed on the PET film.

### **3.3.2. Design and fabrication of matrix nanotopography**

Regularly spaced ridge and groove with the different width of 300, 400, 500, 600, 700, and 800 nm of nanomatrix were replicated from the prefabricated master PUA molds over a large area of  $25 \times 25 \text{ mm}^2$ . Prior to application of the PUA mold, the glass substrate was cleaned with isopropyl alcohol (IPA), thoroughly rinsed in distilled ionized water, and then dried in a stream of nitrogen. Subsequently, an adhesive agent (phosphoric acrylate: propylene glycol monomethyl ether acetate = 1:10, volume ratio) was spin-coated to form a thin layer ( $\sim 100 \text{ nm}$ ) for 30 s at 3000 rpm. A small amount of the same PUA precursor was drop-dispensed on the substrate and a PUA mold was directly placed onto the surface. The PUA precursor spontaneously filled the cavity of the mold by means of capillary action and was cured by exposure to UV light ( $\lambda = 250\text{--}400 \text{ nm}$ ) for  $\sim 30 \text{ s}$  through the transparent backplane (dose =  $100 \text{ mJ cm}^{-2}$ ). After curing, the mold was peeled off from the substrate using a sharp tweezer.



### **3.3.3. Culture of cells on matrix nanotopography**

NIH3T3 fibroblast cells ( $4 \times 10^4$  cells/matrix) were seeded onto nanomatrices and cultured in Dulbecco's modified Eagle's medium (DMEM; Sigma-Aldrich, Milwaukee, WI, USA) with 10% fetal bovine serum (FBS; Sigma-Aldrich, Milwaukee, WI, USA) and 1% antibiotics (Sigma-Aldrich, Milwaukee, WI, USA) at 37°C in a humidified atmosphere containing 5% CO<sub>2</sub>.

### **3.3.4. Immunofluorescence staining**

Adhered cells on samples were fixed with a 4% paraformaldehyde solution (Sigma-Aldrich, Milwaukee, WI, USA) for 20 min, permeabilized with 0.2% Triton X-100 (Sigma-Aldrich, WI, Milwaukee, USA) for 15 min, and stained with TRITC-conjugated phalloidin (Millipore, Billerica, MA, USA) and 4, 6-diamidino-2-phenylindole (DAPI; Millipore, Billerica, MA, USA), or or fibronectin antibody (Sigma-Aldrich, WI, Milwaukee, USA) for 1 h. Focal adhesions (FAs) were also stained with a monoclonal antivinculin antibody (1:100; Millipore, Billerica, MA, USA) and a FITC-conjugated goat antimouse secondary antibody (1:500; Millipore, Billerica, MA, USA). Images of the stained cells were taken using a fluorescence microscope (Zeiss, Germany). For the quantitative analysis of the body and nuclear shape of cells on the substrata, the images obtained by fluorescence microscopy were analyzed using the custom written MATLAB script.

### **3.3.5. Analysis of migration**

We utilized a thin polydimethyl siloxane (PDMS) slab to generate a cell-free area for investigating migration of cells on the samples. Specifically, a 200 mm-thick PDMS sheet was cut into slabs with width of 500 mm and length of 20 mm using two intact sharp blades. The

PDMS slabs were placed onto the samples. Due to conformal sealing of the thin PDMS slab, no cells were shown to grow on the protected area.

### **3.3.6. Statistical analysis**

Student's t-test was used for statistical analysis. All quantitative results were presented as mean  $\pm$  standard deviation (SD).

## **3.4. Results**

### **3.3.1. Design and fabrication of matrix nanotopography with various local densities**

In the body, various ECMs exist in the form of well-organized nanoscale protein fibers, and they are naturally oriented toward certain directions for tissue-specific functions [3,4]. In particular, previous ultrastructural analysis showed that there are naturally anisotropic ECM nanostructures with various length scales in the human tissues including skin [3,4,14], suggesting that the nanotopographical control of ECM, especially according to the local density, may provide an essential route to guiding the structure and function of cells.

Guided by these considerations, we mimicked the anisotropically nanotopographical density of natural ECM using UV-assisted CFL with UV-curable PUA polymer (Fig. 3.1a). The fabricated topographic pattern was composed of an array of parallel ridges/grooves with variable spacing (i.e., 300 – 800 nm) with 400 nm high as verified by SEM (Fig. 3.1b). These platforms were expected to not only provide the local density variation of cell adhesion substratum topography, but also allow collection of sufficient data for statistically significant quantitative analysis.

### **3.3.2. Analysis of cell morphological response to nanotopographical local density**

Using topographically defined ridge/groove patterns on synthetic ECMs as described above, we analyzed cell morphological response to nanotopographical local density. To this end, the NIH3T3 fibroblast cells were culture on the synthetic ECMs for 12 h for allowing fully adhesion of cells to the substrates, and then the immunofluorescence staining analysis was used to observe cell morphology in detail. As shown in Fig 3.2, the nanotopographical local density greatly influenced the cell shape and polarity as supported by the aligned cytoskeletal structure of cells in response to various nanotopographical densities. Regardless of nanotopographical density property, cells were aligned along the direction of nanotopographical features. On the other hand, interestingly, a biphasic trend was observed in terms of cell elongation; the cell elongation first highly increased from the dense nanotopography (defined as 300 and 400 nm ridge/groove sizes) to the intermediate nanotopography (defined as 500 and 600 nm ridge/groove sizes) and then decreased at the sparse nanotopography (defined as 700 and 800 nm ridge/groove sizes). Unlike the no difference trend of cell widths, the lengths of cell body to the nanotopographical density were higher at the intermediate nanotopographies as compared to the other denser or sparser nanotopographies (Fig. 3.2b), eventually guiding the elongation features of cell body (Fig. 3.2c). Taken together, these findings suggest that the local density of ridges/grooves in nanoscale of ECM may play a key role to control cellular shape that can regulate the function of cells.

### **3.3.3. Analysis of cell orientation and migration by nanotopographical local density**

The cell orientation angle relative to the grooves/ridges was measured to determine how cells were directionally sensitive to the nanotopographical local density. As shown in Fig. 3.3a, regardless of nanotopographical density property, NIH3T3 fibroblast cells were well orientated

along the direction of nanotopographical features. This suggests that the nanotopographical local density in the nanoscale ( $< 1 \mu\text{m}$ ) strongly guide the body along the direction of topographical patterns.

Next, we investigated whether cells migration was affected along the direction of topographical local density. To this end, we analyzed the migration speed of NIH3T3 fibroblast cells in the different local topographic densities. Higher cell migration speeds were observed on the nanopatterned substrates regardless of nanotopographical density property compared to that on the flat substrate (Fig. 3.3b). On the other hand, we observed that a significantly higher cell migration speed on the topographical local density with 300 nm ridge/groove sizes compared to those on the other topographical local densities (Fig. 3.3b). Interestingly, it has been found that cell migration speed was in directly inverse proportion to the topographical sizes (i.e., dense  $>$  intermediate  $>$  sparse nanotopography) even though cell elongation depended biphasically on the topographic density. Our data thus suggest that the migration of cells may be sensitive to the local density of nanotopography, and the denser nanotopography may elicit faster migration of cells than the sparser ones.

#### **3.3.4. Analysis of orientation of stress fibers distribution and focal adhesions of cells by nanotopographical local density**

We demonstrated that the nanotopographical local density affected the (i) cell shape and (ii) cell migration (Figs. 3.2 and 3.3) while there was no correlation between two factors. Thus we analyzed the interactions between cell and nanotopographical local density in terms of the orientation of stress fibers distribution and focal adhesions (FAs) of cells. To this end, we cultured NIH3T3 fibroblast cells on the synthetic ECMs for 12 h. To investigate the effects of

cytoskeleton and FA by the nanotopographical local density, the immunofluorescence staining analysis was used (Fig. 3.4a). We observed that the stress fibers of cells were polarized along the direction of nanotopography, being more polarized with the denser nanotopographical local density as compared to the relatively sparser nanotopographical local density (i.g., 300 nm > 500 nm > 800 nm), suggesting that the sparser nanotopographical local density may allow cells enough ridge/groove spaces to form the stress fibers with various orientations whereas the denser nanotopographical local density did not (Fig. 3.4a). In case of formation of FAs, we showed well-polarized FAs along the direction of nanotopography regardless of local density (Fig. 3.4a).

To analyze the effects of FAs and stress fibers distribution of cells by nanotopographical local density in further detail, we performed the quantitative analysis. We observed that the nanotopographical local density affected the size of FAs; as shown in Fig. 3.4b, larger FA sizes were observed on the sparser nanotopographical local density than on the denser nanotopographical local density. In particular, the FA sizes were smaller on the 300 nm ridge/groove sizes than those on the flat surface (Fig. 3.4b). Our correlative analysis between cytoskeleton and FAs showed that there was a higher correlation between the orientations of the actin filaments and vinculin bands in the cells on the denser nanotopographical local density (Fig. 3.4c) compared to that on the sparser nanotopographical local density (Fig. 3.4d). As shown in Fig. 3.4e, we demonstrated that nanotopographical local density greatly affected the co-localization of the stress fibers distribution and FAs in cells, showing in directly inverse proportion to the topographical sizes (i.e., dense > intermediate > sparse nanotopography).

From the analysis of stress fibers distribution and FAs of fibroblast cells with the nanotopographical local density cues, we have shown an interesting finding. That is, the denser nanotopographical local density showed lower affinity and well-distributed stress fibers of cells

on the substrates compared to those on the sparse nanotopographical local density, which was highly correlated with the trend of cell migration speeds (Fig. 3.3b). In addition, to verify whether the nanotopographical local density can affect molecular signaling, we checked the upregulation of phosphorylated-ERK (p-ERK), which is involved in mediating cell functions. As shown in Fig. 3.S1, we found that the ERK was upregulated at the topographical local density with 300 nm ridge/groove sizes and then decreased at the topographical local density with 500 nm ridge/groove sizes, showing a similar trend to the case of migration of cells (Fig. 3.3b). Therefore, our data strongly suggest that the nanotopographical local density may have reconstructed their mechanotransduction pathway, guiding the function of cells.

### **3.3.5. Analysis of cell morphology and organization of produced ECM proteins by nanotopographical local density in multi-cells level**

To investigate the morphology of cells by the nanotopographical local density in the multi-cells level, we cultured NIH3T3 fibroblast cells on the synthetic ECMs for 7 days. As shown in Fig. 3.5a, regardless of the nanotopographical local density, the cells showed aligned and orientated along the direction of nanotopography. When the cells were cultured on the flat and nanopatterned surfaces in one platform, the cells still showed highly aligned and orientated morphologies on the nanopatterned regions (Fig. 3.S2). We also observed a biphasic trend in terms of cell elongation (Fig. 3.5a); the cell elongation first highly increased from the dense nanotopography to the intermediate nanotopography and then decreased at the sparse nanotopography, which was similar to those observations in single cell level (Fig. 3.2). To analyze in detail, the elongation factor of nucleus was calculated (Fig. 3.5b), showing higher values at the 500 nm ridge/groove sizes of synthetic ECMs. This result indicates that the local

density of ridges/grooves in nanoscale of ECM may control the cell organization in multi-cells level, which may influence the tissue organization in various biological processes including wound healing.

Next, we investigated whether the nanotopographical local density could influence the the production of new ECM proteins from cells. To this end, the fibronectin was visualized for the ECM organization analysis (Figs. 3.5a and S2). As shown in Figs. 3.5.a and S3, it was found that the aligned fibronectin fiber bundles was synthesized from NIH3T3 fibroblast cells cultured for 7 days, regardless of the nanotopographical local density. On the other hand, it was also found that the nanotopographical local density biphasically influenced the sizes of polarized fiber bundles on the substrates; the average length sizes of the synthesized fibronectin fiber bundles first increased from the dense nanotopography to the intermediate nanotopography and then decreased at the sparse nanotopography (Figs. 3.5a and c). Interestingly, such increases of length of fiber bundles were highly correlated with the cell elongations (Fig. 3.5.a and b), suggesting that the morphology of cells may be associated with the reorganization of the ECM fibers. Taken together, our data strongly indicate that the angular distribution and length of ECM fibers secreted from the fibroblast cells can be guided through the nanotopographical local density.

### **3.3.6. *In vitro* dermal wound healing assay**

Based on our data in this work (Figs. 3.2-5) (i.e., the nanotopographical local density essentially affected (i) the cell morphology, (ii) the cell migration speed, and (iii) the production of new ECM proteins) as well as inspired from the inherent tension line with different density in dermis (Fig. 3.6a), we hypothesized that nanotopographical local density would be a major factor for dermal wound healing through the topographical cues (i.e., contact guidance). To investigate

the role of the topographic density in dermal wound healing, we cultured NIH3T3 fibroblast cells on the synthetic ECMs in the *in vitro* wound healing model (Fig. 3.6b); the cells migrated into the cell free area (target area), and the covering rate of cells was evaluated with a similar method reported earlier [10].

Fig. 3.6b explained the experimental design where a thin PDMS slab was first placed onto the synthetic ECMs before cell seeding. Then, NIH3T3 fibroblast cells were cultured until confluency. When the confluence monolayer was observed, the PDMS slab was removed, letting the cells migrate and proliferate into the empty region. The images were taken for analyzing covered area in the *in vitro* wound healing model. As shown in Fig. 3.6c, the time-lapse observation for 48 h demonstrated that, regardless of the nanotopographical local density, cells were fully covered in the *in vitro* wound healing model. On the other hand, interestingly, the maximum covering rate was observed on the 300 nm ridge/groove sizes on synthetic ECMs; it was found that the covering rate was in directly inverse proportion to the topographical sizes (i.e., dense > intermediate > sparse nanotopography), showing the similar trends to cell migration speeds (Fig. 3.3b).

Next, we examined the organization of cytoskeleton and synthesized fibronectin fiber bundles in the cell-filled area by wound healing processing for 48 h (Fig. 3.6d). Interestingly, it was found that the denser nanotopographical local density (i.e., 300 and 400 nm ridge/groove sizes) showed highly anisotropically organized cells and synthesized fibronectin fiber bundles, whereas the sparser nanotopographical local density (i.e., 700 and 800 nm ridge/groove sizes) showed less organized cells and synthesized fibronectin fiber bundles (Fig. 3.6d). Taken together, these observations proposed that the nanotopographical local density control the wound healing processing through the topographical contact guidance to the cells (Fig. 3.7).



### 3.5. Discussion

In this work, we fabricated the cell culture platforms with the property of various nanotopographical densities inspired from the well-aligned natural ECMs. Using these platforms, we demonstrated the effects of nanotopographical local density on the morphology and differentiation of NIH3T3 fibroblast cells. We found that the local density of ridges/grooves in nanoscale can control the body and nucleus of cells in single cell or multi-cells level. In particular, the significantly higher cell migration speed on the topographical local density with 300 nm ridge/groove sizes compared to those on the other topographical local densities and the cell migration speed was in directly inverse proportion to the topographical sizes. The stress fibers of cells were polarized along the direction of nanotopography, being more polarized with the denser nanotopographical local density as compared to the relatively sparser nanotopographical local density. The larger FA sizes were observed on the sparser nanotopographical local density than on the denser nanotopographical local density. The denser nanotopographical local density showed lower affinity and well-distributed stress fibers of cells on the substrates compared to those on the sparse nanotopographical local density. Our *in vitro* dermal wound healing study demonstrated that the maximum covering rate was observed on the 300 nm ridge/groove sizes on synthetic ECMs. Interestingly, it was found that the denser nanotopographical local density (i.e., 300 and 400 nm ridge/groove sizes) showed highly anisotropically organized cells and synthesized fibronectin fiber bundles, whereas the sparser nanotopographical local density (i.e., 700 and 800 nm ridge/groove sizes) showed less organized cells and synthesized fibronectin fiber bundles. We believe that the current work has revealed that the local density of nanotopography may be able to regulate the structure and function of cells, which will be an efficient strategy for designing cell culture platforms and scaffolds,

especially for skin regeneration as well as for understanding fundamental stem cell biology.

### **3.6. References**

- [1] Matthew J. Dalby, Nikolaj Gadegaard and Richard O. C. Oreffo. Harnessing nanotopography and integrin–matrix interactions to influence stem cell fate. *Nature materials* 13, 558-569 (2014).
- [2] Yue Shao and Jianping Fu. Integrated micro/nanoengineered functional biomaterials for cell mechanics and mechanobiology: a materials perspective. *Adv. Mater.* 26, 1494-1533 (2014)
- [3] Kim, D. H., Provenzano, P. P., Smith, C. L. & Levchenko, A. Matrix nanotopography as a regulator of cell function. *J. Cell Biol.* 197, 351–360 (2012).
- [4] Kim, H. N. et al. Nanotopography-guided tissue engineering and regenerative medicine. *Adv. Drug Deliv. Rev.* 65, 536–558 (2013).
- [5] Kim J., Kim H.N., Lang Y., Pandit A. Biologically inspired micro- and nanoengineering systems for functional and complex tissues. *Tissue Eng: Part A* (2014).
- [6] Ottani V, Raspanti M, Ruggeri A. Collagen structure and functional implications. *Micron* 32(3):251–60 (2001)
- [7] Teixeira AI, Abrams GA, Bertics PJ, Murphy CJ, Nealey PF. Epithelial contact guidance on well-defined micro- and nanostructured substrates. *J Cell Sci.* 116(10):1881–92 (2003).
- [8] Crouch AS, Miller D, Luebke KJ, Hu W. Correlation of anisotropic cell behaviors with topographic aspect ratio. *Biomaterials* 30(8):1560–7 (2009).
- [9] Kim DH, Seo CH, Han K, Kwon KW, Levchenko A, Suh KY. Guided cell migration on microtextured substrates with variable local density and anisotropy. *Adv Funct Mater* 19, 1579–86 (2009).
- [10] Kim HN et al., Effect of orientation and density of nanotopography in dermal wound

healing. *Biomaterials* 33, 8782–92 (2012)

[11] Diehl KA, Foley JD, Nealey PF, Murphy CJ. Nanoscale topography modulates corneal epithelial cell migration. *J Biomed Mater Res A* 75(3):603–11 (2005).

[12] Liliensiek SJ, Campbell S, Nealey PF, Murphy CJ. The scale of substratum topographic features modulates proliferation of corneal epithelial cells and corneal fibroblasts. *J Biomed Mater Res A* 79(1):185–92 (2006).

[13] Christopherson GT, Song H, Mao H-Q. The influence of fiber diameter of electrospun substrates on neural stem cell differentiation and proliferation. *Biomaterials* 30(4):556–64 (2009).

[14] Kim J et al. Designing nanotopographical density of extracellular matrix for controlled morphology and function of human mesenchymal stem cells. *Sci Rep* 3:3552 (2013).

[15] Kim J et al. Synergistic effects of nanotopography and co-culture with endothelial cells on osteogenesis of mesenchymal stem cells. *Biomaterials* 34, 7257–68 (2013).

[16] McMurray RJ et al. Nanoscale surfaces for the long-term maintenance of mesenchymal stem cell phenotype and multipotency. *Nat Mater* 10, 637–44 (2011).

[17] D. H, Kim et al., Mechanosensitivity of fibroblast cell shape and movement to anisotropic substratum topography gradients. 30, 5433-5444 (2009).

[18] Fisher, G. J., Varani, J. & Voorhees, J. J. Looking older: fibroblast collapse and therapeutic implications. *Arch. Dermatol.* 144, 666–672 (2008).

[19] Klein-Nulend, J., Bacabac, R. & Bakker, A. Mechanical loading and how it affects bone cells: The role of the osteocyte cytoskeleton in maintaining our skeleton. *Eur. Cells Mater.* 24, 278 (2012).

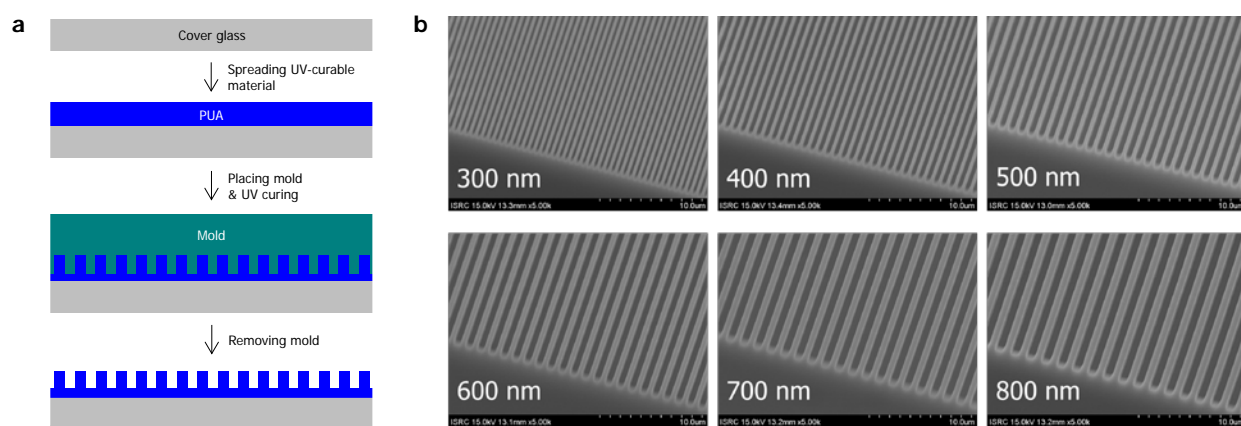


**Figure 3.1. Fabrication of anisotropic nanotopographic pattern arrays with variable local sizes in the form of uniformly-spaced ridge/grooved nanosurfaces as model systems of ECM architectures.** (a) Schematic of the microfabrication process used to generate PUA nanopattern arrays using CFL technology. Drawings are not to scale. (b) SEM image of various nanopatterns used in this study.

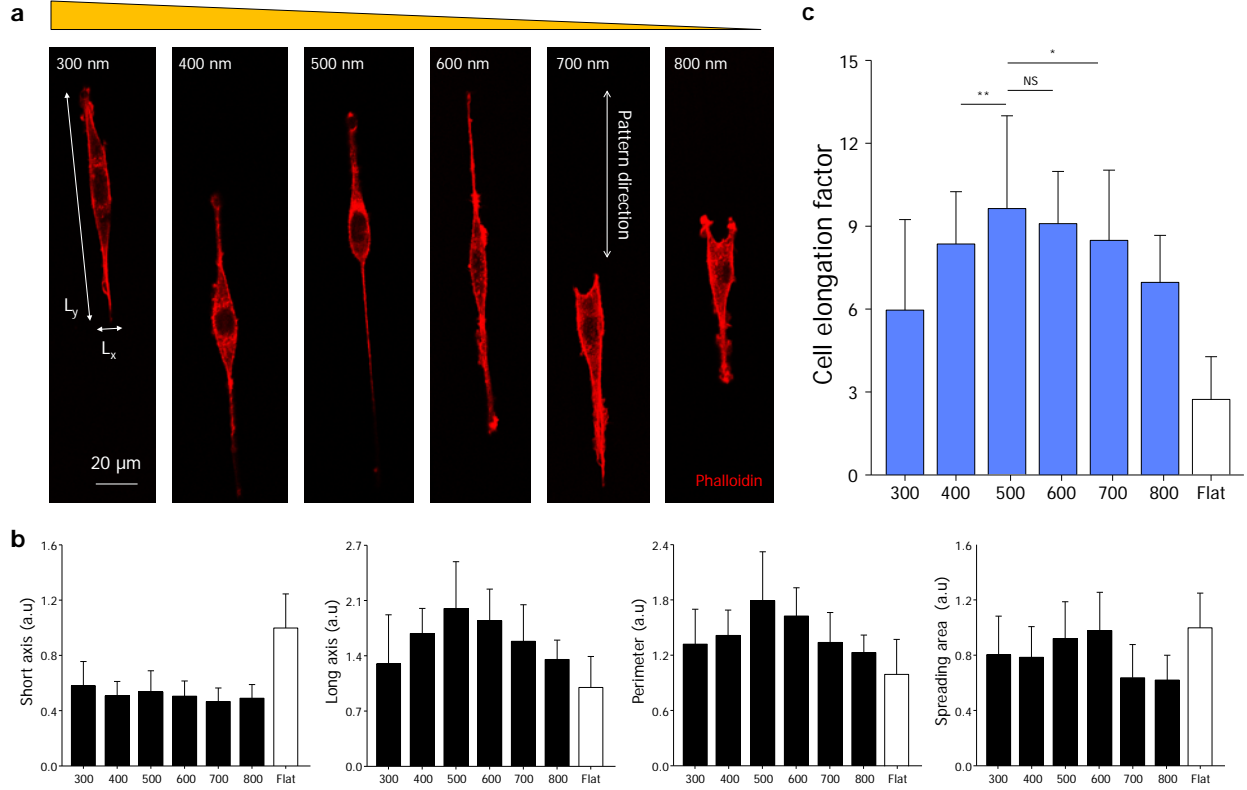


**Figure 3.2. Morphological responses of fibroblast cells to the local density of nanotopographic pattern arrays with variable local sizes in the form of uniformly-spaced ridge/grooved nanosurfaces.** (a) Representative immunostaining images of F-actin (red) of NIH 3T3 fibroblast cells cultured on the various nanopatterned surfaces in single cell level. (b) Quantification of cell body. The values of perimeter and area were normalized to the flat substrates. (c) Quantitative analysis of cell elongation factor (defined as (major axis)/(minor axis)). The 50–100 cells were used for quantification. Error bars represent the SD about the means. The statistical significance was denoted as ‘\*’ ( $p < 0.05$ ) and ‘\*\*’ ( $p < 0.01$ ).

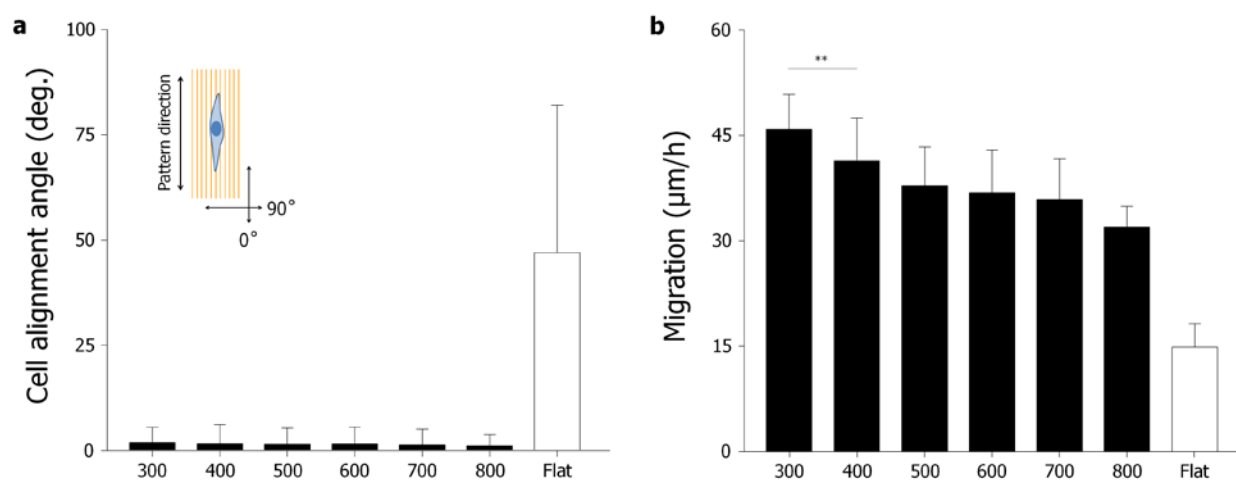


**Figure 3.3. Effects of the local density of nanotopographic pattern arrays on cell alignment and migration.** (a) Quantitative analysis of alignment of fibroblast cells on the platforms with variable local sizes in the form of uniformly-spaced ridge/grooved nanosurfaces. The 50–100 cells were used for quantification. (b) Cell migration speed on the topographic density. Three independent experiments were conducted. Error bars represent the SD about the means. The statistical significance was denoted as “\*\*” ( $p < 0.01$ ).

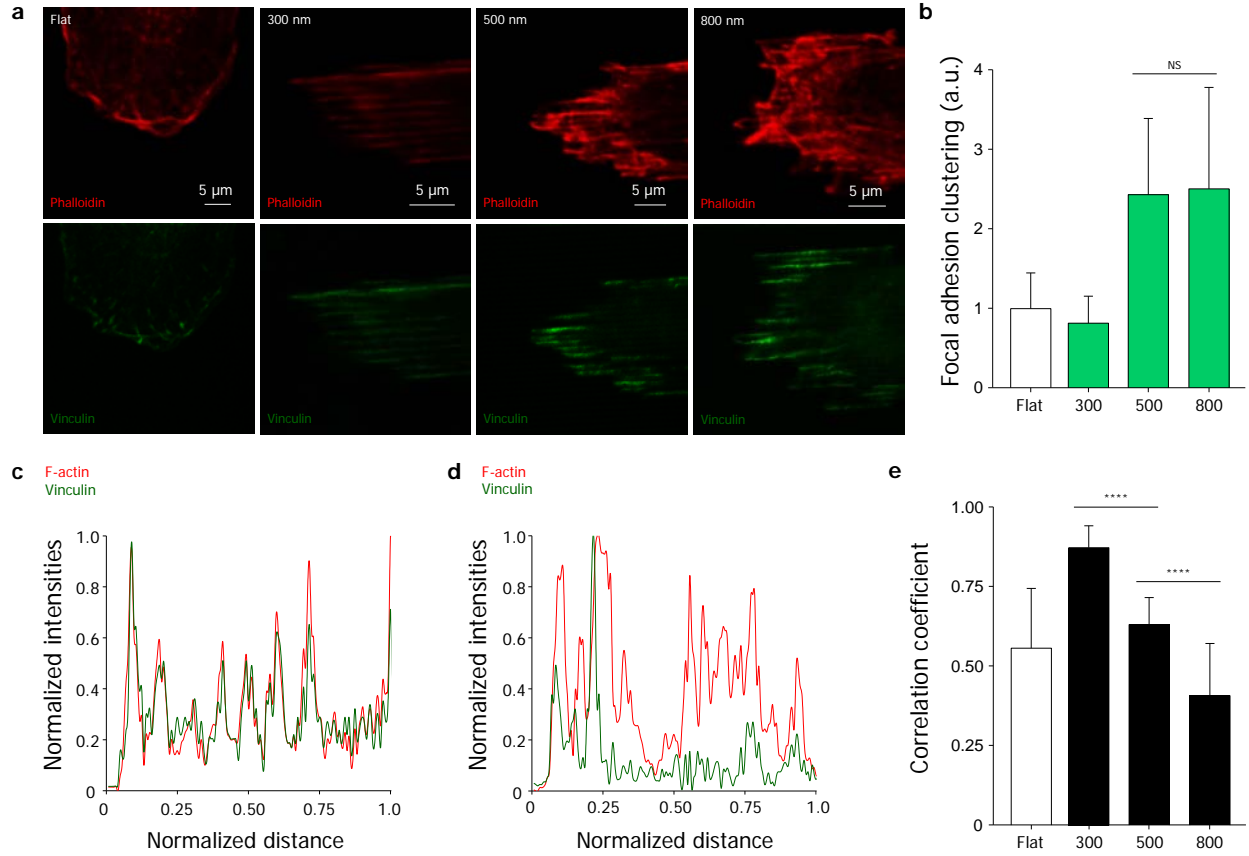


**Figure 3.4. Effects of the local density of nanotopographic pattern arrays on the organization of focal adhesions.** (a) Representative immunostaining images of F-actin (red) and focal adhesion (green), showing the high co-localization between the FAs and actin cytoskeleton of fibroblast cells on the substrates. (b) Focal adhesion clustering index. The 50–100 cells were used for quantification and the values were normalized to the flat substrates. (c-d) Representative spatial co-localization graphs of the actin cytoskeleton and focal adhesions of cells in the lamellipodial region on (c) the dense nanotopography (300 nm) and (d) the sparse nanotopography (800 nm). (e) Quantitative and correlative analysis of the actin cytoskeleton and focal adhesions in the lamellipodial region on the substrates. The 50–100 cells were used for quantification. Error bars represent the SD about the means. The statistical significance was denoted as ‘\*\*\*\*’ ( $p < 0.0001$ ).

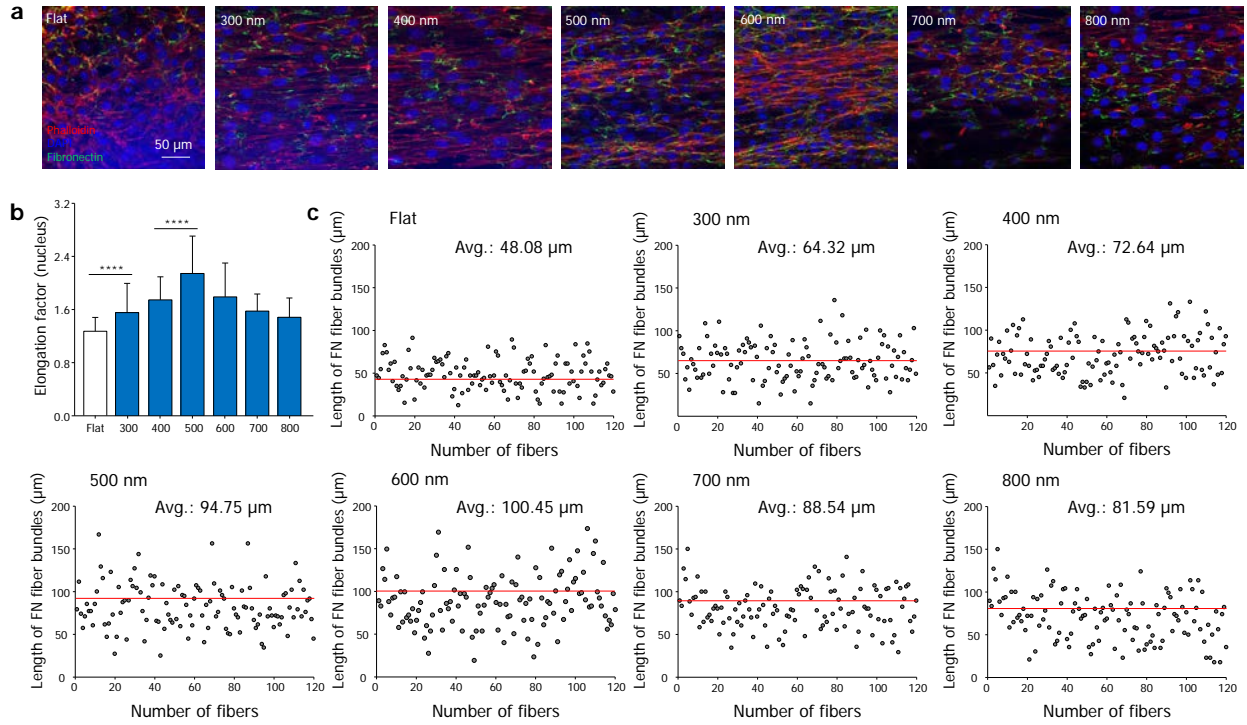


**Figure 3.5. Morphological responses and organizations of produced fibronectin (FN) fibers of fibroblast cells to the local density of nanotopographic pattern arrays with variable local sizes in the form of uniformly-spaced ridge/grooved nanosurfaces in multi cell level. (a)** Representative immunostaining images of F-actin (red), produced FN fibers (green), and nucleus (blue). **(b)** Quantitative analysis of nucleus elongation factor (defined as (major axis)/(minor axis)). The 50–100 cells were used for quantification. **(c)** Quantitative analysis of length of FN fiber bundles synthesized from fibroblast cells cultured on the substrates. Error bars represent the SD about the means. The statistical significance was denoted as ‘\*\*\*\*’ ( $p < 0.0001$ ).



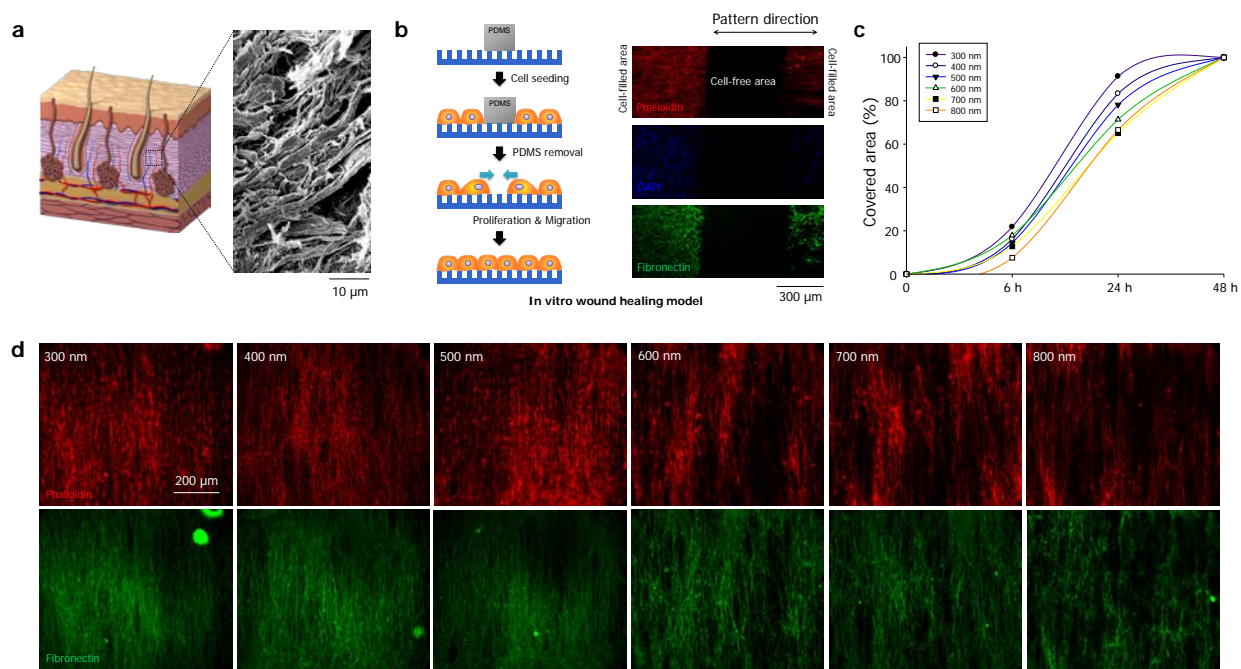


**Figure 3.6. *In vitro* wound healing study with nanotopographic pattern arrays.** (a) A graphical illustration of dermis in skin and SEM image of aligned collagen fiber bundles observed in the dermis of rat skin. The orientation of bundles agrees with the tension line and various tissue densities in skin. (b) Experimental procedure of *in vitro* wound healing study. A thin PDMS sheet was placed onto the nanopatterned surface to be used as a barrier for cell migration. NIH-3T3 fibroblasts were seeded and cultured until reaching confluency. The removal of PDMS sheet allows migration and proliferation of the fibroblasts to fill the cell-free area. (c) Quantification of covered area by fibroblast cells on the local density of nanotopographic pattern arrays with variable local sizes in the form of uniformly-spaced ridge/grooved nanosurfaces. (d) Representative immunostaining images of F-actin (red) and produced FN fibers (green) of repaired area.

Nanotopography	Cell migration	Synthesized FN fiber	Wound healing
<b>Dense</b> (300 – 400 nm)	Fast	Small	<b>Dense repaired matrix</b>
<b>Sparse</b> (700 – 800 nm)	(relatively) Slow	Large	<b>Sparse repaired matrix</b>

**Figure 3.7. A proposed model of the role of nanotopographical density during wound healing.** The nanotopographical sizes of platforms greatly influenced the repaired tissue matrix in the processing dermis wound healing through the controlled cell migration and synthesized fibronectin fibers by topographical cues, showing that the dense, intermediate, and sparse nanotopography repaired the dense, intermediate, and sparse tissue matrix, respectively.

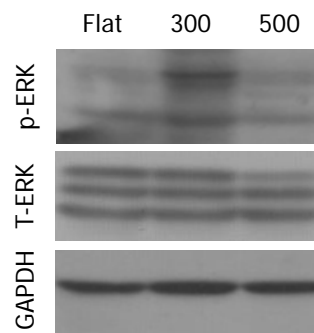


**Figure 3.S1. Western blot analysis of p-ERK and T-ERK expression of fibroblast cells cultured on the substrate.**

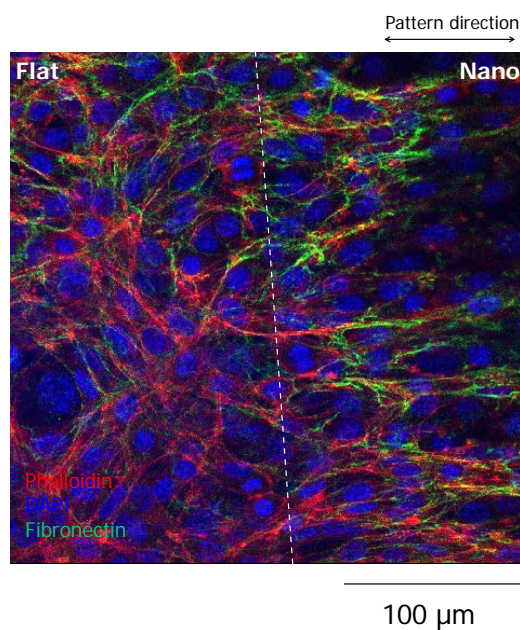


**Figure 3.S2. Morphological responses and organizations of produced fibronectin (FN) fibers of fibroblast cells in multi cell level on the flat and nanosurfaces in one cell culture platform.** Representative immunostaining images of F-actin (red), produced FN fibers (green), and nucleus (blue).

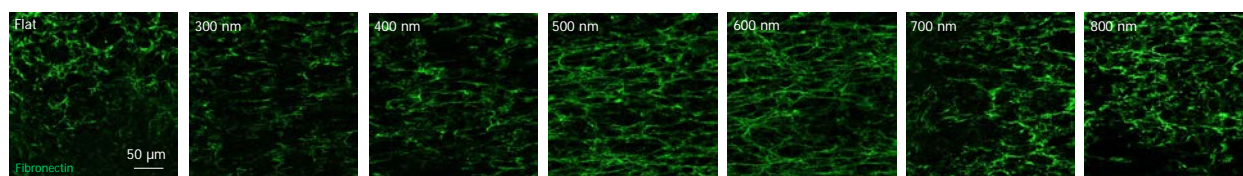


**Figure 3.S3. Organizations of produced fibronectin (FN) fibers of fibroblast cells on the flat and nanopatterned cell culture platform.** Representative immunostaining images of the produced FN fibers (green).

## **Chapter 4. Designing Nanotopographical Density of Extracellular Matrix for Controlled Morphology and Function of Mesenchymal Stem Cells**

### **4.1. Summary**

Inspired by ultrastructural analysis of *ex vivo* human tissues as well as the physiological importance of structural density, we fabricated nanogrooves with 1:1, 1:3, and 1:5 spacing ratio (width:spacing, width=550 nm). In response to the nanotopographical density, the adhesion, migration, and differentiation of human mesenchymal stem cells (hMSCs) were sensitively controlled, but the proliferation showed no significant difference. In particular, the osteo- or neurogenesis of hMSCs were enhanced at the 1:3 spacing ratio rather than 1:1 or 1:5 spacing ratio, implying an existence of potentially optimized nanotopographical density for stem cell function. Furthermore, such cellular behaviors were positively correlated with several cell morphological indexes as well as the expression of integrin  $\beta 1$  or N-cadherin. Our findings propose that nanotopographical density may be a key parameter for the design and manipulation of functional scaffolds for stem cell-based tissue engineering and regenerative medicine.

## 4.2. Introduction

Stem cells are characterized by their unique ability to differentiate into various types of cells, allowing for many alternatives and opportunities in tissue engineering and regenerative medicine [1-3]. It is therefore important to develop a platform to regulate or improve stem cell functions from an integrative aspect of biology and engineering [1-18]. Stem cells reside within instructive and tissue-specific niches in the body, such as complex and controlled biochemical mixtures of soluble and insoluble factors [7,19]. In particular, it is widely accepted that stem cells display high sensitivity to the extracellular matrix (ECM) composed of complex and well-defined nanostructures of protein fibers such as fibrillar collagens and elastins with feature sizes (diameter and spacing) ranging from tens to several hundreds of nanometers. In conjunction with these observations, previous *ex vivo* and *in vitro* studies suggest that the use of nanotopographical cues hold great potentials to control stem cell functions [1-7,19].

The structure of the natural ECM in various tissues including bone, tooth, nerve, skin, muscle, and heart usually reveals highly oriented grooved structures with various length scales in nanometers (Fig. 4.1a) [1,5]. For example, the concentric nanoscale-thick cylinders enhance mechanical properties of cortical bone, while the aligned collagen matrix in the dermis of skin layer presents anisotropic mechanical properties [1]. Inspired by such ultrastructural observations, the utilization of nanoengineering technology to develop a nanogrooved matrix has been greatly attractive to biologists and engineers in the fields of classical stem biology and regenerative medicine [1,5,20-24]. According to previous studies, the controlled polarity and subsequent mechanical tension turned out to be crucial for the cell behaviors such as spreading [25,26], migration [27,28], proliferation [29], cell division [30], tissue function [31], tissue formation [32], and more importantly differentiation in stem cells [20-22, 33-35]. For example,

Leong's group demonstrated that molded nanogrooves could enhance migration [20], stemness [21], and neurogenesis [22] of hMSCs by inducing nuclear polarity. Dalby's group reported that slightly disordered arrangement of nanoimprinted nanopit arrays could further induce osteogenesis compared to the regularly ordered organization [33,34]. In the case of electrospun fibers, Xia's group showed that unidirectionally aligned matrices elicited more neurogenesis than the randomly oriented ones presumably due to an increased stem cell polarity [35]. In this context, ongoing research has provided important insights into the role of nanotopographical cues as an enabling tool to advance the current stem cell-based tissue engineering and regenerative medicine.

Despite the significant findings mentioned above, there appear a large gap and limitation in several aspects, in order to fully understand the response of stem cells to an anisotropic nanotopographical cue such as nanoridges and nanogrooves. First, most studies have dealt with a simple structural design (e.g., nanopattern vs. flat) partly because the nanofabrication techniques were complex, time-consuming, and expensive with less control over feature sizes [20-24]. Second, the underlying mechanisms behind the nanotopography-guided stem cell differentiation have remained unexplored in terms of cell-substrate and cell-cell interactions. Finally, the fate and functions of stem cells in response to a nanotopographical density have been largely unknown not to mention the differentiation of stem cells via various nanotopographical densities even though the density of ECM is known as a critical mediator in maintaining integrity, homeostasis and remodeling of mechano-sensitive tissues such as bone and skin [36-38].

To address these challenges, we designed and fabricated nanogrooved matrices with various groove densities using ultraviolet (UV)-assisted capillary force lithography (CFL) [39]. It is hypothesized that the defined nanotopographical density would an important factor for

controlling morphology and function of stem cells. We investigated whether the focal adhesion, cytoskeletal organization, migration, proliferation, and differentiation of stem cells were regulated by the nanotopographical density. Furthermore, the correlations among the topography-induced morphologies, intracellular and produced protein levels, and stem cell functions were analyzed.

### **4.3. Materials and methods**

#### **4.3.1. Preparation and observation of *ex vivo* human tissues**

Bone, nerve, and skin tissues were obtained from patients during chronic otitis media surgeries under the approval of the Institutional Review Board of the Ajou University School of Medicine (Suwon, Korea). The tissues were fixed overnight with a solution containing 2% glutaraldehyde, 0.1 M sodium cacodylate, and 3 mM calcium chloride (pH 7.4) at 4°C. The tissues were rinsed three times with PBS. The specimen was perfused with 1% osmium tetroxide and placed on a tissue rotator for 30 min. The sample was then rinsed in PBS three times. The tissues were serially dehydrated in 50%, 70%, 90%, 95%, and 100% of acetone. Each specimen was treated with hexamethyldisilazane (HMDS), air dried, and placed on a stub for sputter-coating with gold. The tissue was then observed with a FESEM (JEOL, JSM-5410LV, Japan).

#### **4.3.2. Design and fabrication of nanogrooved matrices as bioinspired substrata**

Regularly-spaced nanogrooves with the width of 550 nm and three different gaps of 550, 1,650 and 2,750 nm (spacing ratio: 1:1, 1:3, and 1:5, respectively) were replicated from the pre-fabricated silicon masters over a large area of  $25 \times 25 \text{ mm}^2$ . The silicon masters had been prepared by standard photolithography and dry etching. In the replication step, a UV-curable

PUA precursor (Minuta Tech., South Korea) was drop-dispensed onto the master and brought into contact with a 100  $\mu\text{m}$ -thick polyethylene terephthalate (PET) film (SKC Inc., South Korea) as a backing plane. After subsequent irradiation of UV for few tens of seconds, a negative PUA replica was formed on the PET film. Then the same replication process was performed onto a cleaned cover slip using the replicated PUA pattern as a mold. The flat and patterned surfaces were generated on the same cover slip in order to maintain the same experimental conditions. The fabricated samples were coated with gold and imaged by a FESEM (JEOL, JSM-5410LV, Japan) at an accelerating voltage of 2 kV.

#### **4.3.3. Isolation and culturing of hMSCs**

Adipose tissues were isolated from the patients undergoing ear surgeries under sufficient informed consent at the Ajou University School of Medicine (Suwon, Korea). The experimental protocol was approved by the Institutional Review Board at the same university. Tissues were washed with PBS and digested with 100 Unit/mL collagenase type I (Sigma-Aldrich, St. Louis, MO, USA) with low glucose Dulbecco's modified Eagle's medium (DMEM; Gibco-BRL, Grand Island, NY, USA) and incubated for 8 h to lyse the adipose tissues. The stromal fraction was collected by centrifugation and then passed through a cell strainer (100  $\mu\text{m}$  size) to remove any large cell clumps and particles. For cell culture and expansion of adipose-derived hMSCs, cells were grown in low glucose DMEM with 10% fetal bovine serum (FBS) and 1% penicillin-streptomycin (Gibco, Milan, Italy) at 37°C in a 5% CO<sub>2</sub> atmosphere. All cells used in this study were at passage 3 or 4.

#### **4.3.4. SEM observation**



Cells adhered onto the sample surfaces were fixed with modified Karnovsky's fixative consisting of 2% paraformaldehyde and 2% glutaraldehyde (Sigma-Aldrich) in a 0.05 M sodium cacodylate buffer (Sigma-Aldrich) for 4 hr. The samples were washed with 0.05 M sodium cacodylate buffer 3 times for 10 min and fixed with 1% osmium tetroxide (Sigma-Aldrich). The samples were then washed with distilled water and dehydrated with graded concentrations (50, 70, 80, 90, and 100% v/v) of ethanol. Then, the samples were treated with hexamethyldisilazane (Sigma-Aldrich) for 15 min. Finally, the samples were coated with gold prior to cell shape observation with FESEM (JEOL, JSM-5410LV, Japan).

#### **4.3.5. Immunofluorescence staining**

Adhered cells on samples were fixed with a 4% paraformaldehyde solution (Sigma-Aldrich, Milwaukee, WI, USA) for 20 min, permeabilized with 0.2% Triton X-100 (Sigma-Aldrich, WI, Milwaukee, USA) for 15 min, and stained with TRITC-conjugated phalloidin (Millipore, Billerica, MA, USA) and 4, 6-diamidino-2-phenylindole (DAPI; Millipore, Billerica, MA, USA) for 1 h. FAs were also stained with a monoclonal anti-vinculin antibody (1:100; Millipore, Billerica, MA, USA) and a FITC-conjugated goat anti-mouse secondary antibody (1:500; Millipore, Billerica, MA, USA). Images of the stained cells were taken using a fluorescence microscope (Zeiss, Germany). For the quantitative analysis of the body and nuclear shape of hMSCs on the substrata, the images obtained by fluorescence microscopy were analyzed using the custom written MATLAB script.

#### **4.3.6. Focal adhesion analysis**

To investigate the effects of FAs with the variation of nanotopographical density, we cultured

hMSCs on the nanogrooved matrices for 12 h followed by immunostaining. To further demonstrate the nanotopographical density-induced changes of FAs, the three-dimensional reconstruction images from the normalized fluorescence intensities of vinculin and F-actin were acquired using custom-written MATLAB 2011b (MathWorks, Natick, MA).

#### **4.3.7. Migration analysis**

We utilized a thin polydimethyl siloxane (PDMS) slab to generate a cell-free area for investigating migration of hMSCs on the samples. Specifically, a 200  $\mu$ m-thick PDMS sheet was cut into slabs with width of 500  $\mu$ m and length of 20  $\mu$ m using two intact sharp blades. The PDMS slabs were placed onto the samples with respect to the nanogrooves. Due to conformal sealing of the thin PDMS slab, no cells were shown to grow on the protected area.

#### **4.3.8. Proliferation analysis**

hMSCs ( $4 \times 10^4$  cells/samples) were seeded onto samples and cultured for up to 7 days in DMEM (Sigma-Aldrich, Milwaukee, WI, USA) with 10% FBS (Sigma-Aldrich, Milwaukee, WI, USA) and 1% antibiotics (Sigma-Aldrich, Milwaukee, WI, USA) at 37°C in a humidified atmosphere containing 5% CO<sub>2</sub>. The quantitative analysis of the cell proliferation on the nanogrooved matrices was performed using WST-1 assay (EZ-Cytox Cell Viability Assay Kit, Daeillab Service Co., LTD). To observe the proliferated hMSCs on the samples, the hMSCs were fixed with a modified Karnovsky's fixative consisting of 2% paraformaldehyde and 2% glutaraldehyde (Sigma-Aldrich, WI, Milwaukee, USA) in a 0.05 M sodium cacodylate buffer (Sigma-Aldrich, WI, Milwaukee, USA) for 4 h. The samples were washed with a 0.05 M sodium cacodylate buffer 3 times for 10 min and fixed with 1% osmium tetroxide (Sigma-Aldrich, WI, Milwaukee,

USA). The samples were then washed with distilled water and dehydrated with graded concentrations (50, 70, 80, 90, and 100% v/v) of ethanol. Then, the samples were treated with hexamethyldisilazane (Sigma-Aldrich, WI, Milwaukee, USA) for 15 min. Finally, the samples were coated with gold using a sputter-coater (JFC-1100E, JEOL) prior to cell shape observation by FESEM (JEOL, JSM-5410LV, Japan).

#### **4.3.9. Osteogenesis analysis**

hMSCs ( $4 \times 10^4$  cells/sample) were cultured for 21 days on the samples in osteogenic differentiation media (100 nM dexamethsone, 50  $\mu$ M ascorbic acid, and 10 mM glycerol 2-phosphate in normal media). Alizarin Red S (Sigma-Aldrich) staining was used for confirming osteogenic differentiation of hMSCs on the sample surfaces. The degree of mineralization was measured by Alizarin Red S staining of hMSCs cultured on the sample surfaces, and this measurement was used for quantification of the osteogenic differentiation of hMSCs. Cells were stained with Alizarin Red S and were destained with cetylpyridinium chloride (Sigma-Aldrich), and then the extracted stains were measured using an ELISA reader (VERSAMAX reader, Molecular Devices, Sunnyvale) at 540 nm.

#### **4.3.10. Neurogenesis analysis**

To differentiate hMSCs into neuronal cells, hMSCs ( $2 \times 10^4$  cells/sample) were cultured in the neurogenesis media (NPBM media (Bio Whittaker) with 5 mM cAMP, 5 mM IBMX, 25 ng/ml NGF, 10 ng/ml BDNF, 2.5 mg/ml insulin, and 50  $\mu$ g/ml ascorbic acid (Sigma-Aldrich)). To check neurogenesis of hMSCs, analysis of the immunostaining of TUJ1 (early neural marker) and Neun (later neural marker) were used.

#### **4.3.11. Western blot analysis**

Total cellular protein was extracted by RIPA lysis buffer (62.5 mM Tris-HCL, 2% SDS, 10% glycerol, pH 7.5) with added proteinase inhibitor cocktail (Invitrogen, USA). Cell lysates were incubated on ice for 30 min and then centrifuged at 13,000 rpm for 30 min at 4°C. Supernatant (protein lysate) was collected and protein concentration was determined by a micro bicinchoninic acid (BCA) Protein Assay Kit (Bio-rad, Hercules, Calif). 25 µg aliquots of the cell lysates were separated by 8% SDS-PAGE under reducing conditions. Separated proteins were transferred to a PVDF membrane (Millipore, Corporation, Bedford, MA, USA) at 30 V for 1 h. After blocking with 5% skim milk in PBST, the membrane were incubated overnight in primary antibody at 4°C. Primary antibody was purchased from the company (Integrin  $\beta$ 1 (Santa Cruz, Biotechnology, Santa Cruz, CA); N-Cadherin (Millipore, Billerica, MA, USA); anti-phospho-SAPK (Cell Signaling Technology, Danvers, MA, USA); Osteopontin (Abcam, Cambridge, MA, USA). After washing, the membranes were probed with horseradish peroxidase-conjugated anti-IgG (Invitrogen), and proteins were visualized using the ECL chemiluminescence detection system (GenDEPOT, Houston, TX, USA). Protein expression was normalized versus  $\beta$ -actin antibody (Cell Signaling Technology, Beverly, MA, USA) on the same blot membrane. Quantification of the Western blot was performed using the Image J software with a normalization of the level of the entire protein.

#### **4.3.12. Quantification of cytokines**

To measure bone morphogenetic proteins (BMPs) and endothelial growth factor (VEGF), hMSCs were cultured for 21 days on the substrata in osteogenic differentiation media. A commercially available ELISA kits (R&D Systems, USA) was used to measure the level of total

BMP-2 and VEGF production from cells. The supernatants (cell culture media) were used for quantification of BMP-2 and VEGF according to the instruction of the manufacturer. The absorbance was measured using a microplate reader at 450 nm.

#### **4.3.13. Statistical analysis**

Student's t-test or one-way ANOVA followed by Duncan's multiple range test was used for statistical analysis. All quantitative results were presented as mean  $\pm$  standard deviation (SD).

### **4.4. Results**

#### **4.4.1. Design and Fabrication of Nanogrooved Matrices**

In the body, various ECMs exist in the form of well-organized nanoscale protein fibers, and they are naturally oriented toward certain directions for tissue-specific functions [1,5]. Thus the ECM's aligned architectures or oriented nanotopographic features may regulate the morphology and function of stem cells through specific cell-surface interactions such as mechanotransduction [2,40-42]. To examine the human tissue organization in detail, we performed ultrastructural analysis of *ex vivo* human bone, nerve, and skin. The results indicate that there are naturally anisotropic ECM nanostructures with various length scales in the human bone, nerve, and skin (Fig. 4.1a). This observation suggests that the nanotopographical control of ECM may provide a simple route to guiding the structure and function of stem cells in bone, nerve, and skin of human. It is hypothesized in this regard that the nanotopographical density (i.e., changing the spacing between nanogrooves) is a key parameter in engineering cell responses, which would allow us to better understand stem cell behaviors as well as to control stem cell functions.

Inspired by the highly oriented nanogrooved structures of natural ECMs in human body

(Fig. 4.1a), we fabricated nanotopographically variable grooved matrices using UV-assisted CFL with UV-curable polyurethane acrylate (PUA) polymer (Figs. 4.1bc and S1) [43]. The 550 nm-wide parallel nanoridges (depth of 600 nm) with the three different inter-groove widths of 550, 1,650, and 2,750 nm (spacing ratios of 1:1, 1:3, and 1:5, respectively) were fabricated onto the glass cover slip along with the flat control (no patterns on PUA surface). Here, the spacing ratio is defined as the ratio of the width of inter-groove spacing to that of nanoridges. The PUA nanogrooved matrices were then coated with gelatin prior to cell plating. As can be seen from Figs. 4.1b and c, the structures were well-defined with high physical integrity and uniformity over an area of  $2.5 \times 2.5 \text{ cm}^2$ .

#### **4.4.2. Analysis of hMSC Shape and Orientation by Nanotopographical Density in Single and Multi-Cell Level**

To investigate the effects of stem cell shape and orientation by the nanotopographical density in the single cell level, the immunofluorescence staining analysis was used. As shown in Figs. 4.2a and b, the nanotopographical density greatly influenced the hMSC polarity as supported by the aligned cytoskeletal structure of hMSCs in response to various nanotopographical densities. The hMSCs on the sparser nanogrooves elongated more strongly than those on the relatively denser nanogrooves (i.e.,  $1:5 > 1:3 > 1:1$  nanogrooved pattern) (Fig. 4.2a). Also, the hMSCs showed relatively spherical shapes on the flat control (unpatterned substrate) compared to those on the nanogrooved matrices (Fig. 4.2a). To quantify the observed cell polarities, cell elongation factors [CEF; defined as (major axis)/(minor axis)] of hMSCs were calculated. Surprisingly, the CEF of hMSCs on the 1:5 nanogrooved pattern was approximately 2 times higher than that on the 1:1 nanogrooved matrices (Fig. 4.2b).

We also analyzed the nucleus of hMSCs on the nanogrooved matrices since it has been known that the nuclear architecture and organization may influence cell function [24,43]. It was reported earlier that the presence of nanogrooves strongly influenced the structural changes of nucleus of hMSC [24]. As shown in the immunofluorescence staining images of Fig. 4.2a, the nucleus of hMSCs on the sparser nanogrooves elongated more than those on the denser nanogrooves, which was also confirmed with a quantitative analysis of the nuclear elongation factor [NEF; defined as (major axis)/(minor axis)] (Fig. 4.2c). Interestingly, the increase of NEF was correlated with the decrease of short axis, not with the increase of long axis.

Unlike the monotonic trends of CEF and NEF, the perimeter of cell body and nucleus pertinent to a specific nanotopographical density was lowest at the 1:3 pattern as compared to the other 1:1 and 1:5 patterns (Figs. 4.2b and c). In parallel, the spreading area of cell body and nucleus monotonically decreased with the decrease of the nanotopographical density (Figs. 4.2b and c). As an alternative morphological index, we introduce here the cell shape index which is calculated as follows: *cell shape index (CSI) = (cell area)/(cell perimeter)<sup>2</sup>*; and *nucleus shape index (NSI) = (nucleus area)/(nucleus perimeter)<sup>2</sup>* [44-46]. Unlike the increasing trend of CEF and NEF, the CSI and NSI showed higher values at the 1:3 pattern. Interestingly, strong correlations were observed between the calculated values of the cell body and nucleus (Fig. 4.2d), indicating that the body and nucleus of hMSCs might be closely interconnected each other to regulate their functions [47,48].

To investigate the polarity of stem cells by the nanotopographical density in the multi-cells level, we cultured hMSCs on the nanogrooved matrices for 148 h, after cell seeding (Fig. 4.S2). Two notable findings were derived from this experiment. First, the hMSCs on the nanogrooves with larger spacing ratio were more orientated along the direction of nanogrooves

than those on the denser nanogrooves in the multi-cell level (i.e., 1:5 > 1:3 > 1:1 nanogrooved pattern). Second, the hMSCs were becoming more orientated along the direction of nanogrooves with time even for the dense nanogroove pattern (1:1 nanogrooved matrix), which was confirmed via a time-resolved quantitative analysis (Fig. 4.S2). Taken together, these findings suggest that the density of nanogrooves can determine the morphology and orientation of stem cells and, thus, may be employed as an efficient regulator of stem cell adhesion and functions.

#### **4.4.3. Analysis of hMSC Adhesion by Nanotopographical Density**

Scanning electron microscope (SEM) observations clearly showed the controlled hMSC adhesion according to the nanotopographical density (Fig. 4.3). As can be seen, the nanogrooved matrices could control the shape and orientation of hMSCs by the density of nanogrooves, suggesting that they may influence interactions at the cell-substrate.

We observed that the focal adhesions (FAs) of hMSCs were polarized along the direction of nanogrooved matrices (Figs. 4.4a and b), being more polarized with the sparser nanogrooved density as compared to the relatively denser nanogrooved density. On the other hand, unpolarized FAs on the 1:5 nanogrooved pattern were observed, which was marked with yellow arrows in Fig. 4.4a, suggesting that some portions of the hMSCs were directly penetrated into the 1:5 nanogrooved pattern (at the bottom of the sparser grooves). In addition, the nanotopographical density affected the size of FAs such that larger FA sizes were observed on the sparser nanogroove patterns (Fig. 4.4). The FAs and cytoskeletal structures of hMSCs were organized along the ridges of the nanogrooved matrices with a high co-localization of the FAs and actin cytoskeleton (Fig. 4.4a); the ridge regions were typically characterized by higher fluorescence intensity compared to the groove regions regardless of the size of nanogrooves.



From the analysis of FAs of hMSCs with the nanotopographical density cues, we have shown several interesting findings (Fig. 4.4): (1) The high co-localization of the FAs and actin cytoskeleton of hMSCs was observed regardless of the nanotopographical density. (2) The FAs of hMSCs were differently formed by the direction and nanotopographical density; the FAs were more polarized on the sparser nanogrooved patterns as compared to the relatively denser ones. (3) The lower density (1:5 nanogrooved pattern in our case) led to the formation of un-polarized FAs at the bottom of the grooves (yellow arrows in Fig. 4.4a; 1:5 pattern), thus showing less polarized FA organization (Fig. 4.4b; 1:5 pattern). (4) The larger sizes of FAs were observed on the sparser patterns than those on the relatively denser patterns. As shown in the probability map of FA area (Fig. 4.4c), the 1:3 pattern shows increased portion of large FA (indicated in white arrows), and the 1:5 pattern demonstrated dual-peaks at 6-8 and 24-26  $\mu\text{m}^2$  ranges (indicated in yellow arrows). (5) The increasing trend of FA size from flat to 1:5 was presumably due to the clustering of integrin at the nanogrooves (Figs. 4.4c and d). Here, the focal adhesion clustering index was calculated by dividing the area of top 10% of large FA sites with that of unit FA (area of unit FA was known in the range of 1-5  $\mu\text{m}^2$ , here we used 5  $\mu\text{m}^2$  as a mean value for the quantification) [56]. As shown in Fig. 4.4d, the FA was highly clustered as the spacing ratio increased from 1:1 to 1:5.

Together, our data strongly suggest that the modified FAs and cytoskeletal structures of hMSCs may have reconstructed their mechanotransduction pathways, guiding the differentiation in a certain direction [47].

#### **4.4.4. Analysis of hMSC Migration by Nanotopographical Density**

In general, migration of cells is an important cell behavior for wound healing [49]. As shown in

Fig. 4.1a, aligned collagen nanofibers with different groove density were observed in the human skin, indicating that the stem cells in skin may be mediated by aligned collagen nanofibers. To investigate whether stem cell migration is affected by the nanotopographical density, we cultured hMSCs on the nanogrooved matrices in the *in vitro* wound healing model; the hMSCs migrated into the cell free area (target area), and the covering rate of hMSCs was evaluated with a similar method reported earlier [49,50]. We observed that the hMSCs on the nanogrooved matrices showed a significantly higher cell migration speed (i.e., covering rate of hMSCs along the direction of nanogrooved matrices) compared to those on the flat control (Fig. 4.S3). In parallel, the covering rate of hMSCs on the 1:5 nanogrooved pattern was significantly lower compared to those on the 1:1 or 1:3 nanogrooved patterns. Our data suggest that the migration of stem cells may be sensitive to the density of nanogrooves, and the denser nanogrooved matrices may elicit faster migration of stem cells than the sparser ones.

#### **4.4.5. Analysis of hMSC Proliferation by Nanotopographical Density**

We cultured hMSCs on the nanogrooved matrices for 148 h and analyzed the cell viability of hMSCs. It turned out that no significant difference among the flat and nanogrooved matrices (Fig. 4.S4) was observed despite the fact that the proliferation of 1:3 nanogrooved pattern was slightly lower than the other samples. These results corroborate with previous observations that the proliferation of cells may be not strongly influenced by the nanogrooves [49,51].

#### **4.4.6. Analysis of hMSC Differentiation by Nanotopographical Density**

Given that naturally anisotropic nanostructures were observed in the human bone (Fig. 4.1a), we cultured hMSCs on the nanogrooved matrices with osteogenic induction media for 21 days.

Then, we analyzed hMSC osteogenesis by the mineralization. The images of Alizarin Red S staining (Fig. 4.5a) and von Kossa staining (Fig. 4.5b) demonstrated that the calcium expression was higher for the nanogrooved patterns than that of the flat control. Specifically, the intensity was highest at the 1:3 nanogrooved pattern, while recognizing that the 1:5 case was comparable to the flat control (Figs. 4.5a and b). To quantify the degree of osteogenesis, the stained calcium deposits by Alizarin Red S staining were destained with cetylpyridinium chloride, and then the extracted stains were measured using an ELISA reader. As shown in Fig. 4.5c, we observed that the 1:3 nanogrooved pattern exhibited the highest osteogenesis, while the cell viability in terms of the number of cells was not altered among the different samples (Fig. 4.5d). It is noted that the osteogenesis showed a biphasic trend; the intensity first increased from the flat control to the 1:3 nanogrooved pattern and then decreased at the 1:5 nanogrooved pattern, revealing possible existence of an optimum nanotopographical density in the stem cell differentiation. We further examined osteocalcin (OCN) as one of the osteogenic genes to confirm the enhanced osteogenic differentiation of hMSCs on the 1:1 nanogrooved pattern as compared to the 1:5 nanogrooved pattern (Fig. 4.5e). Together, we showed that the nanotopographical density could regulate the osteogenesis of hMSCs.

Next, the effect of nanotopographical density on the neurogenesis of hMSCs was investigated inspired by the aligned nanofibril ECMs in the human nerve (Fig. 4.1a). Here, we hypothesized that the nanotopographical density would also be a key factor to regulate the neurogenesis of stem cells. The effect of nanotopographical density on the neurogenesis was investigated by employing immunostaining of neural stem cell markers such as Tuj1 (early neural marker) and NeuN (later neural marker). As shown in Figs. 4.6a and b, the differentiated cells showed different Tuj1 (neuron-specific class III beta-tubulin) and NeuN (neuronal nuclei)

levels depending on the pattern spacing ratio. The number of Tuj1- and NeuN-positive cells was increased at the flat control and the 1:1, 1:3 nanogrooved patterns and then decreased at the 1:5 nanogrooved pattern, demonstrating a similar biphasic trend to the case of osteogenesis (maximum at the 1:3 nanogrooved pattern). The density of nanopatterns also affected apparent cellular morphologies such as number of neurites, length of neurites and elongation of nucleus. The number of neurites of the cells was lower on the grooved patterns compared to the flat control, with its value being lowest at the 1:3 nanogrooved pattern, an opposite trend to the case of neurogenesis. Interestingly, the length of neurites followed the same trend with the osteogenesis, being the highest at the 1:3 nanogrooved pattern. Arguably, the nuclear shape index (elongation of nucleus) did not show a biphasic response, displaying a plateau with the increase of the groove spacing, suggesting that there may be some complex interactions at the cell-surface interface.

Based on our experimental observations with the literatures, we studied how the nanotopographical density could control the differentiation of hMSCs by considering three major factors and their roles: (1) biochemical soluble factors, (2) cell-substrate, (3) cell-cell interactions.

(1) Biochemical soluble factors: It is widely accepted that the soluble chemical factors including cytokine are important for the regulation of cellular function [3,19,53]. For example, the bone morphogenetic protein-2 (BMP-2) and vascular endothelial growth factor (VEGF) are known as important cytokines for osteogenesis [54]. However, our analysis demonstrated that the nanotopographical density did not greatly influence the production of BMP-2 or VEGF during culturing hMSCs on the flat and nanogrooved matrices (Figs. 4.7a and b). Thus it appears that the nanotopographical density may influence the differentiation of hMSCs by altering the cell-

substrate or cell-cell interactions.

(2) Cell-substrate interactions: To investigate whether the nanotopographical density is capable of altering the interactions at the cell-substrate, we cultured hMSCs on the nanogrooved matrices for 7 days before complete confluence of hMSCs. We observed that the hMSCs were mostly adhered on the ridges of the nanogrooved matrices (Fig. 4.3c) although some portions of the hMSCs made direct adhesions at the bottom of 1:5 nanogrooved pattern (Fig. 4.4a). Western blot analysis clearly showed the decreased expression of the integrin  $\beta 1$  in hMSCs cultured on the 1:5 nanogrooved pattern compared to that on the 1:1 or 1:3 nanogrooved patterns (Figs. 4.7c and d). The expression of the integrin  $\beta 1$  showed a biphasic trend, i.e., increasing from flat to 1:3 nanogrooved pattern and decreasing thereafter to the 1:5 nanogrooved pattern. In an alternative analysis, the change of integrin  $\beta 1$  was similar to the CSI and NSI, but not to the CEF and NEF (Figs. 4.2b and c).

(3) Cell-cell interactions: Next, we discuss the cell-cell contacts on the nanogrooved matrices. To this end, we checked the expression levels of the N-cadherin. We found higher expressions of N-cadherin on the nanogrooved matrices regardless of the nanogroove density compared to the flat substrate (Figs. 4.7c and e). We also showed that the expression of N-cadherin was increased on the 1:1 and 1:3 nanogrooved pattern whereas it was reduced on the 1:5 nanogrooved pattern.

## 4.5. Discussion

Designing materials from the concept of “stem cell niche” has been emerging as a powerful strategy for quantitative analysis of stem cell behaviors as well as stem cell-based regenerative therapies [7,40]. In this study, we designed various anisotropic nanotopographical cues inspired

from our observations that the ECMs in skin, bone, and nerve of human exist in the form of nanogroove structures with various length feature scales (diameter and spacing) (Fig. 4.1a). We thus fabricated variable grooved matrices, which have proven effective for investigating the effects of nanotopographical density on the morphology and function of stem cells. Using our platforms, we found considerable differences in the morphologies of hMSCs according to the nanotopographical density (Figs. 4.2 and 4a). This finding is especially important because it has been recently reported that shape of hMSCs may lead to regulating the cell functions, in particular for differentiation, by regulating the levels of RhoA, ROCK, and myosin light chain phosphorylation [47]. Namely, one can expect that the nanotopographical density may play a key role in controlling the differentiation of stem cells by regulation of cytoskeletal tension as well as its related signaling pathways.

Kirmizidis *et al.* reported that the microfabricated grooved substrates decreased the osteoblast differentiation compared to the flat substrates even though the cells on the microgrooved substrates were highly elongated [52]. In contrast to this study, we found that the nano grooved substrates increased the osteoblast differentiation of hMSCs, where the topographical density played a key role in the detailed morphological changes and functions of the cells. It appears that the interaction or contact at the cell-bound interface may be more important than the elongated cell shape itself for the regulation of stem cell differentiation.

We also showed that the anisotropic nanotopography enhanced the neurogenesis of hMSCs as well as neurite growth. In this experiment, the nanotopographical density *per se* could control the neural differentiation of hMSCs and their cellular morphologies such as number of neurites, length of neurites, and elongation of nucleus. We further observed that the later neural markers such as NeuN were more expressed by culturing hMSCs on the 1:3 nanogrooved pattern

than those on the 1:5 nanogrooved pattern even though their nuclear elongation was not significantly different (Fig. 4.6), suggesting that the interactions associated with the hMSCs and nanotopographical density might be important for the neurogenesis of hMSCs.

Previous studies have proven the role of various nanotopographical cues such as feature size [4,20-23] and degree of ordering [33,34] to direct stem cell fate. Especially for the last several years the elongation of nucleus or cytoskeleton has been recognized as a crucial factor for the topography-induced stem cell differentiation [2,3,20-24,47]. In this study, only the spacing of nanogrooves was varied with the fixed width of nanoridges, thus modulating the pattern densities. As a result, although the nuclear shape index showed less significant difference between 1:3 and 1:5 spacing ratio, the osteo- and neurogenesis were even decreased with increasing the spacing ratio from 1:3 to 1:5 cases. This indicates that the elongation of nucleus might not be a major indicator for the stem cell fate despite that a further basic research on this issue is required to elucidate the specific signaling pathway.

At this stage, the analysis of FAs may give guidance in explaining the biphasic trends of osteo- and neurogenesis via polarization of the cell body and nucleus. FA is known as a potential mechanosensor to be important in cellular functions [47,55], and it has been reported that nanogrooved topographies may influence directly the formation of FAs in stem cells [20,23,47]. As shown in Fig. 4, the results suggest that nanotopographical density may control the formation of FAs of stem cells, which would be an important regulator of stem cell functions. In terms of the polarity, the 1:5 spacing ratio showed maximum polarity due to the presence of (i) very large FA cluster size (Fig. 4.4a yellow arrows), thick F-actin bundles, and (ii) highly oriented FA clusters. These observations were strongly supported by the increasing trend of cell body and nucleus elongation (Fig 4.2b). Such polarization may induce anisotropic organization of F-actin

and internal tension, and accordingly migration and differentiation behaviors. Our findings suggest that too much polarization might decrease the differentiation of hMSCs as supported by the reduced osteo- and neurogenesis with the 1:5 spacing ratio compared to the 1:3 ratio. Such a hypothesis was further supported by the controlled elongation of cell body through the microcontact printing of ECM [57,59]. In this work, when comparing the aspect ratios of 1:1, 1:3, and 1:5 islands, reduced differentiation of hMSCs was observed with the aspect ratio of 1:5, suggesting that there might be an optimum polarity for stem cell differentiation.

Taken together, our data collectively suggest that the nanotopographical density may be able to control the interactions at cell-substrate and cell-cell interfaces. Specifically, our analyses based on biochemical soluble factors, western blot assay and FAs reveal that the nanotopographical density provides specific cues to the differentiation of hMSCs (Figs. 4.8a-d). Namely, according to the western blot assay, the expression of integrin  $\beta 1$  and N-cadherin showed a similar biphasic trend to osteo- and neurogenesis. As shown in Figs. 4.8b and c, the expression and organization of integrin and cadherin can be controlled by the topography-induced cell body and nucleus shape through the cell-substrate or cell-cell interactions on nanotopographical density. These results further confirm that the anisotropic topographical density *per se* has ability to mediate the cell-substrate and cell-cell interactions, and thus osteo- and neurogenesis of the cells. We showed a highly positive correlation coefficient between the expression of integrin  $\beta 1$  or N-cadherin and the osteo- and neurogenesis (Figs. 4.8c and d).

Further discussion follows regarding additional correlation between the morphology (CEF, NEF, CSI and NSI) and the osteo- and neurogenesis of hMSCs. Overall, it seems that the elongation of nucleus mediates stem cell differentiation through tethered intracellular tension. However, the results shown in Fig. 4.2 indicate two interesting aspects: (i) the difference of



nucleus shapes according to various nanopatterns was less correlated to the trend of cell body, and (ii) the tendency of osteo- and neurogenesis decreased between 1:3 and 1:5 spacing ratio in spite of the increasing trend of NEF, showing discrepancy with previous studies [22]. These results imply the necessity of alternative factors instead of the CEF and NEF which simply describes cell morphology with the ratio of long and short axes. For example, although the trend of CSI and NSI could not explain the osteo- and neurogenic trends between flat vs. nanopatterned surfaces, they showed interesting coincidence with the osteo- and neurogenesis on various nanotopographical densities. Such difference of CEF/NEF and CSI/NSI is due to the relatively less deformed nucleus. As shown in Fig. 4.2, the increased elongation factor of cell body mainly resulted from the decrease of the short axis, not from the elongation of the long axis. However, as the spacing ratio increased from 1:3 to 1:5, the short axis of cell body became similar to the short axis of nucleus. For this reason, in the 1:5 spacing ratio the cells showed bulged morphology in the position of nucleus, with a slender cell body. Therefore, the elongation factor itself cannot present sufficient information as to whether the cell body is smooth or bulged, except for the aspect ratio. On the other hand, as an alternative indicator, CSI and NSI can present more reasonable quantification on the cell and nucleus morphologies since they contain ‘perimeter’ and ‘spreading area’ as parameters. The correspondence between the osteo- and neurogenic trends and CSI and NSI strongly support the significance of cell and nucleus shape as an indirect, complementary indicator (Figs. 4.8b and d). Therefore, CEF and NEF may possess better ability when simply comparing flat vs. nanopatterned surfaces, but CSI and NSI present more valuable information when various patterned surfaces are involved. Our results therefore imply that the elongation of nucleus or cell body, which has been identified as a key regulator, may be not the sufficient condition for the stem differentiation, but the moderate cell

polarity-induced cell-substrate (up-regulation) and cell-cell interactions (down-regulation) may be more responsible for the stem cell fate and functions.

In this work, we used the gelatin to improve the initial cell attachment on the nanogrooves. To verify whether the gelatin coating truly affects the cell behavior, we cultured the hMSCs on the gelatin-uncoated nanogrooved matrices for 7 days before complete confluence of hMSCs (Fig. 4.S5). We checked the expression levels of the N-cadherin in the absence of gelatin coating. The western blot assay showed that higher expressions of N-cadherin on the nanogrooved matrices (1:1 and 1:3 spacing ratio) compared to the flat substrate, and the expression of N-cadherin was significant on the 1:1 and 1:3 nanogrooved pattern whereas it was reduced on the 1:5 nanogrooved pattern, which is similar trend to the gelatin-coated nanogrooved matrices (Fig. 4.7c). Furthermore, to verify whether the nanotopographical density can affect molecular signaling, we checked the upregulation of phosphorylated-ERK (p-ERK) in the absence and presence of gelatin coating. As shown in Figs 4.S5, and S6, we found that the nanotopographical density affected the p-ERK pathway, which is involved in mediating cell functions (especially in differentiation). Interestingly, the ERK was upregulated at the 1:1 and 1:3 nanogrooved patterns and then decreased at the 1:5 nanogrooved pattern, showing a similar biphasic trend to the case of differentiation of hMSCs (maximum at the 1:3 nanogrooved pattern). Although the in-depth studies are still required to understand the underlying molecular mechanisms accurately, the current work has revealed that the density of nanotopography may be able to regulate the cell signaling pathway.

In summary, we demonstrated the effects of nanotopographical density on the morphology and differentiation of mesenchymal stem cells. Using nanogrooved matrices mimicking the native tissues, we found that the body and nucleus of hMSCs with the sparser

nanogrooved pattern elongated and orientated more along the direction of nanogrooves than those with the relatively denser nanogroove patterns. In contrast, the perimeter of the cells was lower at the 1:3 pattern as compared to the 1:1 and 1:5 patterns. We also found that the topographical density-dependent shape of cell body and nucleus, formation of FAs, and interactions at the cell-substrate and cell-cell interfaces might collectively regulate the functions of hMSCs. In addition, we have investigated the role of nanotopographical density on the function of hMSCs. It was observed that the denser nanogrooved matrices guided faster migration of hMSCs than the sparser nanogrooved matrices. Furthermore, the effect of nanotopographical density on the osteo- or neurogenesis of hMSCs was significant at the 1:1 and 1:3 nanogrooved patterns, but not significant at 1:5 nanogrooved pattern compared to that at the flat substrate. We showed a high positive correlation between the expression of integrin  $\beta 1$  or N-cadherin and the osteo- and neurogenesis. We also found some intriguing correlations between the cell body- or nucleus perimeter/spreading-based shape index and the osteo- and neurogenesis of hMSCs. Although the in-depth studies are still required to understand the underlying molecular mechanisms accurately, the current work has revealed that the density of nanogrooves may be able to regulate the structure and enhanced osteo- or neurogenesis of stem cells, which would allow us to set up an efficient strategy for designing scaffolds for stem cell and tissue engineering applications as well as for understanding fundamental stem cell biology.

#### **4.6. References**

- [1] Kim, H. N. *et al.* Nanotopography-guided tissue engineering and regenerative medicine. *Adv. Drug Deliv. Rev.* **65**, 536-558 (2013).
- [2] Guilak, F. *et al.* Control of stem cell fate by physical interactions with the extracellular

matrix. *Cell Stem Cell* **5**, 17-26 (2009).

[3] Nelson, T. J., Behfar, A., Yamada, S., Martinez-Fernandez, A. & Terzic, A. Stem cell platforms for regenerative medicine. *Clinical and Translational Science* **2**, 222-227 (2009).

[4] Chen, W. *et al.* Nanotopography influences adhesion, spreading, and self-renewal of human embryonic stem cells. *Acs Nano* **6**, 4094-4103 (2012).

[5] Kim, D. H., Provenzano, P. P., Smith, C. L. & Levchenko, A. Matrix nanotopography as a regulator of cell function. *J. Cell Biol.* **197**, 351-360 (2012).

[6] Vunjak-Novakovic, G. & Scadden, D. T. Biomimetic platforms for human stem cell research. *Cell Stem Cell* **8**, 252-261 (2011).

[7] Lutolf, M. P., Gilbert, P. M. & Blau, H. M. Designing materials to direct stem-cell fate. *Nature* **462**, 433-441 (2009).

[8] Shi, X., Chen, S., Zhao, Y., Lai, C. & Wu, H. Enhanced osteogenesis by a biomimic pseudo-periosteum-involved tissue engineering strategy. *Adv. Healthcare Mater* **2**, 1229-1235 (2013).

[9] Place, E. S., Evans, N. D. & Stevens, M. M. Complexity in biomaterials for tissue engineering. *Nat. Mater.* **8**, 457-470 (2009).

[10] Stevens, M. M. & George, J. H. Exploring and engineering the cell surface interface. *Science* **310**, 1135-1138 (2005).

[11] Zorlutuna, P. *et al.* Microfabricated biomaterials for engineering 3D tissues. *Adv. Mater.* **24**, 1782-1804 (2012).

[12] Fisher, O. Z., Khademhosseini, A., Langer, R. & Peppas, N. A. Bioinspired materials for controlling stem cell fate. *Acc. Chem. Res.* **43**, 419-428 (2010).

[13] Coelho, M. B., Cabral, J. M. & Karp, J. M. Intraoperative stem cell therapy. *Annu. Rev. Biomed. Eng.* **14**, 325-349 (2012).

- [14] Ferreira, L., Karp, J. M., Nobre, L. & Langer, R. New opportunities: The use of Nanotechnologies to manipulate and track stem cells. *Cell Stem Cell* **3**, 136-146 (2008).
- [15] Bettinger, C. J., Langer, R. & Borenstein, J. T. Engineering substrate topography at the micro- and nanoscale to control cell function. *Angew. Chem. Int. Edit.* **48**, 5406-5415 (2009).
- [16] Pham, Q. P., Sharma, U. & Mikos, A. G. Electrospinning of polymeric nanofibers for tissue engineering applications: A review. *Tissue Eng.* **12**, 1197-1211 (2006).
- [17] Atala, A., Kasper, F. K. & Mikos, A. G. Engineering Complex Tissues. *Sci. Transl. Med.* **4**, 160rv112 (2012).
- [18] Fong, E. L. S., Watson, B. M., Kasper, F. K. & Mikos, A. G. Building bridges: leveraging interdisciplinary collaborations in the development of biomaterials to meet clinical needs. *Adv. Mater.* **24**, 4995-5013 (2012).
- [19] Lutolf, M. P. & Blau, H. M. Artificial stem cell niches. *Adv. Mater.* **21**, 3255-3268 (2009).
- [20] Kulangara, K., Yang, Y., Yang, J. & Leong, K. W. Nanotopography as modulator of human mesenchymal stem cell function. *Biomaterials* **33**, 4998-5003 (2012).
- [21] Zhao, F. *et al.* Low Oxygen Tension and Synthetic Nanogratings Improve the Uniformity and Stemness of Human Mesenchymal Stem Cell Layer. *Mol. Ther.* **18**, 1010-1018 (2010).
- [22] Yim, E. K. F., Pang, S. W. & Leong, K. W. Synthetic nanostructures inducing differentiation of human mesenchymal stem cells into neuronal lineage. *Exp. Cell Res.* **313**, 1820-1829 (2007).
- [23] Yim, E. K. F., Darling, E. M., Kulangara, K., Guilak, F. & Leong, K. W. Nanotopography-induced changes in focal adhesions, cytoskeletal organization, and mechanical properties of human mesenchymal stem cells. *Biomaterials* **31**, 1299-1306 (2010).
- [24] Chalut, K. J., Kulangara, K., Giacomelli, M. G., Wax, A. & Leong, K. W. Deformation of stem cell nuclei by nanotopographical cues. *Soft Matter* **6**, 1675-1681 (2010).

- [25] Kim, D. H. *et al.* Mechanosensitivity of fibroblast cell shape and movement to anisotropic substratum topography gradients. *Biomaterials* **30**, 5433-5444 (2009).
- [26] Prager-Khoutorsky, M. *et al.* Fibroblast polarization is a matrix-rigidity-dependent process controlled by focal adhesion mechanosensing. *Nat. Cell Biol.* **13**, 1457-1465 (2011).
- [27] Kim, D. H. *et al.* Guided cell migration on microtextured substrates with variable local density and anisotropy. *Adv. Funct. Mater.* **19**, 1579-1586 (2009).
- [28] Jiang, X. Y., Bruzewicz, D. A., Wong, A. P., Piel, M. & Whitesides, G. M. Directing cell migration with asymmetric micropatterns. *Proc. Natl. Acad. Sci. USA* **102**, 975-978 (2005).
- [29] Yim, E. K. F. *et al.* Nanopattern-induced changes in morphology and motility of smooth muscle cells. *Biomaterials* **26**, 5405-5413 (2005).
- [30] Thery, M., Jimenez-Dalmaroni, A., Racine, V., Bornens, M. & Julicher, F. Experimental and theoretical study of mitotic spindle orientation. *Nature* **447**, 493-496 (2007).
- [31] Kim, D. H. *et al.* Nanoscale cues regulate the structure and function of macroscopic cardiac tissue constructs. *Proc. Natl. Acad. Sci. USA* **107**, 565-570 (2010).
- [32] Bettinger, C. J., Zhang, Z. T., Gerecht, S., Borenstein, J. T. & Langer, R. Enhancement of in vitro capillary tube formation by substrate nanotopography. *Adv. Mater.* **20**, 99-103 (2008).
- [33] Dalby, M. J. *et al.* The control of human mesenchymal cell differentiation using nanoscale symmetry and disorder. *Nat. Mater.* **6**, 997-1003 (2007).
- [34] McMurray, R. J. *et al.* Nanoscale surfaces for the long-term maintenance of mesenchymal stem cell phenotype and multipotency. *Nat. Mater.* **10**, 637-644 (2011).
- [35] Xie, J. W. *et al.* The differentiation of embryonic stem cells seeded on electrospun nanofibers into neural lineages. *Biomaterials* **30**, 354-362 (2009).
- [36] Fisher, G. J., Varani, J. & Voorhees, J. J. Looking older: fibroblast collapse and therapeutic

implications. *Arch. Dermatol.* **144**, 666-672 (2008).

[37] Klein-Nulend, J., Bacabac, R. & Bakker, A. Mechanical loading and how it affects bone cells: The role of the osteocyte cytoskeleton in maintaining our skeleton. *Eur. Cells Mater.* **24**, 278 (2012).

[38] Burger, E. H. & KLEIN-NULEND, J. Mechanotransduction in bone—role of the lacuno-canalicular network. *FASEB J.* **13**, S101-S112 (1999).

[39] Suh, K. Y., Park, M. C. & Kim, P. Capillary force lithography: a versatile tool for structured biomaterials interface towards cell and tissue engineering. *Adv. Funct. Mater.* **19**, 2699-2712 (2009).

[40] McNamara, L. E. *et al.* Nanotopographical control of stem cell differentiation. *J. Tissue Eng.* **1**, 120623; DOI:10.4061/2010/120623 (2010)

[41] Teixeira, A. I., Abrams, G. A., Bertics, P. J., Murphy, C. J. & Nealey, P. F. Epithelial contact guidance on well-defined micro- and nanostructured substrates. *J. Cell Sci.* **116**, 1881-1892 (2003).

[42] Cha, C., B., L. W., Khademhosseini, A. & Peppas, N. A. Designing biomaterials to direct stem cell fate. *Acs Nano* **6**, 9353-9358 (2012).

[43] Choi, S. J., Kim, H. N., Bae, W. G. & Suh, K. Y. Modulus- and surface energy-tunable ultraviolet-curable polyurethane acrylate: properties and applications. *J. Mater. Chem.* **21**, 14325-14335 (2011).

[44] Malek, A. M. & Izumo, S. Mechanism of endothelial cell shape change and cytoskeletal remodeling in response to fluid shear stress. *J. Cell Sci.* **109**, 713-726 (1996).

[45] Kim, J. *et al.* Charged nanomatrices as efficient platforms for modulating cell adhesion and shape. *Tissue Eng. Part C Methods* **18**, 913-923 (2012).

- [46] Versaevel, M., Grevesse, T. & Gabriele, S. Spatial coordination between cell and nuclear shape within micropatterned endothelial cells. *Nat. Commun.* **3**, 671 (2012).
- [47] McBeath, R., Pirone, D. M., Nelson, C. M., Bhadriraju, K. & Chen, C. S. Cell shape, cytoskeletal tension, and RhoA regulate stem cell lineage commitment. *Dev. Cell* **6**, 483-495 (2004).
- [48] Tang, J., Peng, R. & Ding, J. D. The regulation of stem cell differentiation by cell-cell contact on micropatterned material surfaces. *Biomaterials* **31**, 2470-2476 (2010).
- [49] Kim, H. N., Hong, Y., Kim, M. S., Kim, S. M. & Suh, K. Y. Effect of orientation and density of nanotopography in dermal wound healing. *Biomaterials* **33**, 8782-8792 (2012).
- [50] Kim, J. *et al.* Bacterial Cellulose Nanofibrillar Patch as a Wound Healing Platform of Tympanic Membrane Perforation. *Adv. Healthc. Mater.* **2**, 1525-1531 (2013).
- [51] Liliensiek, S. J., Campbell, S., Nealey, P. F. & Murphy, C. J. The scale of substratum topographic features modulates proliferation of corneal epithelial cells and corneal fibroblasts. *J. Biomed. Mater. Res. A* **79A**, 185-192 (2006).
- [52] Kirmizidis, G. & Birch, M. A. Microfabricated grooved substrates influence cell-cell communication and osteoblast differentiation in vitro. *Tissue Eng. Part A* **15**, 1427-1436 (2009).
- [53] Kim, D. H., Lee, H., Lee, Y. K., Nam, J. M. & Levchenko, A. Biomimetic nanopatterns as enabling tools for analysis and control of live cells. *Adv. Mater.* **22**, 4551-4566 (2010).
- [54] Grellier, M., Bordenave, L. & Amedee, J. Cell-to-cell communication between osteogenic and endothelial lineages: implications for tissue engineering. *Trends Biotechnol.* **27**, 562-571 (2009).
- [55] Biggs, M. J. P., Richards, R. G. & Dalby, M. J. Nanotopographical modification: a regulator of cellular function through focal adhesions. *Nanomed.-Nanotechnol.* **6**, 619-633 (2010).



- [56] Owen, G. R., Meredith, D. O., ap Gwynn, I. & Richards, R. G. Focal adhesion quantification - a new assay of material biocompatibility? Review. *Eur. Cell Mater.* **9**, 85-96 (2005).
- [57] Peng, R., Yao, X. & Ding, J. D. Effect of cell anisotropy on differentiation of stem cells on micropatterned surfaces through the controlled single cell adhesion. *Biomaterials* **32**, 8048-8057 (2011).
- [58] Yao, X., Peng, R. & Ding, J. Effects of aspect ratios of stem cells on lineage commitments with and without induction media. *Biomaterials* **34**, 930-939 (2013).
- [59] Kilian, K. A., Bugarija, B., Lahn, B. T. & Mrksich, M. Geometric cues for directing the differentiation of mesenchymal stem cells. *Proc. Natl. Acad. Sci. USA* **107**, 4872-4877 (2010).

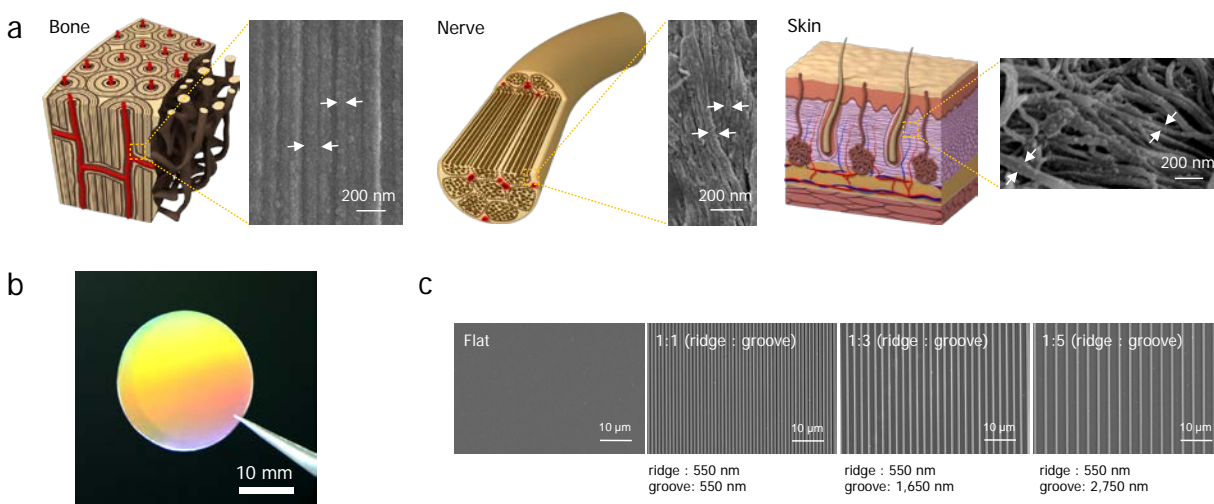


**Figure 4.1. Rational design and fabrication of bio-inspired anisotropic nanotopography with various nanogroove sizes.** (a) Graphical illustrations and SEM images of *ex vivo* bone, nerve and skin of human, showing the well aligned nanostructures with various nanogrooves. The white arrows indicate different sizes of nanogrooves. (b) A photograph of tissue-inspired nanopattern on 1-inch scale coverslip fabricated with PUA. (c) Flat and various nanogroove pattern matrices of 1:1, 1:3, and 1:5 spacing ratios (ridge to groove width) used in this study.

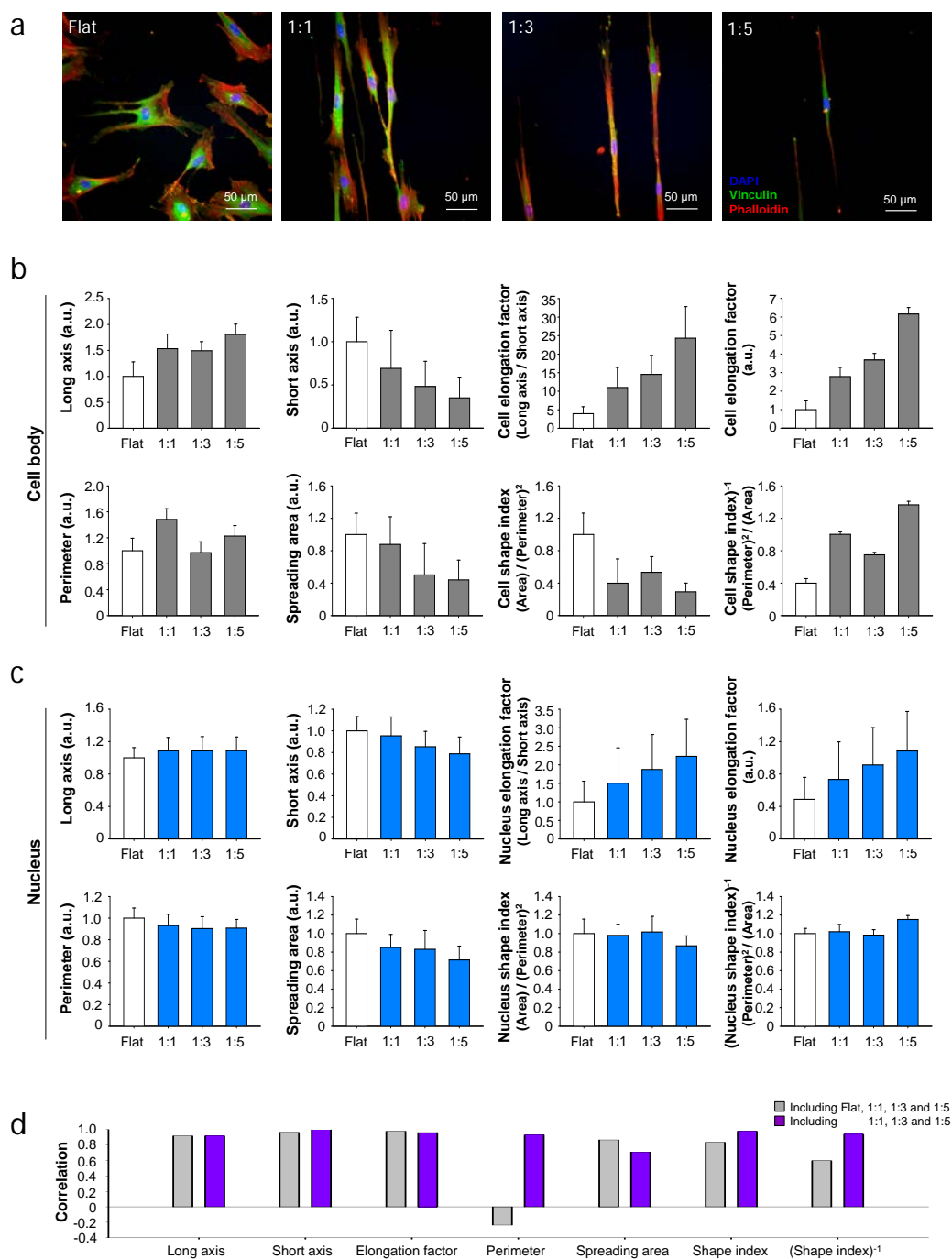


**Figure 4.2. Effect of nanotopographical density on the cell morphology.** (a) Representative immunofluorescent images of F-actin (red), vinculin (green), and DAPI (blue) of hMSCs cultured on the flat and various nanopatterned surfaces, indicating that the structure of hMSCs was sensitively regulated by nanotopographical density. (b and c) Quantification of cell body and nucleus. The values of perimeter and area were normalized to the flat substrates. The 50 - 100 cells were used for quantification. Error bars represent the SD about the means. (d) Correlation between cell body and nucleus.

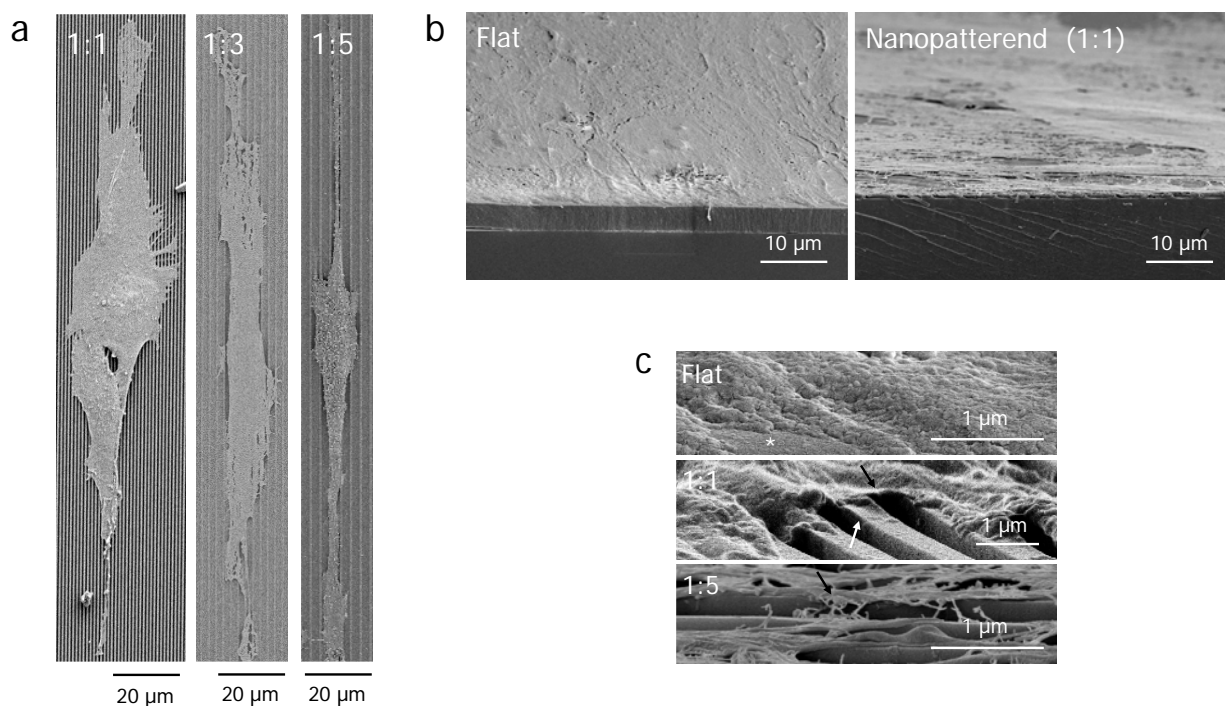


**Figure 4.3. Representative SEM images of cellular morphologies on various nanopatterned surfaces.** (a) SEM images of cellular morphologies on 1:1, 1:3, and 1:5 nanogrooved matrices (top view). (b) Low- and (c) high- magnification images of the tilted view of hMSCs on the flat and nanogrooved matrices. The (\*) indicates the flat substrate. The black arrows indicate that the cells were adhered on the ridge of the nanogrooved matrices. The deformation of ridges on the nanopattern was observed (black arrow).

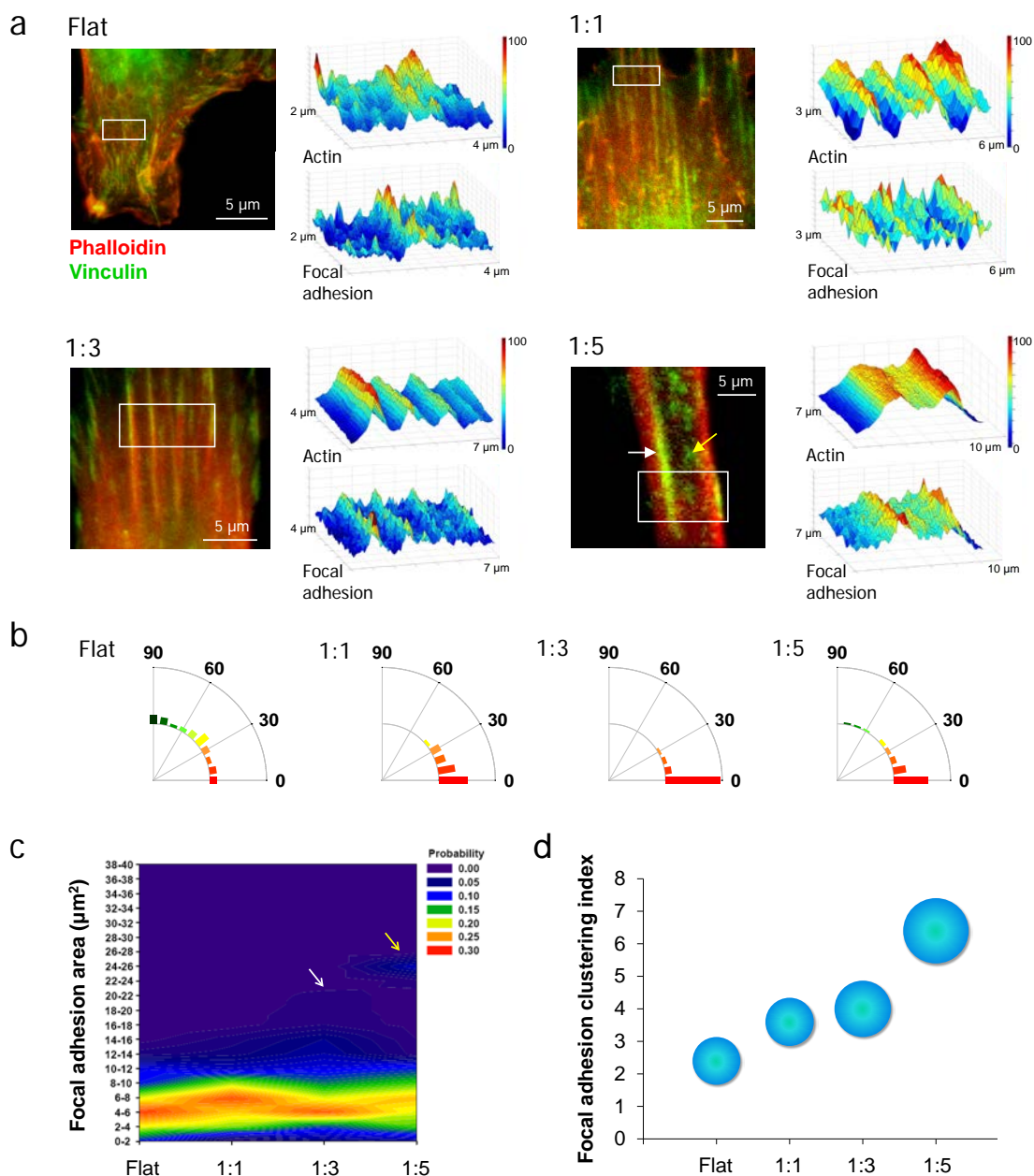


**Figure 4.4. Effect of nanotopographical density on the organization of focal adhesions.** (a) Immunostaining images and colorimetric plot of F-actin and focal adhesions, showing the high co-localization between the FAs and actin cytoskeleton of hMSCs. F-actin (red) and vinculin (green). (b) Angular distribution of focal adhesions. An orientation of  $0^\circ$  represents perfect alignment with the ridge/groove direction. The 200 cells were used for quantification. (c) Probability colorimetric map of focal adhesion (FA) area. Increased portion of large FA in 1:3 (white arrow) and 1:5 (yellow arrow). The 1:5 spacing ratio show dual-peak at 6-8 and 24-26  $\mu\text{m}^2$  ranges. The 200 cells were used for quantification. (d) Focal adhesion clustering index. The focal adhesion clustering index was calculated by dividing the area of top 10% of large focal adhesion sites with the area of unit FA ( $5 \mu\text{m}^2$ ). The radius of circle represents SD.

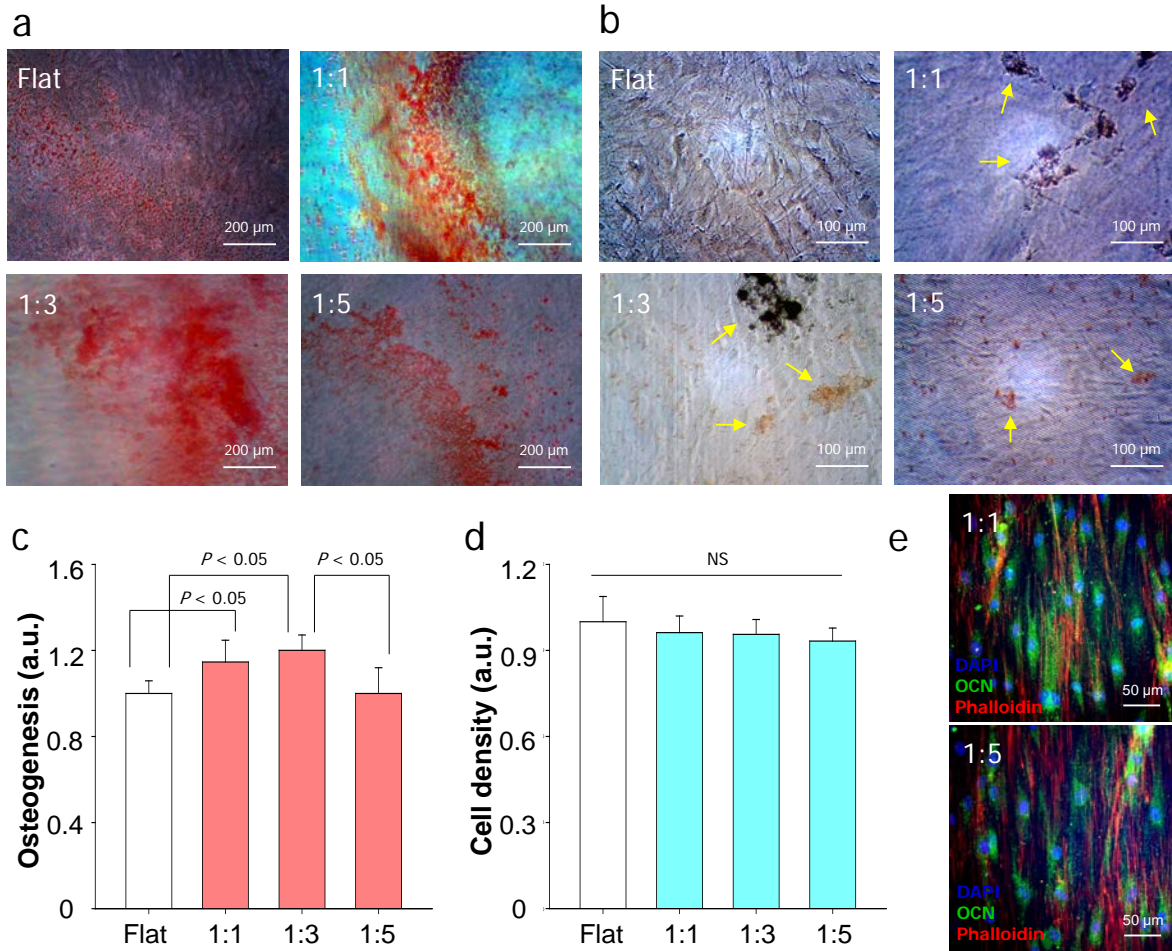


**Figure 4.5. Osteogenesis of hMSCs on various nanopatterned surfaces.** (a) Alizarin Red S and (b) Von Kossa staining of hMSCs cultured on the nanogrooved matrices and flat as a control for 21 days in osteogenic medium. The arrows indicate the mineralized bone nodules formed. Quantification of (c) the degree of mineralization as measured by Alizarin red S staining (d) cell viability of cells for 21 days and. All values were normalized to the control. Error bars represent the SD about mean ( $n = 3$  for each group). (e) Representative immunofluorescent staining of OCN (osteogenesis marker; green) of hMSCs on the nanogrooved matrices for 7 days in osteogenic medium, showing the higher expression of the OCN of cells on the 1:1 nanopattern than that on the 1:5 nanopattern.

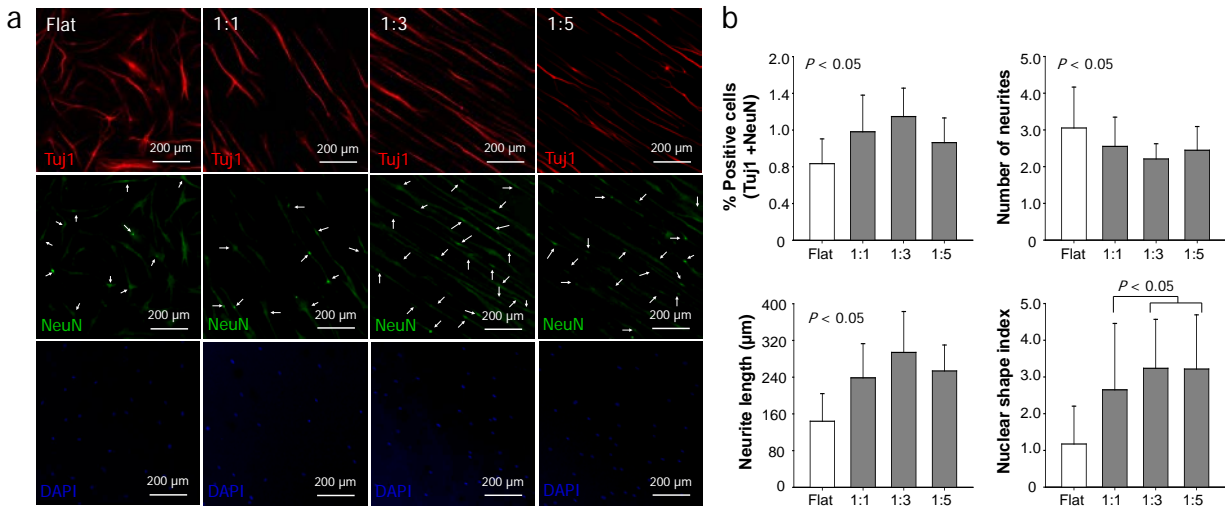


**Figure 4.6. Neurogenesis of hMSCs on various nanopatterned surfaces.** (a) Representative immunofluorescent staining of TUJ1 (red), NeuN (green), and DAPI (blue) of hMSCs on flat and nanogrooved matrices with the use of neurogenesis medium. (b) Quantification of the degree of neurogenesis (number of cells stained with TUJ1 and NeuN/total number of cells (DAPI)), number of neuritis, length of neuritis, and nuclear shape index. The nuclear shape index was normalized to the flat substrate. The ten images per each substratum were used for quantification, respectively.



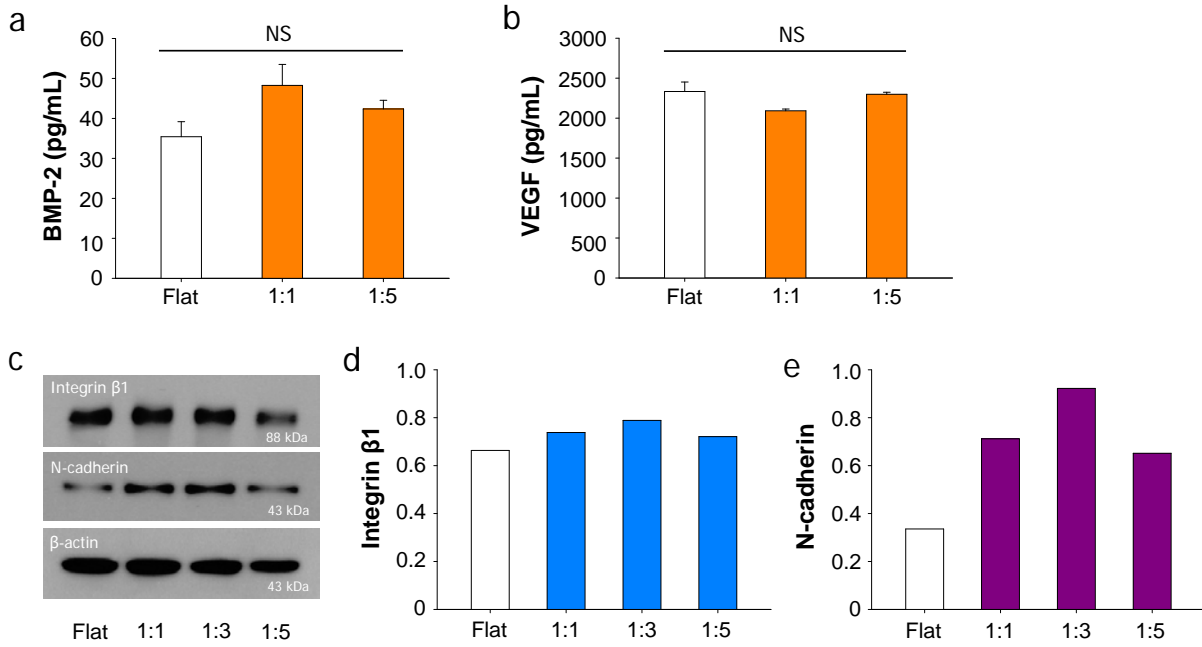


**Figure 4.7. Quantification of biochemical soluble factors and proteins according to nanotopographical density.** Quantification of (a) BMP-2 and (b) VEGF protein in conditioned medium of hMSCs on the nanogrooved matrices and flat substrate for 21 days. The results indicate no significant difference between the nanotopography and flat ( $P > 0.05$ ). (c) Western blot analysis and (d) quantification of the values of integrin  $\beta$ 1 and N-cadherin expression of hMSCs cultured on nanogrooved matrices and flat substrate. The hMSCs were cultured for 7 days and the western blot study was performed under same experimental conditions.



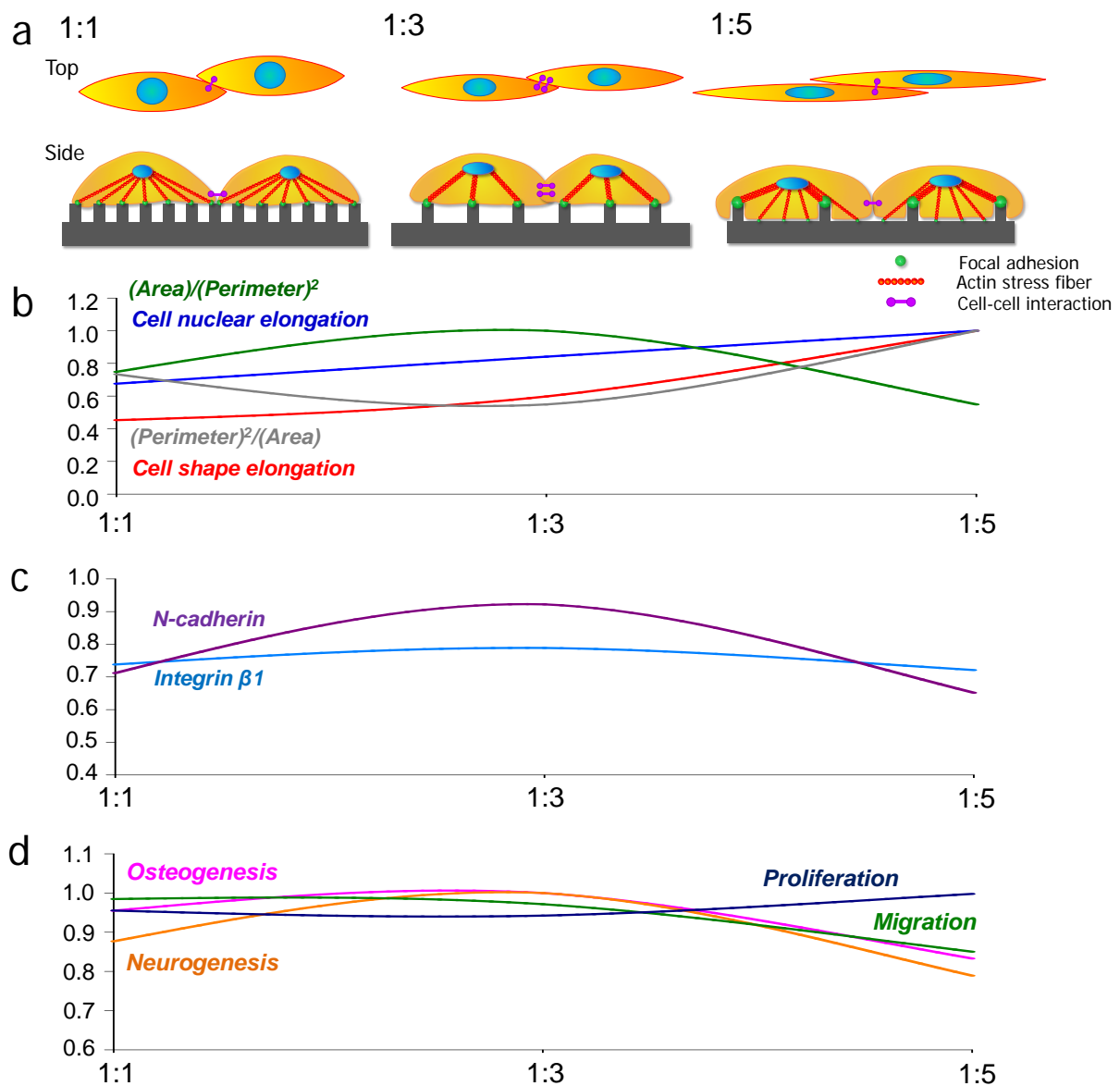


**Figure 4.8. Relative trends of morphological factors, intracellular protein levels and cell functions with respect to the nanopatterned densities.** (a) Illustrative summary of cellular responses on various nanopatterned surfaces. (b) Trends of morphological index according to the nanopatterned density such as cell body elongation, nuclear elongation, CSI  $[(area)/(perimeter)^2]$  and a reciprocal of CSI  $[(perimeter)^2/(area)]$ . (c) Trends of intracellular proteins for cell-substrate interaction (integrin  $\beta 1$ ) and cell-cell interaction (N-cadherin). (d) Relative trends of osteogenesis, neurogenesis, migration, and proliferation according to the pattern density. All values obtained in this study were normalized from 0 and 1.

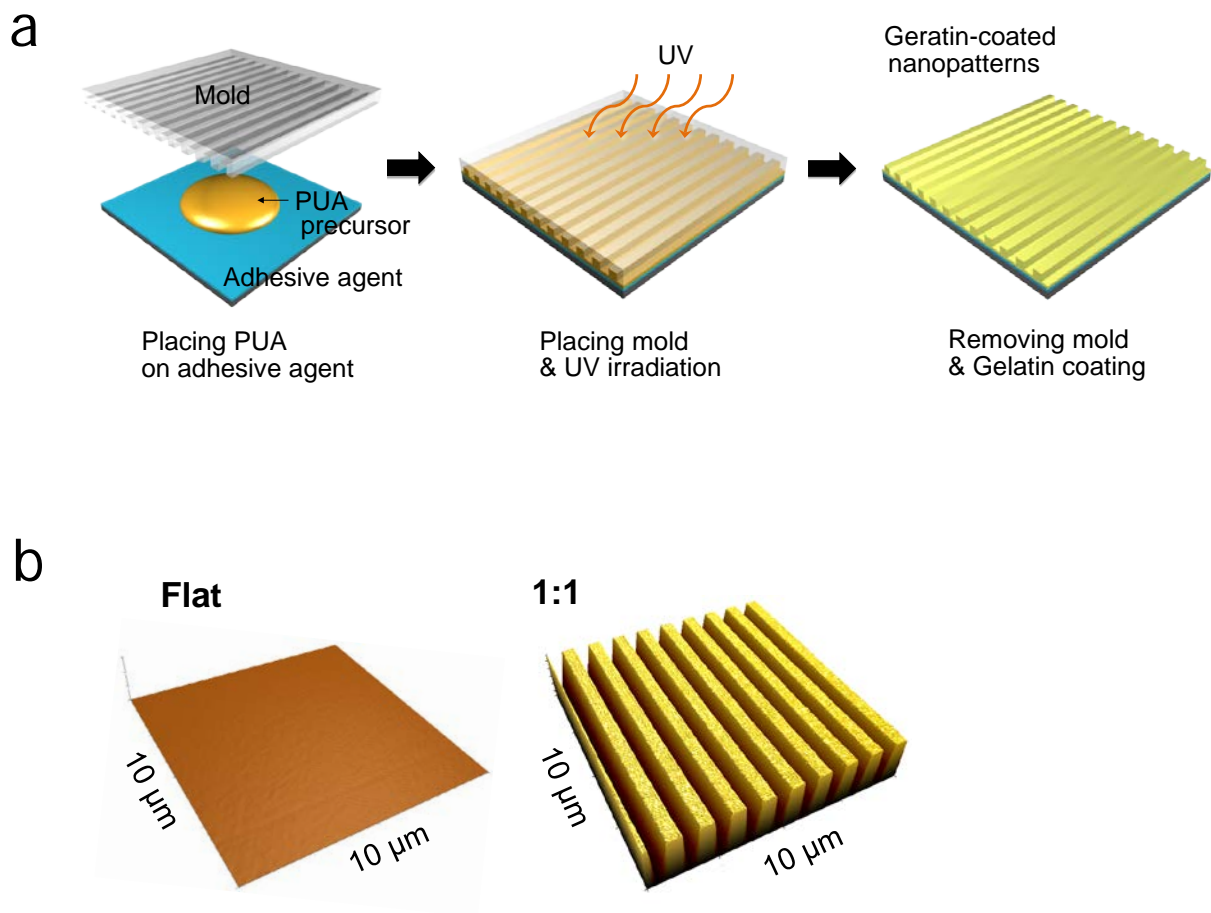


**Figure 4.S1. Schematic illustration of fabricating nanogroove patterns.** (a) Fabrication step of nanopatterns with UV-assisted capillary force lithography. (b) AFM images of representative flat and 1:1 patterns.

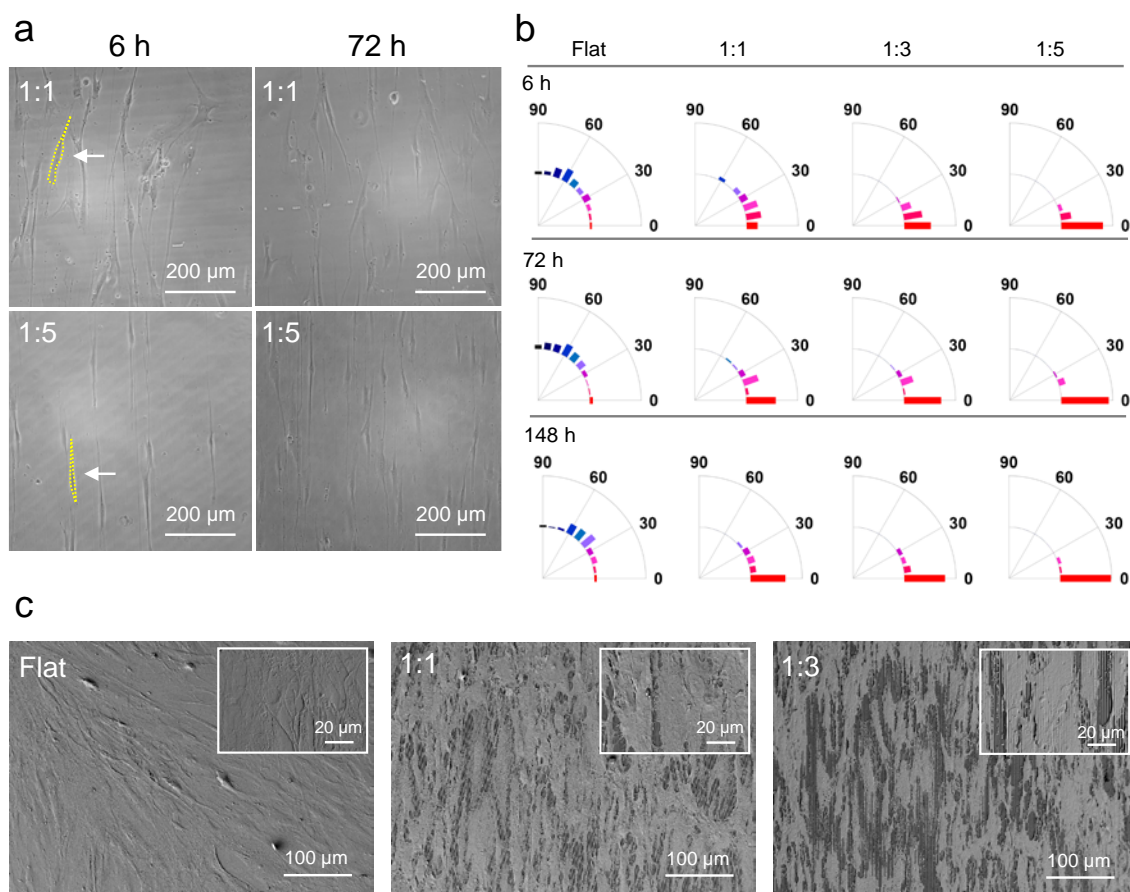


**Figure 4.S2. Time-dependent change of hMSC morphology and orientation by nanotopographical density.** (a) Representative phase contrast images, showing the initial cell adhesion (6 h), and fully adhesion (72 h) on the 1:1 and 1:5 nanogrooved matrices. (b) Quantification of time-dependent orientation of hMSC body on the flat vs. nanogrooved matrices. Each dot represents a single cell, and an orientation of  $0^\circ$  represents perfect alignment with the ridge/groove direction. The 50 - 100 cells were used for quantification. (d) Representative scanning electron microscopy images of hMSCs after 148 h culture on the flat and nanogrooved matrices. The insets show the high-magnification images.

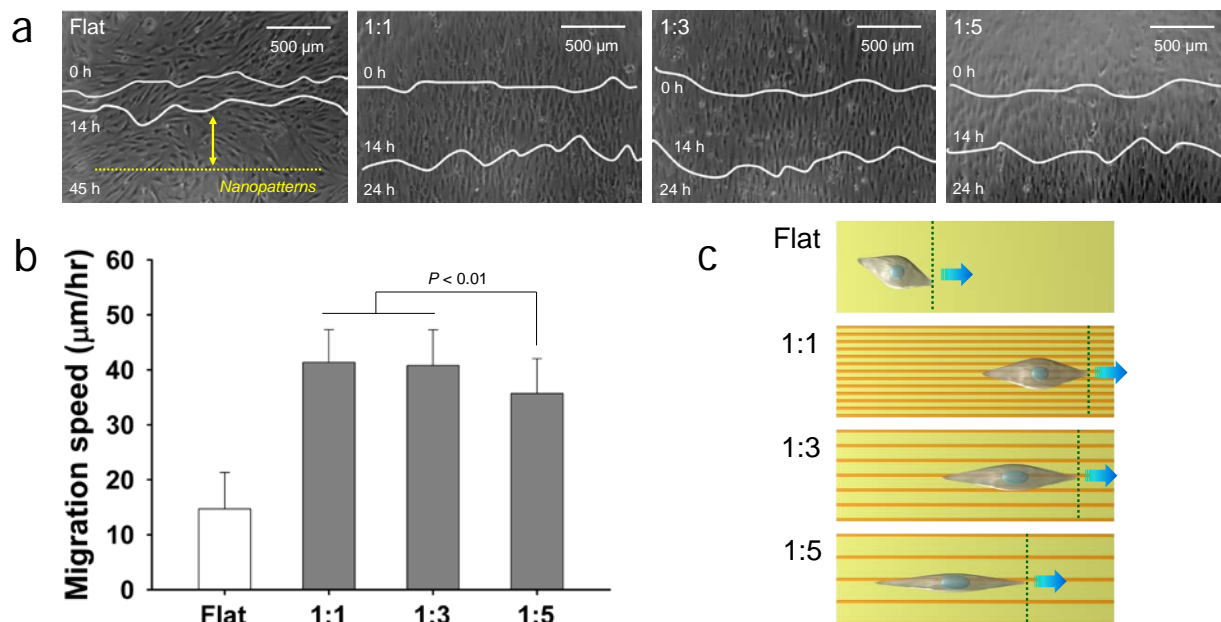


**Figure 4.S3. Cell migration assay with wound healing model.** (a) Representative microscopic images of cell migration according to nanotopographical density. (b) Migration speed of hMSCs according to the nanotopographical density. (c) A schematic illustration of cell migration result.

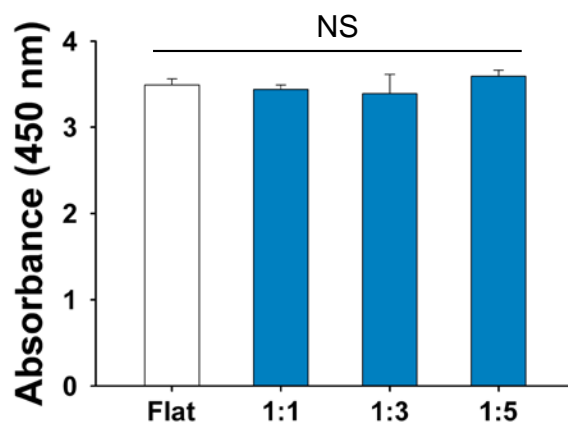


**Figure 4.S4. Proliferation of hMSCs on the nanogrooved matrices and flat substrate for 7 days.** The result indicates no significant difference between the nanotopography and flat ( $P > 0.05$ ).

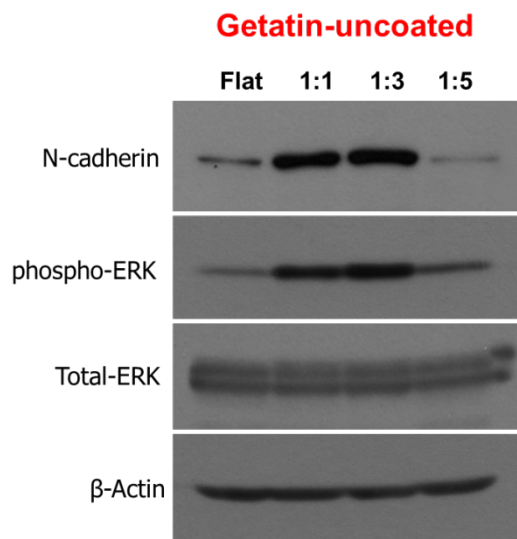


**Figure 4.S5. Western blot analysis of N-cadherin, pERK, and tERK expression of hMSCs cultured on the gelatin-uncoated nanogrooved matrices.** The hMSCs were cultured for 7 days and the western blot study was performed under same experimental conditions.

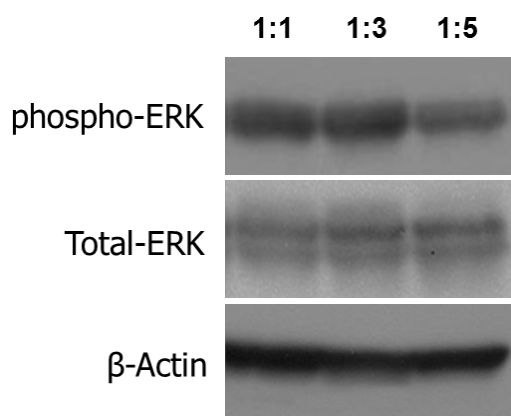


**Figure 4.S6. Western blot analysis of pERK and tERK expression of hMSCs cultured on the gelatin-coated nanogrooved matrices.** The hMSCs were cultured for 7 days and the western blot study was performed under same experimental conditions.

## **PART II: DESIGNING AND MANIPULATING NANOPATTERNED HIERARCHICAL PLATFORMS WITH PRECISELY CONTROLLED TOPOGRAPHICAL ARCHITECTURES AND SIZES**

---

### **Overview**

In previous Part I, we have developed the matrix nanotopography with defined ridge/groove patterns with precisely controlled various sizes, inspired from the topographical features of extracellular matrix (ECM). Despite the potentially importance of engineering ECMs described previously, there still appears a gap in order to fully mimic the topography features of complex ECMs and tissues such as hierarchically organized protein fibers with micro-, nano-, and sub-nano scale sizes (i.e., from tens of nanometers to several hundreds of micrometers). To address this challenge, Part II develops a series of nanopatterned hierarchical platforms using CFL in combination with micro wrinkling technique and nanomaterials. To mimic hierarchically micro and nanopatterned architecture of ECMs or tissues, the novel methods that combine CFL with micro wrinkling technique were developed (Chapter 5). Using this methodology, anisotropically multiscale patterned substrata with precisely defined micro- and nanotopography (i.e., micro- and nanopatterned hierarchical platforms) were fabricated. With variable multiscale topographies in cell substrates, various cells including fibroblasts, osteoblast-like cells, endothelial cells, and stem cells are quantitatively analyzed in terms of cellular adhesion and function, demonstrating the importance of nanotopography in micro- and nanoscale hierarchical topography of ECM for regulating cellular functions. In Chapter 6, we developed the platforms with nano and sub-nanopatterned hierarchical topographies fabricated by using matrix nanotopography and graphene (a type of carbon-based nanomaterials). The graphene was coated on the matrix nanotopography with various nanoscale parallel ridges and grooves (ranged from 300 nm to 800

nm). We showed that the graphene-matrix nanotopography hybrid platforms could promote the functions of cells through the synergically enhanced cell alignment and elongation from nanotopography as well as cell spreading from graphene in the platforms. Taken together, these results in Part II propose that nanopatterned hierarchical platforms mimicking micro/nano- or nano/sub-nanotopographical properties of ECMs or tissues may be able to promote the function of cells, which would allow us to set up an efficient strategy for designing advanced biomimetic engineering systems.

## **Chapter 5. Bioinspired Configurable Hierarchical Micro- and Nanostructure with Precisely Controlled Sizes for Functional Alignment and Guided Orientation of Cells**

### **5.1. Summary**

This work reports the design and manipulation of multiscale architectures of extracellular matrix for understating a role of nanotopography on cellular structure and function for tissue engineering and fundamental cell biology. Using capillary force lithography in combination with micro wrinkling technique, we fabricate anisotropically multiscale patterned substrates with precisely defined micro- and nanotopography. With variable multiscale topographies in cell substrates, various cells including fibroblasts, osteoblast-like cells, endothelial cells, and stem cells are quantitatively analyzed in terms of cellular adhesion and function. It is found that cells could sensitively recognize the nanotopography in multiscale patterned substrates, showing highly aligned and orientated cell shapes as well as enhanced cell functions such as fibronectin synthetics from fibroblasts, bone mineralization from osteoblast-like cells, and differentiation of stem cells compared to those on micropatterned substrates. Furthermore, it is demonstrated that multiscale topography could enhance the cell-substrate or cell-cell interactions (i.e., focal adhesion, integrin  $\beta 1$ , and connexin 43) as a potential role of nanotopography in multiscale patterned substrates on enhanced cellular functions. Biomimetic multiscale topography not only could provide a new route for enhancing cellular function in advanced tissue engineering but serve a new platform for understanding of cell-matrix or cell-cell interactions in fundamental cell biology.



## 5.2. Introduction

Living cells are exposed to complex and functional microenvironments including soluble macromolecules, biophysical cues, and interactions between cell-cell and cell-extracellular matrix (ECM) [1-3]. Thus the design and manipulation of engineered cellular microenvironments is of great important in a wide variety of biomedical applications such as fundamental biology, therapeutic and diagnostic research, stem cells and regenerative medicine, and developing *in vitro* human disease models [1-4]. Among various cellular microenvironmental factors mentioned above, it is widely accepted that ECM may play an essential role which directly signals to cells by providing spatial and mechanical cues for regulating their own shape, function, and fate [1-3,5,6]. For example, the ECMs affect pathophysiologic and physiological events (e.g., development or remodeling of cardiovascular tissue) by their architectures whereas several pathological conditions (e.g., cancer cell invasion) are commonly influenced by ECM remodeling [6].

Inspired by the analysis of well-defined structures in ECMs, for example collagen micro- and nanofibrils in connective tissues, cell culture platforms mimicking structural *in vivo* ECM have been designed and developed using micro- and nanofabrication technologies [1-6]. For example, Kim *et al.*, reported that the anisotropically aligned matrix that mimics the nanotopography of ECM in heart can engineer the cardiac myocytes for constructing their structural and functional properties like native cardiac tissues [7]. Despite the potentially importance of engineering ECM mentioned above, there still appears a large gap in order to fully mimic the topographies of complex ECM for cell and tissue engineering. Even though the native ECM is composed of (i) very complex and well-defined nanostructures of protein fibrils such as collagen and fibronectin in specific directions as well as (ii) hierarchically organized protein

fibers with microscale sizes (i.e., from tens of nanometers to several hundreds of micrometers), most studies have dealt with fabrication of a very simple nanotopography (e.g., nanogrooves or nanoposts) and frequently neglected a microscale hierarchical topography of ECM because of the technical limitation for multiscale fabrication [1-3,6-12]. Namely, the current simple patterns cannot provide cells and tissues the precisely defined biophysical cues of native physiological microenvironments composed of nano- and microscale topography, which may eventually be one of the main hurdles for constructing functional tissues or organs. Thus, it is very important to develop a methodology for creation of truly biomimetic ECM-like architecture to regulate structure and function of cell and tissue toward advanced tissue engineering and regenerative medicine.

In this study, we present a simple but robust method based both on capillary force lithography (CFL) and original wrinkling technique, by which we fabricated precisely controllable multiscale hierarchical structure using polyurethane acrylate (PUA) [13] without any deformation in periodic wrinkles of polyethylene glycol-diacrylate (PEG-DA) mold and UV/O treated PDMS sheet. Using the multiscale hierarchical platforms that could mimic the nano- and microtopography as well as defined structure direction of complex ECM, the precisely controlled cellular morphology and function was demonstrated. We also proposed a role of nanotopography on cellular structure and function in native-like ECM micro- and nanopatterned hierarchical platforms

### **5.3. Materials and methods**

#### **5.3.1. Fabrication of nanopatterned PUA mother mold**

The polyurethane acrylate (PUA) mother mold was fabricated by curing PUA pre-polymer

(301RM, Minuta Inc.) on silicon master molds prepared by conventional photolithography. To fabricate a sheet-type flexible mold, the liquid precursor was drop-dispensed onto a silicon master mold (250 nm groove and 250 nm spacing), and then transparent polyethylene terephthalate (PET) film was brought into contact with the precursor surface. Subsequently, the mold was exposed to UV light ( $\lambda = 250 \sim 400$  nm) for 30 s through the transparent backplane (dose = 100 mJ/cm<sup>2</sup>). Finally, the PUA mold was peeled from the silicon master mold and additionally cured overnight to terminate the remaining active acrylate groups on surface.

### **5.3.2. Fabrication of hierarchically multiscale patterned substrata**

To prepare multiscale patterned substrata, a PDMS sheet was treated with UV/O and coated with adhesion promoter; TMSPMA (step 1). Then, a small amount (0.1 ~ 0.5 mL) of PEG-DA precursor solution containing 1% (v/v) photoinitiator was drop-dispensed onto TMSPMA treated PDMS that had been prepared by step 1. Next, PUA mother mold was placed on the liquid precursor, followed by UV exposure for a few tens of seconds. After the UV curing, the mold was peeled from the PDMS, leaving behind a replica of nanogrooves and fully cured by exposing UV for 10 h to render the surface inactive during subsequence pattern replication steps (step 2). To generate micro wrinkle structure, PDMS assembly was compressed in the one direction and got available to be continuously replicated with PUA mold (step 3).

### **5.3.3. Cell culture on hierarchically multiscale patterned substrata**

Cells were grown in DMEM with 10% FBS and 1% penicillin-streptomycin (Gibco, Milan, Italy) at 37°C in a 5% CO<sub>2</sub> atmosphere. For immunohistochemical analysis, adhered cells on samples were fixed with a 4% paraformaldehyde solution (Sigma-Aldrich, Milwaukee, WI,

USA) for 20 min, permeabilized with 0.2% Triton X-100 (Sigma-Aldrich, WI, Milwaukee, USA) for 15 min, and stained with TRIT conjugated phalloidin (Millipore, Billerica, MA, USA), 4, 6-diamidino-2-phrnykinodole (DAPI; Millipore, Billerica, MA, USA), or fibronectin antibody (Sigma-Aldrich, WI, Milwaukee, USA) for 1 h. Images of the stained cells were taken using a fluorescence microscope (Zeiss, Germany). For SEM imaging cells on the substrates, cells adhered to the sample surfaces were fixed with modified Karnovsky's fixative consisting of 2% paraformaldehyde and 2% glutaraldehyde (Sigma-Aldrich) in a 0.05 M sodium cacodylate buffer (Sigma-Aldrich) for 4 h. The samples were washed with 0.05 M sodium cacodylate buffer 3 times for 10 min and fixed with 1% osmium tetroxide (Sigma-Aldrich). The samples were then washed with distilled water and dehydrated with graded concentrations (50, 70, 80, 90, and 100% v/v) of ethanol. Then, the samples were treated with hexamethyldisilazane (Sigma-Aldrich) for 15 min. Finally, the samples were coated with gold prior to cell shape observation by FESEM (JEOL, JSM-5410LV, Japan). The quantitative analysis was analyzed using a custom-written MATLAB script using the images by obtained.

#### **5.3.4. SEM observation**

Cells adhered onto the sample surfaces were fixed with modified Karnovsky's fixative consisting of 2% paraformaldehyde and 2% glutaraldehyde (Sigma-Aldrich) in a 0.05 M sodium cacodylate buffer (Sigma-Aldrich) for 4 hr. The samples were washed with 0.05 M sodium cacodylate buffer 3 times for 10 min and fixed with 1% osmium tetroxide (Sigma- Aldrich). The samples were then washed with distilled water and dehydrated with graded concentrations (50, 70, 80, 90, and 100% v/v) of ethanol. Then, the samples were treated with hexamethyldisilazane (Sigma-Aldrich) for 15 min. Finally, the samples were coated with gold prior to cell shape observation

with FESEM (JEOL, JSM-5410LV, Japan).

### **5.3.5. Focal adhesion analysis**

To investigate the effects of FAs with the variation of nanotopographical density, we cultured cells on the substrates for 12 h followed by immunostaining. The fluorescence intensities of vinculin and F-actin were analyzed using custom-written MATLAB 2011b (MathWorks, Natick, MA).

### **5.3.6. Proliferation analysis**

Cells ( $4 \times 10^4$  cells/samples) were seeded onto samples and cultured for up to 2 and 3 days, respectively, in DMEM (Sigma-Aldrich, Milwaukee, WI, USA) with 10% FBS (Sigma-Aldrich, Milwaukee, WI, USA) and 1% antibiotics (Sigma-Aldrich, Milwaukee, WI, USA) at 37°C in a humidified atmosphere containing 5% CO<sub>2</sub>. The quantitative analysis of the cell proliferation on the nanogrooved matrices was performed using WST-1 assay (EZ-Cytox Cell Viability Assay Kit, Daeillab Service Co., LTD).

### **5.3.7. Osteogenesis and neurogenesis analysis**

Human mesenchymal stem cells (hMSCs) ( $4 \times 10^4$  cells/sample) or MG-63 cells were cultured for 14 days on the samples in osteogenic differentiation media (100 nM dexamethsone, 50 µM ascorbic acid, and 10 mM glycerol 2-phosphate in normal media). Alizarin Red S (Sigma-Aldrich) staining was used for confirming osteogenic differentiation of hMSCs on the sample surfaces. The degree of mineralization was measured by Alizarin Red S staining of hMSCs cultured on the sample surfaces, and this measurement was used for quantification of the

osteogenic differentiation of hMSCs. Cells were stained with Alizarin Red S and were destained with cetylpyridinium chloride (Sigma-Aldrich), and then the extracted stains were measured using an ELISA reader (VERSAMAX reader, Molecular Devices, Sunnyvale) at 540 nm. To differentiate hMSCs into neuronal cells, hMSCs ( $2 \times 10^4$  cells/sample) were cultured in the neurogenesis media (NPBM media (Bio Whittaker) with 5 mM cAMP, 5 mM IBMX, 25 ng/ml NGF, 10 ng/ml BDNF, 2.5 mg/ml insulin, and 50  $\mu$ g/ml ascorbic acid (Sigma-Aldrich)).

#### **5.3.8. Western blot analysis**

Total cellular protein was extracted by RIPA lysis buffer (62.5 mM Tris-HCL, 2% SDS, 10% glycerol, pH 7.5) with added proteinase inhibitor cocktail (Invitrogen, USA). Cell lysates were incubated on ice for 30 min and then centrifuged at 13,000 rpm for 30 min at 4°C. Supernatant (protein lysate) was collected and protein concentration was determined by a micro bicinchoninic acid (BCA) Protein Assay Kit (Bio-rad, Hercules, Calif). 25  $\mu$ g aliquots of the cell lysates were separated by 8% SDS-PAGE under reducing conditions. Separated proteins were transferred to a PVDF membrane (Millipore, Corporation, Bedford, MA, USA) at 30 V for 1 h. After blocking with 5% skim milk in PBST, the membrane were incubated overnight in primary antibody at 4°C. Primary antibody was purchased from the company (Integrin  $\beta$ 1 (Santa Cruz, Biotechnology, Santa Cruz, CA); N-Cadherin (Millipore, Billerica, MA, USA). After washing, the membranes were probed with horseradish peroxidase-conjugated anti-IgG (Invitrogen), and proteins were visualized using the ECL chemiluminescence detection system (GenDEPOT, Houston, TX, USA). Protein expression was normalized versus  $\beta$ -actin antibody (Cell Signaling Technology, Beverly, MA, USA) on the same blot membrane. Quantification of the Western blot was performed using the Image J software with a normalization of the level of the entire protein.

### 5.3.9. Statistical analysis

Student's t-test was used for statistical analysis. All quantitative results were presented as mean  $\pm$  standard deviation (SD).

## 5.4. Results

### 5.4.1. Fabrication of micro- and nanopatterned hierarchical platforms

The current fabrication methods of hierarchical wrinkle structures have overlooked two important issues from an engineering perspective; (1) the wrinkles should be formed in a precisely controlled way and (2) the patterned buckles or wrinkles should be easily self-replicated for further processes and control cellular behaviors. Features of materials which they used could not allow to self-replicate their mother mold due to their affinity between them. In other words, the adhesion force of the materials could be, if any, so weak to be in vain taken off from a mold, which can raise some difficulties in replication. In addition, as far as UV/O treatment was not performed, a period of wrinkles would not be precisely controlled. To address this challenge, we have developed a new method to create micro- and nanopatterned structures.

Fig. 5.1a shows a schematic of the fabrication of multiscale wrinkle-patterned mold. A PDMS sheet was treated with UV/O and coated with adhesion promoter 3-trimethoxysilylpropyl methacrylate (TMSPMA), which was 1 cm thick enough to endure quite a large compressive strain lest it was torn during fabrication (step 1). When a few droplets of PEG-DA precursor solution containing 1% (v/v) photoinitiator were dispersed using PUA mother mold (250 nm groove and 250 nm spacing), acryl groups of the photoinitiator under UV exposure started to covalently bond with projected acryl groups of surface bound TMSPMA and polymerize PEG-DA, by which TMSPMA made the adhesion of PEG-DA to UV/O treated PDMS sheet enhanced

to prevent this PDMS assembly from detaching each other during demolding step [14]. PEG-DA has been widely used in tissue constructs and in definite mold fabrication; not only as templates for cell encapsulation [15] and cell-laden microgel [16] but also master molds by its comparable resolution to conventional photoresist-based patterns [17]. In this experiment, we confirmed that preloads approximately at 10 bar for one hour induced PUA mother mold with linear grooves patterned to be filled conformably with PEG-DA precursor via capillary force between the grooves (step 2). After PUA mother mold peeled off, the PDMS assembly was compressed in the one direction for micrometer-sized wrinkling. The assembly kept the nanometer-sized grooves along with micrometer-sized wrinkle, and got available to be continuously replicated with rigiflex PUA mold (step 3).

It is meaningful that the multiscale hierarchical patterns were produced on the surface of the micrometer-sized wrinkled PDMS sheet in a precisely controlled way, keeping their periods and nanopatterns on each wrinkle. A wide variety of studies about wrinkling demonstrated that UV/O treatment played significant roles not only to volatilize prepolymer solution but also to change the molecular moieties of PDMS surface into a stiff SiOx [18]. The UV/O treatment converted the PDMS surface within depth of the several nanometers into an oxidized state [19]. Thus, the sheet had the stiffer silica-like property on its surface. In this experiment, when compressive stress was applied to the UVO-treated PDMS sheet, relatively rigid silica-like oxidized surface was less shrunk due to the discrepancy in modulus of both sides, causing the wrinkling phenomenon; The modulus of the the PDMS sheet was measured as ~1.5 MPa, but after UV/O treatment, the modulus of the silica-like oxidized layer estimated as ~40 GPa [20]. In respect to the modulus of PEG-DA, it was generally observed to range from 2 to 5 MPa, which could be modified dependently with various parameters such as the monomer molecular weight,



the water content and the photoinitiator concentration [21]. Because PEG-DA had much lower modulus than silica-like stiff PDMS film, we can ignore the effect of the patterned PEG-DA on the buckling phenomenon. This interesting wrinkling phenomenon has given a motivation to researchers who study about a principle of wrinkle formation and its theoretical analysis of mechanics and kinetics [22, 24]. The wrinkling phenomenon was described based on their buckling theories as in the Supporting Information.

#### **5.4.2. Effects of micro- and nanopatterned hierarchical topography on cellular alignment and orientation**

Living cells can display high sensitivity to the local nano and micro scale topography of extracellular matrix (ECM) [1-4]. The ECMs in our body are composed a complex and well-defined nanostructure of proteins fibres such as fibrillar collagens and elastins with feature sizes ranging from tens to several hundreds of nanometers [1-3,5-6]. The organization of ECM is frequently hierarchical, with many proteins capable of forming large scale structures with micro and nanoscale sizes (~several hundred microns). From the inspired aspect on the hierarchical micro- and nanostructures of ECMs, We fabricated bio-inspired multiscale hierarchical wrinkles by combining surface wrinkling and nanopatterned PUA films. In this study, we prepared 30  $\mu\text{m}$  wavelength (defined as ‘small micro size’) and 100  $\mu\text{m}$  wavelength (defined as ‘large micro size’) wrinkle substrates, and 250 nm/30  $\mu\text{m}$  (250 nm groove/ridge nanopatterned on the 30  $\mu\text{m}$  micro hierarchical wrinkle substrates; 250/30 anisotropic nanotopography in micro hierarchical wrinkle substrates (ANMSs)) and 250 nm/100  $\mu\text{m}$  wrinkle substrates (250 nm groove/ridge nanopatterned on the 100  $\mu\text{m}$  micro hierarchical wrinkle substrates; 250/100 ANMSs) (Fig. 5.1).

To verify the hypothesis that the ANMSs can effectively guide on the cellular alignment

and orientation in the initial adhesion and fully adhesion, we first cultured NIH3T3 fibroblast cells, known as a representative mechano-sensitive cell) on the flat, micro hierarchical wrinkle, and nano/micro hierarchical wrinkle substrates. At 2 h and 14 h after cell seeding, we observed the NIH3T3 fibroblast cells on the substrates and found that the cells were well-attached on the 250 nm/30  $\mu$ m and 250 nm/100  $\mu$ m ANMSs with formation of strong alignment and orientation of cells along the direction of nanotopography on the substrates compared to those on the flat and 30 and  $\mu$ m wrinkle substrates (Fig. 5.2). The quantification results of cell orientation on the flat vs. micro hierarchical wrinkle vs. and nano/micro hierarchical wrinkle substrates were also agreed to our observation (Fig. 5.2b and c).

Next, we checked whether various types of cells were also sensitively influenced on the nanotopography in the micro hierarchical wrinkle substrates. We cultured MG-63 cells, HUVECs, and hMSCs on the 30  $\mu$ m wrinkle substrates and 250 nm/30  $\mu$ m ANMSs (Fig. 5.3). We found that the alignment and orientation of various types of cells were also very strongly influenced along the direction of nanotopography in the micro hierarchical substrates, which was also checked by the quantification results (Fig. 5.3). Together, we here demonstrated for the first time that the anisotropically nanotopography in the micro hierarchical substrates critically have an important regulator of the alignment and orientation of cells probably due to similar property with the natural organization of ECMs.

#### **5.4.3. Mechanosensitivity of cells to micro- and nanopatterned topography**

Importantly, the SEM image of the NIH3T3 fibroblast cell on the 250 nm/30  $\mu$ m ANMSs indicate that the cell showed the highly aligned morphology along the direction of anisotropically nanotopography in micro hierarchical wrinkle substrate and affected the deformation of ridges on

the nanopatterns in the micro hierarchical wrinkle substrates (Fig. 5.4), which may be an important mechanical cues by an interaction between cell and substrate for regulating cell functions (Fig. 5.5).

Next, we investigated the effects of anisotropically nanotopography in micro hierarchical wrinkles on cytoskeleton organization and nucleus alignment of cells. We cultured NIH3T3 fibroblast cells on the 30  $\mu\text{m}$  hierarchical wrinkle substrates and 250 nm/30  $\mu\text{m}$  ANMSs for 14 hr. As shown in Fig. 5.6, it was found that the nanotopography in micro hierarchical wrinkles greatly influenced the cytoskeleton organization and nucleus alignment of cells. Immunofluorescence staining images clearly showed that the extent of aligned cytoskeletal structure of NIH3T3 fibroblast cells on the 250 nm/30  $\mu\text{m}$  hierarchical wrinkle substrates compared to those on the 30  $\mu\text{m}$  hierarchical wrinkle substrates (Figs. 5.6a and b). As expected, we showed that the nucleus of NIH3T3 fibroblast cells on the 250 nm/30  $\mu\text{m}$  ANMSs elongated more than those on the 30  $\mu\text{m}$  hierarchical wrinkle substrates, which is also confirmed by through performing the quantitative analysis of nuclear shape factor (NSF; defined as (major axis)/(minor axis)) (Fig. 5.5c). Furthermore, it is demonstrated that multiscale topography could enhance the cell-substrate or cell-cell interactions (i.e., focal adhesion, integrin  $\beta 1$ , and connexin 43) as a potential role of nanotopography in multiscale patterned substrates on enhanced cellular functions (Fig. 5.6d).

#### **6.4.4. Effects of micro- and nanopatterned topography on cellular function**

This work is driven by the following key question whether the anisotropically nanotopography in micro hierarchical wrinkle substrates have a role for cellular functions by the enhanced alignment and orientation of cells. Although a detailed basic research on this issue remains to be

performed including specific signaling pathway, we here showed the representative function of various types of cells by the anisotropically nanotopography in micro hierarchical wrinkle substrates. Interestingly, we found that the ANMSs collectively promoted the functions of cells (Fig. 5.7). NIH3T3 fibroblast cells were proliferated with aligned orientation along the direction of nanotopography as well showed the enhanced fibronectin production from cells on the ANMSs (Fig. 5.7). The high amounts of mineralization were observed on the MG63 cells on the ANMSs (Fig. 5.S2). We also showed that the ANMSs promoted the differentiation of hMSCs; the neural-like cells from the differentiation of hMSCs into neuron on the ANMSs had longer lengths of neurite than those on the micro hierarchical wrinkle substrate (Fig. 5.S2). In addition, we observed higher mineralization of hMSCs by osteogenesis of cells on the ANMSs compared to that on the micro hierarchical wrinkle substrate (Fig. 5.S2). Although it is noted that further studies on the effects ANMSs on cell functions are needed, these results strongly suggest that the high degree of sensitivity of cells to the nanoscale topography in micro-scale hierarchical structures may promote cell niche formation for promoting their functions.

## **5.5. Discussion**

This work is driven by the following key question: how do the multi-scale hierarchical structures enhance the function of cells compared to the micro-scale structures? Although detailed basic research on this issue remains to be performed including specific signaling pathway, we hypothesize that the unique characteristics of the nanoscale topographical cues on multi-scale hierarchical structures might play a crucial role in the enhancement of cell function as follows. Our data collectively reveal that the nanotopographical cues in the multi-scale hierarchical structures may be able to control the interactions at cell-substrate and cell-cell interfaces (i.e.,

enhanced focal adhesion alignment, integrin  $\beta 1$ , and connexin 43), which may influence the function of cells. Simply, the proposed mechanism follows these steps: nanotopography cues in substrate  $\rightarrow$  enhancing cell adhesion on substrata and interactions between cells-substrate  $\rightarrow$  enhancing function of cells (see Fig. 5.8 for a summary of this possible mechanism).

In summary, hierarchically nanopatterned platforms were designed and developed for better mimicking complex topography of ECM. To mimic hierarchically micro and nanopatterned architecture of ECMs or tissues, the novel methods that combine capillary force lithography with micro wrinkling technique were developed. Using this methodology, anisotropically multiscale patterned polyurethane acrylate substrates with precisely defined micro- and nanotopography (i.e., micro- and nanopatterned hierarchical platforms) were developed. With variable multiscale topographies in cell substrates, various cells including fibroblasts, osteoblast-like cells, endothelial cells, and stem cells are quantitatively analyzed in terms of cellular adhesion and function. It was found that cells could sensitively recognize the nanotopography in multiscale patterned substrates, showing highly aligned and orientated cell shapes as well as enhanced cell functions such as fibronectin synthetics from NIH 3T3 fibroblast cells, bone mineralization from MG-63 cells, and differentiation of hMSCs compared to those on micropatterned substrates. Furthermore, it was demonstrated that multiscale topography could enhance the cell-substrate or cell-cell interactions (i.e., focal adhesion, integrin  $\beta 1$ , and connexin 43) as a potential role of nanotopography in multiscale patterned substrates on enhanced cellular functions. Our work thus reveals the multiscale architecture-based devices can be a new route for enhancing cellular function in advanced tissue engineering but serve a new platform for understanding of cell-matrix or cell-cell interactions in fundamental cell biology.

## 5.6. References

- [1] Kim J, Kim HN, Lang Y, Pandit A. Biologically inspired micro- and nanoengineering systems for functional and complex tissues. *Tissue Eng Part A*. 2014 Mar 11 [Epub ahead of print].
- [2] Kim HN, Jiao A, Hwang NS, Kim MS, Kang do H, Kim DH, Suh KY. Nanotopography-guided tissue engineering and regenerative medicine. *Adv Drug Deliv Rev*. 2013;65(4):536-58.
- [3] Shao Y, Fu J. Integrated micro/nanoengineered functional biomaterials for cell mechanics and mechanobiology: a materials perspective. *Adv Mater*. 2014;26(10):1494-533.
- [4] Huh D, Hamilton GA, Ingber DE. From 3D cell culture to organs-on-chips. *Trends Cell Biol*. 2011;21(12):745-54.
- [5] Kim DH, Lee H, Lee YK, Nam JM, Levchenko A. Biomimetic Nanopatterns as Enabling Tools for Analysis and Control of Live Cells. *Adv Mater*. 2010;22(41):4551-66
- [6] Kim DH, Provenzano PP, Smith CL, Levchenko A. Matrix nanotopography as a regulator of cell function. *J Cell Biol*. 2012;197(3):351-60
- [7] Kim DH, Lipke EA, Kim P, Cheong R, Thompson S, Delannoy M, Suh KY, Tung L, Levchenko A. Nanoscale cues regulate the structure and function of macroscopic cardiac tissue constructs. *Proc Natl Acad Sci U S A*. 2010;107(2):565-70.
- [8] Trappmann B, Gautrot JE, Connelly JT, Strange DG, Li Y, Oyen ML, Cohen Stuart MA, Boehm H, Li B, Vogel V, Spatz JP, Watt FM, Huck WT. Extracellular-matrix tethering regulates stem-cell fate. *Nat Mater*. 2012;11(7):642-9.
- [9] Kim J, Kim HN, Lim KT, Kim Y, Seonwoo H, Park SH, Lim HJ, Kim DH, Suh KY, Choung PH, Choung YH, Chung JH. Designing nanotopographical density of extracellular matrix for controlled morphology and function of human mesenchymal stem cells. *Sci Rep*. 2013;3:3552.
- [10] Kim J, Kim HN, Lim KT, Kim Y, Pandey S, Garg P, Choung YH, Choung PH, Suh KY,

Chung JH. Synergistic effects of nanotopography and co-culture with endothelial cells on osteogenesis of mesenchymal stem cells. *Biomaterials*. 2013;30:7257-68

[11] McMurray RJ, Gadegaard N, Tsimbouri PM, Burgess KV, McNamara LE, Tare R, Murawski K, Kingham E, Oreffo RO, Dalby MJ. Nanoscale surfaces for the long-term maintenance of mesenchymal stem cell phenotype and multipotency. *Nat Mater*. 2011;10(8):637-44.

[12] Yim EK, Darling EM, Kulangara K, Guilak F, Leong KW. Nanotopography-induced changes in focal adhesions, cytoskeletal organization, and mechanical properties of human mesenchymal stem cells. *Biomaterials*. 2010;31(6):1299-306

[13] Choi SJ, Kim HN, Bae WG, Suh KY. Modulus- and surface energy-tunable ultraviolet-curable polyurethane acrylate: properties and applications. *J. Mater. Chem*. 2011;21:14325-35.

[14] Hwang CM, Sim WY, Lee SH, Foudeh A, Bae H, Lee SH, Khademhosseini A. Benchtop fabrication of PDMS microstructures by an unconventional photolithographic method. *Biofabrication*. 2010;2:045001

[15] Burdick JA, Anseth KS. Photoencapsulation of osteoblasts in injectable RGD-modified PEG hydrogels for bone tissue engineering. *Biomaterials*. 2002;23(22):4315-23.

[16] Du Y, Lo E, Ali S, Khademhosseini A. Directed assembly of cell-laden microgels for fabrication of 3D tissue constructs. *Proc Natl Acad Sci U S A*. 2008;105(28):9522-7.

[17] Efimenko K, Rackaitis M, Manias E, Vaziri A, Mahadevan L, Genzer J. Nested self-similar wrinkling patterns in skins. *Nat Mater*. 2005;4(4):293-7.

[18] Ouyang M, Yuan C, Muisener RJ, Boulares A, Koberstein JT. Conversion of Some Siloxane Polymers to Silicon Oxide by UV/Ozone Photochemical Processes. *Chemistry of Materials*. 2000;12(6):1591-6.

- [19] Bowden N, Brittain S, Evans AG, Hutchinson JW, Whitesides GW. Spontaneous formation of ordered structures in thin films of metals supported on an elastomeric polymer. *Nature*. 1998;393:146-9.
- [20] Ji YM, Jeon SH, Park JY, Chung JH, Choung YH, Choung PH. Dental Stem Cell Therapy with Calcium Hydroxide in Dental Pulp Capping. *Tissue Eng Part A*. 2010;16(6):1823-33.
- [21] Drira Z, Yadavalli VK. Nanomechanical measurements of polyethylene glycol hydrogels using atomic force microscopy. *J Mech Behav Biomed Mater*. 2013;18:20-8.
- [22] Bowden N, Huck WTS, Paul K, Whitesides GW. The controlled formation of ordered, sinusoidal structures by plasma oxidation of an elastomeric polymer. *Appl. Phys. Lett*. 1999;75:2557-9.
- [23] Huck WTS, Bowden N, Onck P, Pardoën T, Hutchinson JW, Whitesides GW. Ordering of spontaneously formed buckles on planar surfaces. *Langmuir*. 2000;16:3497–501.
- [24] Schweikart A, Fery A. Controlled wrinkling as a novel method for the fabrication of patterned surfaces. *Microchim. Acta*. 2009;165:249-63.



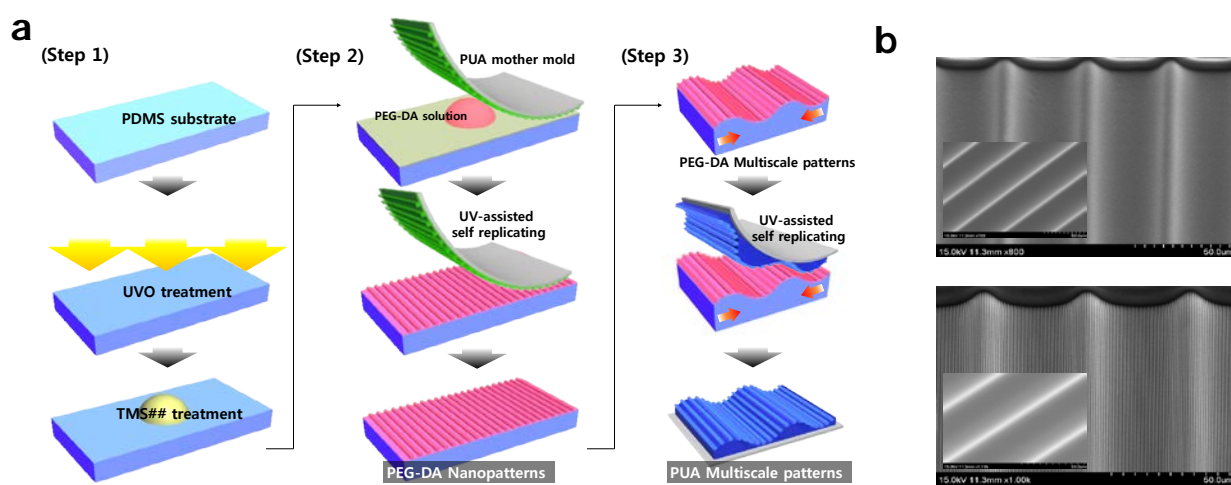


**Figure 5.1. Fabrication of micro- and nanopatterned hierarchical ECM-like platforms.** (a) Schematic illustration of two fabrication methods; UV-assisted CFL and wrinkling. Firstly, nanopatterned PDMS substrate was obtained by UV-assisted CFL method and subsequently the PDMS substrate was pressed resulting micro-sized wrinkling patterned. (b) A tilted SEM images of 350 nm/30  $\mu\text{m}$  patterned PUA mother mold (upper image) and fabricated 350 nm/ 100  $\mu\text{m}$  PUA multiscale substrate (lower image).

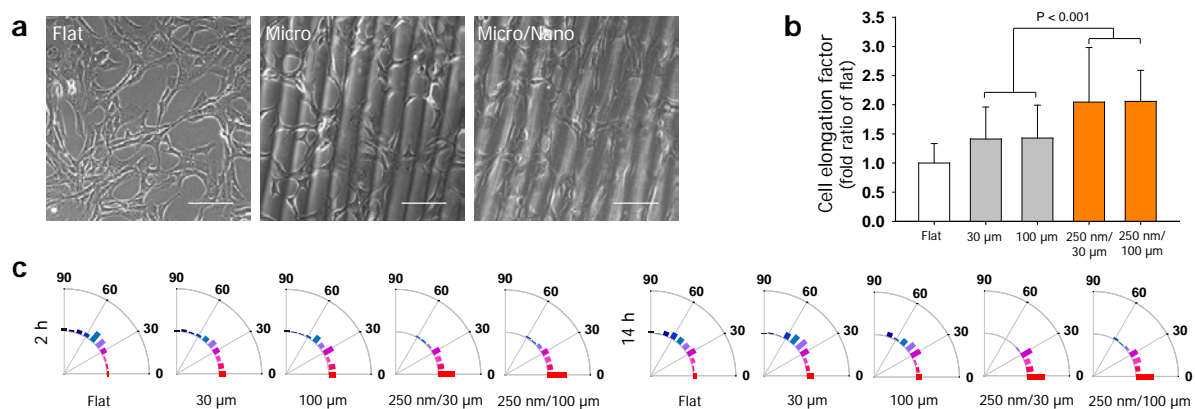


**Figure 5.2. Morphological responses of fibroblast cells to the micro- and nanopatterned topography with variable local sizes in the form of uniformly-spaced ridge/grooved surfaces.** (a) Representative phase contrast images of NIH 3T3 fibroblast cells cultured on substrates. (b) Quantitative analysis of cell elongation factor (defined as (major axis)/(minor axis)). (c) Quantification of time-dependent orientation of cell body on the substrates. Each dot represents a single cell, and an orientation of  $0^\circ$  represents perfect alignment with the ridge/groove direction. The 50–100 cells were used for quantification. Error bars represent the SD about the means.

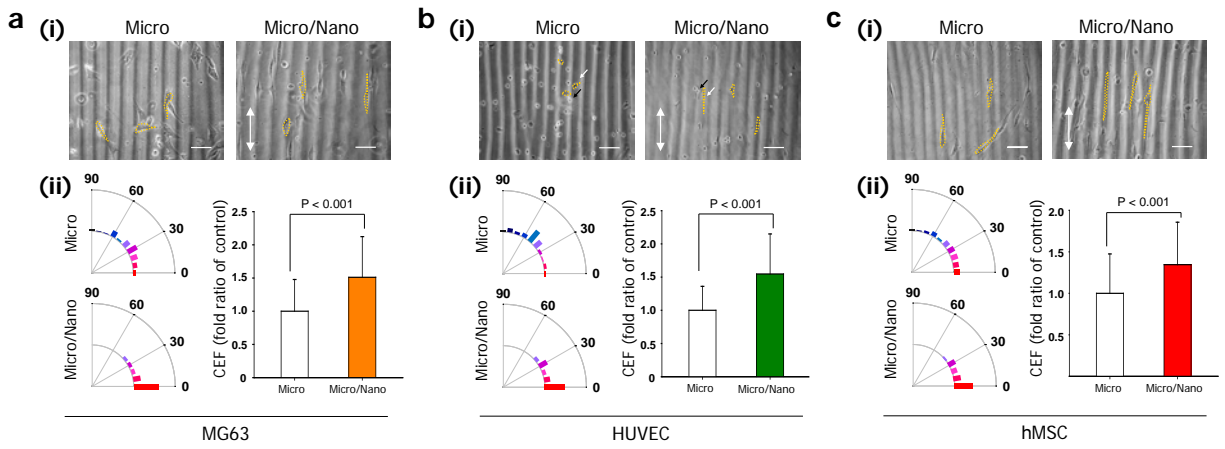


**Figure 5.3. Morphological responses of osteoblast-like cells, endothelial cells, and stem cells.** Quantitative analysis of cell elongation factor (defined as (major axis)/(minor axis)). Quantification of time-dependent orientation of cell body on the substrates. Each dot represents a single cell, and an orientation of  $0^\circ$  represents perfect alignment with the ridge/groove direction. The 50–100 cells were used for quantification. Error bars represent the SD about the means.

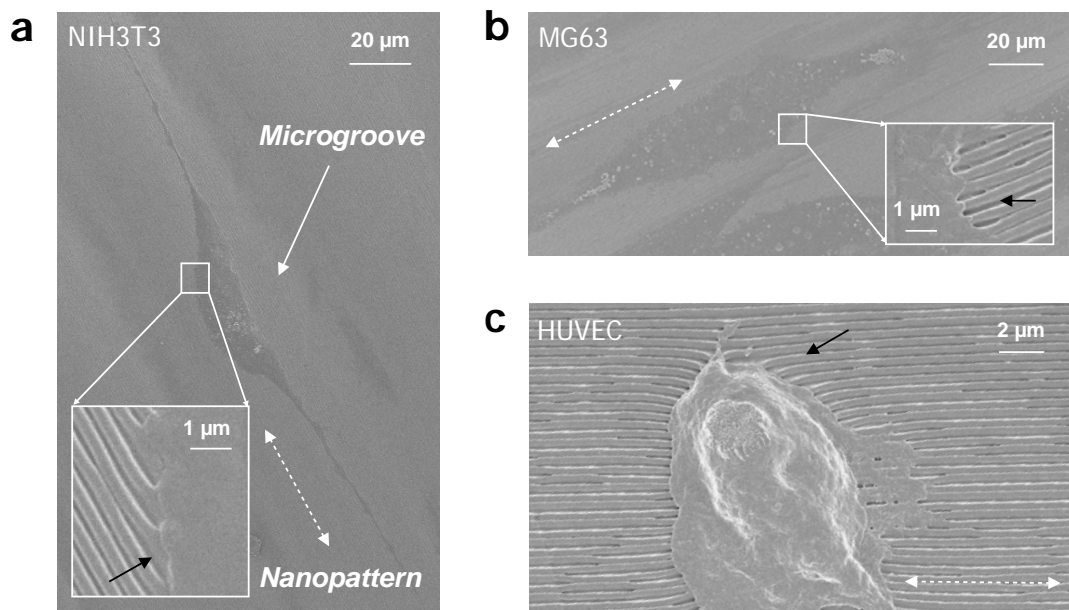


**Figure 5.4. Representative SEM images of morphologies of (a) fibroblast cells, (b) osteoblast-like cells, and (c) endothelial cells on micro- and nanopatterned surfaces.**

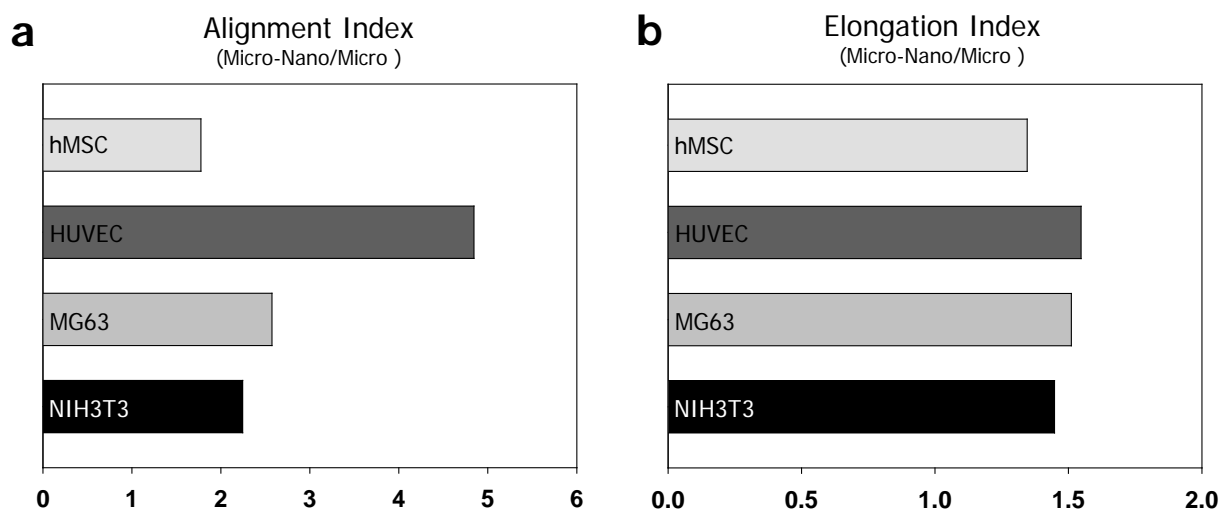


**Figure 5.5. Mechanosensitivity of cell alignment and elongation to nanotopography in multiscale surfaces.** (a) Alignment index (defined as (average of cell alignment on micro- and nanopatterned substrates)/( average of cell alignment on micropatterned substrates)). (b) Elongation index (defined as (average of cell elongation on micro- and nanopatterned substrates)/( average of cell elongation on micropatterned substrates)). The 50–100 cells were used for quantification.

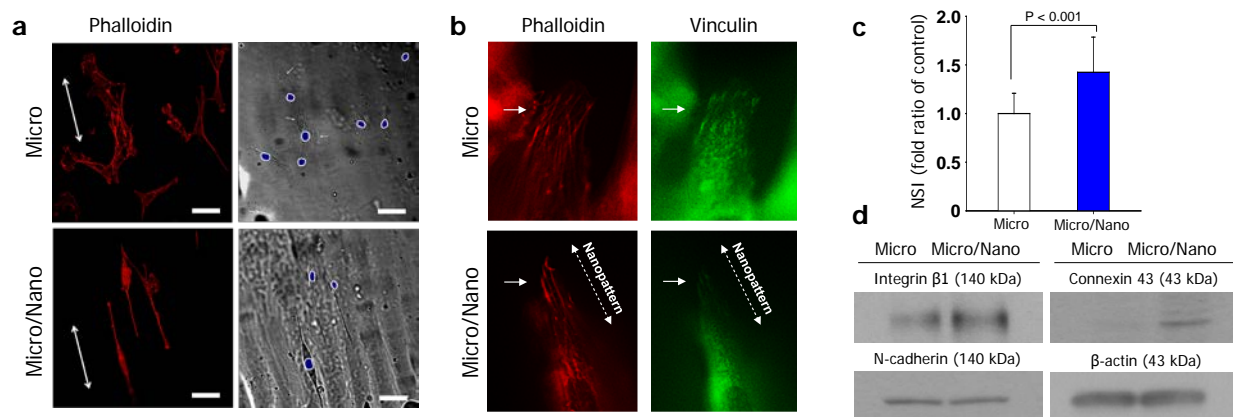


**Figure 5.6. Analysis of cell-substrate and cell-cell interaction in fibroblast cells on micro- and nanopatterned substrates.** (a) Representative immunofluorescent images of F-actin (red) and phase contrast images of NIH 3T3 fibroblast cells cultured on substrates. Blue color was marked to show the nucleus clearly. (b) Representative immunofluorescent high magnification images of F-actin (red) and focal adhesion (green) on the substrates. (c) Quantitative analysis of nucleus elongation factor (defined as (major axis)/(minor axis)). (d) Western blot analysis. The cells were cultured for 7 days and the western blot study was performed under same experimental conditions. Bars = 100  $\mu$ m.

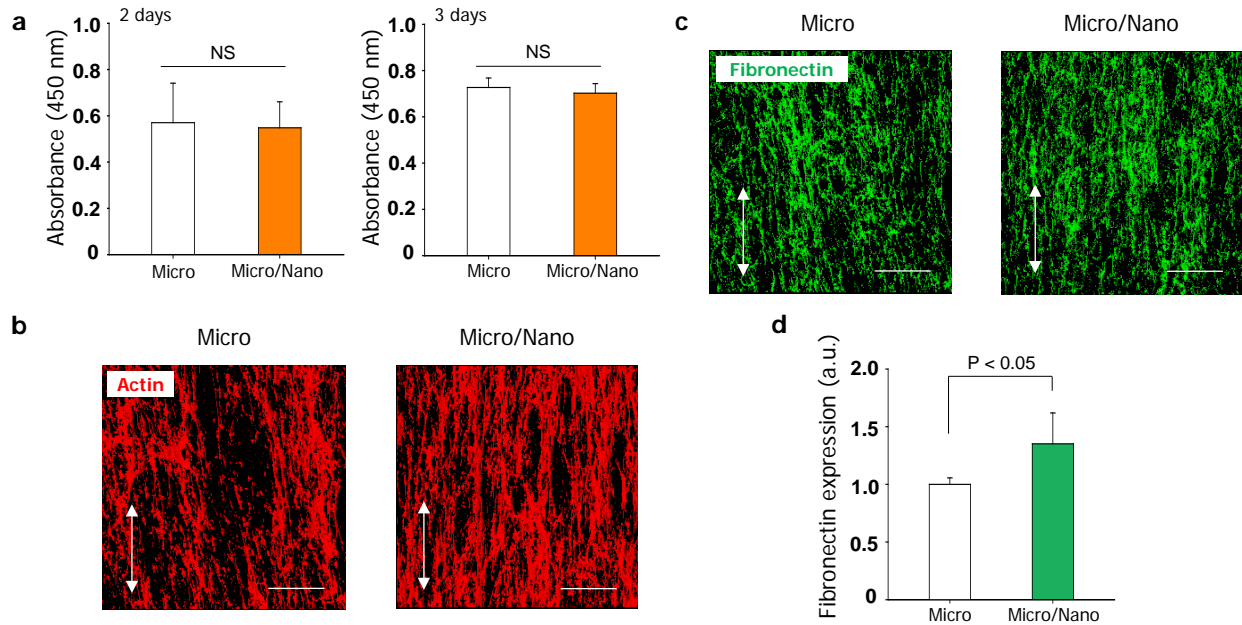


**Figure 5.7. Analysis of proliferation, cell organization, and produced fibronectin (FN) fibers of fibroblast cells in multi cell level on the micropatterned and the micro- and nanopatterned substrates.** (a) Proliferation of NIH 3T3 fibroblast cells on the substrates for 2 and 3 days. The result indicates no significant difference between the samples ( $P > 0.05$ ). (b) Cellular organization of fibroblast cells in multi cell level. (c) Representative immunostaining images of the synthesized fibronectin (FN) fibers and (d) quantitative analysis of expression of FN fibers on the substrates. Ten images were used for quantification. Bars = 100  $\mu\text{m}$ .

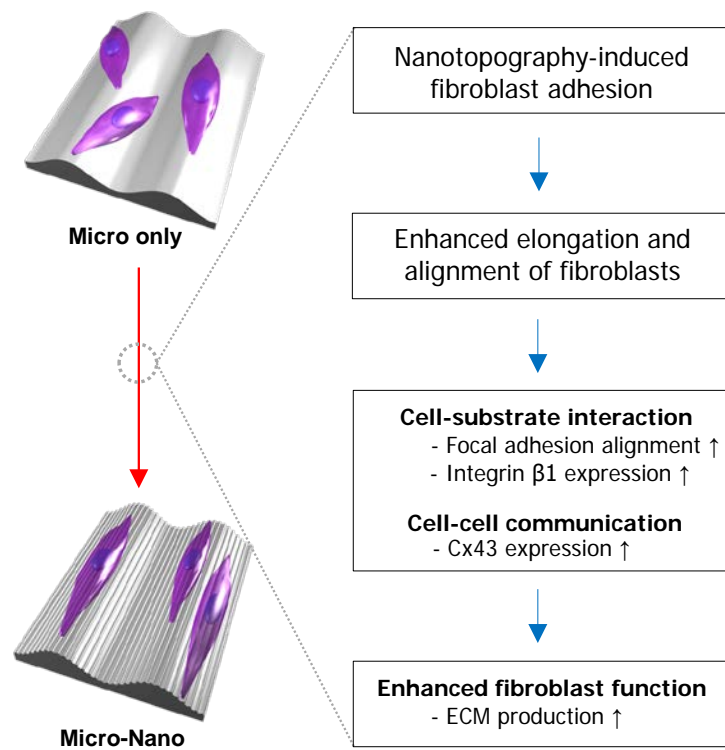


**Figure 5.8. A proposed model for mechanosensitivity of fibroblast cells to nanotopography in micro- and nanopatterned substrates.**



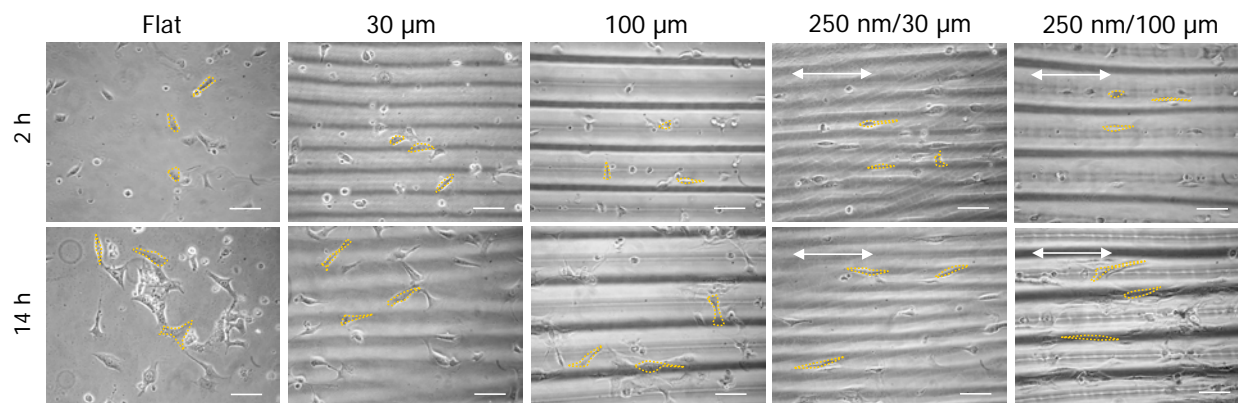


**Figure 5.S1.** Phase contrast images of NIH 3T3 fibroblast cells cultured on substrates for 2 h and 14 h, respectively.

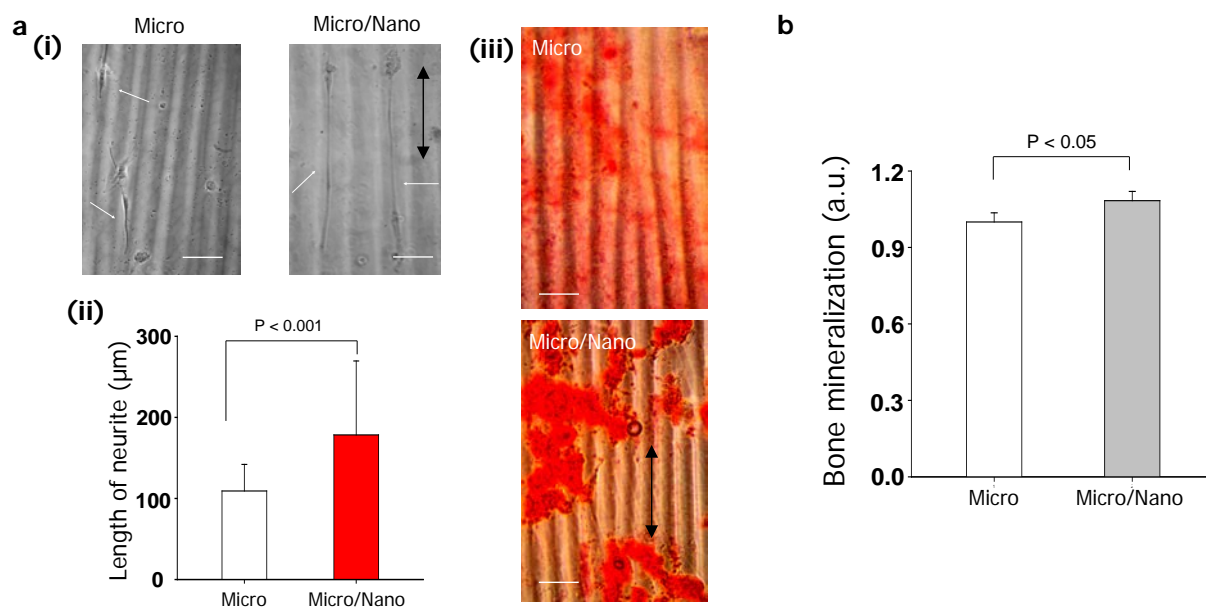


**Figure 5.S2.** Function of stem cells and osteoblast-like cells on the micro- and nanopatterned substrates. (a) Differentiation of hMSCs into (i and ii) neurogenesis and (iii) osteogenesis. (b) Bone mineralization of MG-63 cells.

## **Chapter 6. Nano- and Sub-Nanopatterned Hierarchical Platforms Composed of Graphene and Matrix Nanotopography for Promoting Cellular Function**

### **6.1. Summary**

It is a great challenge to develop hierarchical platforms composed of nano and sub-nanopatterned topography for biological applications including cell and tissue engineering. In this Chapter, we try to address this challenge using graphene and nanopatterned substrates developed in this dissertation. Graphene, one of carbon-based nanomaterials, was coated on the matrix nanotopography with various nanoscale parallel ridges and grooves (ranged from 300 nm to 800 nm) as a novel hierarchical platform comprised of nano and sub-nanopatterned topography. Strictly, it was found that graphene-matrix nanotopography hybrid platforms as a cell culture device could promote the functions of cells including stem cells, osteoblast cells, and endothelial cells through the synergically controlled cell-substrate and cell-cell interactions via matrix nanotopography and graphene. Our results thus proposed that the graphene-based nanopatterned hierarchical platforms mimicking nano/sub-nano topographical properties of the *in vivo*-like topographical cell environment would allow us to set up an efficient strategy for designing advanced biomimetic engineering systems.

## 6.2. Introduction

As we already mentioned clearly in the previous parts, living cells and tissues can display high sensitivity to local topographic cues. The initial attempts including the previous results in this dissertation at engineering cell control of cell function have frequently not been biomimetic in terms of nano and sub-nanopatterned topography in extracellular matrix (ECM) or *in vivo* topographical environments due to the technical limitations. In this Chapter, we report the development of nano- and sub-nanopatterned hierarchical platforms as *in vitro* model that can promote the function of cells. As a key design criterion for developing hierarchically nano- and sub-nanopatterned structures, the ridge/groove nanopatterned matrix and nanomaterials were used.

Recently, the fusion of graphene, one of carbon-based nanomaterials, and stem cells has emerged as a potential strategy for regenerative medicine [1,2]. Nowadays, there are three distinct graphene-based platforms for controlling or improving stem cell functions with specific emphasis on differentiation into various tissue lineages: (1) graphene-coated flat substrata [3,4,5], (2) surface-modified graphene-coated flat substrata [6,7], and (3) graphene-incorporated substrata [8]. The previous studies have shown that the graphene-based platforms promoted the osteogenesis [4,5,7,8], neurogenesis [3,7], and epithelial genesis [7] of stem cells. Here, we report a novel graphene-based platform from an integrative aspect of biology and engineering. It is widely accepted that stem cells can display high sensitivity to the ECM composed of a complex and well-defined nanostructure of protein fibers such as fibrillar collagens and elastins in various tissues [9-12]. Thus we hypothesize that the combination of graphene and ECM-like nanotopography that can provide nano- and sub-nanopatterned hierarchical structures would be an effective strategy for stem cell and tissue engineering. In this study, we developed bioinspired

graphene-matrix nanotopography hybrid platforms, showing that they can control the structure of cells to promote their functions by synergic effects of graphene and nanotopography cues.

## **6.2. Materials and methods**

### **6.2.1. Fabrication of nanostructured substrata by UV-Assisted CFL**

To prepare PUA molds, a UV curable PUA prepolymer (0.5 mL) was drop-dispensed on silicon master mold having positive patterns, which has been prepared by photolithography or electron-beam lithography. Then a poly(ethylene terephthalate) (PET) film of 50  $\mu\text{m}$  thickness was placed on the liquid prepolymer, followed by UV exposure (wavelength: 250-400 nm) for a few tens of seconds. After the UV curing, the mold was peeled from the master, and fully cured by exposing UV for 10 h. Next, the second replica was prepared by using capillary force lithography (CFL) on glass coverslips with the overcured first PUA.

### **6.2.2. Fabrication of nano- and sub-nanotopography-based substrata**

Large-area high-quality graphene film was synthesized on Cu foil and transferred onto a PUA nano patterned substrate, according to a previously reported transfer method. First, Cu foil was inserted in a tubular quartz tube and heated to 1000°C with an  $\text{H}_2$  flow at 8 standard cubic centimeters per minute (sccm) at 90 mTorr. Then, high-quality graphene films were grown on the Cu foil under a mixture  $\text{CH}_4/\text{H}_2$  gases at flow rates of 24 and 8 sccm for 30 min, respectively. During growth, the reactor pressure was maintained at 460 mTorr. After that, the CVD-grown monolayer graphene films were covered with PMMA ( $M_w = 240 \text{ kg mol}^{-1}$ ) and floated in Cu etchant and subsequently the graphene film with the PMMA support was transferred to a PUA nanopatterned substrate. Finally, the suspended monolayer graphene membrane on the PUA

nanoline structure was removed the PMMA support with acetone.

### **6.2.3. Isolation and culturing of hMSCs**

Adipose tissues were isolated from the patients undergoing ear surgeries under sufficient informed consent at the Ajou University School of Medicine (Suwon, Korea). The experimental protocol was approved by the Institutional Review Board at the same university. Tissues were washed with PBS and digested with 100 Unit/mL collagenase type I (Sigma-Aldrich, St. Louis, MO, USA) with low glucose Dulbecco's modified Eagle's medium (DMEM; Gibco-BRL, Grand Island, NY, USA) and incubated for 8 h to lyse the adipose tissues. The stromal fraction was collected by centrifugation and then passed through a cell strainer (100  $\mu$ m size) to remove any large cell clumps and particles. For cell culture and expansion of adipose-derived hMSCs, cells were grown in low glucose DMEM with 10% fetal bovine serum (FBS) and 1% penicillin-streptomycin (Gibco, Milan, Italy) at 37°C in a 5% CO<sub>2</sub> atmosphere. All cells used in this study were at passage 3 or 4.

### **6.2.4. Immunofluorescence staining**

Adhered cells on samples were fixed with a 4% paraformaldehyde solution (Sigma-Aldrich, Milwaukee, WI, USA) for 20 min, permeabilized with 0.2% Triton X-100 (Sigma-Aldrich, WI, Milwaukee, USA) for 15 min, and stained with TRITC-conjugated phalloidin (Millipore, Billerica, MA, USA) and 4, 6-diamidino-2-phenylindole (DAPI; Millipore, Billerica, MA, USA) for 1 h. FAs were also stained with a monoclonal anti-vinculin antibody (1:100; Millipore, Billerica, MA, USA) and a FITC-conjugated goat anti-mouse secondary antibody (1:500; Millipore, Billerica, MA, USA). Images of the stained cells were taken using a fluorescence

microscope (Zeiss, Germany). For the quantitative analysis of the body and nuclear shape as well as focal adhesion of hMSCs on the substrata, the images obtained by fluorescence microscopy were analyzed using the custom written MATLAB script.

#### **6.2.5. Proliferation analysis**

hMSCs ( $4 \times 10^4$  cells/samples) were seeded onto samples and cultured for up to 5 days in DMEM (Sigma-Aldrich, Milwaukee, WI, USA) with 10% FBS (Sigma-Aldrich, Milwaukee, WI, USA) and 1% antibiotics (Sigma-Aldrich, Milwaukee, WI, USA) at 37°C in a humidified atmosphere containing 5% CO<sub>2</sub>. The quantitative analysis of the cell proliferation on the nanogrooved matrices was performed using WST-1 assay (EZ-Cytox Cell Viability Assay Kit, Daeillab Service Co., LTD).

#### **6.2.6. Osteogenesis analysis**

hMSCs ( $4 \times 10^4$  cells/sample) were cultured for 14 days on the samples in osteogenic differentiation media (100 nM dexamethsone, 50 µM ascorbic acid, and 10 mM glycerol 2-phosphate in normal media). Alizarin Red S (Sigma-Aldrich) staining was used for confirming osteogenic differentiation of hMSCs on the sample surfaces. The degree of mineralization was measured by Alizarin Red S staining of hMSCs cultured on the sample surfaces, and this measurement was used for quantification of the osteogenic differentiation of hMSCs. Cells were stained with Alizarin Red S and were destained with cetylpyridinium chloride (Sigma-Aldrich), and then the extracted stains were measured using an ELISA reader (VERSAMAX reader, Molecular Devices, Sunnyvale) at 540 nm.

### **6.2.7. Neurogenesis analysis**

To differentiate hMSCs into neuronal cells, hMSCs ( $2 \times 10^4$  cells/sample) were cultured in the neurogenesis media (NPBM media (Bio Whittaker) with 5 mM cAMP, 5 mM IBMX, 25 ng/ml NGF, 10 ng/ml BDNF, 2.5 mg/ml insulin, and 50  $\mu$ g/ml ascorbic acid (Sigma-Aldrich)). To evaluate neurogenesisin mRNA expression levels, quantitative real time PCR (qRT-PCR) was performed. Total RNA was extracted from cells according to the manufacturer's instructions using an Easy-BLUE RNA extraction kit (iNtRON Biotech, Sungnam, Korea). First-strand cDNA synthesis was carried out in a 20  $\mu$ l reverse transcription (RT) reaction with oligo dT, dNTPs and reverse transcriptase (GenDEPOT, Barker, TX, USA). Fluorescence based real-time PCR was carried out using SYBR Green Premix Ex Taq (TaKaRa, Dalian, China) and an applied Biosystems 7500 Real-Time PCR system (Applied Biosystems; Foster City, CA, USA). The following primers were used for qRT-PCR: human Nestin (Fw) 5'- GAA ACA GCC ATA GAG GGC AAA-3'; (Rv) 5'- TGG TTT TCC AGA GTC TTC AGT GA-3', beta III tubulin (Fw) 5'- CGA AGC CAG CAG TGT CTA AA-3'; (Rv) 5'- GGA GGA CGA GGC CAT AAA TA -3', beta III tubulin (Fw) 5'- CCA ATG GAT TCC CAT ACA GG -3'; (Rv) 5'- TCC TTG CAG ACA CCT CCT CT--3', GAPDH (Fw) 5'- GCA AAT TCC ATG GCA CCG TC -3'; (Rv) 5'- TCG CCC CAC TTG ATT TTG G--3'. For quantification, GAPDH was used as the reference for normalization of each sample.

### **6.2.8. Statistical analysis**

Student's t-test was used for statistical analysis. All quantitative results were presented as mean  $\pm$  standard deviation (SD).

### 6.3. Results

The structure of the natural ECM in various tissues including bone, tooth, nerve, skin, muscle, and heart usually reveals highly aligned nanomatrices [9,13]. Inspired from the highly oriented ECM's structure, we developed nano- and sub-nanotopographically variable matrices using graphene and nanopatterned matrix fabricated by capillary force lithography (CFL) (Fig. 6.S1). That is, we fabricated graphene integrated nanomatrices by using the simple transfer method. Bioinspired ECM-like substrate and graphene applying substrate are schematically illustrated in Fig. 6.1 for fabricating nano- and sub-nanostructures. Firstly, for fabricating the ECM-like cell culture substrate, various nanoscale line patterns of PUA material were fabricated on optically transparent glass coverslips by UV-assisted CFL and self-replication (Fig. 6.1a). Subsequently, graphene was synthesized on a large scale using chemical vapor deposition (CVD) and transferred onto the fabricated nanoscale line patterns (Fig. 6.1b), following a previously reported simple method. Representative scanning electron microscope (SEM) image of a nanoscale patterned surface with a 600 nm ridge, 600 nm groove, and 800 nm height are shown in right of Fig. 6.1b, demonstrating that the patterns exhibited high structural fidelity with well-defined vertical edge profiles (Figs. 6.S2 and 6.S3). Representative SEM image of an ECM-like graphene surface; suspended graphene membranes is shown in right of Fig. 6.1a, showing a good conformal contact to the upper part of nanostructures and physical integrity. It is noted that the adhesion energy of monolayer graphene sheets with opposite substrate is influenced by van der Waals force, resulting in a strong adhesion force between graphene membrane and PUA nanopatterns. It was also observed that the monolayer graphene membrane adheres to the vertical wall of the PUA nanoline for 5 to ~ 10 nm, because of the van der Waals attraction to the PUA substrate. Their high adhesion energy prevented the separation of graphene form nanopattern,



when they were used as a cell culturing substrate.

In the experiment, topographical features with six different ridge/groove dimensions were used: 300 nm/300 nm, 400 nm/400 nm, 500 nm/500 nm, 600 nm/600 nm, 700 nm/700 nm, 800 nm/800 nm (Fig. 6). For consistency, the pattern height was fixed at a constant height of 800 nm, as verified by atomic force microscopy (AFM) measurements (Fig. 6.1f).

To verify the hypothesis that the bioinspired graphene-matrix nanotopography hybrid platforms prepared in this study could be an effective strategy for stem cell-based therapy, we investigated the effects of the substrata on the structure and function of hMSCs. To check the preliminary adhesion of the PUA and graphene-applied PUA flat substrata, we first cultured hMSCs on substrata without any ECM molecules for 14 h. As shown in Fig. 6.2a, the immunohistochemical analysis showed that much more spread shape of hMSCs on the graphene region was observed compared to that on the pure PUA region. This result suggests that the graphene-applied PUA substrata can provide a suitable environment for good adhesion of hMSCs and can control the shape of them which may be able to use to regulate their functions.

Cell shape and orientation are known as one of very important regulators to determine characteristic functions of cells and tissues [13]. In particular, substrate topography can strongly influence the polarity of cells including stem cells through a phenomenon known as contact guidance [15]. For example, Leong group demonstrated the nanogrooves could induce the polarity of hMSC shape, which might regulate functions of them such as migration and differentiation [16,17]. To investigate whether orientation and polarity of stem cells were influenced by the bioinspired ECM-like graphene substrata, we cultured hMSCs on the graphene-matrix nanotopography hybrid platforms (GNS) and pure PUA nanopatterned substrata (PNS) for 14 h, respectively (Fig. 6.2). We observed the aligned hMSC shapes along the

direction of the nanopatterns regardless of use of graphene (Fig. 6.2a). As expected, the hMSCs on the flat substrates maintained a random orientation. In addition, we learned that the nanopatterned substrata with moderate size (i.e., 500\_500 nm nanopattern in our case) showed the highest alignment of hMSCs. Interestingly, we found that the hMSCs on the GNS were less orientated along the direction of the nanopatterns than those on the PNS, which is also clearly demonstrated by the quantitative analysis (Fig. 6.2b). This might be due to the smaller groove heights of the GNS than those of the PNS (Table 6.1). Together, these findings suggested that the graphene-matrix nanotopography hybrid platforms can determine the average of alignment of stem cells and, thus, may influence the interaction between cell-cell, which would be an important regulator of cell functions.

The effects of stem cell polarity by the GNS were investigated. As shown in Fig 6.2, we found that the nanopatterned substrata regardless of use of graphene greatly promoted polarity and extent of aligned cytoskeletal structure of hMSCs compared to the flat substrata. To quantify the cell polarity observations, aspect ratio [defined as (major axis)/(minor axis)] of hMSCs on the substrata were calculated. In case of PNS, the aspect ratio of hMSCs showed biphasic trend which increases from flat to 600\_600 nm nanopatterns and then decreases at 700/700 nm nanopatterns. On the other hand, the GNS showed that the larger sizes of nanopatterns usually increase the aspect ratio of hMSCs (i.e., 800\_800 nm > 500\_500 nm > flat). It has been reported that shape of hMSCs may lead to regulating function of them by regulation of levels of RhoA, ROCK, and myosin light chain phosphorylation [18]. Thus we can speculate that the graphene-matrix nanotopography hybrid platforms may be able to improve the functions of stem cells by regulation of cytoskeletal tension within stem cells.

It is widely accepted that cell spreading can be considered as an important factor for

regulating function of stem cells, especially for differentiation [19-20]. In addition, our group recently showed that there might be somewhat correlation between cell spreading and enhanced osteogenesis of hMSCs on the graphene-based substrata [8]. Interestingly, GNS greatly increased hMSC spreading compared to the PNS, regardless of sizes of nanopatterns. It is noted that the cell area of hMSCs were usually increased according to the larger sizes of nanopatterns (i.e., 800\_800 nm > 300\_300 nm) in case of PNS. Our data suggest that the enhanced cell spreading on graphene-applied nanopatterned substrata may influence regulating functions of stem cells.

From the cell adhesion study, we found three notable findings. First, the hMSCs on the on graphene-matrix nanotopography hybrid platforms more highly orientated along the direction of nanopatterns than those on the graphene-based flat substrata. Second, the hMSCs on the on graphene-matrix nanotopography hybrid platforms more highly elongated than those on the graphene-based flat substrata. Third, the cell areas of hMSCs greatly increased on the graphene-matrix nanotopography hybrid platforms than those on the nanopatterned substrata without graphene. Therefore, these findings strongly suggest that graphene-matrix nanotopography hybrid platforms would regulate function of stem cells. Namely, we can speculate that the synergic effects of graphene and nanotopography cues that may be able to improve stem cell functions.

We continually investigated the attachment and proliferation of hMSCs on the graphene-matrix nanotopography hybrid platforms. To quantify the attachment of hMSCs on the substrata, we cultured hMSCs on the GNS and PNS for 6 h. We carefully removed unattached cells from the substrata by washing with phosphate buffered saline. We then measured the cell viability on the substrata (Fig. 6.3). We found that the about 70-80% cells were attached on the substrata, regardless of the graphene and nanopatterns. We also showed that no significant differences were

observed statistically ( $P > 0.05$ ). The proliferation of hMSCs on graphene-applied nanopatterned substrata was continually observed. We cultured hMSCs on the GNS substrata and PNS for 5 days. All substrata showed significantly proliferation of hMSCs compared to the initial cell seeding numbers (Fig. 6.3). On the other hand, we found that the graphene-matrix nanotopography hybrid platforms did not significantly promote the proliferation of hMSCs. Together, our data indicate that graphene-matrix nanotopography hybrid platforms may not significantly influence on the attachment and proliferation of hMSCs.

We checked the osteogenesis of hMSCs on the GNS. We cultured hMSCs on the substrata with osteogenic induction media for 14 days. We analyzed hMSC osteogenesis by the mineralization [4,8]. The stained calcium deposits by Alizarin Red S staining were destained with cetylpyridinium chloride to quantify the degree of osteogenesis of hMSCs. The extracted stains were measured using an ELISA reader. As shown in Figs. 6.3c, we observed that the graphene-applied PUA substrata promoted the osteogenesis of hMSCs compared to the pure PUA substrata. In addition, we showed that moderate GNS (i.e., 400\_400 nm, 500\_500 nm, 600\_600 nm in our case) enhanced the osteogenesis of hMSCs compared to the graphene-applied PUA flat substrata. Interestingly, we observed that the 500\_500 nm GNS exhibited the highest osteogenesis. Surprisingly, compared to the osteogenesis of hMSCs on PNS or graphene-applied PUA flat substrata, the degree of osteogenesis of hMSCs on 500\_500 nm GNS was approximately 2 times higher ( $P < 0.05$ ). We also showed the enhanced the neurogenesis of hMSCs on the graphene-based platforms (Figs. 6.3d and e).

In this work, we propose that the combination of graphene with bioinspired nanotopography is an effective strategy for the design and manipulation of engineered substrata for stem cell and tissue engineering applications. Our *in vitro* cell study provides three interesting

consequences on the graphene-applied nanopatterned substrata for hMSCs compared to the flat substrata (Fig. 6.4): (i) The nanotopography cues of the substrata can induce the elongation of hMSCs. (ii) The graphene cues of the substrata can induce the spreading of hMSCs due to the property of graphene (Fig. 6.S3). (iii) Because controlled elongating and spreading of hMSCs may synergically influence the mechanical stimulation within them, the behavior of hMSCs may be regulated [8,18-21]. In our work, we showed that the graphene-applied nanopatterned substrata quite accelerated the osteogenesis of hMSCs (Fig. 6.3).

Next, we demonstrated whether the graphene-matrix nanotopography hybrid platforms could promote the function of other cell types. To this end, we cultured osteoblast and endothelial cells on the platforms and showed that they enhanced their function (Fig. 6.5). The bone mineralization of MC-3T3 was significantly enhanced on the graphene-matrix nanotopography hybrid platforms compared to that on the graphene substrate (Fig. 6.5a). In particular, compared to the graphene substrate, we have demonstrated that the graphene-matrix nanotopography hybrid platforms could promote the *in vitro* capillary tube formation of HUVEC with the controlled orientation (Fig. 6.5b). Taken together, our results indicate that the nanopatterned hierarchical platforms mimicking nano/sub-nano topographical properties of the *in vivo*-like topographical cell environment can promote the function of cells, which would allow us to set up an efficient strategy for designing advanced biomimetic engineering systems.

#### **6.4. Discussion**

Here, we suggest possible applications using graphene-matrix nanotopography hybrid platforms developed here based on our findings. Firstly, our platforms may have great potentials as a strategy for enhancing function of electro-active cells (e.g., cardiomyocytes, vascular cells,

neural cells, skeletal muscle cells, and stem cells). It is noted that aligned nanofibril ECMs in the tissues including heart, vascular, nerve, and muscle are usually observed. For example, it has been reported that graphene on flat substrata can enhance the neurogenesis of stem cells [3, 6]. In addition, Yim *et al.* reported that the anisotropic nanotopography can induce the neural differentiation of hMSCs even without requiring the use of any differentiation-inducing chemicals [22]. Thus we can expect that graphene-matrix nanotopography hybrid platforms would promote the better neurogenesis of stem cells than graphene on flat substrata. Secondly, coating ECM molecules (e.g., fibronectin) or growth factors on our platforms may further improve the functions of cells. In this work, we did not use any ECM molecules or growth factors on the stem for *in vitro* cell study. Thirdly, stem may be used as a novel strategy for the design and fabrication of scaffolds in tissue regeneration fields. In particular, we can expect that our platform-based scaffolds would be effective for bone, nerve, vascular and regeneration (Figs. 6.3 and 6.5)

In summary, we have developed for the first time the bioinspired graphene-matrix nanotopography hybrid platforms as a new strategy for controlling the structure and function of cells. Our results indicate that the graphene and nanotopography cues of the substrata guided the elongation and spreading of hMSCs, which could promote the functions of cells. Our work implies that the methodology for the fabrication of graphene-matrix nanotopography hybrid platforms can be adapted for the design and manipulation of novel scaffolds, which may be a powerful strategy for advanced tissue engineering and regenerative fields.

## 6.5. References

[1] Park J, Park S, Ryu S, Bhang SH, Kim J, Yoon JK, Park YH, Cho SP, Lee S, Hong BH, Kim

BS. Graphene-regulated cardiomyogenic differentiation process of mesenchymal stem cells by enhancing the expression of extracellular matrix proteins and cell signaling molecules. *Adv Healthc Mater.* 2014;3(2):176-81.

[2] Ku SH, Park CB. Myoblast differentiation on graphene oxide. *Biomaterials.* 2013;34(8):2017-23.

[3] Park SY, Park J, Sim SH, Sung MG, Kim KS, Hong BH, Hong S. Enhanced differentiation of human neural stem cells into neurons on graphene. *Adv Mater.* 2011;23(36):H263-7.

[4] Nayak TR, Andersen H, Makam VS, Khaw C, Bae S, Xu X, Ee PL, Ahn JH, Hong BH, Pastorin G, Özyilmaz B. Graphene for controlled and accelerated osteogenic differentiation of human mesenchymal stem cells. *ACS Nano.* 2011;5(6):4670-8.

[5] Kim J, Choi KS, Kim Y, Lim KT, Seonwoo H, Park Y, Kim DH, Choung PH, Cho CS, Kim SY, Choung YH, Chung JH. Bioactive effects of graphene oxide cell culture substratum on structure and function of human adipose-derived stem cells. *J Biomed Mater Res A.* 2013;101(12):3520-30.

[6] Wang Y, Lee WC, Manga KK, Ang PK, Lu J, Liu YP, Lim CT, Loh KP. Fluorinated graphene for promoting neuro-induction of stem cells. *Adv Mater.* 2012;24(31):4285-90.

[7] Shi X, Chang H, Chen S, Lai C, Khademhosseini A, Wu H. Regulating cellular behavior on few-layer reduced graphene oxide films with well-controlled reduction states. *Advanced Functional Materials.* 2010;22:751-9.

[8] Kim J, Kim YR, Kim Y, Lim KT, Seonwoo H, Park S, Cho SP, Hong BH, Choung PH, Chung TD, Choung YH, Chung JH. Graphene-incorporated chitosan substrata for adhesion and differentiation of human mesenchymal stem cells. *J. Mater. Chem. B.* 2013;1:933-8.

[9] Kim HN, Jiao A, Hwang NS, Kim MS, Kang do H, Kim DH, Suh KY. Nanotopography-

guided tissue engineering and regenerative medicine. *Adv Drug Deliv Rev.* 2013;65(4):536-58.

[10] Guilak F, Cohen DM, Estes BT, Gimble JM, Liedtke W, Chen CS. Control of Stem Cell Fate by Physical Interactions with the Extracellular Matrix. *Cell Stem Cell.* 2009;5:17-26.

[11] Vunjak-Novakovic G, Scadden DT. Biomimetic platforms for human stem cell research, *Cell Stem Cell.* 2011;8:252-61.

[12] Lutolf MP, Blau HM. Artificial stem cell niches. *Adv. Mater.* 2009;21:3255-68.

[13] Kim DH, Provenzano PP, Smith CL, Levchenko A. Matrix nanotopography as a regulator of cell function. *J Cell Biol.* 2012;197(3):351-60.

[14] Suh KY, Park MC, Kim P. Capillary force lithography: a versatile tool for structured biomaterials interface towards cell and tissue engineering, *Adv. Funct. Mater.* 2009;19:2699-412.

[15] Teixeira AI, Abrams GA, Bertics PJ, Murphy CJ, Nealey PF. Epithelial contact guidance on well-defined micro- and nanostructured substrates. *J Cell Sci.* 2003;116:1881-92.

[16] Kulangara K, Yang Y, Yang J, Leong KW. Nanotopography as modulator of human mesenchymal stem cell function. *Biomaterials.* 2012;33(20):4998-5003.

[17] Yim EKF, Darling EM, Kulangara K, Guilak F, Leong KW. Nanotopography-induced changes in focal adhesions, cytoskeletal organization, and mechanical properties of human mesenchymal stem cells. *Biomaterials.* 2010;31:1299-306.

[18] McBeath R, Pirone DM, Nelson CM, Bhadriraju K, Chen CS. Cell shape, cytoskeletal tension, and RhoA regulate stem cell lineage commitment. *Dev Cell.* 2004;6(4):483-95.

[19] Kilian KA, Bugarija B, Lahn BT, Mrksich M. Geometric cues for directing the differentiation of mesenchymal stem cells. *Proc Natl Acad Sci U S A.* 2010;107(11):4872-7.

[20] Tang J, Peng R, Ding J. The regulation of stem cell differentiation by cell-cell contact on micropatterned material surfaces. *Biomaterials.* 2010;31(9):2470-6.



[21] Yim EK, Pang SW, Leong KW. Synthetic nanostructures inducing differentiation of human mesenchymal stem cells into neuronal lineage. *Exp Cell Res*. 2007;313(9):1820-9

PUA nanopattern Ridge/groove size (nm)	PUA nanopattern Height (nm)	Graphene/ nanopattern Height (nm)	Graphene/nanopattern Sub-ridge/groove size (nm)
300 nm	800 nm	$21.2 \pm 5.0$	$5.3 \pm 3.2$
400 nm	800 nm	$23.2 \pm 10.1$	$5.8 \pm 3.8$
500 nm	800 nm	$23.3 \pm 4.0$	$7.6 \pm 3.8$
600 nm	800 nm	$23.6 \pm 1.8$	$8.5 \pm 2.8$
700 nm	800 nm	$26.7 \pm 3.0$	$9.8 \pm 1.1$
800 nm	800 nm	$13.9 \pm 3.5$	$3.5 \pm 2.1$

**Table 6.1.** Topographical characteristics of the graphene-matrix nanotopography, showing the nano- and sub-nanopatterned hierarchical topography

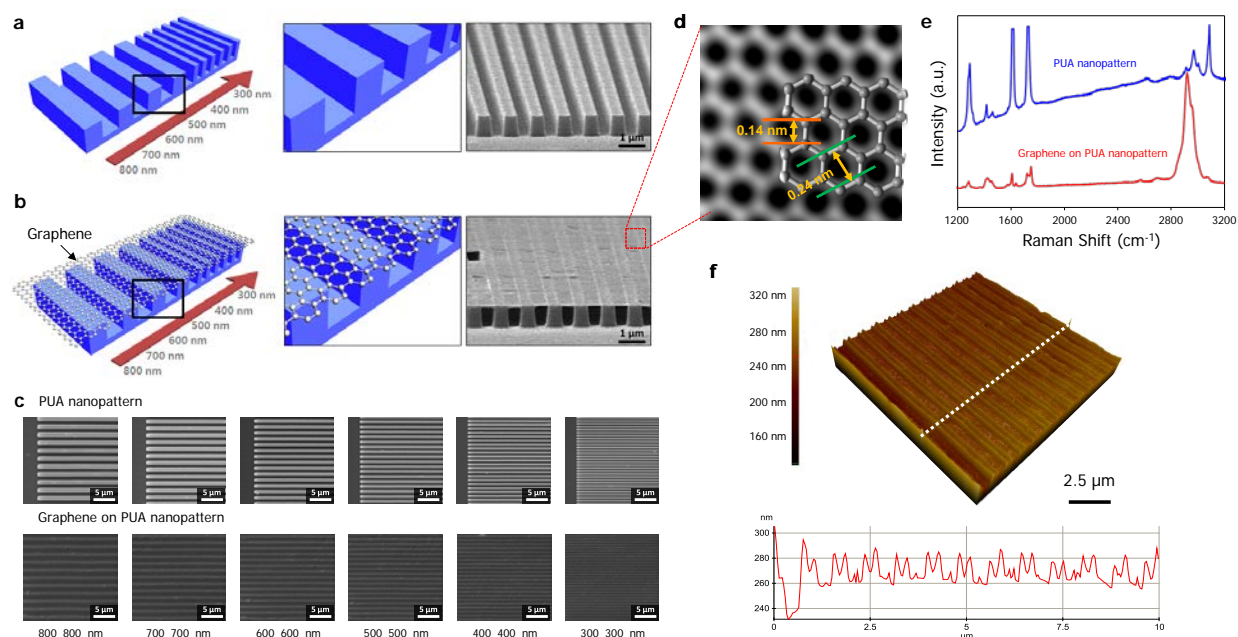


**Figure 6.1. Rational design and fabrication of nano- and sub-nanopatterned hierarchical platforms with matrix nanopography as a biomimetic ECM.** Graphical illustrations and SEM images of (a) anisotropic nanopatterned pattern arrays with variable local sizes in the form of uniformly-spaced ridge/grooved nanosurfaces and (b) graphene-matrix nanopatterned hybrid platforms. (c) SEM image of platforms developed. (d) High-resolution STEM image of graphene sheet used in this study. (e) Raman spectroscopy of the PUA matrix nanopatterned and graphene-matrix nanopatterned hybrid platforms. (f) Representative AFM image of the graphene-matrix nanopatterned hybrid platform, showing the nano and sub-nanopatterned hierarchical topography.

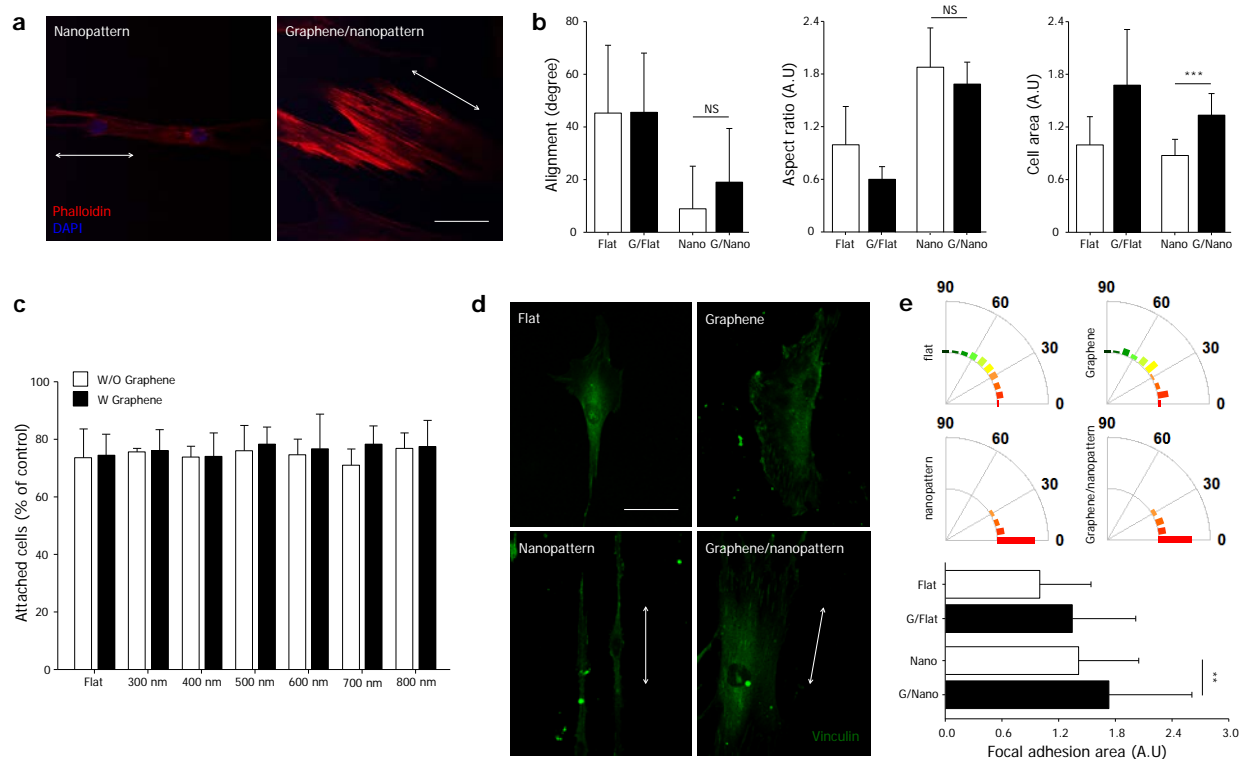


**Figure 6.2. Effects of graphene-matrix nanotopography hybrid platforms on adhesion and structure of hMSCs.** (a) Representative immunostaining images of F-actin (red) and nucleus (blue) of hMSCs on the PUA matrix nanotopography and the graphene-matrix nanotopography hybrid platforms. (b) Quantitative analysis of cell alignment, axial ratio (defined as (major axis)/(minor axis)), and cell spreading area. (c) Quantitative analysis of cell adhesion. Cells were cultured for 6 h. The values were normalized to the initial cell viability. (d) Representative immunostaining images of focal adhesion (green) on the substrates. (e) Quantitative analysis of alignment and area focal adhesion. The 50–100 cells were used for quantification. The error bars represent the standard deviation. The statistical significance was denoted as ‘\*\*’ ( $p < 0.01$ ) and ‘\*\*\*’ ( $p < 0.001$ ).

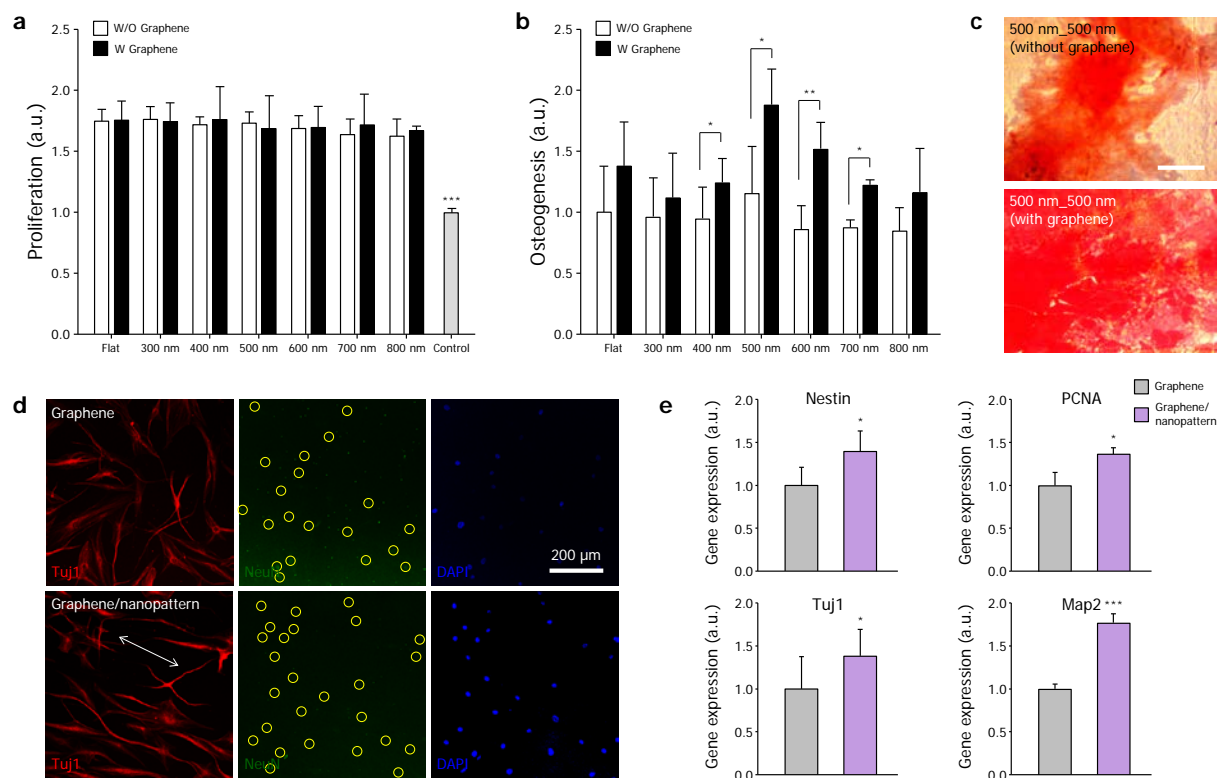


**Figure 6.3. Enhanced differentiation of hMSCs on the graphene-matrix nanotopography hybrid platforms.** (a) Quantitative analysis of cell proliferation. (b) Osteogenesis of hMSCs on the graphene-matrix nanotopography hybrid platforms. Quantification of the degree of mineralization as measured by Alizarin Red S staining and Representative images of Alizarin Red S staining cells cultured on substrates. All values were normalized to the PUA flat substrate. (d) Neurogenesis of hMSCs on the graphene and the graphene-matrix nanotopography hybrid platforms. Representative immunofluorescent staining of Tuj1 (red), NeuN (green), and DAPI (blue) of hMSCs on the substrates with the use of neurogenesis medium. The yellow circles indicate the location of the NeuN expression. (e) qRT-PCR analysis of hMSCs cultured in the neuronal differentiation medium for 5 days. Four independent experiments were conducted, and the error bars represent the standard deviation. The statistical significance was denoted as ‘\*’ ( $p < 0.05$ ) and ‘\*\*’ ( $p < 0.01$ ).

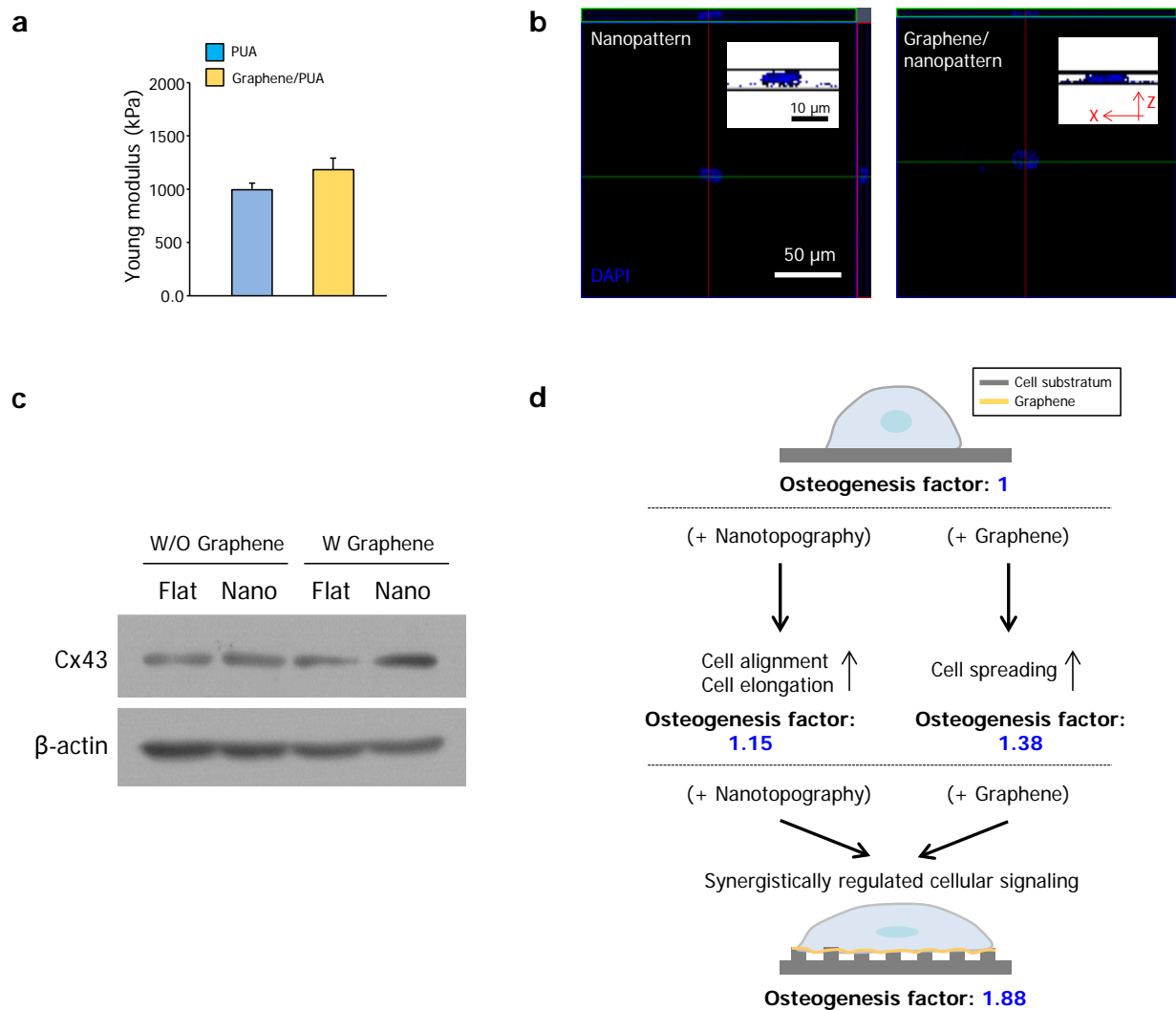


**Figure 6.4. Effects of graphene-matrix nanotopography hybrid platforms on cell-substrate and cell-cell interaction.** (a) Stiffness of the PUA flat and graphene/PUA. (b) Representative immunofluorescent staining and three-dimensional images of nucleus in hMSCs, showing the highly spread thickness of nucleus on the graphene-matrix nanotopography hybrid platform. (c) Western blot analysis of gap junction. (d) A model for the synergistically enhanced osteogenesis of hMSCs on graphene-matrix nanotopography hybrid platforms.

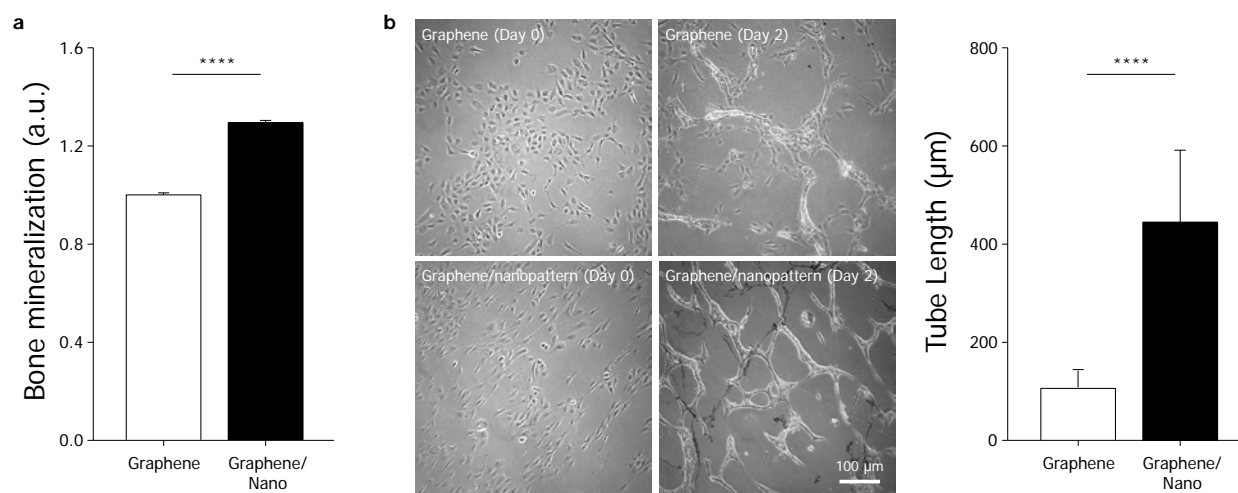


**Figure 6.5. Enhanced cellular function of osteoblast and endothelial cells on graphene-matrix nanotopography hybrid platforms.** (a) Quantification of the degree of mineralization of MC-3T3 on the substrates as measured by Alizarin Red S staining. The cells stained with Alizarin Red S were destained with cetylpyridinium chloride, and then the extracted stains were measured ( $n = 4$ ). The values were normalized to the flat substrate. (b) *In vitro* capillary tube formation of HUVEC on the substrates. Phase contrast images (left) and quantification of the degree of capillary tube formation (right). Results were quantified from the phase contrast image ( $n = 5$ ). The error bars represent the standard deviation. The statistical significance was denoted as ‘\*\*\*\*’ ( $p < 0.0001$ ).

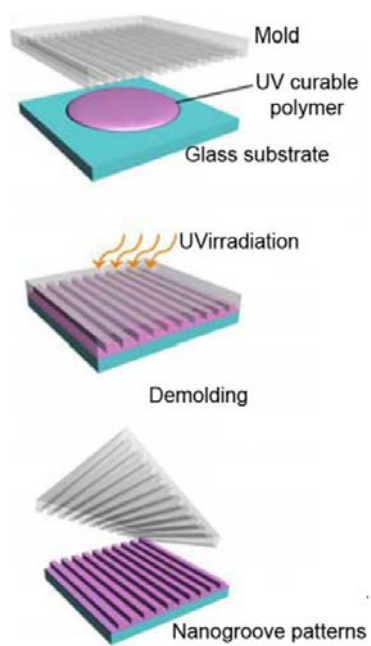


**Figure 6.S1. Schematic diagram for fabrication of PUA nanopatterns by self-replication and capillary force lithography (CFL)**



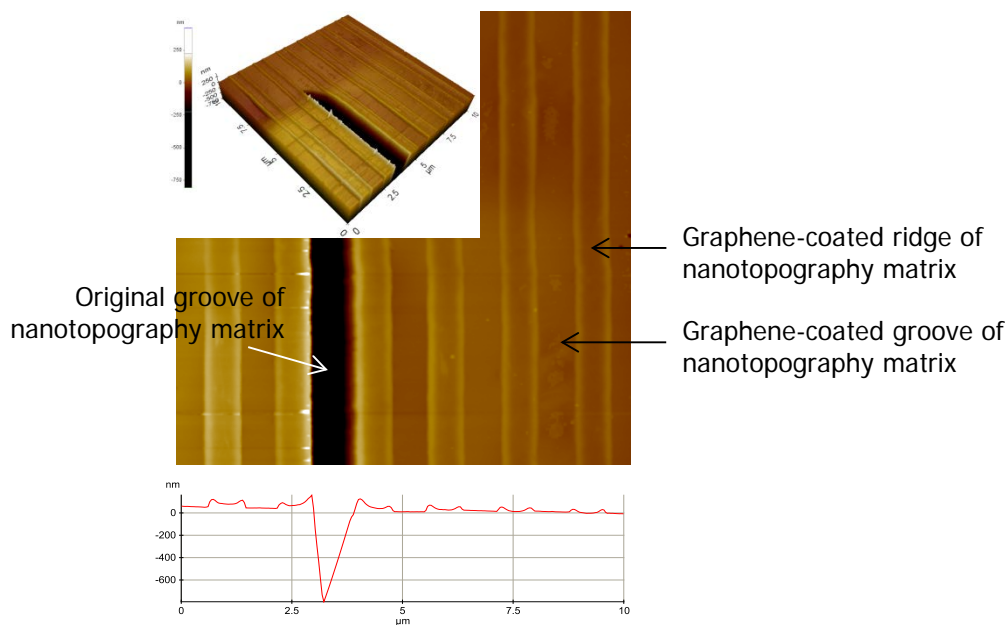


**Figure 6.S2. AFM image of graphene-matrix nanotopography hybrid platforms, showing the well-coated graphene on matrix nanotopography.**

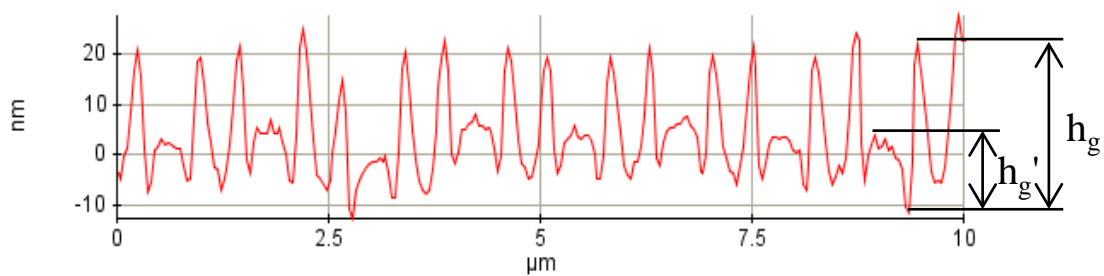


**Figure 6.S2. Representative surface property of graphene-matrix nanotopography hybrid platforms, showing the nano- and sub-nanopatterned hierarchical topography.**

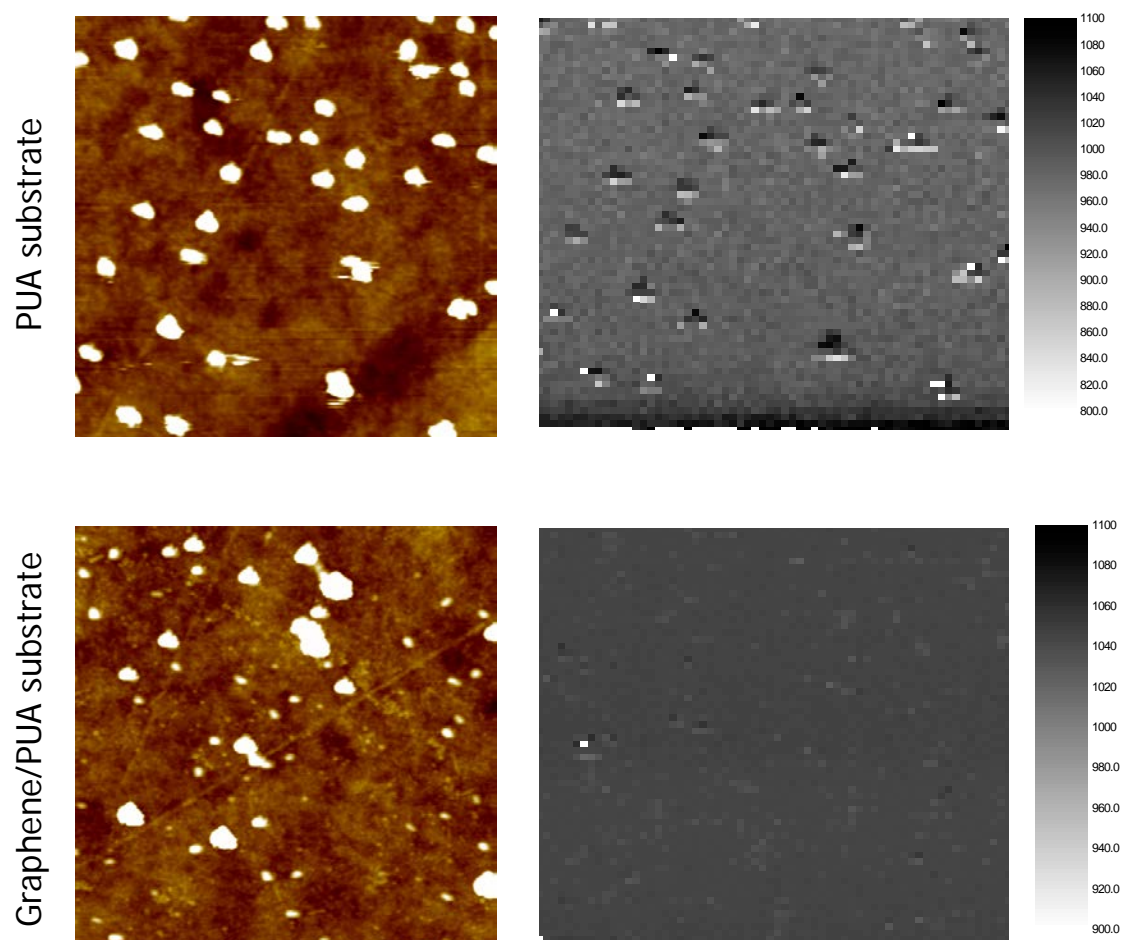


**Figure 6.S3. Surface profile of Young's modulus (E) of the PUA and graphene/PUA substrate.** The Young's modulus was calculated using the AFM image and Hertzian model equation. Poisson's ratio ( $\nu$ ) was used as 0.5 and parabolic geometry of the indenter was used.

## PART III: DEVELOPMENT OF NANOENGINEERED BIOMIMETIC SYSTEMS FOR TISSUE REGENERATION

---

### Overview

In previous Part I and II, we have developed a series of advanced nanopatterned platforms inspired by the unique architectures of native tissues and ECMs in a detailed and comprehensive fashion using nanofabrication technologies, and demonstrated that the platforms can improve the function of cells. In Part III, we used these platforms as a strategy to regenerate the damaged tissues without complex surgical treatments. Inspired by the aligned nanostructures and co-existence of vascular cells and stem cells in human cancellous bone, we proposed a biomimetic platforms composed of nanotopography and coculture with HUVECs for enhancing the osteogenesis of hMSCs for bone regeneration (Chapter 7). We found that both nanotopography and co-culture independently enhanced the osteogenesis of hMSCs, whereas the osteogenesis was further enhanced by the two factors in combination, indicating the importance of synergistic cues in bone tissue regeneration. Based on these considerations, we approached a new conceptual system that can integrate stem cells into nanopatterned substrates for bone regeneration (Chapter 8). Inspired from ECMs in a human bone tissue, we developed hierarchically micro and nanopatterned transplantable substrates by employing capillary force lithography in combination with a surface micro-wrinkling method using a Food and Drug Administration (FDA)-approved polymer. Importantly, we showed that the nanopatterned stem cell patches can guide the bone regeneration without complex surgical treatments or tissue transplantation. Finally, we have demonstrated the nanofibrillar patch synthesized from *Gluconacetobacter xylinus* can promote the tympanic membrane regeneration (Chapter 9).

## **Chapter 7. Synergistic Effects of Nanotopography and Co-Culture with Endothelial Cells on Osteogenesis of Mesenchymal Stem Cells**

### **7.1. Summary**

Inspired by the aligned nanostructures and co-existence of vascular cells and stem cells in human cancellous bone, we quantitatively investigated the relative contributions of nanotopography and co-culture with human umbilical endothelial cells (HUVECs) to the osteogenesis of human mesenchymal stem cells (hMSCs). Although both nanotopography and co-culture independently enhanced the osteogenesis of hMSCs, osteogenesis was further enhanced by the two factors in combination, indicating the importance of synergistic cues in stem cell engineering. Interestingly, nanotopography provided a larger relative contribution to the osteogenesis of hMSCs than did co-culture with HUVECs. Furthermore, the osteogenesis of hMSCs was also affected by the density of parallel nanogrooves, exhibiting a maximum at a 1:3 spacing ratio, as defined as the ratio of ridge width to groove width. Analysis of (i) biochemical soluble factors, (ii) hMSC-substrate interaction and (iii) hMSC-HUVEC interaction suggests that (ii) and (iii) play a crucial role in mediating osteogenic phenotypes.

## **7.2. Introduction**

Bone defects are still highly common pathological problems in the world, requiring approximately 2.2 million orthopedic procedures worldwide every year [1]. In spite of the availability of surgical treatments using alloplastic materials or autologous and allogeneic tissues, the regeneration of large bone defects remains one of the most critical orthopedic diseases [2,3]. Stem cell-based bone tissue engineering provides a strategy for creating new functional bone constructs by combining stem cells with scaffolds [2]. Specifically, the engineering of functional bone constructs using stem cells and scaffolds may offer new opportunities not only for the repair of orthopedic diseases but also for improvements in the fundamental understanding of the development and regeneration of bone pathologies. Therefore, an important step in this strategy is to develop an effective platform to improve stem cell functions, especially osteogenesis, for bone regeneration [2-5].

Stem cells are located within an instructive and tissue-specific niche, containing complex and controlled biochemical mixtures of soluble and insoluble factors and surrounded by the extracellular microenvironment [6,7]. In the native environment in cancellous bone, stem cells [usually mesenchymal stem cells (MSCs)] physically interact with unique topographical cues at the nanometer length scale, suggesting that nanotopography may play an important role in regulating stem cell function [2]. For example, it has been reported that nanopits or nanotubes can promote osteogenesis of MSCs [8,9]. Although these studies have provided important insights into nanotopography as an enabling tool for advanced stem cell-based bone tissue engineering, further progress is required for the recapitulation of the natural nanotopography observed in the native bone environment. Accordingly, considerable benefits may be derived from improving stem cell function with a combination of bio-inspired nanotopography fabricated

from the aspect of native bone structures and the traditional soluble signaling molecules (e.g., differentiation-inducing chemicals).

In addition, it has been recognized that the cells adjacent to a stem cell niche would also be important regulators of the fate and functions of stem cells through extracellular communication via direct or indirect cell-cell interactions [7,10,11]. Because bone is a highly vascularized tissue, it can be inferred that bone cells or stem cells must inevitably interact with vascular cells [12]. It has recently been reported that the osteogenesis of human MSCs (hMSCs) was greatly enhanced by co-culture with human umbilical vein endothelial cells (HUVECs) in two-dimensional cultures in standard cell culture dishes [12,13]. These studies showed that the extent of cell-cell communication between hMSCs and HUVECs in a co-culture system in combination with secreted cytokines, such as bone morphogenetic proteins (BMPs) and endothelial growth factor (VEGF), might be able to enhance the osteogenesis of hMSCs.

Guided by these considerations, we propose a rational design for engineering platforms for stem cell-based bone tissue engineering using the combination of tissue-mimetic nanotopography and co-culture with endothelial cells. We hypothesized that the bone tissue-like matrix nanotopography and endothelial cell co-culture would provide a more physiologically relevant microenvironment, which could synergistically regulate the structure and functions of stem cells. To address this challenge, we prepared precisely defined bone-mimetic nanotopography using ultraviolet (UV)-assisted capillary force lithography (CFL) [14] and investigated how this platform synergistically influenced the function of hMSCs with the goal of promoting a more osteogenic phenotype.

### **7.3. Materials and methods**

### **7.3.1. Preparation and observation of *ex vivo* human bone tissue**

Bone tissue was obtained from patients during chronic otitis media surgeries under the approval of the Institutional Review Board of the Ajou University School of Medicine (Suwon, Korea). The bone tissue was fixed overnight with a solution containing 2% glutaraldehyde, 0.1 M sodium cacodylate, and 3 mM calcium chloride (pH 7.4) at 4°C. The bone tissue was rinsed three times with PBS. The specimen was perfused with 1% osmium tetroxide and placed on a tissue rotator for 30 min. The sample was then rinsed in PBS three times. The tissue was serially dehydrated in 50%, 70%, 90%, 95%, and 100% of acetone. Each specimen was treated with hexamethyldisilazane (HMDS), air dried, and placed on a stub for sputter-coating with gold. The tissue was then observed with a field-emission scanning electron microscope (FESEM; JEOL, JSM-5410LV, Japan).

### **7.3.2. Design and fabrication of nanopatterned matrix as a bone tissue-like substratum**

The bone tissue-like matrix nanotopography was fabricated by UV-assisted capillary molding technique with polyurethane acrylate (PUA) [14,15]. Regularly-spaced nanogrooves with the width of 550 nm and three different gaps of 550, 1,650 and 2,750 nm (spacing ratio: 1:1, 1:3 and 1:5, respectively) were replicated from the pre-fabricated silicon masters over a large area of  $25 \times 25 \text{ mm}^2$ . The silicon masters had been prepared by standard photolithography and dry etching. In the replication step, a UV-curable PUA precursor (Minuta Tech., South Korea) was drop-dispensed onto the master and brought into contact with a 100  $\mu\text{m}$ -thick polyethylene terephthalate (PET) film (SKC Inc., South Korea) as a backing plane. After subsequent irradiation of UV for few tens of seconds, a negative PUA replica was formed on the PET film. Then the same replication process was performed onto a cleaned cover slip using the replicated

PUA pattern as a mold. The flat and patterned surfaces were generated on the same cover slip in order to maintain the same experimental conditions. The fabricated samples were coated with gold and imaged by a FESEM (JEOL, JSM-5410LV) at an accelerating voltage of 2 kV.

### **7.3.3. Isolation and culturing of hMSCs**

Adipose tissues were isolated from the patients undergoing ear surgeries under sufficient informed consent at the Ajou University School of Medicine (Suwon, Korea). The experimental protocol was approved by the Institutional Review Board at the same university. Tissues were washed with PBS and digested with 100 Unit/mL collagenase type I (Sigma-Aldrich, St. Louis, MO, USA) with low glucose Dulbecco's modified Eagle's medium (DMEM; Gibco-BRL, Grand Island, NY, USA) and incubated for 8 h to lyse the adipose tissues. The stromal fraction was collected by centrifugation and then passed through a cell strainer (100  $\mu$ m size) to remove any large cell clumps and particles. For cell culture and expansion of adipose-derived hMSCs, cells were grown in low glucose DMEM with 10% fetal bovine serum (FBS) and 1% penicillin-streptomycin (Gibco, Milan, Italy) at 37°C in a 5% CO<sub>2</sub> atmosphere. All cells used in this study were at passage 3 or 4.

### **7.3.4. Culturing of HUVECs**

HUVECs were purchased from Lonza (Walkerville, USA) and cultured in endothelial growth medium with 2% FBS, 0.4% fibroblast growth factor, 0.04% hydrocortisone, 0.1% insulin-like growth factor, 0.1% ascorbic acid, 0.1% heparin, and 0.1% gentamicin (Gibco, Milan, Italy) at 37 °C in a 5% CO<sub>2</sub> atmosphere. All cells used in this study were at passage 3 or 4.



### **7.3.5. Culturing of cells seeded on substrata**

hMSCs and HUVECs were cultured with 1:1 ratio of hMSCs:HUVECs on nanopatterned and flat substrata (unpatterned) in normal media (DMEM with 10% FBS and 1% antibiotics) or osteogenic differentiation media (100 nM dexamethsone, 50  $\mu$ M ascorbic acid, and 10 mM glycerol 2-phosphate in normal media). The medium was changed twice or three times a week. To visualize cell types, the hMSCs and HUVECs were stained with the lipophilic fluorescent dyes Vybrant-DiO and DiD (Invitrogen, USA), respectively, before seeding cells on the substrata.

### **7.3.6. Quantification of cell morphology and orientation**

For the quantitative analysis of the morphology and orientation of hMSCs and HUVECs on the substrata, the images of the cells obtained by fluorescence microscopy (Zeiss, Germany), and analyzed using a custom written MATLAB script. Ten fluorescent images with 50-100 cells were used to quantify the cell morphology and orientation.

### **7.3.7. Imaging cell morphology using FESEM**

hMSCs and HUVECs ( $0.5 \times 10^4$  cells/sample, respectively) were cultured for 14 h on the substrata. Cells adhered onto the sample surfaces were fixed with modified Karnovsky's fixative consisting of 2% paraformaldehyde and 2% glutaraldehyde (Sigma-Aldrich) in a 0.05 M sodium cacodylate buffer (Sigma-Aldrich) for 4 hr. The samples were washed with 0.05 M sodium cacodylate buffer 3 times for 10 min and fixed with 1% osmium tetroxide (Sigma- Aldrich). The samples were then washed with distilled water and dehydrated with graded concentrations (50, 70, 80, 90, and 100% v/v) of ethanol. Then, the samples were treated with hexamethyldisilazane

(Sigma-Aldrich) for 15 min. Finally, the samples were coated with gold prior to cell shape observation with FESEM (JEOL, JSM-5410LV, Japan).

### **7.3.8. Immunofluorescence staining**

Adhered cells on samples were fixed with a 4% paraformaldehyde solution (Sigma-Aldrich, Milwaukee, WI, USA) for 20 min, permeabilized with 0.2% Triton X-100 (Sigma-Aldrich, WI, Milwaukee, USA) for 15 min, and stained with TRITC-conjugated phalloidin (Millipore, Billerica, MA, USA) and 4, 6-diamidino-2-phenylindole (DAPI; Millipore, Billerica, MA, USA) for 1 h. Focal adhesions (FAs) were also stained with a monoclonal anti-vinculin antibody (1:100; Millipore, Billerica, MA, USA) and a FITC-conjugated goat anti-mouse secondary antibody (1:500; Millipore, Billerica, MA, USA). Images of the stained cells were taken using a fluorescence microscope (Zeiss, Germany). For the quantitative analysis of the nuclear elongation factor [NEF = (major axis)/(minor axis) of nucleus] and FA sizes of hMSCs on the substrata, the images obtained by fluorescence microscopy were analyzed using the custom written MATLAB script.

### **7.3.9. Western blot analysis**

Total cellular protein was extracted by RIPA lysis buffer (62.5 mM Tris-HCL, 2% SDS, 10% glycerol, pH 7.5) with added proteinase inhibitor cocktail (Invitrogen, USA). Cell lysates were incubated on ice for 30 min and then centrifuged at 13,000 rpm for 30 min at 4°C. Supernatant (protein lysate) was collected and protein concentration was determined by a micro bicinchoninic acid (BCA) Protein Assay Kit (Bio-rad, Hercules, Calif). 25 µg aliquots of the cell lysates were separated by 8% SDS-PAGE under reducing conditions. Separated proteins were transferred to a

PVDF membrane (Millipore, Corporation, Bedford, MA, USA) at 30 V for 1 h. After blocking with 5% skim milk in PBST, the membrane were incubated overnight in primary antibody at 4°C. Primary antibody was purchased from the company (Integrin  $\beta$ 1 (Santa Cruz, Biotechnology, Santa Cruz, CA); Connexin 43 (Cell Signaling Technology, Beverly, MA); Osteopontin (Abcam, Cambridge, MA, USA). After washing, the membranes were probed with horseradish peroxidase-conjugated anti-IgG (Invitrogen), and proteins were visualized using the ECL chemiluminescence detection system (GenDEPOT, Hous-ton, TX, USA). Protein expression was normalized versus  $\beta$ -actin antibody (Cell Signaling Technology, Beverly, MA, USA) on the same blot membrane. Quantification of the Western blot was performed using the Image J software with a normalization of the level of the entire protein.

#### **7.3.10. Proliferation of hMSCs and HUVECs on substrata**

For the quantitative analysis of proliferation of hMSCs and HUVECs on the substrata, the cells were cultured for 7 days and 21 days in normal media, respectively. After careful removal of the unattached cells by washing the sample surfaces with PBS, we conducted WST assays (EZ-Cytox Cell Viability Assay Kit; Daeillab Service Co., Ltd.) following the instruction of the manufacturer.

#### **7.3.11. Osteogenesis of hMSCs on substrata in co-culture with HUVECs**

hMSCs and HUVECs were cultured for 21 days on the substrata in osteogenic differentiation media. The degree of mineralization was measured by Alizarin Red S (Sigma-Aldrich) staining of hMSCs cultured on the substrata, and this measurement was used for quantification of the osteogenic differentiation of hMSCs. The cells stained with Alizarin Red S were destained with

cetylpyridinium chloride (Sigma-Aldrich), and then the extracted stains were measured using an ELISA reader (VERSAMAX reader, Molecular Devices, Sunnyvale) at 540 nm. The immunofluorescent staining of osteocalcin (OCN; osteogenesis marker) of cells was also used to show the osteogenesis of hMSCs on substrata.

#### **7.3.12. Quantification of cytokines**

To measure BMP-2 and VEGF, hMSCs and HUVECs were cultured for 21 days on the substrata in osteogenic differentiation media. A commercially available ELISA kits (R&D Systems, USA) was used to measure the level of total BMP-2 and VEGF production from cells. The supernatants (cell culture media) were used for quantification of BMP-2 and VEGF according to the instruction of the manufacturer. The absorbance was measured using a microplate reader at 450 nm.

#### **7.3.13. Statistical analysis**

Student's t-test or Duncan's multiple range test was used for statistical analysis. All quantitative results were presented as mean  $\pm$  standard deviation (SD).

### **7.4. Results**

#### **7.4.1. Bone tissue-inspired *in vivo*-like microenvironment**

At the site of bone formation, osteoblasts and hMSCs are usually observed within close range of blood vessels, indicating that endothelial cells may play an important role in regulating the functions of osteoblasts and hMSCs in bone regeneration [2,12]. In addition, it is well-known that human tissues, including bone, exist in the form of naturally well-organized nanoscale

topographies for tissue-specific functions [2,16]. Our ultrastructural analysis of *ex vivo* human cancellous bone tissue showed highly aligned nanogrooves (Fig. 7.1a). This observation suggests that the aligned nanostructures in human bone may provide specific topographical cues which guide the structure and function of hMSCs and endothelial cells for bone regeneration. We hypothesized that the well-defined nanotopography and endothelial cells would provide a more physiologically relevant stem cell niche to improve the functions of stem cells, especially osteogenesis, for bone regeneration.

Inspired by the highly anisotropic nanostructures of natural human bone tissue (Fig. 7.1a), we fabricate cell culture substrata with a bone tissue-like nanopatterned matrix by using UV-assisted CFL. The 550 nm-wide nanogrooves (600 nm-deep) with inter-groove distances of 550, 1,650 and 2,750 nm (width to spacing ratio, defined by the ridge width, of 1:1, 1:3 and 1:5, respectively) were fabricated onto glass coverslips along with the flat control (no patterns on PUA surface) (Figs. 8.1b and c). To improve cell adhesion, we coated the flat and nanotopographic PUA matrices with gelatin prior to cell culture. Next, we cultured hMSCs and HUVECs on the substrata to investigate the effects of nanotopography and endothelial cell co-culture in terms of the adhesion, proliferation, and osteogenesis of hMSCs (Fig. 8.1d). In this study, we used a 1:1 ratio of hMSCs:HUVECs in the co-culture system, as suggested by Ma *et al.* [13], who reported optimal osteogenesis at a 1:1 ratio of hMSCs and HUVECs on normal culture dishes with flat surfaces. Therefore, we expected that the bone tissue-like nanotopography and co-culture system in combination with traditional chemical factors of osteogenic differentiation could synergistically promote osteogenesis of hMSCs. This combination will therefore be able to act as a platform or a strategy for stem cell-based bone tissue regeneration.

#### **7.4.2. Effects of nanopatterned matrix on morphology and orientation of hMSCs and HUVECs**

It has been accepted that topography can strongly influence the morphology and orientation of living cells through a phenomenon known as contact guidance and through integrin-mediated intracellular tension, which may play an essential role in determining characteristic functions of complex tissues [2,16-19]. To investigate the effects of the bone tissue-like nanopatterned matrix on the morphology and orientation of hMSCs and HUVECs, we cultured hMSCs and HUVECs on the gelatin-coated PUA matrix nanotopography for 14 h. We first observed the morphology and orientation of hMSCs with a phase contrast microscope (Fig. 7.2a). We found highly aligned shapes of both cells on the anisotropically nanopatterned substrata. In contrast, we observed that the hMSCs and HUVECs on the flat substratum maintained a random morphology and orientation.

To investigate the effects of nanotopography on the morphology of hMSCs and HUVECs in further detail, SEM and immunofluorescence staining analysis were used. As shown in the SEM images in Figs. 7.2b and c, the morphologies of hMSCs and HUVECs were strictly regulated by the nanotopographical density. We confirmed that both cell types elongated more strongly on the sparser nanogrooved density (e.g., 550\_2,750) than on the relatively denser nanogrooved density (e.g., 550\_550). The immunofluorescence results also demonstrate that the cytoskeletal alignments in both cell types appeared notably sensitive to the nanopatterned matrix (Fig. 7.2d). Taken together, our data indicate that the bone tissue-like nanopatterned matrix strongly influences the aligned and orientated shapes of hMSCs and HUVECs in the co-culture system, which precisely coincides with the natural orientations of both cell types *in vivo* [20,21].

#### **7.4.3. Time-dependent morphology and orientation of hMSCs and HUVECs by nanopatterned matrix**

To analyze the time-dependent shape and spatial distribution of hMSCs and HUVECs, we stained hMSCs in red and HUVECs in green using lipophilic fluorescent dyes and later cultured them on the bone tissue-like nanopatterned matrix for 6 h and 7 days (Fig. 7.3a). At 6 h after cell seeding, we carefully removed unattached cells from the substrata by washing with PBS to determine the attachment characteristics of hMSCs and HUVECs onto the substrata. We showed that the hMSCs and HUVECs were well adhered on both the flat and nanopatterned substrata. Interestingly, we observed that each population showed a spatially distributed arrangement, presumably due to the low cell density (Fig. 7.3a). In addition, we showed that both types of cells were usually oriented along the direction of the nanotopography. At 7 days after cell seeding, we observed that the hMSCs and HUVECs had proliferated, and they were highly aligned on the nanopatterned matrix (Fig. 7.3a). Interestingly, we observed yellow fluorescence in cultures from both flat and nanopatterned substrata, most likely due to overlapped cells or to the transfer of lipophilic fluorescent dyes between hMSC and HUVEC; we did not observe this phenomenon in the fluorescence staining results from cells cultured for 6 h.

We report two notable findings from this experiment. First, the hMSCs and HUVECs were more elongated and orientated along the nanotopography over time. Second, the hMSCs interacted with one another when sufficient numbers of cells were present. To quantify these observations in terms of morphology and orientation of hMSCs and HUVECs, we analyzed the cell elongation factor [CEF; defined as (major axis)/(minor axis) of cell body] of both cell types on the substrata. As shown in Fig. 7.3b, we confirmed that the cells on the nanopatterned substrata showed higher CEFs than those on the flat substratum, especially over time.

Interestingly, we showed that the CEFs of hMSCs and HUVECs on the nanopatterned substrata were approximately 2 or 3 times higher than those on the flat substratum ( $P < 0.05$ ). Fig. 7.3c shows the quantitative analysis of hMSC and HUVEC orientation on the substrata, also demonstrating that the hMSCs and HUVECs were more orientated along the nanotopography over time in the co-culture system, whereas such behaviors were not observed on the flat substratum.

#### **7.4.4. Effects of nanopatterned matrix on proliferation of hMSCs and HUVECs**

Proliferation of hMSCs and HUVECs is an important factor in bone regeneration. To demonstrate that the bone tissue-like nanopatterned matrix would provide an environment for proliferation of hMSCs and HUVECs in the co-culture system, we cultured hMSCs and HUVECs on the anisotropically nanopatterned substrata and flat substratum for 3 and 7 days, respectively. All samples showed good time-dependent proliferation of cells (Fig. 7.4a). To confirm the proliferation of hMSCs and HUVECs on the nanopatterned substrata, we examined the cells using the FESEM after 1 day (initially attached cells) and 7 days (proliferated cells) (Fig. 7.4b). The hMSCs and HUVECs were adhered and spread properly on nearly the entire surface of the substrata at 7 days, whereas those on the substrata for 1 day were more sparsely distributed. Still, we found no significant difference in cell proliferation rates among the nanopatterned and flat substrata using the co-culture system (Fig. 7.4a). In addition, the proliferation rate of hMSCs on the nanopatterned and flat substrata may not be significantly different, as seen in Fig. 7.3a. This result is consistent with previous results reporting that the anisotropic nanotopography did not alter cell proliferation from that observed with flat culture surfaces [22,23].



#### **7.4.5. Effects of nanopatterned matrix and co-culture with HUVECs on osteogenesis of hMSCs**

To verify the hypothesis that the bone tissue-like nanopatterned matrix can enhance the osteogenesis of hMSCs in a co-culture system, we first analyzed hMSC osteogenesis by mineralization. We cultured hMSCs on the anisotropically nanopatterned and flat substrata in osteogenic induction media for 21 days. The Alizarin Red S staining shown in Fig. 7.5a demonstrated that the calcium expression levels were higher on the nanopatterned substrata than on the flat substratum. To quantify the degree of hMSC osteogenesis, the stained calcium deposits were destained with cetylpyridinium chloride, and the quantity of extracted stains was measured using an ELISA reader. We again showed that the nanopatterned substrata exhibited higher osteogenesis than the flat substratum ( $P < 0.05$ ) (Fig. 7.5b). It should be noted that there were no significant differences in cell viability (number of cells) ( $P > 0.05$ ) (Fig. 7.5c). We further examined OCN as one of the osteogenic genes to confirm the enhancement of osteogenic differentiation of hMSCs on the nanopatterned substrata as compared to the flat substratum (Fig. 7.5d). Interestingly, we also observed a biphasic trend: the signal increases from the flat substratum to the 550\_1,650 nanopatterned substratum and then decreases at 550\_2,750 nanopatterned substratum, suggesting that the nanotopographical density influence the osteogenesis of hMSCs. To demonstrate better the effect of the bone tissue-like nanotopography on the osteogenesis of hMSCs, we cultured hMSCs as a monoculture on the 550\_550 nanopatterned substratum. Our western blot analysis clearly showed upregulation of osteopontin (OPN) on the nanopatterned substratum versus the flat substratum (Fig. 7.5e). In addition, to better show the effect of the co-culture system on the osteogenesis of hMSCs in the bone tissue like-nanotopography, we cultured hMSCs ( $1 \times 10^4$  cells/sample) as a monoculture and hMSCs

and HUVECs ( $0.5 \times 10^4$  cells/sample, respectively) together as a co-culture on the anisotropically nanopatterned substrata. Surprisingly, even though the initial seeded number of hMSCs in the co-culture system was half that in the monoculture system, the osteogenesis of hMSCs in the co-culture system was significantly higher than that in the monoculture system (Fig. 7.5f). This finding suggests that the co-culture with endothelial cells strongly promotes the osteogenesis of hMSCs in the environment of the bone tissue-like nanotopography.

This interesting synergistic effect raises the following question: how much do the bone tissue-like nanotopography and endothelial cell co-culture synergistically or individually enhance the osteogenesis of hMSCs? To decouple the effects of these factors, we cultured hMSCs and HUVECs on the anisotropically nanopatterned and flat substrata as a mono- or co-culture system in osteogenic induction media for 14 days. For simplicity, we named our four cases as follows: (i) mono/flat, (ii) mono/nano, (iii) co/flat and (iv) co/nano. In this experiment, we used the same numbers of hMSCs ( $2 \times 10^4$  cells/sample) for initial cell seeding onto the substrata in the mono- or co-culture systems. As shown in Fig. 7.6a, the nanopatterned substrata and the co-culture with HUVECs showed different degrees of osteogenesis of hMSCs. As expected, the osteogenesis of hMSCs on the flat or nanopatterned substrata in the co-culture systems [(iii) 1.248 and (iv) 1.561] was higher than that in the monoculture systems [(i) 1 and (ii) 1.089], respectively. Surprisingly, we also observed that the osteogenesis of hMSCs on the nanopatterned substrata in the monoculture system [(ii) 1.248] was higher than that on the flat substrata even in the co-culture system [(iii) 1.089]. The nanopatterned substrata in the co-culture system exhibited the highest osteogenesis [(iv) 1.561] (Fig. 7.6a). This result was confirmed by the quantification of the calcium deposits stained by Alizarin Red S ( $P > 0.05$ ) (Fig. 7.6b). Based on our results, the bone tissue-like nanopatterned matrix and endothelial cell co-culture synergistically enhance the

osteogenesis of hMSCs. In addition, our results suggest that the nanotopography is a more crucial factor in the osteogenesis of hMSCs. Moreover, there still may be further opportunities to enhance the osteogenesis of hMSCs using our platforms with different ratio of hMSCs and HUVECs or adding some growth factors (e.g., VEGF) into osteogenic media to enhance the activity of HUVECs. These results emphasize the importance of establishing *in vivo*-like microenvironments in stem cell engineering through the use of a variety of cues, including topography, multiple cell types, and others.

## **7.5. Discussion**

Designing an effective material-based platform is an important part of regenerative medicine because such platforms can control or improve cellular functions, as well as construct artificial tissues for tissue regeneration [2,24-27]. From the concept of a “stem cell niche,” in this study, we developed an *in vivo*-like microenvironment, including a bone tissue-like nanopatterned matrix and endothelial cell co-culture, to regulate the adhesion and function of hMSCs. Using this platform, we demonstrated that the bone tissue-like nanopatterned matrix and co-culture with endothelial cells synergistically enhanced the osteogenesis of hMSCs. We assert that our strategy provides better formation of a stem cell niche to promote the osteogenesis of hMSCs and that it would be an effective tool for stem cell and bone tissue engineering.

We hypothesize that the general progression of stem cell behavior follows these steps: (i) stem cell adhesion on substrata; (ii) spreading; (iii) focal adhesion formation and cytoskeleton development; (iv) functions (e.g., differentiation into specific tissue cells) [2,10,11]. Thus, the linkage between stem cells and topography may be crucial for regulating important functions of stem cells through the topography-induced mechanical cues (e.g., cytoskeletal tension)

[10,11,24,28]. Advanced nanofabrication technologies have recently begun to allow the development of various nanoscale topographies, such as nanofibers, electrospun nanofibrous mats, and substrata with nanoroughness [29-34]. These techniques have proven useful for the systematical investigation of the effects of stem cell-nanotopography interactions, especially on the differentiation of stem cells [24,28]. For example, several studies have demonstrated that nanopits usually reduce cell spreading [28]. However, the underlying mechanism in between cell spreading and stem cell function still remains unclear. Dalby's group reported that disordered nanopits enhanced the osteogenesis of hMSCs compared to well-ordered nanopits or a flat surface [35], reflecting an important effect of cell-nanotopography interactions. In our research, we demonstrated that the bone tissue-like nanopatterned matrix regulated the anisotropic morphology and orientation of hMSCs and that it enhanced osteogenesis of hMSCs compared to a flat substratum (Fig. 7.6). Our finding also suggests that the controlled morphology and subsequent intracellular organization of hMSCs is important regulator of their functions as stem cells. Therefore, an in-depth study on the interactions between stem cell function and bio-inspired nanotopography is potentially of great benefit and would enhance our understanding of the functions of stem cells, as well as their applications in regenerative medicine.

It has been known that cell-cell interactions influence cell proliferation, cell differentiation, and tissue formation by direct physical and indirect paracrine signaling [36]. Stem cell functions can also be profoundly affected by various macromolecules that mediate extracellular cell-cell communication via direct or indirect manners [7,10,11]. Several co-culture systems have been proposed for investigating the interaction between hMSCs and neighboring cells *in vitro* with respect to the behaviors of hMSCs [13,36]. Ma *et al.* reported that co-culture with endothelial cells enhanced the osteogenesis of hMSCs [13]. Although the mechanism

underlying the effects of co-culture systems on the enhanced osteogenesis of hMSCs remains unknown, such an effect is plausible. In our work, by combining the endothelial cell co-culture system with bone tissue-mimetic nanotopography, we demonstrated that these factors could synergistically promote the osteogenesis of hMSCs (Figs. 7.5 and 7.6). Wein *et al.* recently reported that co-culture with endothelial cells and fibroblasts could improve the proliferation and osteogenesis of hMSCs [36]. This finding suggests that a co-culture system with both fibroblasts and endothelial cells combined with bio-inspired nanotopography may be an appropriate strategy for promoting the osteogenesis of hMSCs to regenerate bones.

In this study, we discuss how the bone tissue-like nanopatterned matrix and co-culture with endothelial cells may synergistically enhance the osteogenesis of hMSCs. We consider three major factors: (i) biochemical soluble factors, (ii) cell-substrate interaction, and (iii) cell-cell interaction. To explore the possible mechanism, we investigated various factors in the hMSC and HUVEC cultures on the 550\_550 nm nanopatterned and flat substrata, respectively.

(i) Biochemical soluble factors: In co-culture systems, it has been found that soluble chemical factors including cytokines such as BMP-2 and VEGF may be important factors for regulation of hMSC function, especially for osteogenesis [12]. We thus investigated whether the nanopatterned substrata influenced the production of BMP-2 or VEGF during co-culture of hMSCs and HUVECs on the nanopatterned and flat substrata, respectively. As shown in Fig. 8.7a, we learned that the nanopatterned substrata did not greatly influence the production of BMP-2 or VEGF, though the production of BMP-2 in the co-culture system was slightly higher on the nanopatterned substrata than on the flat substrata. We therefore speculated that the other factors were more relevant to the osteogenesis of hMSCs.

(ii) Cell-substrate interaction: First, we investigated the nuclear shape of hMSCs on the

nanopatterned and flat substrata, respectively, because it is known that nuclear shape influences cellular functions [25,37]. As shown in Fig. 7.7b, immunofluorescence staining images demonstrate that the nuclei of hMSCs on nanopatterned substratum elongated considerably more than those on the flat substratum. Our quantitative analysis of the nuclear elongation factor [NEF: defined as (major axis)/(minor axis)] indicates that the NEF of hMSCs on the nanopatterned substratum was approximately 50% higher than that on the flat substratum [Fig. 7b(ii)] ( $P < 0.05$ ), suggesting that the hMSCs on the nanopatterned substratum received more mechanical cues than those on the flat substratum. Second, we investigated the focal adhesions (FAs) of hMSCs on the nanopatterned and flat substratum, respectively. It should be noted that FAs are known as a potential mechanosensor that is important in cellular functions [19,38]. We observed that the FAs of hMSCs on nanopatterned substratum were polarized along the direction of nanotopography with negligible polarization on the flat substratum [Fig. 7.7c(i)]. We also showed that the average size of FAs of hMSCs was higher on the nanopatterned substratum than on the flat substratum [Fig. 7.7c(ii)]. Furthermore, western blot analysis clearly indicated greatly enhanced expression of integrin  $\beta 1$  in cultured hMSCs on the nanopatterned substratum compared with that on the flat substratum [Fig. 7.7e(i)]. Thus, our data strongly suggest that the control of nuclear shape and FAs in hMSCs by nanotopographical cues might affect their mechanotransductional pathways, thereby influencing their osteogenesis.

(iii) Cell-cell interaction: Finally, we investigated the expression levels of the major gap junction protein, connexin 43 (Cx43), between hMSCs-HUVECs or hMSCs-hMSCs as one of the important factors for the osteogenesis of hMSCs [39,40]. Interestingly, it was found that the cells on the nanopattern in the co-culture system showed interconnected structures to each other (Fig. 7.S1), and the expression of Cx43 in cells in the co-culture systems was increased on the

nanopatterned substratum compared to the flat substratum [Figs. 7.7d and e(ii)], suggesting that the nanopatterned substratum might provide a more suitable environment for cell-cell communication, most likely due to the controlled cell shapes. Thus, the enhanced cell-cell contacts on the nanopatterned substratum might influence the osteogenesis of hMSCs in the co-culture systems.

In summary, (i) secreted BMP-2, (ii) elongated nuclei and increased average size of FAs, and (iii) enhanced Cx43 expression of hMSCs on the bone tissue-like matrix nanotopography in co-culture with HUVECs may collectively influence the enhanced osteogenesis of hMSCs. Based on our observations (Figs. 7.7a-e) and decoupling study on the osteogenesis of hMSCs (Fig. 7.6), we propose the following possible mechanism for the synergistic promotion of an osteogenic phenotype in hMSCs by bone tissue-like matrix nanotopography and co-culture with HUVECs (Fig. 7.8):

(1) Enhanced osteogenesis of hMSCs on the flat substratum in the co-culture system follows these steps: (i) culturing hMSCs with HUVECs; (ii) enhanced hMSC-HUVEC interaction [Cx43 expression ↑] and BMP-2 production; (iii) enhanced osteogenesis of hMSCs [increased osteogenesis factor: from 1 (hMSCs alone on the flat substratum) to 1.089 (hMSCs and HUVECs together on the flat substratum)].

(2) Enhanced osteogenesis of hMSCs on the nanopatterned substratum in monoculture system follows these steps: (i) culturing hMSCs with nanotopography cues; (ii) enhanced hMSC-substrate interaction [elongated nucleus and controlled FA of hMSCs by nanotopography cues]; (iii) enhanced osteogenesis of hMSCs [increased osteogenesis factor: from 1 (hMSCs alone on the flat substratum) to 1.248 (hMSCs alone on the nanopatterned substratum)].

(3) Synergistically enhanced osteogenesis of hMSCs on the nanopatterned substratum in

co-culture system follows these steps: (i) enhanced hMSC-HUVEC and hMSC-substrate interaction; (ii) enhanced osteogenesis of hMSCs [increased osteogenesis factor: from 1 (hMSCs alone on the flat substratum) to 1.561 (hMSCs and HUVECs together on the nanopatterned substratum)].

In this study, the synergistic effect of nanotopography and co-culture with HUVECs on the osteogenesis of hMSCs has been investigated quantitatively. We demonstrated that either factor alone could enhance the osteogenesis of hMSCs. The osteogenic phenotypes were further increased when both factors were combined in a synergistic manner. Interestingly, our findings also suggested that the nanotopography contributed to the osteogenesis more than did co-culture with HUVECs. Although we have focused on the enhancement of osteogenesis, our platforms are equally applicable to other systems, such as enhancement of vasculogenic differentiation for neovascularization during bone regeneration. We believe that our study provides new insight into the importance of tissue-inspired nanotopography and co-culture systems in designing engineered platforms for stem cell-based bone tissue engineering, as well as for the fundamental study of stem cell biology. Although in-depth studies are required to understand the underlying molecular mechanisms accurately, the results presented in this report collectively demonstrated that the *in vivo*-mimetic synergistic effect of various factors may have significant implications for stem cell engineering and regenerative medicine.

## **7.6. References**

- [1] Giannoudis PV, Dinopoulos H, Tsiridis E. Bone substitutes: an update. *Injury* 2005;36: S20-S27.
- [2] Kim HN, Jiao A, Hwang NS, Kim MS, Kang DH, Kim DH, et al. Nanotopography-guided



tissue engineering and regenerative medicine. *Adv Drug Deliv Rev* 2013;65:536-58.

[3] McMahon RE, Wang L, Skoracki R, Mathur AB. Development of nanomaterials for bone repair and regeneration. *J Biomed Mater Res B Appl Biomater* 2013;101:387-397.

[4] Wang Y, Kim HJ, Vunjak-Novakovic G, Kaplan DL. Stem cell-based tissue engineering with silk biomaterials. *Biomaterials* 2006;27:6064-6082.

[5] Davis HE, Case EM, Miller SL, Genetos DC, Leach JK. Osteogenic response to BMP-2 of hMSCs grown on apatite-coated scaffolds. *Biotechnol Bioeng* 2011;108:2727-2735.

[6] Lutolf MP, Gilbert PM, Blau HM. Designing materials to direct stem-cell fate. *Nature* 2009;462:433-441.

[7] Lutolf MP, Blau HM. Artificial stem cell niches. *Adv Mater* 2009;21:3255-3268.

[8] Dalby MJ, Gadegaard N, Tare R, Andar A, Riehle MO, Herzyk P, et al. The control of human mesenchymal cell differentiation using nanoscale symmetry and disorder. *Nat Mater* 2007;6:997-1003.

[9] Oh S, Brammer KS, Li YSJ, Teng D, Engler AJ, Chien S, et al. Stem cell fate dictated solely by altered nanotube dimension. *Proc Natl Acad Sci USA* 2009;106:2130-35.

[10] Guilak F, Cohen DM, Estes BT, Gimble JM, Liedtke W, Chen CS. Control of stem cell fate by physical interactions with the extracellular matrix. *Cell Stem Cell* 2009;5:17-26.

[11] Nelson TJ, Behfar A, Yamada S, Martinez-Fernandez A, Terzic A. Stem cell platforms for regenerative medicine. *Clin Transl Sci* 2009;2:222-227.

[12] Xue Y, Xing Z, Hellem S, Arvidson K, Mustafa K. Endothelial cells influence the osteogenic potential of bone marrow stromal cells. *Biomed Eng Online* 2009;8:34.

[13] Ma J, van den Beucken JJ, Yang F, Both SK, Cui FZ, Pan J, et al. Coculture of osteoblasts and endothelial cells: optimization of culture medium and cell ratio. *Tissue Eng Part C Methods*

2011;17:349-357.

[14] Suh KY, Park MC, Kim P. Capillary force lithography: a versatile tool for structured biomaterials interface towards cell and tissue engineering. *Adv Funct Mater* 2009;19:2699-2712.

[15] Choi SJ, Kim HN, Bae WG, Suh KY. Modulus- and surface energy-tunable ultraviolet-curable polyurethane acrylate: properties and applications. *J Mater Chem* 2011;21:14325-14335.

[16] Kim DH, Provenzano PP, Smith CL, Levchenko A. Matrix nanotopography as a regulator of cell function. *J Cell Biol* 2012;197:351-360.

[17] Teixeira AI, Abrams GA, Bertics PJ, Murphy CJ, Nealey PF. Epithelial contact guidance on well-defined micro- and nanostructured substrates. *J Cell Sci* 2003;116:1881-1892.

[18] McNamara LE, McMurray RJ, Biggs MJ, Kantawong F, Oreffo RO, Dalby MJ. Nanotopographical control of stem cell differentiation. *J Tissue Eng* 2010;2010:120623.

[19] Biggs MJP, Richards RG, Dalby MJ. Nanotopographical modification: a regulator of cellular function through focal adhesions. *Nanomedicine* 2010;6:619-633.

[20] Kerschnitzki M, Wagermaier W, Roschger P, Seto J, Shahar R, Duda GN, et al. The organization of the osteocyte network mirrors the extracellular matrix orientation in bone. *J Struct Biol* 2011;173:303-311.

[21] Isenberg BC, Wong JY. Building structure into engineered tissues. *Mater Today* 2006;9:54-60.

[22] Kim HN, Hong Y, Kim MS, Kim SM, Suh KY. Effect of orientation and density of nanotopography in dermal wound healing. *Biomaterials* 2012;33:8782-8792.

[23] Liliensiek SJ, Campbell S, Nealey PF, Murphy CJ. The scale of substratum topographic features modulates proliferation of corneal epithelial cells and corneal fibroblasts. *J Biomed Mater Res A* 2006;79:185-192.

- [24] Kim DH, Lee H, Lee YK, Nam JM, Levchenko A. Biomimetic nanopatterns as enabling tools for analysis and control of live cells. *Adv Mater* 2010;22:4551-4566.
- [25] Cha C, Liechty WB, Khademhosseini A, Peppas NA. Designing biomaterials to direct stem cell fate. *ACS Nano* 2012;6:9353-9358.
- [26] Kim J, Kim DH, Lim KT, Seonwoo H, Park SH, Kim YR, et al. Charged nanomatrices as efficient platforms for modulating cell adhesion and shape. *Tissue Eng Part C Methods* 2012;18:913-923.
- [27] Kim J, Kim YR, Kim Y, Lim KT, Seonwoo H, Park S, et al. Graphene-incorporated chitosan substrata for adhesion and differentiation of human mesenchymal stem cells. *J MATER CHEM B* 2013;1:933-938.
- [28] Bettinger CJ, Langer R, Borenstein JT. Engineering substrate topography at the micro- and nanoscale to control cell function. *Angew Chem Int Ed Engl* 2009;48:5406-5415.
- [29] Yim EK, Pang SW, Leong KW. Synthetic nanostructures inducing differentiation of human mesenchymal stem cells into neuronal lineage. *Exp Cell Res* 2007;313:1820-1829.
- [30] Chen W, Villa-Diaz LG, Sun Y, Weng S, Kim JK, Lam RH, et al. Nanotopography influences adhesion, spreading, and self-renewal of human embryonic stem cells. *ACS Nano* 2012;6:4094-4103.
- [31] Park J, Bauer S, von der Mark K, Schmuki P. Nanosize and vitality: TiO<sub>2</sub> nanotube diameter directs cell fate. *Nano Lett* 2007;7:1686-1691.
- [32] Mahdavi A, Ferreira L, Sundback C, Nichol JW, Chan EP, Carter DJD, et al. A biodegradable and biocompatible gecko-inspired tissue adhesive. *Proc Natl Acad Sci USA* 2008;105:2307-2312.
- [33] Xie J, Willerth SM, Li X, Macewan MR, Rader A, Sakiyama-Elbert SE, et al. The

differentiation of embryonic stem cells seeded on electrospun nanofibers into neural lineages. *Biomaterials* 2009;30:354-362.

[34] Dolatshahi-Pirouz A, Nikkhah M, Kolind K, Dokmeci M, Khademhosseini A. Micro- and nanoengineering approaches to control stem cell-biomaterial interactions. *J Funct Biomater* 2011;2:88-106.

[35] McMurray RJ, Gadegaard N, Tsimbouri PM, Burgess KV, McNamara LE, Tare R, et al. Nanoscale surfaces for the long-term maintenance of mesenchymal stem cell phenotype and multipotency. *Nat Mater* 2011;10:637-644.

[36] Wein F, Bruinink A. Human triple cell co-culture for evaluation of bone implant materials. *Integr Biol* 2013;5:703-11.

[37] Chalut KJ, Kulangara K, Giacomelli MG, Wax A, Leong KW. Deformation of stem cell nuclei by nanotopographical cues. *Soft Matter* 2010;6:1675-1681.

[38] McBeath R, Pirone DM, Nelson CM, Bhadriraju K, Chen CS. Cell shape, cytoskeletal tension, and RhoA regulate stem cell lineage commitment. *Dev Cell* 2004;6:483-495.

[39] Kirmizidis G, Birch MA. Microfabricated grooved substrates influence cell-cell communication and osteoblast differentiation in vitro. *Tissue Eng Part A* 2009;15:1427-1436.

[40] Grellier M, Bordenave L, Amedee J. Cell-to-cell communication between osteogenic and endothelial lineages: implications for tissue engineering. *Trends Biotechnol* 2009;27:562-571.

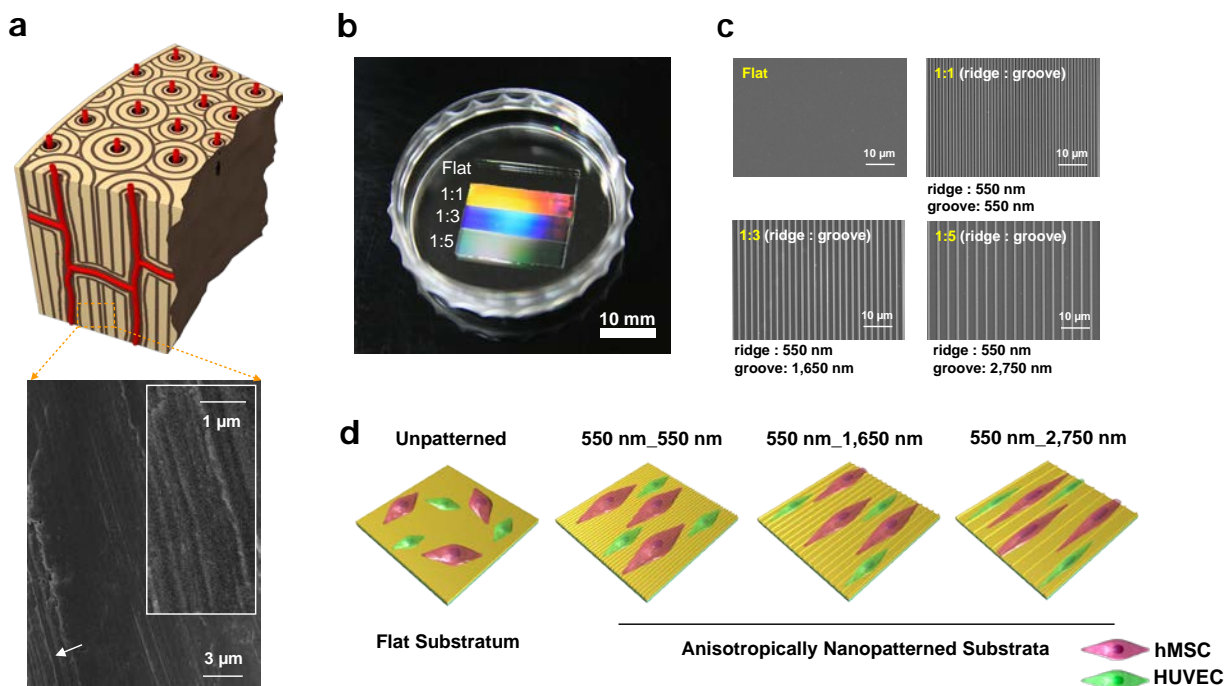


**Figure 7.1. Rational design and fabrication of bone tissue-like nanopatterned matrix with various groove sizes.** (a) Graphical illustrations and SEM images of *ex vivo* bone tissue. The insert is a high-magnification image of the region indicated by the white arrow, showing the well-aligned nanostructures in bone tissue. (b) A photograph and (c) SEM images of PUA matrix nanotopography on glass slide. The spacing ratio is the ratio of the width to the spacing of nanogrooves. (d) Schematic illustration showing the engineered platforms consisting of hMSCs, HUVECs, and nanopatterned matrix.

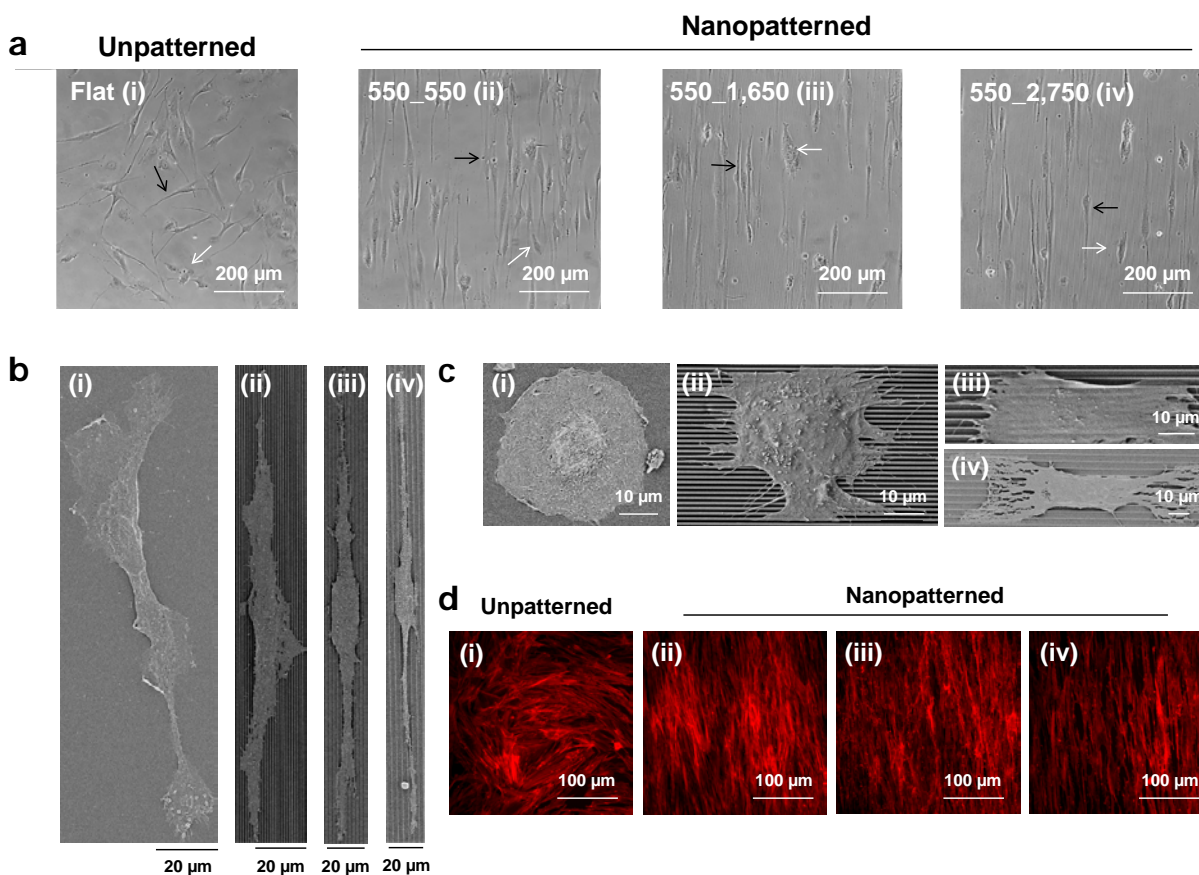


**Figure 7.2. Effects of nanopatterned matrix on the morphology and orientation of hMSCs and HUVECs.** (a) Representative phase-contrast images of hMSCs and HUVECs cultured on the substrata for 14 h. The black and white arrows indicate the hMSCs and the HUVECs, respectively. Representative SEM images of (b) hMSCs and (c) HUVECs on the substrata. (d) Representative immunostaining images of F-actin (red) in co-culture systems, showing aligned cytoskeletal structure of cells on the nanopatterned matrix.

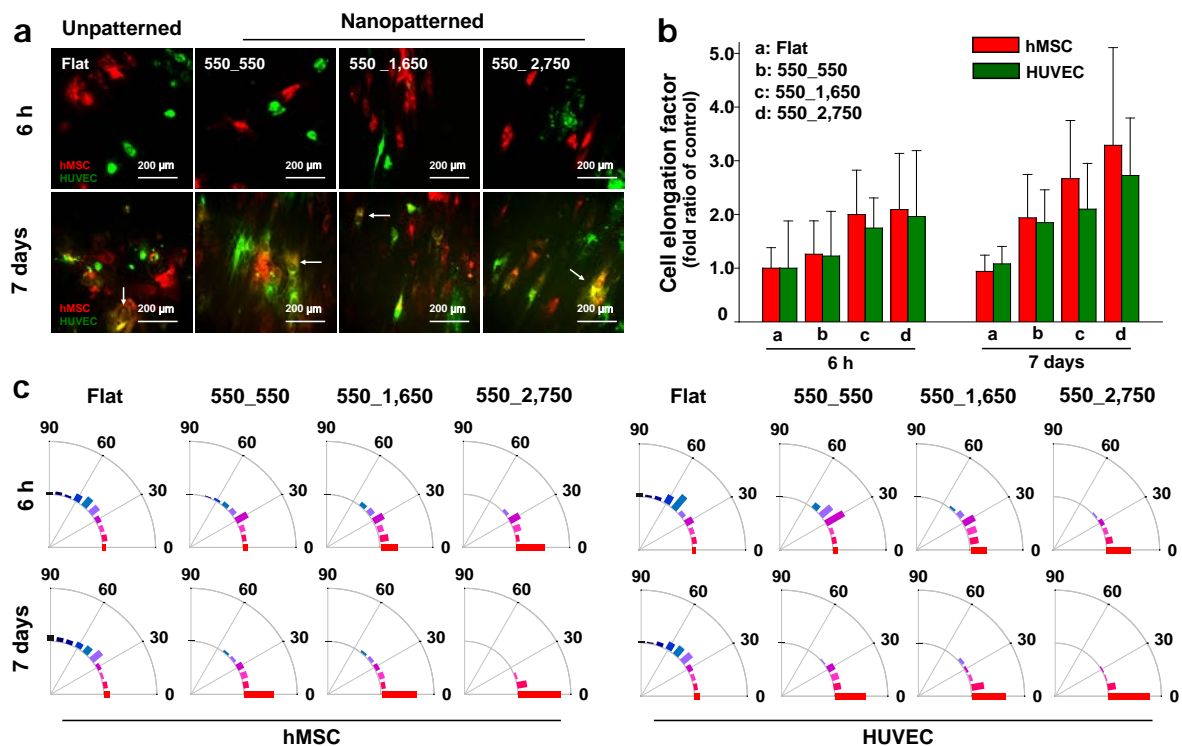


**Figure 7.3. Time-dependent morphology and orientation of hMSCs and HUVECs guided by nanopatterned matrix.** (a) Representative fluorescence images of hMSC-HUVEC co-cultures on the substrata, showing the initial cell adhesion (6 h) and proliferated cells (7 days). The hMSCs and the HUVECs were labeled with red and green fluorescence, respectively. (b) Quantification of cell elongation, indexed by axial ratio of cell width and length; the cell elongation factors were normalized to the axial ratio of cells on the flat substrata. (c) Quantification of cell orientation. Each bar represents relative probability corresponding to the polarized angle of cell body. Here, orientation of  $0^\circ$  represents perfect alignment with the ridge/groove direction. Results are quantified from 50 - 100 cells. Error bars represent the standard deviation.

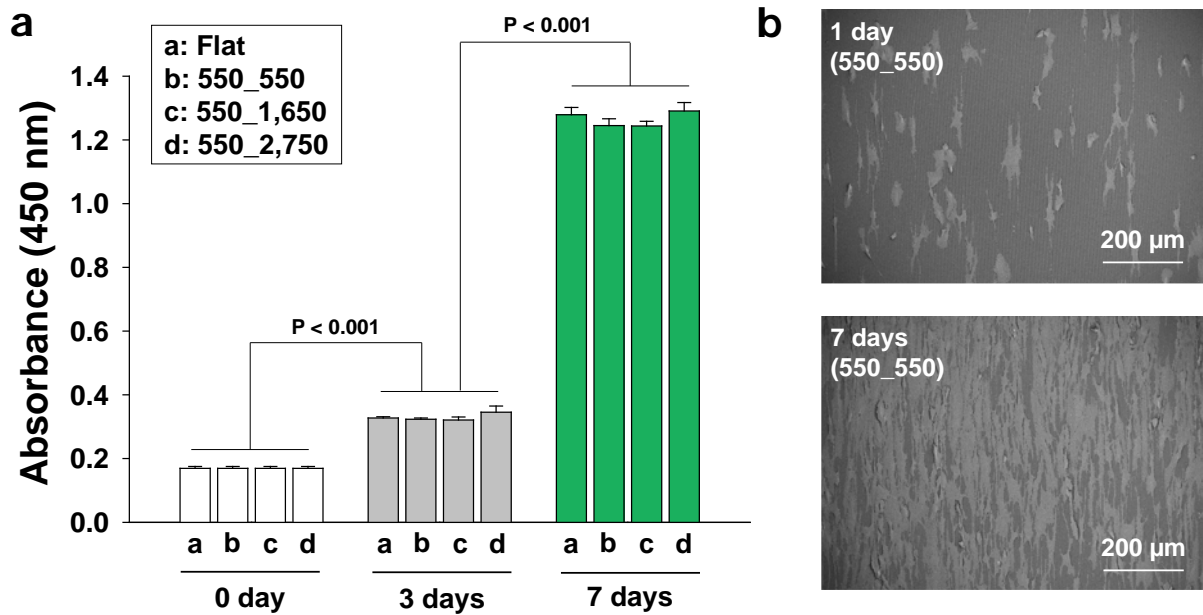


**Figure 7.4. Proliferation of cells on nanopatterned matrix in co-culture systems for 7 days.** (a) Viability of cells on the nanopatterned and flat substrata for 3 and 7 days after cell seeding (day 0). The cells in all samples show time-dependent cell viability for 7 days ( $p < 0.05$ ). Three independent experiments were conducted, and the error bars represent the standard deviation. (b) Representative SEM images of adhered cells (1 day) and proliferated cells (7 days).



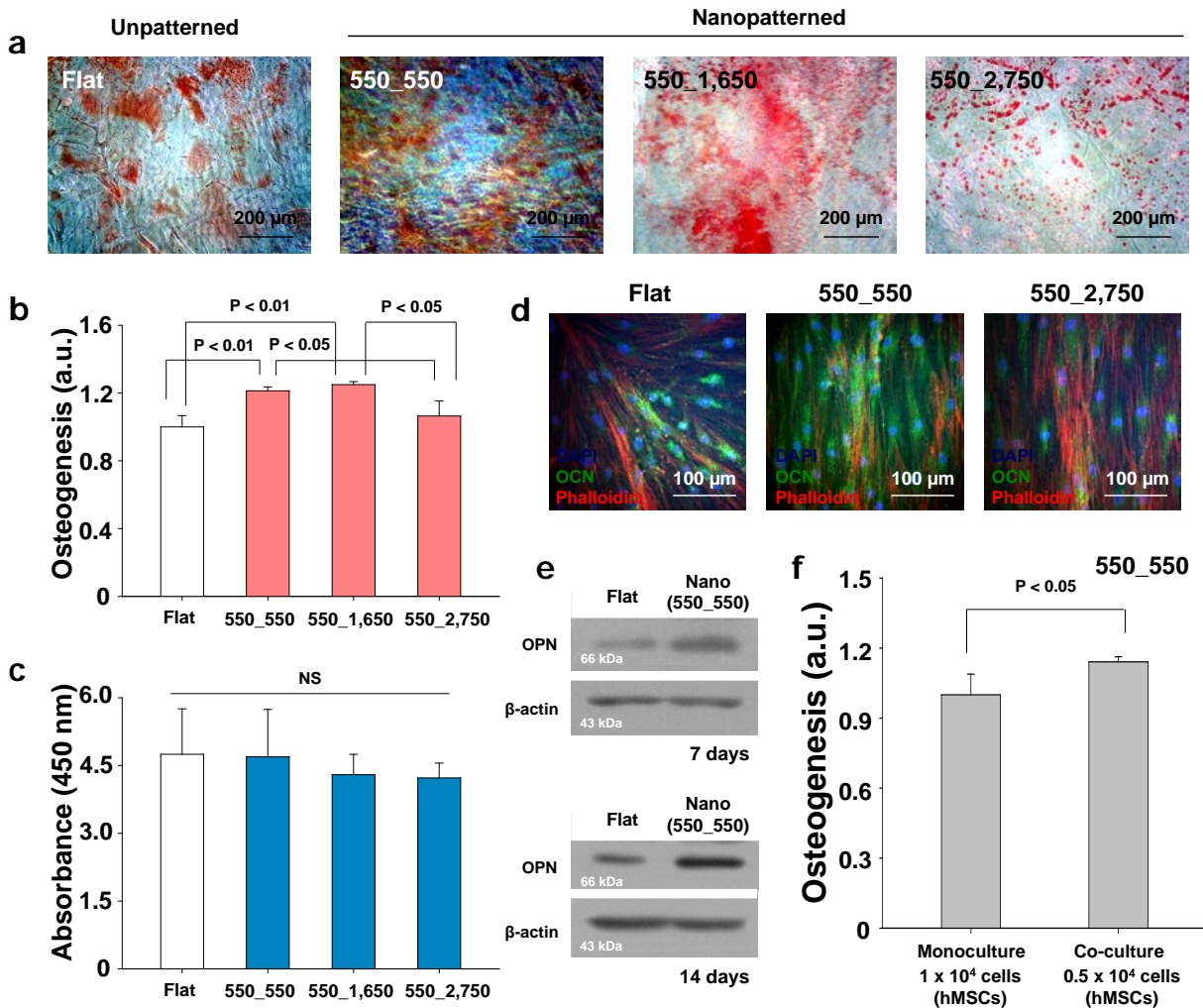


**Figure 7.5. Osteogenesis of hMSCs on nanopatterned matrix in co-culture with HUVECs.** (a) Representative images of Alizarin Red S staining. Cells were cultured on the nanopatterned and flat substrata in osteogenic media for 21 days. (b) Quantification of the degree of mineralization as measured by Alizarin Red S staining and (c) cell viability (i.e., cell number) at day 21. All values were normalized to the flat substrata. Error bars represent the SD about the mean ( $n = 3$  for each group). (d) Representative immunostaining images of OCN (osteogenesis marker; green) of hMSCs cultured on the substrata in co-culture with HUVECs in osteogenic media for 7 days. (e) Western blot analysis of OPN expression in hMSCs cultured on the substrata in monoculture system for 7 and 14 days, respectively. (f) Comparison of the osteogenesis of hMSCs on the nanopatterned substratum in the mono- and co-culture systems. Error bars represent the SD about the mean ( $n = 3$  for each group).

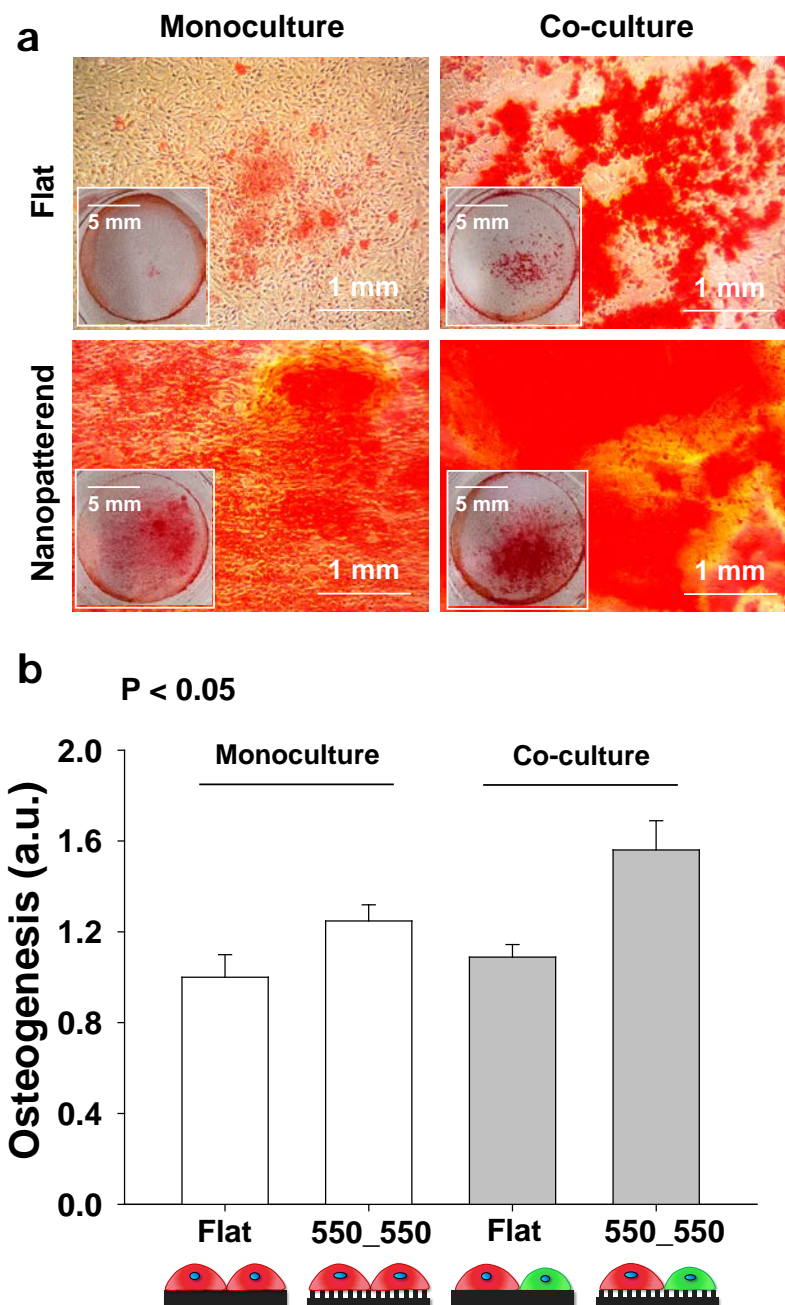


**Figure 7.6. Synergistically enhanced osteogenesis of hMSCs on nanopatterned matrix in co-culture with HUVECs.** (a) Representative images of Alizarin Red S staining cells cultured on the nanopatterned and flat substrata in mono- and co-culture systems. (b) Quantification of the degree of mineralization as measured by Alizarin Red S staining. Error bars represent the SD about the mean ( $n = 3$  for each group). All values were normalized to the flat substrata. In the illustrations, the red and green colors indicate hMSCs and HUVECs, respectively.

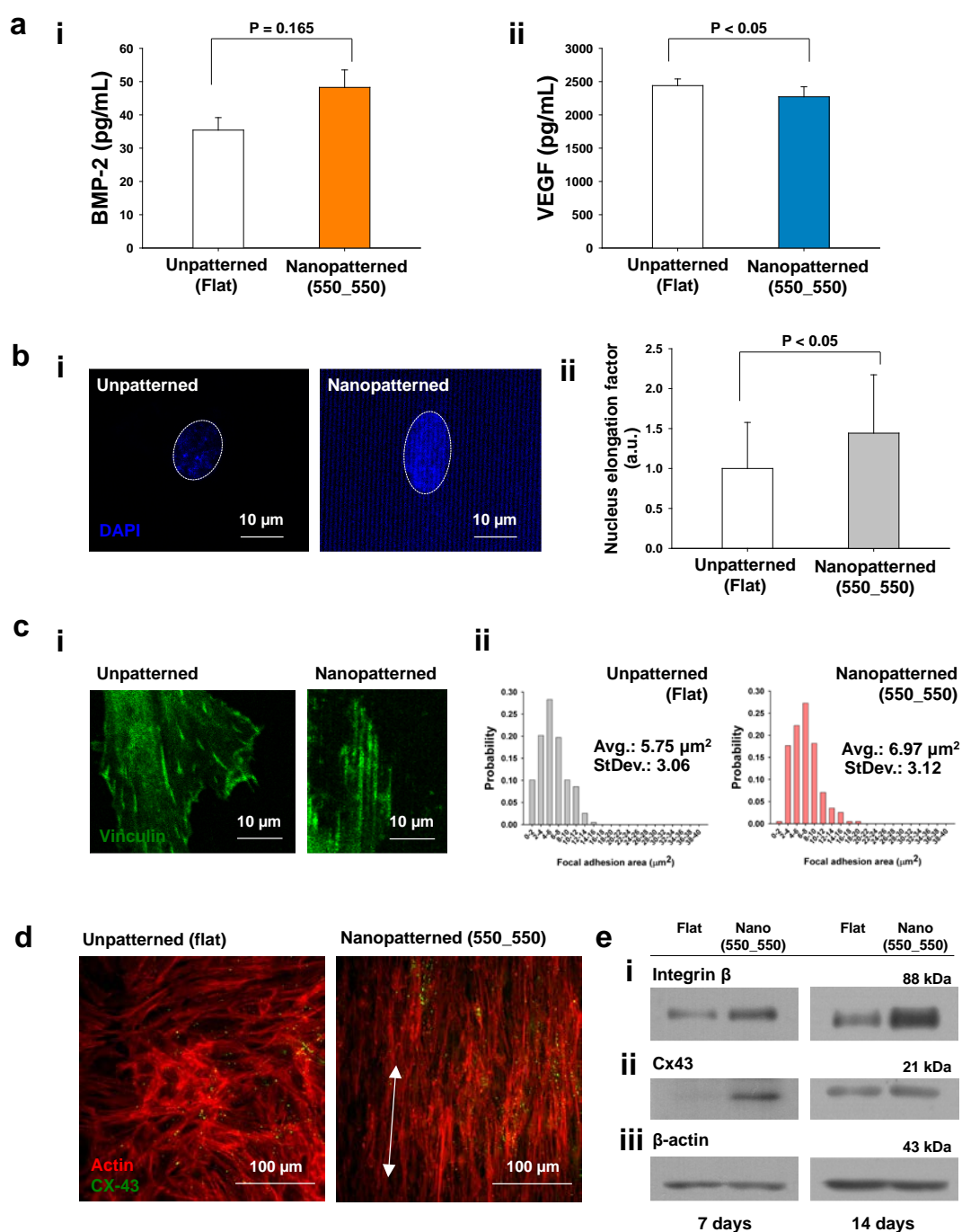


**Figure 7.7. Synergistically enhanced osteogenesis of hMSCs on nanopatterned matrix in co-culture with HUVECs.** (a) Representative images of Alizarin Red S staining cells cultured on the nanopatterned and flat substrata in mono- and co-culture systems. (b) Quantification of the degree of mineralization as measured by Alizarin Red S staining. Error bars represent the SD about the mean ( $n = 3$  for each group). All values were normalized to the flat substrata. In the illustrations, the red and green colors indicate hMSCs and HUVECs, respectively.

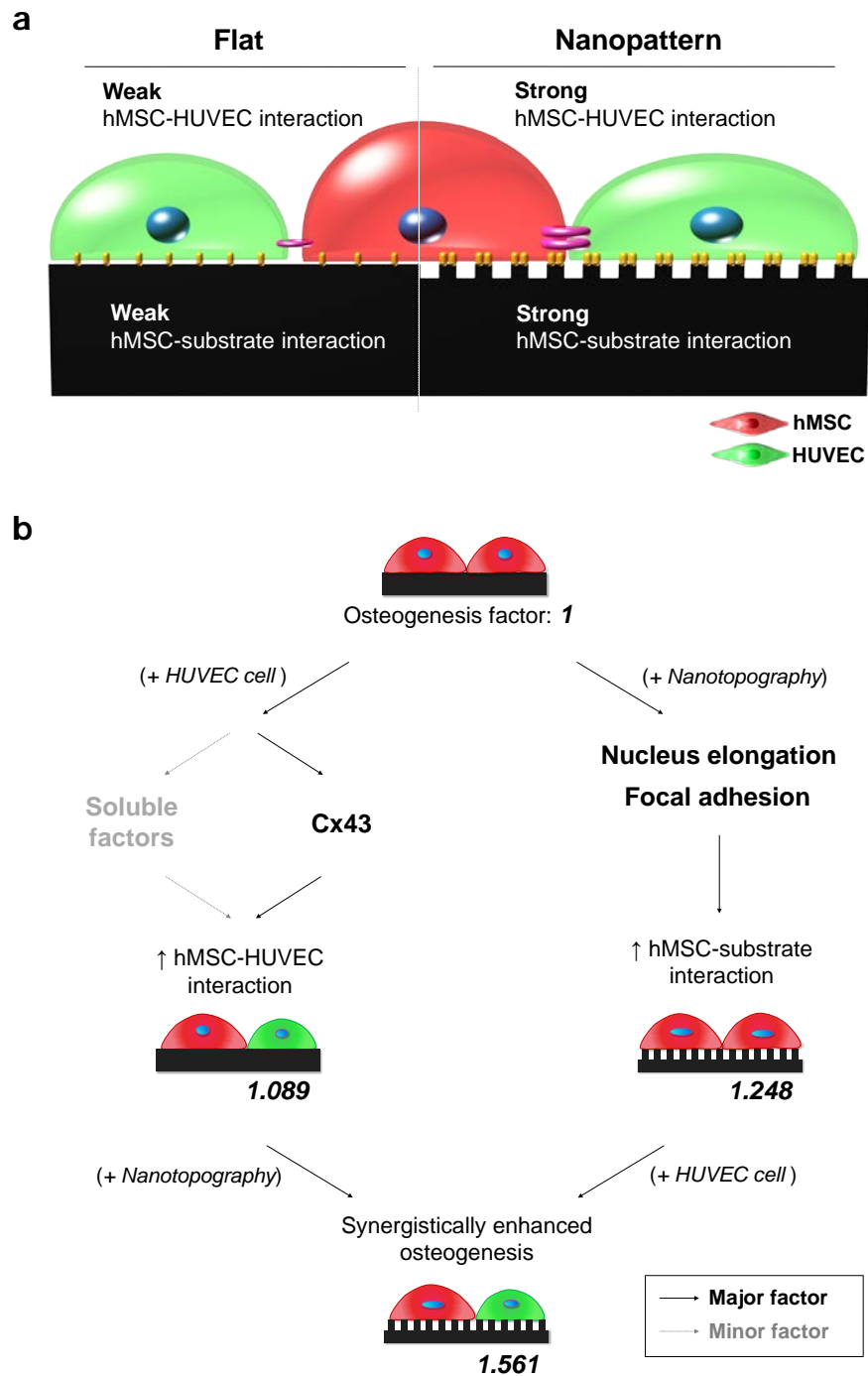


**Figure 7.8. A model for the synergistically enhanced osteogenesis of hMSCs on nanopatterned matrix in co-culture with HUVECs.** (a) Graphical representation of the relative enhancement of cell-cell and cell-substrate interactions. The presence of nanopatterns might enhance both cell-cell and cell-substrate interactions. Quantified improvements from both effects are displayed in (b). (b) A model for the decoupled and synergistic effects of cell-cell and cell-substrate interactions. The relative improvements are displayed with osteogenesis factor value.

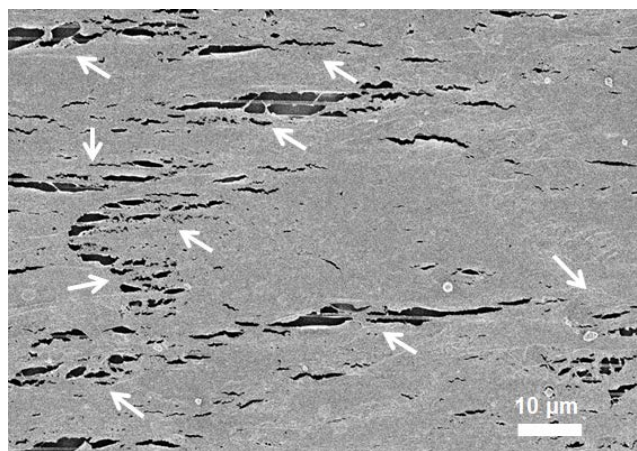


**Figure 7.S1. High magnification SEM image of hMSCs and HUVECs cultured on the nanopatterns showing aligned cells with interconnected structures. The white arrows indicate the intercellular junctional structures of cells.**

## **Chapter 8. Multiscale Patterned Transplantable Stem Cell Patches for Bone Tissue Regeneration**

### **8.1. Summary**

Stem cell-based therapy has been proposed as an enabling alternative not only for the treatment of diseases but also for the regeneration of tissues beyond complex surgical treatments or tissue transplantation. In this study, we approached a conceptual platform that can integrate stem cells into a biocompatible multiscale patterned substrate for bone regeneration. Inspired by human bone tissue, we developed hierarchically micro- and nanopatterned transplantable patches as synthetic extracellular matrices by employing capillary force lithography in combination with a surface micro-wrinkling method using a biocompatible poly(lactic-co-glycolic acid) (PLGA) polymer. The multiscale patterned PLGA patches were highly flexible and showed higher tissue adhesion to the underlying tissue than did the single nanopatterned patches. In response to the anisotropically multiscale patterned topography, the adhesion and differentiation of human mesenchymal stem cells (hMSCs) were sensitively controlled. Furthermore, the stem cell patch composed of hMSCs and transplantable PLGA substrate promoted bone regeneration *in vivo* when both the micro- and nanotopography of the substrate surfaces were synergistically combined. Thus, our study concludes that multiscale patterned transplantable stem cell patches may have a great potential for bone regeneration as well as for various regenerative medicine approaches.

### **8.2. Introduction**

Stem cells are capable of differentiating into various types of cells, offering opportunities and alternatives not only for the treatment of diseases but also for the regeneration of tissues and

organs beyond complex surgical treatments or tissue/organ transplantation [1-5]. Therefore, developing a viable and practical stem cell-based therapy for clinical applications is important. The most commonly proposed stem cell therapy in current clinical trials is to inject autologous stem cells isolated from a patient into the targeted area after expanding sufficient numbers of stem cells *in vitro* [3-5]. However, this strategy has critical limitations [1-5]: (i) the efficiency of transplanted stem cells located in the targeted area is very low (i.e. cells could easily be washed from the targeted tissues), and (ii) the transplanted stem cells often fail to maintain their viability and function in the host tissues, which has resulted in only limited success in restoring the damaged tissues and organ, especially in large scale tissue repair or regeneration. Consequently, an efficient platform that could help transplanted stem cells to integrate into host tissues effectively is urgently needed in order to achieve the goal of tissue repair and regeneration.

The construction of synthetic extracellular matrices (ECMs) inspired by tissue-specific niches for programmed stem cell fate and response, such as proliferation and differentiation, is a topic of interest in the field of tissue regeneration [6,7]. For example, inspired by the highly oriented topographical features of natural ECMs in various tissues, including bone, tooth, nerve, skin, muscle, and heart, previous studies have developed nanogrooved matrices using nanofabrication technologies, demonstrating a critical role for topographical cues in the controlled structure and functions of stem cells [8-14]. Importantly, the nanotopographical cues could reportedly promote the differentiation of stem cells; for example, nanogrooved matrices enhanced the osteo- or neurogenesis of human mesenchymal stem cells (hMSCs) compared to a flat substrate or microgrooved matrices [8,9,12]. In conjunction with the significant findings mentioned above, a platform that can integrate stem cells into synthetic ECMs (called a ‘stem cell patch’) has been newly proposed as an approach that facilitates the repair or regeneration of

tissues [15,16].

Despite growing interest in the use of synthetic ECMs for stem cell therapy for clinical applications, further mimicking the complexity of ECMs remains a pressing challenge to improve such platforms. Most studies have examined simple topographical designs for fabricating synthetic ECMs (i.e. single-scale micro- or nanotopography), partly because of limited fabrication techniques. However, native ECMs are composed of complex and hierarchical structures with various sizes ranging from nanometers to micrometers [8,17,18]. For example, individual collagen fibrils in ECMs tend to be approximately a few hundred nanometers in size, whereas actual collagen fibers formed by multiple fibrils are a few tens of micrometers in size [19]. Thus, the hierarchically micro- and nanotopographical cues from the ECM structures where cells populate *in vivo* may be an essential element for regulating or improving stem cell fate and function, which may be an important factor to consider for the design and manipulation of synthetic ECMs. In addition, the enhanced tissue bonding ability of synthetic ECMs may provide another opportunity for improving stem cell-based therapy, i.e. it may allow precise tissue adaptation and bonding to the underlying tissue, which could eventually promote topography-induced spontaneous tissue regeneration as well as enhance the efficiency of transplanted stem cells in the targeted area.

Here, we propose the rational design and manipulation of transplantable substrates as a synthetic ECM to meet the challenges mentioned above for advanced stem cell therapy. As a key design criterion for more physiologically relevant ECMs, hierarchically micro- and nanopatterned multiscale topographies with precisely controlled sizes were developed by employing capillary force lithography in combination with a surface micro-wrinkling method using a Food and Drug Administration (FDA)-approved poly(lactic-co-glycolic acid) (PLGA)



polymer due to its biocompatibility and biodegradability. Using these platforms, we investigated the influence of multiscale hierarchical topography on the adhesion, proliferation, and differentiation of stem cells. Furthermore, multiscale patterned transplantable stem cell patches were proposed as an approach for bone regeneration.

### **8.3. Materials and methods**

#### **8.3.1. Preparation and observation of *ex vivo* human bone tissue**

Bone tissue was obtained from a patient during dental surgery under the approval of the Institutional Review Board of Seoul National University (Seoul, Korea). The tissue was fixed overnight with a solution containing 2% glutaraldehyde, 0.1 M sodium cacodylate, and 3 mM calcium chloride (pH 7.4) at 4°C. The tissue was rinsed three times with PBS. The specimen was perfused with 1% osmium tetroxide and placed on a tissue rotator for 30 min. The sample was then rinsed three times in PBS. Subsequently, the sample was serially dehydrated in 50%, 70%, 90%, 95%, and 100% acetone. The sample was treated with hexamethyldisilazane (HMDS), air dried, and placed on a stub for sputter-coating with gold. The tissue was then observed with a FESEM (JEOL, JSM-5410LV, Japan).

#### **8.3.2. Fabrication of PUA mother mold**

Fig. 8.S1 shows the schematic procedure for fabricating a multi-scale patterned poly(urethane acrylate) (PUA) mother mold (350 nm ridge and groove width). A droplet of UV-curable PUA (Minuta Tech., Korea) precursor solution with photo-initiator was dropped on the silicon master mold, on which nanosized linear grooves (350 nm) were etched using conventional

photolithography and reactive ion etching. The mold was then uniformly covered with a transparent poly(ethylene terephthalate) (PET) film utilizing capillary force. After the master was exposed to UV light ( $\lambda = 250 \sim 400$  nm,  $100 \text{ mJ/cm}^2$ ) for 15 sec, the cured PUA replica was peeled off from the master mold using tweezers and again exposed to UV light for 10 h to completely annihilate any residual reactive acrylate groups.

### **8.3.3. Design and fabrication of multiscale PUA mold**

First, PDMS pre-polymer (Sylgard 184 Silicon elastomer, Dow corning) was mixed with 10% curing agent, poured into a petri dish to a sufficient thickness ( $\sim 1$  cm), and baked at  $70^\circ\text{C}$  for at least 2 h to ensure curing without any residue. The polymer was then peeled off from the petri dish and oxidized with UV/ozone treatment system (Yuil Ultra Violet system, Korea) in 5 min and 15 min for  $30 \mu\text{m}$  and  $100 \mu\text{m}$  wavelength respectively. To ensure uniform oxidation, the distance from the UV lamp was constant at 5 cm. The dose of UV/ozone was  $15 \text{ mW/cm}^2$  (measured at a 10 mm distance) at wavelengths of 185 and 254 nm. Thereafter, a small quantity of 10% (w/v) adhesion promoter TMSPMA ( $100 \mu\text{L}$ ) was drop-dispensed onto the UV/ozone-treated PDMS sheet and spread evenly using a spin coater set to 3000 RPM, after which the sheet was baked for 1 h to dry the promoter (Fig S1; Step 1). Subsequently,  $100 \mu\text{L}$  of PEG-DA (Sigma-Aldrich) precursor solution was drop-dispensed and covered with the prepared PUA mother mold ( $350 \text{ nm}$  ridge and groove width). The assembly was pressed at 0.7 bar for 1 h. After UV curing for 5 min, the PUA mother mold was carefully peeled off using tweezers (Fig 8.S1; Step 2). Second, based on the study of wrinkle phenomena, 10% compressive strain was then applied using a custom-designed strain apparatus resulting  $30 \mu\text{m}$  (5 min UV/ozone) or  $100$  ( $15 \text{ min UV/ozone}$ )  $\mu\text{m}$  wavelength. To replicate multiscale structures ( $350 \text{ nm}/30 \mu\text{m}$  and  $350$

nm/100  $\mu\text{m}$ ) on PDMS, a PUA precursor was drop-dispensed and UV-cured for use as a self-replicating mold (Fig S1; Step 3). Finally, additional UV-curing was performed for more than 10 h to remove any non-cured acrylate groups.

#### **8.3.4. Fabrication of multiscale patterned PLGA substrates**

A 3% (w/v) solution of PLGA prepared in chloroform (200  $\mu\text{l}$ ) was drop-dispensed onto the PDMS block, and a flat PDMS upper block was placed to obtain a smooth PLGA film layer and remove the solvent. Subsequently, the PDMS block was preheated on a hot plate to remove additional solvent. A multiscale patterned PUA mother mold (350 nm ridge and groove width on a 30  $\mu\text{m}$  or 100  $\mu\text{m}$  wavelength) was then placed on the preheated PLGA film and embossed into the molten PLGA by applying constant pressure ( $\sim 0.7$  bar) while heating at 100°C for 10 min (glass transition temperature ( $T_g$ ) of PLGA = 59°C). After the thermal imprinting process, the assembly of the PDMS block and mother mold was cooled to room temperature, and the mold was peeled off the substrate resulting in multiscale patterned PLGA substrates with 350 nm ridge and groove width on a 30  $\mu\text{m}$  or 100  $\mu\text{m}$  wavelength.

#### **8.3.5. Surface property of multiscale patterned PLGA substrates**

The static contact angles (CAs) of liquids used in the experiment were measured using DSA100 goniometer (Kruss, Germany). For each measurement, 10  $\mu\text{l}$  of liquid was drop-dispensed on the surface over a time span of 1 min. The measurement was averaged over at least ten different locations for each sample condition.

High-resolution scanning electron microscopy (SEM) images of the nanometer sized PUA and PLGA structures were obtained using a HITACHI S-4800 microscope (Hitachi, Japan)

at an acceleration voltage of 10.0 kV and an average working distance of 11.4 mm. To avoid charging effects, the substrates were sputter-coated with Au to a thickness of 3 nm prior to the measurements.

#### **8.3.6. Measurement of adhesion force with porcine small intestine**

The macroscopic normal and shear adhesion forces of multiscale PLGA patches against the porcine small intestine surface were measured using custom-built equipment. Prior to the adhesion test, fresh porcine intestine tissue was rinsed several times with DI water and then placed onto a gel ice pack to prevent spoiling. A PLGA patch (area:  $1 \times 1 \text{ cm}^2$ ) was then attached to the surface of the small intestine under a preload of  $\sim 0.5 \text{ N/cm}^2$ , and the adhesion force was measured by gradually increasing the pulling weight until adhesion force failure occurred. To ensure statistical significance, the adhesion force was measured 30 times for each sample under identical conditions at a relative humidity of 40% and ambient temperature of  $25^\circ\text{C}$ , and the averaged data were used throughout the experiment.

#### **8.3.7. Isolation and culturing of hMSCs**

The experimental protocol was approved by the Institutional Review Board of the Seoul National University (Seoul, Korea), and the detailed method to isolate hMSCs has already been reported by our group [20]. The bone segments were digested in a solution of 3 mg/ml collagenase type I and 4 mg/mL dispase for 1 hour at  $37^\circ\text{C}$ . Single-cell suspensions were obtained by passing the cells through a  $70 \mu\text{m}$  cell strainer (Falcon, BD Labware, Franklin Lakes, NJ) [20]. All cells used in this study were at passage 3 or 4.

#### **8.3.8. Immunofluorescence staining**

Adhered cells on samples were fixed with a 4% paraformaldehyde solution (Sigma-Aldrich, Milwaukee, WI, USA) for 20 min, permeabilized with 0.2% Triton X-100 (Sigma-Aldrich, WI, Milwaukee, USA) for 15 min, and stained with TRITC-conjugated phalloidin (Millipore, Billerica, MA, USA) and 4, 6-diamidino-2-phenylindole (DAPI; Millipore, Billerica, MA, USA) for 1 h. The FAs were also stained with a monoclonal anti-vinculin antibody (1:100; Millipore, Billerica, MA, USA) and a FITC-conjugated goat anti-mouse secondary antibody (1:500; Millipore, Billerica, MA, USA). The images of the stained cells were taken using a fluorescence microscope (Zeiss, Germany). For the quantitative analysis of the body and nuclear shape of hMSCs on the substrata, the images obtained by fluorescence microscopy were analyzed using a custom MATLAB script.

#### **8.3.9. SEM observation of cells**

Cells that adhered onto the sample surfaces were fixed with modified Karnovsky's fixative consisting of 2% paraformaldehyde and 2% glutaraldehyde (Sigma-Aldrich) in a 0.05 M sodium cacodylate buffer (Sigma-Aldrich) for 4 h. The samples were washed 3 times with 0.05 M sodium cacodylate buffer for 10 min and fixed with 1% osmium tetroxide (Sigma-Aldrich). The samples were then washed with distilled water and dehydrated with graded concentrations (50, 70, 80, 90, and 100% v/v) of ethanol. The samples were then treated with hexamethyldisilazane (Sigma-Aldrich) for 15 min. Finally, the samples were coated with gold prior to cell shape observation with FESEM (JEOL, JSM-5410LV, Japan).

#### **8.3.10. Proliferation analysis**

hMSCs ( $4 \times 10^4$  cells/samples) were seeded onto samples and cultured for up to 7 days in DMEM (Sigma-Aldrich, Milwaukee, WI, USA) containing 10% FBS (Sigma-Aldrich, Milwaukee, WI, USA) and 1% antibiotics (Sigma-Aldrich, Milwaukee, WI, USA) at 37°C in a humidified atmosphere containing 5% CO<sub>2</sub>. The quantitative analysis of the cell proliferation on the substrates was performed using a WST-1 assay (EZ-Cytox Cell Viability Assay Kit, Daeillab Service Co., LTD).

#### **8.3.11. Osteogenesis analysis**

hMSCs ( $4 \times 10^4$  cells/sample) were cultured for 14 days on the samples in osteogenic differentiation medium (100 nM dexamethasone, 50 µM ascorbic acid, and 10 mM glycerol 2-phosphate in normal media). Alizarin Red S (Sigma-Aldrich) staining was used to confirm the osteogenic differentiation of hMSCs on the sample surfaces. The degree of mineralization was measured by staining hMSCs cultured on the sample surfaces with Alizarin Red S. The stained cells were de-stained with cetylpyridinium chloride (Sigma-Aldrich), and the extracted stains were then measured using an ELISA reader (VERSAMAX reader, Molecular Devices, Sunnyvale) at 540 nm to quantify the osteogenic differentiation of hMSCs.

#### **8.3.12. *In vivo* animal study**

All experiments using animals in these studies followed protocols approved by the Institutional Animal Care and Use Committee of the Seoul National University. Ten healthy immunocompromised mice (NIH-bg-nu/nu-xid, Harlan Sprague Dawley, Indianapolis, IN, USA) were used as experimental animals. After intraperitoneal anesthesia with tiletamine-zolazepam (Zoletil 50, Virbac Laboratory, Carros, France) and xylazine (Rompun, Bayer, Canada), the

skulls were shaved and disinfected. An approximately 10-mm incision was made on the skin of the dorsal region of the skull to expose the parietal bone. A calvarial hole defect was created in the parietal region using a trephine bur with a diameter of 5 mm, and the intact meninges was exposed. The wound was irrigated with sterilized saline and bleeding was controlled. Approximately  $2.0 \times 10^6$  adherent hMSCs were expanded on each patch for 24 h at 37°C in a 5% CO<sub>2</sub> humidified atmosphere. After the incubation, the cells were transplanted and placed on the calvarial defects beneath the skin. An equal number of *ex vivo* expanded cells with 0.5% fibrin-gel were transplanted into the calvarial defects in the cells only group, and only fibrin-gel was inserted into the defect area in the control group. Subsequently, the skin was sutured, and a post-operative dressing was applied. Bone biopsies, including the defect region and the lateral side of the calvarial bone, were obtained 4 weeks after surgery. The biopsies were fixed in 4% paraformaldehyde and decalcified in a 10% EDTA (pH 7.4) solution at 4°C. The specimens were embedded in paraffin, sliced into 5 µm-thick sections and stained with hematoxylin and eosin (H&E).

### **8.3.13. Statistical analysis**

All quantitative results are presented as the mean  $\pm$  standard deviation (SD), and unpaired Student's t-tests were used for statistical analysis.

## **8.4. Results**

### **8.3.1. Design and fabrication of multiscale PLGA substrates as a synthetic ECM**

To manipulate a transplantable multiscale patterned synthetic ECM, a methodology to fabricate micro- and nanopatterned hierarchical PLGA substrates with tunable topographical structures

and sizes was first developed by combining capillary force lithography and the surface micro-wrinkling method (Fig. 1). To design the topographical features of native ECM in our body, we examined the tissue organization in detail using an ultra-structural analysis of *ex vivo* human bone tissue, which showed naturally anisotropic ECM structures of various length scales (Fig. 8.1a). Interestingly, the protein fibers in ECMs formed by multiple nanoscale fibrils tended to show microgrooved structures that were approximately a few tens of micrometers in size. This observation suggested that the micro- and nanoscale hierarchical structures in human bone tissue may provide specific topographical cues that guide the fate and function of stem cells during bone repair or regeneration. Thus, we hypothesized that well defined hierarchically nanopatterned topography would provide a more physiologically relevant cellular environment that can improve stem cell-based therapy.

To fabricate hierarchically micro- and nanopatterned biocompatible PLGA substrates, PUA films with multiscale topography were prepared to be used as a master mold (see Fig. 8.S1 in detail). Fig. 8.1b shows a schematic of the fabrication of multiscale hierarchical PLGA substrates (see the detailed produce in Materials and methods). As shown in Fig. 8.1c, the fabricated PLGA substrate was confirmed to contain well-defined multiscale hierarchical structures (i.e. microgrooves with a nanoscale ridge/groove structure), which was similar to the naturally anisotropic ECM structures in human bone tissue (Fig. 8.1a).

### **8.3.2. Characteristics of multiscale PLGA patches**

The cross-sectional SEM images clearly showed the micro- and nanopatterned hierarchical topography (Fig. 8.2a). Interestingly, the multiscale topography of patches enhanced the hydrophilicity of the surface compared to flat or nanopatterned substrates (Fig. 8.2b). The



multiscale PLGA patches of controlled sizes were highly flexible and thin ( $\sim 20 \mu\text{m}$ ), showing highly bent nanostructures on microgrooves (Fig. 8.1c and Fig. 8.S2). We showed that these properties allowed the PLGA patches to attach well to the intestine surface, exhibiting conformal contact with the curved surface of the biological tissue (Fig. 1d). To analyze the effect of micro- and nanopatterned hierarchical topography on the tissue bonding performance in detail, we measured the normal and shear adhesion forces of the PLGA patches against a real intestine tissue surface under a preload of  $\sim 0.1 \text{ N cm}^{-2}$  using custom-built equipment (Fig. 3a). As shown in Fig. 3b, the multiscale patterned patches displayed large normal ( $\sim 0.9 \text{ N cm}^{-2}$ ) and shear ( $\sim 2.3 \text{ N cm}^{-2}$ ) adhesion forces compared to the nanopatterned single-scale patches (i.e. normal ( $\sim 0.7 \text{ N cm}^{-2}$ ) and shear ( $\sim 1.7 \text{ N cm}^{-2}$ ) adhesion forces), likely due to the enlarged surface area and enhanced ability to form conformal contacts via the synergistic effects of micro- and nanoscale hierarchical topography. Together, our results demonstrated that micro- and nanopatterned hierarchical PLGA patches were successfully fabricated and could be used as a synthetic ECM to modulate stem cell behaviors and repair or regenerate tissue *in vivo*.

### 8.3.3. Morphology and orientation of hMSCs by multiscale topography

Using the micro- and nanopatterned hierarchical patches as cell culture substrates, we explored the role of hierarchical topography, which may direct the behavior of stem cells. To this end, we fabricated two types of micro- and nanopatterned hierarchical substrates (350 nm ridge and groove width on a 30  $\mu\text{m}$  or 100  $\mu\text{m}$  wavelength) as well as flat (unpatterned) and nanopatterned substrates (350 nm ridge and groove width) as controls. We cultured hMSCs on the substrates for 14 h (Fig. 8.4). Over the first 3 h after cell seeding, the hMSCs on the patterned substrates were well-attached and aligned along the topographical direction, whereas cells were not fully

attached on the flat substrate (Fig. 8.4a), suggesting that micro- and nanotopography could enhance the initial attachment of stem cells. After 14 h of culture, well-attached hMSCs were observed on the flat substrate, but these cells maintained a random shape and orientation, whereas hMSCs on the patterned substrates continuously showed a highly aligned and oriented morphology (Fig. 4a and S3). The cells on pure micropatterned substrates were less aligned and oriented compared to those on the multiscale or nanopatterned substrates (data not shown).

We examined the observed cellular orientation and shape on multiscale patterned substrates in further detail via quantitative analysis (Fig. 8.4b and c). As shown in Fig. 4b, the multiscale topography strongly influenced the hMSC orientation, as also supported by the aligned cytoskeletal structures and nucleus structures of hMSCs in response to the micro- and nanotopography (Fig. 8.4d and Fig. 8.S4). Interestingly, compared to the hMSC orientation on nanopatterned substrates, the hMSCs on 350 nm/30  $\mu$ m substrates orientated more strongly along the direction of patterns, whereas the hMSCs on 350 nm/100  $\mu$ m substrates were less orientated (Fig. 8.4b). The cellular morphologies defined by width, length, perimeter, and area were continuously quantified (Fig. 8.4c). The hMSCs on the multiscale patterned substrates were considerably smaller than those on the nanopatterned ones. Specifically, the hMSCs on 350 nm/100  $\mu$ m substrates were significantly longer than those on the 350 nm/30  $\mu$ m substrates (Fig. 8.4c and d). As shown in Fig. 4e and f, the cytoskeletal structures of hMSCs were nanotopographically organized on the multiscale patterned substrates. Our SEM analysis clearly showed that the 350 nm/100  $\mu$ m substrates promoted hMSC alignment more readily than the 350 nm substrates (Fig. 8.4g and h). Together, these data indicate that the multiscale topography can control the morphology and orientation of hMSCs.

#### **8.3.4. Proliferation and osteogenesis of hMSCs by multiscale topography**

To investigate whether the micro- and nanopatterned hierarchical topographies influence the proliferation of stem cells, we cultured hMSCs on the flat, nanopatterned (350 nm), and two types of multiscale patterned (350 nm/30  $\mu$ m (i.e. small microscale) and 350 nm/100  $\mu$ m (i.e. large microscale)) substrates for 7 days. The cells on the substrates proliferated well irrespective of the topographical properties, whereas no significant difference was found among the flat, nanopatterned, and multiscale patterned substrates (Fig. 8.5a). This result reveals that anisotropic multiscale topographic cues may not alter cell proliferation from that observed with flat or single patterned culture surfaces.

Because naturally hierarchical structures were observed in human bone (Fig. 8.1a), we assessed the effect of micro- and nanopatterned hierarchical topography on the osteogenesis of stem cells. To this end, we cultured hMSCs on the substrates in osteogenic induction medium for 14 days. The osteogenesis of hMSCs was analyzed based on the mineralization. The images of Alizarin Red S staining demonstrated that the calcium expression was higher on the patterned substrates than on the flat substrates (Fig. 8.5b). To quantify the degree of hMSC osteogenesis, the stained calcium deposits were de-stained, which demonstrated that the micro- and nanopatterned substrates exhibited higher osteogenesis than the flat substrates (Fig. 8.5b).

#### **8.3.5. *In vivo* bone regeneration by transplantation of multiscale stem cell patches into animal models.**

Developing a methodology to repair or regenerate bone to overcome current complex surgical treatments using alloplastic materials or autologous and allogeneic tissues remains a major challenge in current clinical trials [22]. Stem cell-based therapy has been considered a promising

strategy for engineering functional bone constructs [12,17]. Here, we proposed an approach for bone regeneration using stem cells and biomimetic ECMs. In this study, we showed that multiscale PLGA patches mimicking the hierarchically anisotropic ECM structures in human bone tissue could provide an efficient environment for the adhesion and osteogenesis of hMSCs and enhance the tissue bonding ability (Fig. 8.2-4). Thus, we hypothesized that a stem cell patch composed of hMSCs and nanopatterned hierarchical PLGA substrate would effectively guide bone regeneration.

To this end, we first integrated the hMSCs into flat, nanopatterned (350 nm) and multiscale patterned (350 nm/30  $\mu$ m) PLGA substrates by culturing them for 12 h *in vitro* in order to prepare stem cell patches. The stem cell patches were then engrafted onto a 5 mm diameter calvarial bone defect in nude mice (Fig. 8.5c). We evaluated the bone regeneration after 4 weeks of implantation. As shown in Fig. 8.5d, signs of infection or inflammation were not evident in any of the samples. The sectioned bony specimens were stained with H&E. The control groups showed non-specific fibrous healing in the defect site without any bony regeneration. Fibrous and some adipose tissue grew in the defect area. A few giant cells (the black arrow in Fig. 8.5d) were visible inside the heterogeneous fibrous tissue with no specific inflammatory changes. In the hMSC only group, a layer of fibrous tissue was generated at the cell-transplanted area. However, the thickness and density of the generated layer were irregular, which contained thin and loose tissue as well as thick and dense tissue due to the absence of the covering adhesives patches. The fibrous layer of the hMSC only group was generally thinner than that of the control group. Conversely, the hMSCs formed relatively thick fibrous layers in the flat and single nanopatterned patches; however, new bone formation could not be detected in either group (Fig. 8.5d). Surprisingly, the hMSCs integrated in multiscale hierarchical patches

induced the regeneration of new bone along the direction of micro- and nanopatterns at the margin of the hole defect (Fig. 8.5d). These results provide insight into the importance of multiscale topography in synthetic ECMs for guiding bone tissue regeneration.

## **8.5. Discussion**

Designing an effective platform that can control or improve cellular functions or construct artificial tissues is very important for the development of a viable and practical stem cell-based therapy for clinical applications [1-7,22-24]. Based on the concept of a “stem cell niche”, stem cells are thought to be exposed to very complex and controlled microenvironments, such as biochemical mixtures of soluble and insoluble factors [2,6-8,22-24]. In conjunction with these aspects, previous studies have focused on the fabrication of synthetic ECMs as a platform for stem cells, demonstrating that the fate and function of stem cells are sensitively regulated by the rigidity and topography of substrates [2,6,17]. Regarding fabricating platforms that mimic the topographical features of ECMs, most studies unfortunately largely neglected the hierarchical property of ECMs or included limited hierarchical topographical features because of technical limitations [8-16]. To address this challenge, we developed synthetic ECMs with hierarchically micro- and nanopatterned surfaces of precisely controlled sizes for stem cell-based therapy (Fig. 8.1-5).

In this study, we demonstrated for the first time a simple but robust method to manipulate FDA-approved PLGA multiscale substrates using capillary force lithography and the wrinkling technique (Fig. 8.1). Specifically, this technology can easily control the micro- or nanotopography sizes and structures with scalable and highly reproducible properties using various biomaterials. For example, while we have fabricated the hierarchically micro- and

nanopatterned PLGA substrates in this work, our method is expected to be applicable to other polymers, such as polycaprolactone (PCL) (Fig. 8.S5) and polyethylene glycol (PEG) (Fig. 8.S6), and other nanotopographical features.

Our *in vitro* study yielded two interesting findings in terms of the nanotopographical role of multiscale hierarchical structures in cellular behaviors. First, multiscale topographical cues can synergistically control cellular morphology along the direction of micro- and nanotopography (Fig. 8.4). In particular, the size features of the underlying micro-topography in micro- and nano-scale hierarchical structures influenced the cellular orientation and shape (Fig. 8.4b and h). Second, compared with the osteogenesis degree of hMSCs on nanopatterned substrates, the hMSCs on 350 nm/30  $\mu$ m substrates showed a similar degree of osteogenesis, whereas the osteogenesis of hMSCs on 350 nm/100  $\mu$ m substrates was significantly decreased. The osteogenesis of hMSCs on micropatterned substrates also significantly decreased compared to those on nano or multiscale patterned substrates (data not shown). This finding suggests that (i) nanotopography cues, as opposed to microtopography cues, may be the most crucial factor for the osteogenesis of hMSCs, and (ii) the size features of the underlying micro-topography may also be an important factor to determine stem cell differentiation, although additional in-depth studies remain necessary to understand the underlying molecular mechanism.

Kirmizidis *et al.* reported that microgrooved substrates decreased the osteoblast differentiation compared to flat substrates, even though the cells on the microgrooved substrates were highly elongated [21]. Conversely, we have learned that topographies whose features are a few tens of micrometers in size in our hierarchical platforms could allow cell elongation and resulted in the increased osteogenesis of hMSCs compared to the flat substrates. In other words, our current results suggest an important role of micro- and nano-scale topography: the interaction

or contact at the cell-substrate interface may be a more important factor for the regulation of stem cell differentiation than the elongated cell shape itself. As we observed the nanotopographically organized cytoskeletal structures of hMSCs on micro- and nanopatterned hierarchical substrates (Fig. 8.4d and e), the nanotopography on hierarchical structures in the living cell environments may play an important role in guiding stem cell function via cell-topography interaction.

Our *in vivo* study showed that the hMSCs integrated in multiscale PLGA patches could promote bone regeneration (Fig. 8.5d). Although in-depth studies are required to accurately understand the underlying mechanisms, this finding was proposed to be due to the following: (i) enhanced tissue bonding and (ii) enhanced osteogenesis of hMSCs due to the multiscale patterned topography (Fig. 8.5e and f). Compared to single-scale patterned patches, the multiscale patterned topography patches were easier to handle during surgical procedures. Moreover, the multiscale patterned topography-based patches provided more precise tissue adaptation and bonding to the defected bone tissue than single-scale patterned patches (Fig. 8.3). This finding suggests that the enhanced patch adhesion to the bony tissue surfaces might help to promote topography-guided spontaneous bone regeneration. In addition, our *in vitro* differentiation study showed that nanotopography was essential to promote the osteogenesis of hMSCs, likely due to the biomimetic topography cues of ECMs in the bone. Thus, the integrated hMSCs on the multi-scale patterned patches might be induced to begin osteogenesis, which eventually promotes bone regeneration.

Here, we propose other possible applications of our multiscale hierarchical substrates. First, this platform or technology may allow the fabrication of precisely defined micro- and nanopatterned substrates, which may be a strategy for the design and manipulation of functional

scaffolds for stem cell-based tissue regeneration. While we have focused on bone regeneration using nanopatterned hierarchical stem cell patches (Fig. 8.5), we could expect to manipulate engineered constructs to mimic the hierarchical topography of other tissues, such as skin, nerve, tooth, muscle, and heart, in combination with the use of appropriate biochemical factors (e.g. growth factor-conjugated nanopatterned hierarchical stem cell patches). Second, we propose that our nanopatterned hierarchical patches can be used for various biomedical applications, such as patch-type tissue adhesives, because we have demonstrated that hierarchical nanopatterned patches enhanced tissue adhesion to the underlying tissue compared to the single-patterned patches (Fig. 8.3). Thus, our methods can be used to design and fabricate a patch-type tissue adhesive in combination with chemical adhesive glues [25]. Third, this platform can be used as a tool to better understand the fundamental biology at the cell and tissue levels *in vitro* as well as to manipulate disease models or drug screen platforms by fabricating precisely defined micro- and nanopatterned hierarchical substrates of varying topography and stiffness. For example, a platform fabricated using our technology and appropriate materials (e.g. PUA with different stiffness) can be used to study the synergistic effects hierarchical topography and rigidity on cells.

Our study supports the notion that multiscale hierarchical topography can be used as an efficient strategy for the design and manipulation of synthetic ECMs for stem cell-based bone regeneration. Nanopatterned hierarchical transplantable patches with precisely defined architectures and sizes were fabricated via capillary force lithography in combination with a micro-wrinkling method using a biocompatible PLGA polymer. We propose that a type of synthetic ECM comprised of hierarchically multiscale structures could provide native ECM-like topographical cues for controlling the adhesion and differentiation of hMSCs. Interestingly, the



platform that integrates hMSCs into the multiscale hierarchical PLGA patch showed the potential to regenerate the bone tissues without complex surgical treatments. Our work provides insight into the design and manipulation of functional engineered constructs using multiscale hierarchical topography-based substrates for various biomedical applications, including stem cell therapy and tissue engineering.

## **8.6. References**

- [1] Strauer BE, Kornowski R. Stem cell therapy in perspective. *Circulation* 2003;107:929-34.
- [2] Hansson M, Lindsay ME, Chien KR. Regeneration next: toward heart stem cell therapeutics. *Cell Stem Cell* 2009;5:364-77.
- [3] Laird DJ, von Andrian UH, Wagers AJ. Stem cell trafficking in tissue development, growth, and disease. *Cell* 2008;132:612-30.
- [4] Salem HK, Thiemermann C. Mesenchymal stromal cells: current understanding and clinical status. *Stem Cells* 2010;28:585-96.
- [5] Hoch AI, Leach JK. Concise review: optimizing expansion of bone marrow mesenchymal stem/stromal cells for clinical applications. *Stem Cells Transl Med* 2014; doi: 10.5966/sctm.2013-0196.
- [6] Das RK, Zouani OF. A review of the effects of the cell environment physicochemical nanoarchitecture on stem cell commitment. *Biomaterials* 2014;35:5227-93.
- [7] Kim J, Kim HN, Lang Y, Pandit A. Biologically inspired micro- and nanoengineering systems for functional and complex tissues. *Tissue Eng Part A* 2014;doi:10.1089/ten.tea.2013.0707.
- [8] Kim J, Kim HN, Lim KT, Kim Y, Seonwoo H, Park SH, et al. Designing nanotopographical

density of extracellular matrix for controlled morphology and function of human mesenchymal stem cells. *Sci Rep* 2013;3552.

[9] Yim EKF, Pang SW, Leong KW. Synthetic nanostructures inducing differentiation of human mesenchymal stem cells into neuronal lineage. *Exp Cell Res* 2007;313:1820–9.

[10] Yim EKF, Darling EM, Kulangara K, Guilak F, Leong KW. Nanotopography-induced changes in focal adhesions, cytoskeletal organization, and mechanical properties of human mesenchymal stem cells. *Biomaterials* 2010;31:1299–306.

[11] Xie J, Willerth SM, Li X, Macewan MR, Rader A, Sakiyama-Elbert SE, et al. The differentiation of embryonic stem cells seeded on electrospun nanofibers into neural lineages. *Biomaterials* 2009;30:354–62.

[12] Kim J, Kim HN, Lim KT, Kim Y, Pandey S, Garg P, et al. Synergistic effects of nanotopography and co-culture with endothelial cells on osteogenesis of mesenchymal stem cells. *Biomaterials* 2013;34:7257-68.

[13] Chen W, Villa-Diaz LG, Sun Y, Weng S, Kim JK, Lam RHW, et al. Nanotopography influences adhesion, spreading, and self-renewal of human embryonic stem cells. *ACS NANO* 2012;6:4094-103.

[14] Teo BKK, Wong ST, Lim CK, Kung TYS, Yap CH, Ramagopal Y, et al. Nanotopography modulates mechanotransduction of stem cells and induces differentiation through focal adhesion kinase. *ACS NANO* 2013;7:4785-98.

[15] Kim DH, Smith RR, Kim P, Ahn EH, Kim HN, Marbán E, et al. Nanopatterned cardiac cell patches promote stem cell niche formation and myocardial regeneration. *Integrative Biology* 2012;4:1019-33.

[16] Kang BJ, Kim H, Lee SK, Kim J, Shen Y, Jung S, et al. The umbilical cord blood-derived

mesenchymal stem cells seeded onto fibronectin-immobilized PCL nanofiber improve the cardiac function. *Acta Biomaterialia* 2014;10:3007-17.

[17] Kim HN, Jiao A, Hwang NS, Kim MS, Kang DH, Kim DH, et al. Nanotopography-guided tissue engineering and regenerative medicine. *Advanced Drug Delivery Reviews* 2013;65:536-58.

[18] Kim DH, Provenzano PP, Smith CL, Levchenko A. Matrix nanotopography as a regulator of cell function. *The Journal of Cell Biology* 2012;197:351-60.

[19] Gautieri A, Vesentini S, Redaelli A, Buehler MJ. Hierarchical structure and nanomechanics of collagen microfibrils from the atomistic scale up. *Nano Lett* 2011;11:757-66.

[20] Jo YY, Lee HJ, Kook SY, Choung HW, Park JY, Chung JH, et al. Isolation and characterization of postnatal stem cells from human dental tissues. *Tissue Eng* 2007;13:767-73.

[21] Kirmizidis G, Birch MA. Microfabricated grooved substrates influence cell-cell communication and osteoblast differentiation in vitro. *Tissue Eng Part A* 2009;15:1427-36.

[22] Lutolf MP, Gilbert PM, Blau HM. Designing materials to direct stem-cell fate. *Nature* 2009;26:433-441.

[23] Cha C, Liechty WB, Khademhosseini A, Peppas NA. Designing biomaterials to direct stem cell fate. *ACS NANO* 2012;6:9353-8.

[24] Pashuck ET, Stevens MM. Designing regenerative biomaterial therapies for the clinic. *Sci Transl Med* 2012;4:160sr4.

[25] Mahdavi A, Ferreira L, Sundback C, Nichol JW, Chan EP, Carter DJ, et al. A biodegradable and biocompatible gecko-inspired tissue adhesive. *Proc Natl Acad Sci U S A*. 2008;105:2307-12.

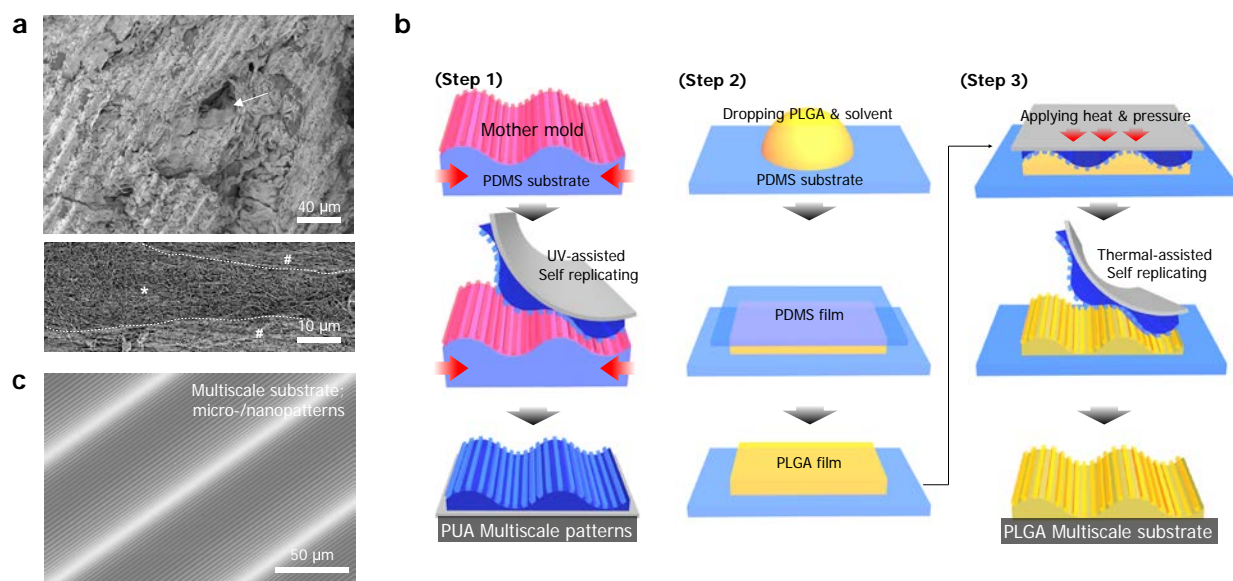


**Figure 8.1. Fabrication of multiscale hierarchical PLGA substrates.** (a) Low (upper) and high (bottom) magnification of SEM images of *ex vivo* human bone tissue. The white arrows indicate the ECM in the bone. The high magnification image (bottom) of ECM in the bone shows the micro- and nano-scale fibers. \*: groove, #: ridge structures. The ECM fiber layers shows anisotropic nano-fibrils (marked by \*), which were eventually assembled as micro-scale ECM fiber layers (marked by #). (b) Schematic diagram of PLGA micro- and nanoscale hierarchical substrates using capillary force lithography and surface micro-wrinkling method. (c) Representative SEM images of the micro- and nanopatterned hierarchical PLGA substrates mimicking the ECM in the bone.

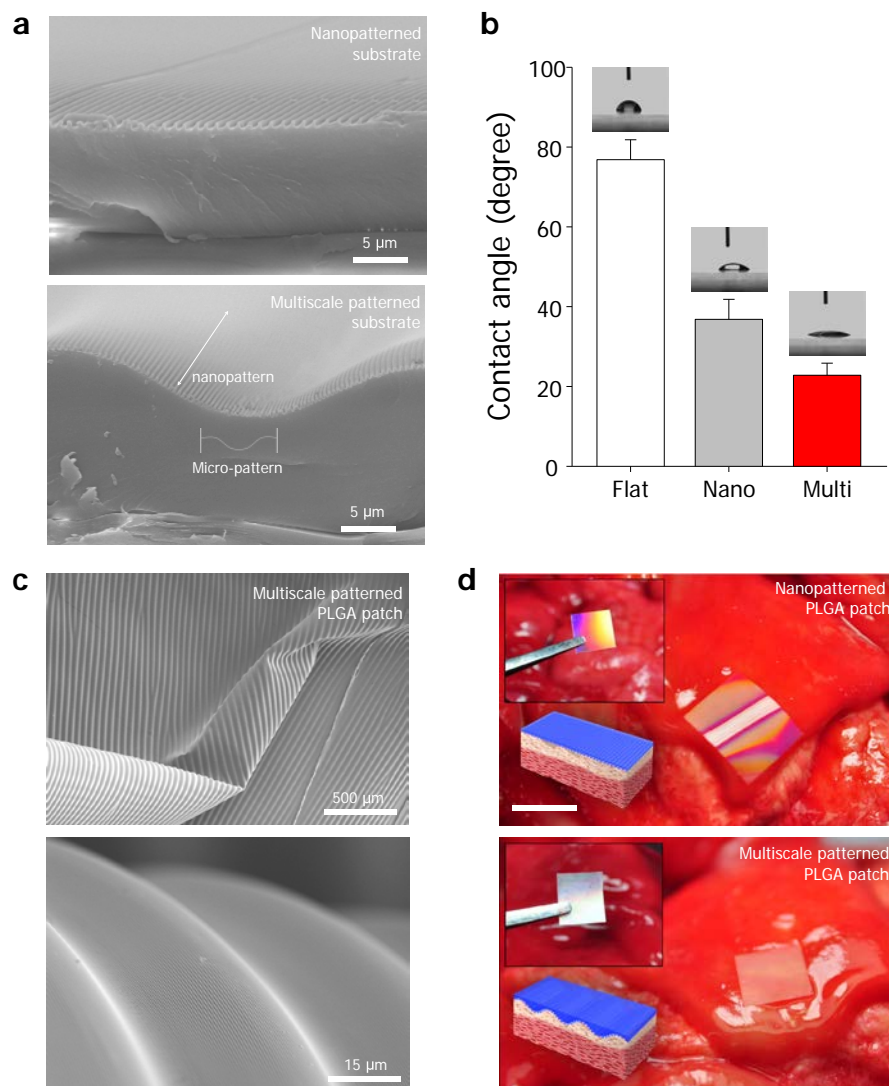


**Figure 8.2. Surface characteristics of multiscale hierarchical PLGA patch.** (a) Representative cross-sectional SEM images of 350 nm patterned and multiscale (350 nm/30  $\mu\text{m}$  patterned hierarchical topography) PLGA patch. (b) Contact angle measurement of flat, nanopatterned, and multiscale patterned PLGA patch ( $n=10$  for each sample). Error bars represent the SD from the mean. (c) Representative SEM images of crumpled PLGA patches showing high flexibility on the curved substrate. (d) Photographs of the nano-patterned PLGA and the multiscale PLGA patches attached to the intestinal tissue and their conceptual images, showing the well-attached patches on the tissue. Bar = 1 cm.

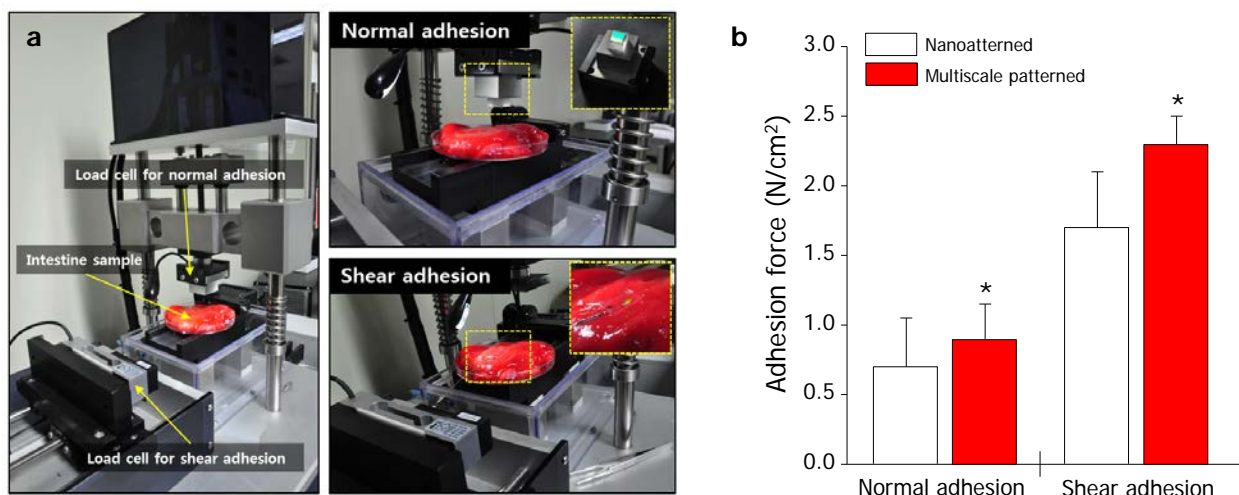


**Figure 8.3. Normal and shear adhesion forces of the multiscale hierarchical PLGA patch.** (a) Optical images of the custom-built equipment used in our experiment for the adhesion test for normal and shear adhesion. The sample is fixed on a load cell with a patterned area of  $1 \times 1 \text{ cm}^2$ . (b) Measurement of the macroscopic normal and shear adhesion forces ( $n = 30$  for each sample). The multiscale ( $350 \text{ nm}/30 \text{ }\mu\text{m}$  patterned hierarchical topography) PLGA patches displayed larger normal ( $\sim 0.9 \text{ N cm}^{-2}$ ) and shear ( $\sim 2.3 \text{ N cm}^{-2}$ ) adhesion forces compared to the  $350 \text{ nm}$  patterned PLGA patches normal ( $\sim 0.7 \text{ N cm}^{-2}$ ) and shear ( $\sim 1.7 \text{ N cm}^{-2}$ ) adhesion forces.

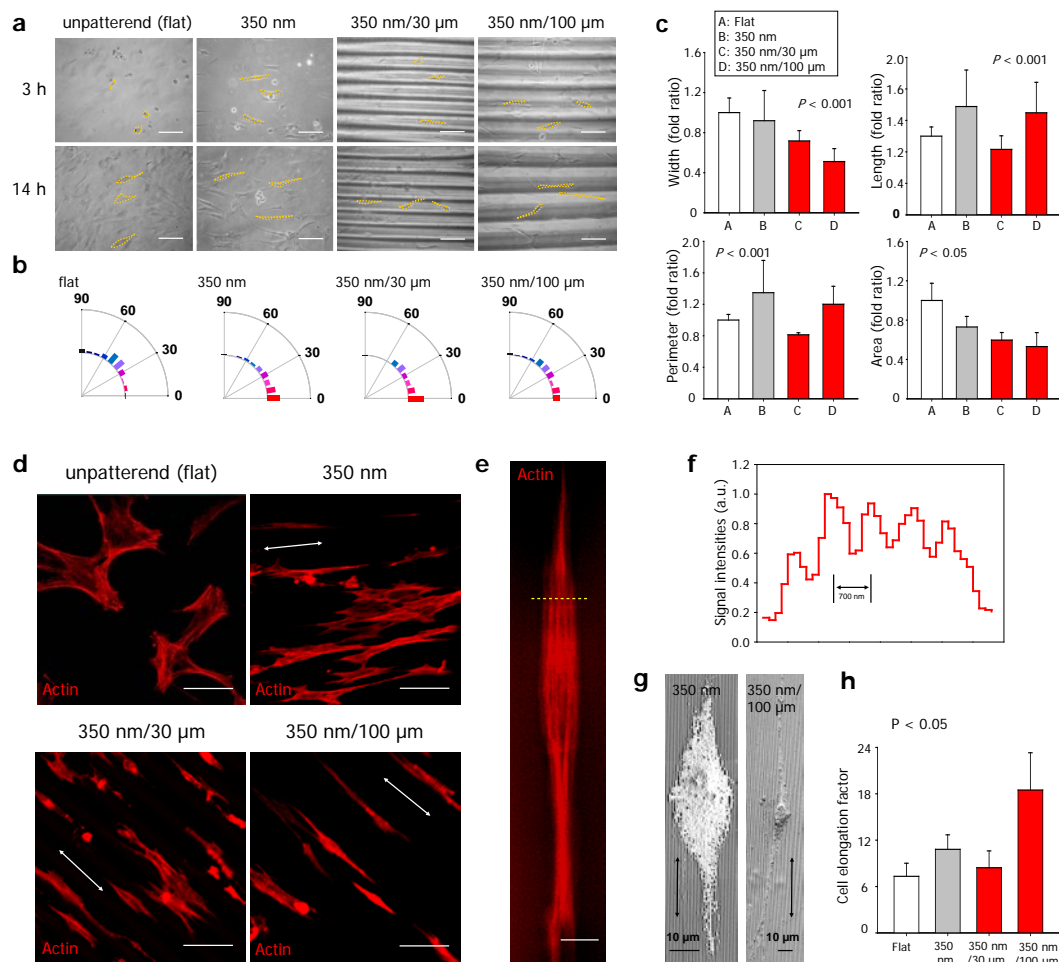


**Figure 8.4. Adhesion of hMSCs with controlled macroscopic alignment and orientation on the multiscale hierarchical topography.** (a) Phase contrast images, showing the initial cell adhesion (3 h) and full adhesion (14 h) on the flat, nano, and multi-scale patterned substrates. The 350 nm indicates the nano-patterned substrates and 350 nm/30  $\mu$ m or 100  $\mu$ m indicates anisotropic nanotopography in the micro-patterned substrates. (b) Quantification of cell orientation on flat vs. nano vs. multiscale topography. Each dot represents a single cell, and an orientation of 0° represents perfect alignment with the topography direction. (c) Quantification of cell width, length, perimeter, and area on the adhesive patches; the values were normalized to the flat substrates. A total of 50 - 100 cells were used for quantification. Error bars represent the SD from the mean. (d) Immunofluorescent images of actin (in red) of cells. The double arrows indicate the direction of the micro or nanotopography in the substrates. (e) Representative high magnification immunofluorescent image of the cell, indicating that the cytoskeleton of the cell was highly organized along the direction of the nanotopography in the micro-hierarchical substrates. (f) Normalized fluorescence intensity measured along the yellow line in (e). (g) Representative SEM images of hMSCs; the black arrows indicate the direction of the nanotopography. (h) Quantification of cell elongation on the substrates, described by the axial ratio of cell width and length. A total of 50 - 100 cells were used for quantification. Error bars represent the SD from the means.

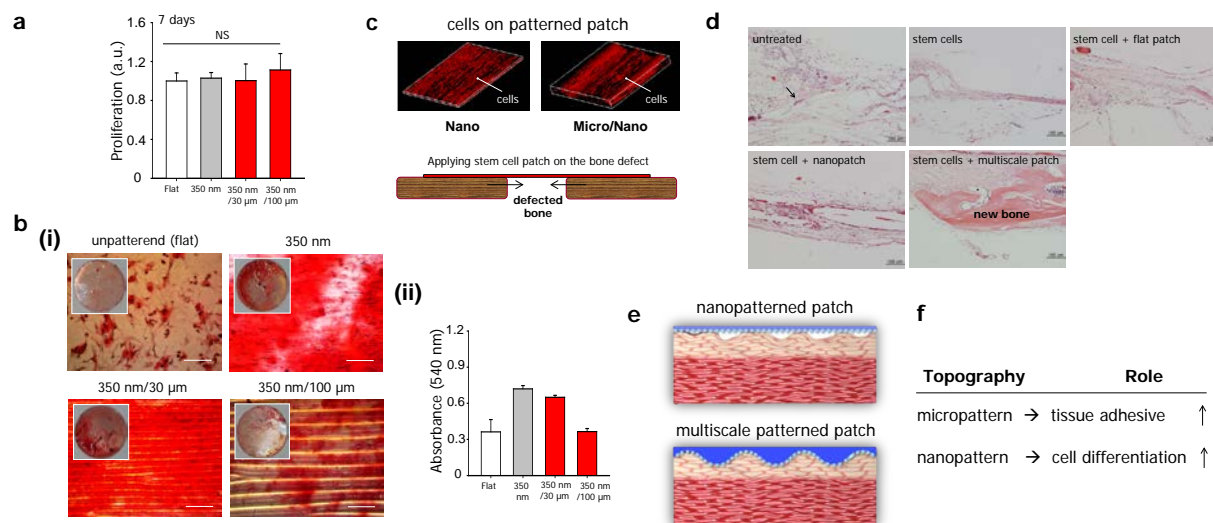


**Figure 8.5. Bone regeneration using multiscale patterned stem cell patches.** (a) Proliferation of hMSCs on the substrates. (b) Mineralization of hMSCs by osteogenesis on the multiscale patterned substrates; (i) Alizarin red staining and (ii) quantification of osteogenesis degree showed that the 350 nm and 350 nm/30 μm features on the hierarchical substrates promoted a greater degree of osteogenesis of hMSCs compared to the other substrates. More anisotropically mineralized areas were observed on the 350 nm/30 μm hierarchical topography, indicating that the multiscale topography may have great potential for hard tissue regeneration using stem cells. Bars indicate 200 μm. (c) Schematic of a stem cell patch. The hMSCs were integrated into the patterned PLGA patches. The stem cell patches were then grafted onto the defected bone tissue of rats for bone regeneration. (d) *In vivo* bone regeneration by transplantation of nanopatterned hierarchical stem cell patches into animal models; Representative H&E staining images after applying stem cell patches into the bone defects. Two independent animal experiments were performed. (e and f) A possible role for micro- and nanopatterned hierarchical topography to improve tissue regeneration with stem cells.



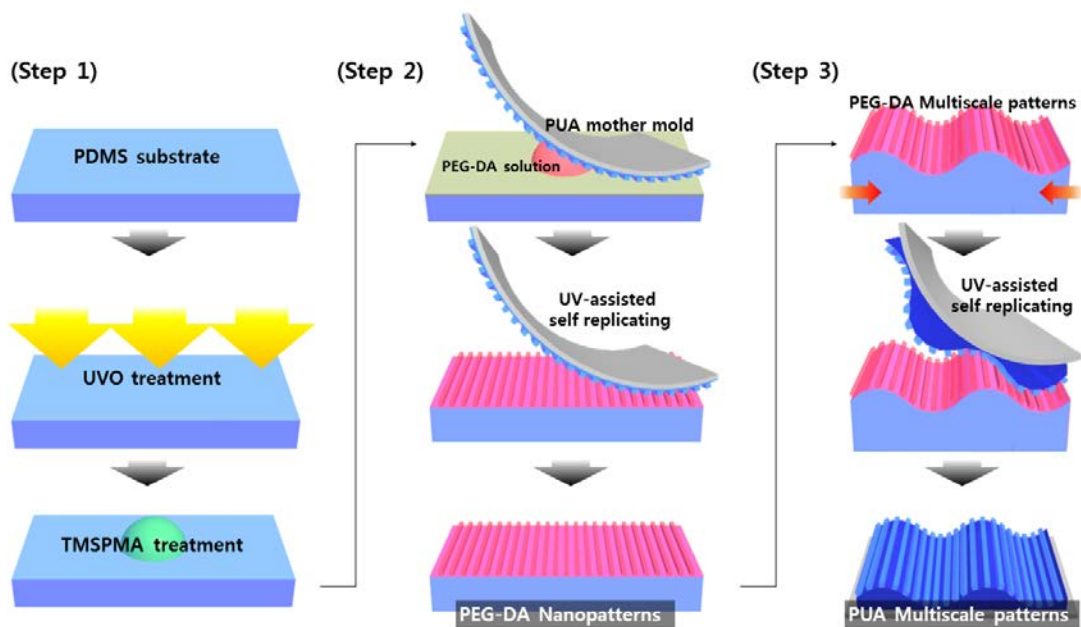


**Figure 8.S1. Schematic illustration of PUA micro- and nanopatterned hierarchical patterns.** Precisely controlled micro- and nanoscale hierarchical patterned substrate was fabricated by capillary force lithography and surface wrinkling method.

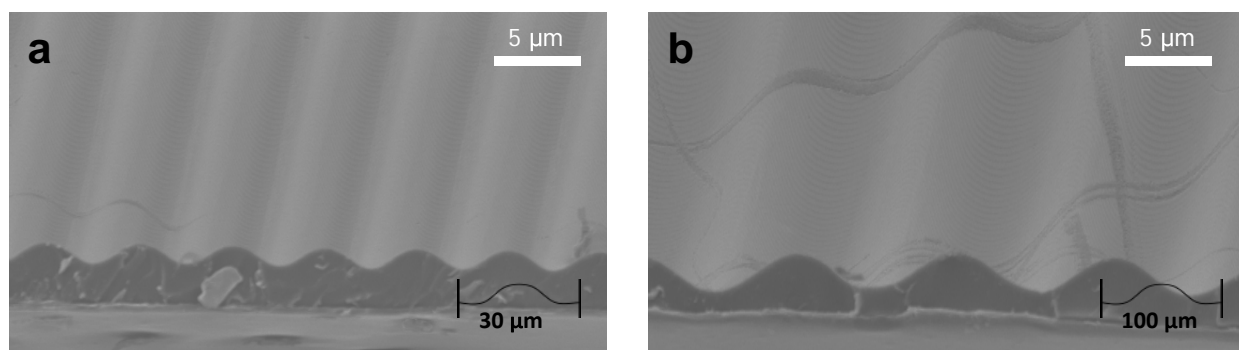


**Figure 8.S2. Representative SEM images of micro- and nanopatterned substrates with controlled sizes.** (a) 350 nm nanopatterns on 30  $\mu\text{m}$  micro patterned substrate. (b) 350 nm nanopatterns on 100  $\mu\text{m}$  micro patterned substrate.

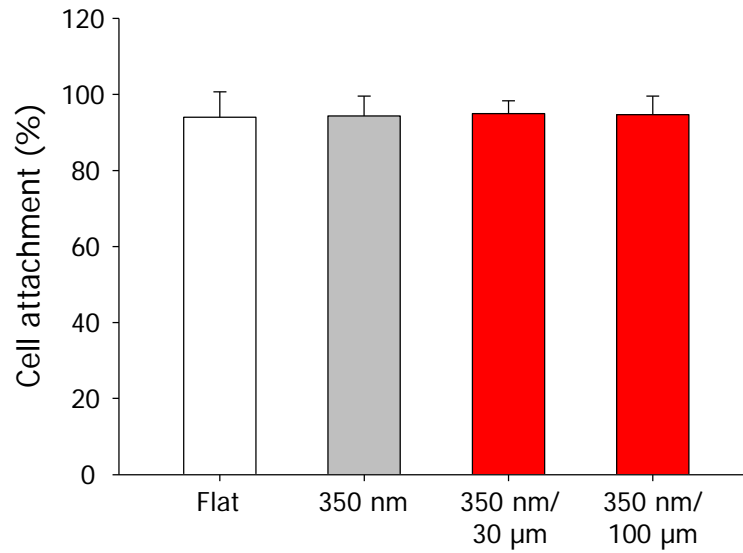


**Figure 8.S3. Attachment of hMSCs on substrates.** hMSCs were cultured on the substrates for 14 h. Quantification was performed by WST-1 assay. The control means the initial cell density. The error bars represent the SD about the mean ( $n = 3$  for each group)

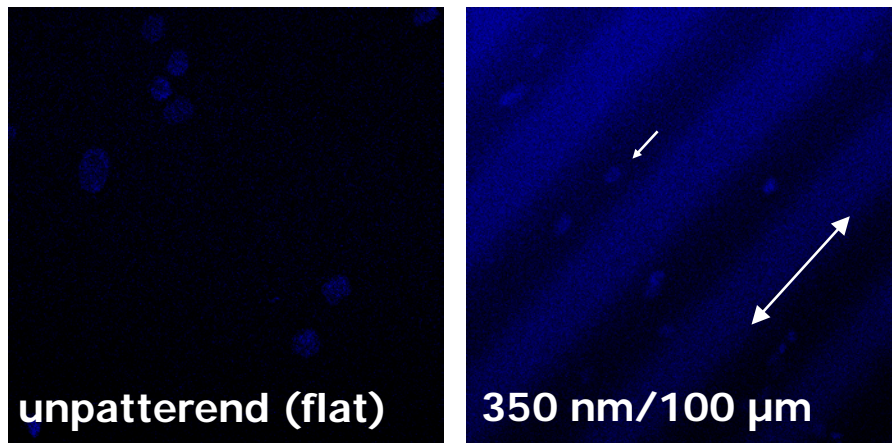


**Figure 8.S4. Immunofluorescent images of nucleus of hMSCs on the flat and micro- and nanopatterned hierarchical topography.** The white arrow indicates the nucleus, stained by DAPI, was elongated along the direction of nanotopography in the substrates. The double arrows indicate the direction of the micro- and nanotopography in the substrate.

## **Chapter 9. Bacterial Cellulose Nanofibrillar Patch as a Wound Healing Platform of Tympanic Membrane Perforation**

### **9.1. Summary**

Here, we report the fabrication of a nanofibrillar patch by using BC and its application as a new wound-healing platform for traumatic tympanic membrane (TM) perforation. TM perforation is a very common clinical problem worldwide and presents as conductive hearing loss and chronic perforations. The BC nanofibrillar patch can be synthesized from *Gluconacetobacter xylinus*; it was found that the patch contained a network of nanofibrils and was transparent. The thickness of the BC nanofibrillar patch was found to be approximately  $10.33 \pm 0.58 \mu\text{m}$ , and the tensile strength and Young's modulus of the BC nanofibrillar patch were  $11.85 \pm 2.43$  and  $11.90 \pm 0.48$  MPa, respectively, satisfying the requirements of an ideal wound-healing platform for TM regeneration. *In vitro* studies involving TM cells showed that TM cell proliferation and migration were stimulated under the guidance of the BC nanofibrillar patch. *In vivo* animal studies demonstrated that the BC nanofibrillar patch promotes the rate of TM healing as well as aids in the recovery of TM function. Our data demonstrate that the BC nanofibrillar patch is a useful wound-healing platform for TM perforation without complex surgical treatments.

### **9.2. Introduction**

Bacterial cellulose (BC) produced by *Gluconacetobacter xylinus* (*G. xylinus*) has gained significant interest as a biomaterial in various biomedical fields due to its unique properties such as biocompatibility, high water-holding capacity, ultrafine network structure, transparency, and high mechanical properties, as well as its relatively simple and cost-efficient production process [1-4]. In particular, recent studies have revealed the potential of BC-based biomaterials for

medical device platforms that can be used in regenerative medicine for tissue-engineered scaffolds or engraftment materials, including bone, cartilage, tooth, skin, and muscle [1-6]. It is widely accepted that nanostructured biomaterials mimicking the structural extracellular matrix (ECM) play key roles as regulators of cellular and tissue functions, which would present an advanced strategy for regenerative medicine [7-14]. A unique property of BC-based platforms is their ultrafine and highly pure nanofibril network structure that may be used as an efficient wound-healing platform since cell migration into a wound site is strongly mediated by the structural properties of the ECM [1,5,8,11-13]. Thus, BC-based platforms with their unique nanostructures may be useful in wound healing in various tissues.

The tympanic membrane (TM) is composed of 3 tissue layers, including the epidermal, connective, and mucosal layers, and TM regeneration is representative of the typical wound healing procedure [16]. Traumatic TM perforation, caused by physical external factors or insults to the middle ear, is a very common clinical problem worldwide, which may present with conductive hearing loss and chronic perforations [16-19]. In such cases, the TM is typically regenerated spontaneously. However, during spontaneous TM regeneration, the patient has to endure many difficulties; strenuous sports, swimming, and blowing are prohibited, and the patient has to be kept under careful observation. Additionally, TM perforations that are large are combined with chronic otorrhea or inflammation cannot undergo spontaneous TM regeneration [16]. The paper patch graft technique has been frequently used to heal traumatic TM perforations in outpatient department clinics to overcome the limitations of spontaneous TM regeneration; the paper patch guides the growth and migration of TM cells to the patch from the borders of the perforation, which can lead to TM regeneration more quickly than in spontaneous TM regeneration [16-19]. However, the paper patch has several disadvantages, such as

nonbiocompatibility, nontransparency, and nonflexibility, as well as ease of detachment and nonresistance to infection [16]. Therefore, developing an efficient TM-healing platform as an alternative to the paper patch is necessary for clinical applications.

Here, we describe the fabrication of a nanofibrillar patch using BC and its application as a new healing platform for TM perforation. We hypothesized that the unique properties of the BC nanofibrillar patch, such as its nanostructured surface, which is similar to ECM structure; biocompatibility; transparency; and high mechanical properties make it an excellent candidate as a wound-healing platform for TM perforation. Fig. 9.1 shows the conceptual rationale for this study. BC was synthesized from *G. xylinus*, and the BC patch was fabricated by removing the *G. xylinus*. It was found that the surface of the fabricated BC patch was a network of nanofibrils and was transparent. We investigated various characteristics of the BC nanofibrillar patches and confirmed their suitability as efficient wound-healing platforms for TM perforation. Our *in vitro* proliferation and wound-healing study demonstrated the significant potential of using the BC nanofibrillar patch for TM regeneration. Strikingly, the *in vivo* study revealed that the BC nanofibrillar patch could promote TM regeneration in animal models of traumatic TM perforations and improve the function of regenerated TMs.

### **9.3. Materials and methods**

#### **9.3.1. Preparation of BC and fabrication of nanofibrillar patch**

*G. xylinus* (KCCM 40216) was obtained from the Korean Culture Center of Microorganisms. The bacterium was cultured on mannitol medium composed of 2.5% (w/w) mannitol, 0.5% (w/w) yeast extract, and 0.3% (w/w) bacto-peptone. The culture media were sterilized in an autoclave at 120°C for 20 min and then poured into 500 mL flasks. The pre-inoculum for all

experiments was prepared by transferring a single *G. xylinus* colony grown on agar culture medium into a 100 mL Erlenmeyer flask filled with mannitol culture medium. The pre-cultured culture cell suspension was introduced into culture medium (pH 6.0) and incubated at 28°C for 2 weeks. The BC membrane biosynthesized in the medium was simply harvested and purified by boiling in 1 wt% sodium hydroxide for 2 h at 90°C. Subsequently, the membrane was thoroughly washed with running distilled water, after which it was soaked in 1 wt% aqueous sodium hydroxide solution for 24 h at room temperature to eliminate the cell debris and components of the culture liquid. The pH was then reduced to 7.0 by repetitive washing with distilled water. Next, the membrane was bleached by immersion in 1 wt% aqueous sodium hypochlorite for 2 h, after which it was washed with running distilled water until pH 7 was attained. Finally, the membrane was vacuum-dried at 60°C for 12 h.

### **9.3.2. Characterizations of BC nanofibrillar patch**

The morphology of the BC nanofibrillar patches to show their transparent property at room temperature. Also, the patches were imaged by a SEM (JEOL, JSM-5410LV, Japan) at an accelerating voltage of 2 kV.

The thickness of the BC nanofibrillar patches were measured by a micrometer (Mitutoyo, Kawasaki, Japan). Measurements were repeated at 5 times for each sample and averaged. All experiments were performed at room temperature.

The BC nanofibrillar patches, 2 mm wide and 70 mm long, were cut. Tensile strength was measured by a texture analyzer (Stable Micro Systems Ltd., London, England). The cross-head speed was set at 500 mm/mm. Measurements were repeated at 5 times for each sample and averaged. All experiments were performed at room temperature.

Water contact angles on the BC nanofibrillar patches were measured using a video contact angle analyzer (VCA; Phoenix 600, Seoul, South Korea). Ten  $\mu\text{l}$  of water was dropped onto the surface of each patch. The water contact angle was measured as the tangent to the interface of the droplet on the BC nanofibrillar patches. Measurements were repeated at least 10 times for each sample and averaged. All experiments were performed at room temperature.

### **9.3.3. *In vitro* adhesion and proliferation of TM cells study**

TM cells ( $4 \times 10^4$  cells/patch) were seeded onto the BC nanofibrillar patches and cultured for up to 6 h, 3, 5, and 7 days in Dulbecco's modified Eagle's medium (DMEM; Sigma-Aldrich, Milwaukee, WI, USA) with 10% fetal bovine serum (FBS; Sigma-Aldrich, Milwaukee, WI, USA) and 1% antibiotics (Sigma-Aldrich, Milwaukee, WI, USA) at 37°C in a humidified atmosphere containing 5% CO<sub>2</sub>. The quantitative analysis of the cell adhesion and proliferation on the BC nanofibrillar patches was performed using WST-1 assay (EZ-Cytox Cell Viability Assay Kit, Daeillab Service Co., LTD).

### **9.3.4. *In vitro* wound healing study**

The effects of the BC nanofibrillar patches on growth and migration of the TM cells in an *in vitro* system were analyzed [11]. To mimic the TM perforation status *in vitro*, we cultured TM cells on the TCPS and observed the TM cells grown to confluence after 24 h, and then a wound was induced on the confluent monolayer TM cells by scraping a space with a plastic pipette tip. The TM cells were then directly covered with the BC nanofibrillar patch. On the other hand, the control sample was grown without any patches. The wound closure was checked by microscopy at 24 and 36 h after the scratch.

### **9.3.5. *In vivo* animal study**

The experimental protocol of *in vivo* animal study was approved by the Institutional Review Board of the Ajou University School of Medicine (Suwon, Korea). Sprague-Dawley rats (12 weeks, 250–300 g) were anesthetized with chloral hydrate (1 g/mL, 10% dilution). A 50% sized perforation was mechanically created on the anterior half of TM. The BC nanofibrillar patches were applied on the perforated TMs. We checked the TMs every 2 days to determine whether the placed patch remained in the perforated areas. If the patch was displaced from the hole, it was replaced. As a control group, the spontaneous TM regeneration was used. The healing states of the perforated TMs were checked at 1, 3, 5, 7, 9, and 11 days after application of the patches under a surgical microscope. The perforated TM sizes were checked using a custom-written MATLAB script.

### **9.3.6. Evaluation of regenerated TMs**

ABR was performed before TM perforation and after TM regeneration with the BC nanofibrillar patches. Rats were anesthetized as previously described. ABR was measured for both ears of each animal using broadband clicks. A differential active needle electrode was placed subcutaneously below the tested ear, a reference electrode at the vertex, and a ground electrode below the contralateral ear. ABRs were recorded by using an evoked potential averaging system (Tucker-Davis Technologies) in an electrically shielded, sound-treated booth. Sound was presented through an earphone, which was placed directly in the ear canal. ABR waveforms were recorded in 5 dB sound pressure level intervals down from the maximum amplitude. Threshold by visual inspection was defined as the lowest stimulus level at which response peaks for wave I–V were clearly present. The mean value of thresholds checked by visual inspection and



computer analysis was defined as ABR threshold at each stimulus. Data were obtained from each group.

All experimental animals were sacrificed at post 2 weeks by injecting 5 mL chloral hydrate (1 g/mL, 10% dilution) intraperitoneally. If the TMs had healed completely, then 5 mL chloral hydrate (1 g/mL, 10% dilution) was injected intraperitoneally to sacrifice the rats. Tympanic bulla were obtained immediately from the heads of the rats and fixed in formaldehyde. Some specimens were decalcified in formic acid for 2 weeks, and cross-sectional findings were stained with hematoxylin and eosin, along with examination under an optical microscope. We also observed the regenerated TMs using a TEM (EM 902A, Zeiss).

#### **9.3.7. Statistical analysis**

All quantitative results are presented as mean  $\pm$  standard deviation (SD) and unpaired student's t-tests or chi-square test for *in vivo* study were used for statistical analysis. Statistical analyses were performed using the Statistical Analysis System (SAS) for Windows Ver. 8.2 (SAS Institute) and SPSS (SPSS Inc.).

### **9.4. Results**

#### **9.4.1. Fabrication of BC nanofibrillar patch**

To fabricate the BC nanofibrillar patch as a wound-healing platform for TM regeneration, *G. xylinus* was first cultivated for 14 days to synthesize BC. *G. xylinus* was then removed, leaving the BC gels. The gels were washed with deionized water. Finally, the BC nanofibrillar patches were purified by boiling in 1 wt% NaOH for 2 h at 90°C and then washed with deionized water (Fig. 9.1) [20].

#### 9.4.2. Characterizations of BC nanofibrillar patch

From a clinical perspective, an ideal wound-healing platform for TM regeneration should have the following properties: (1) noncytotoxicity, (2) efficient environment for promoting TM cell growth and migration on the perforated TMs, (3) adequate mechanical strength to withstand the vibration of sound conduction, and (4) transparency to enable observation of the growing TM [16-19,21-24].

We analyzed the BC nanofibrillar patches to determine whether they had these characteristics (Fig. 9.2 and Table 9.1). BC biocompatibility has been well studied previously [1-6]. Fig. 9.2 shows the morphological features of the BC nanofibrillar patches. The BC nanofibrillar patch was found to be transparent, which will allow observation of the TM during TM regeneration (Fig. 9.2a). Scanning electron microscope (SEM) images showed that the BC nanofibrillar patch contained nanoscale fibrous networks with a structure similar to that of the ECM (Fig. 9.2b). As described above, the nanoscale fibrous structures of the BC nanofibrillar patch indicates its usefulness as an efficient TM-healing platform through its ability to mediate TM cell proliferation and migration into the site of the perforated TM with nanoscale structure cues similar to those of the natural ECM. Additionally, we observed that the BC patch had an extremely dense surface, which will improve resistance to infection by preventing foreign bodies from entering external ear canals (Fig. 9.2b).

Varying values have been reported for the elastic modulus of the human TM, that is, 1–400 MPa, depending on the analysis method used [16]. The elasticity of TMs is important for sound conduction; therefore, the mechanical strength and elasticity of the artificial patch should be considered. The BC nanofibrillar patch thickness was approximately  $10.33 \pm 0.58 \mu\text{m}$ , while the tensile strength and Young's modulus of the patch were  $11.85 \pm 2.43$  and  $11.90 \pm 0.48$  MPa,

respectively (Table 9.1). Our group already reported that the tensile strength of paper patch was  $\sim 12.45 \pm 1.17$  MPa [16], indicating that the tensile strength of BC patch is quite similar to that of the paper patch. Additionally, based on the results of a water contact-angle test, we found that the BC nanofibrillar patch was hydrophilic (Table 9.1).

Together, the results suggest that the BC nanofibrillar patch can be used as a suitable wound-healing platform for TM perforations.

#### **10.4.3. *In vitro* proliferation of TM cells on BC nanofibrillar patch**

For the *in vitro* study, we first isolated TM cells from 5-d-old rats [16]. The TM is composed of keratinocytes and fibroblasts, and we confirmed that the fibroblasts are the primary component. Fluorescence-activated cell sorting showed that the fibroblasts constituted more than 95% of the cells, while keratinocytes (epithelial cells) accounted for approximately 0.1% [16].

The extent of adhesion and proliferation of TM cells on the BC nanofibrillar patch was analyzed using *in vitro* experiments. We cultured TM cells on the BC nanofibrillar patch and tissue culture polystyrene (TCPS) as a control for 6 h and 3, 5, and 7 days and observed the time-dependent cell viability of TM cells on the samples. TM cells were found to be well attached to the BC nanofibrillar patch (Fig. 9.3). Interestingly, the cell viability at 6 hr did not significantly differ between cells on the patch and those on the TCPS ( $P < 0.05$ ), indicating that the BC nanofibrillar patch surface provides a suitable environment for TM cell attachment. We also observed a similar time-dependent cell viability of TM cells on the BC nanofibrillar patch compared to that on the TCPS (Fig. 9.3). Our results support that the BC nanofibrillar patch's use as a wound-healing platform for TM regeneration.

#### **9.4.4. *In vitro* wound healing of TM Cells by using BC nanofibrillar patch**

To investigate whether wound healing is influenced by the BC nanofibrillar patch, we analyzed the extent of cell proliferation and migration by using an *in vitro* wound healing assay. We attempted to mimic the TM perforation status for the *in vitro* wound-healing test [16]. TM cells were cultured on TCPS and the cells grew to confluence after 24 h. A wound was induced on confluent monolayer TM cells by scraping with a plastic pipette tip. TM cells were then covered with the BC nanofibrillar patch (see the schematic in Fig. 9.1 for the TM-regeneration strategy). A control sample was grown without a patch. Wound closure was evaluated by microscopy at 24 and 36 h after scratching.

The TM cells with the BC nanofibrillar patch showed significantly greater TM cell migration and proliferation than the TM cells without patches (Fig. 9.4). This result was also supported by quantitative and statistical analyses ( $P < 0.05$ ) (Fig. 9.4c). These results suggest that TM cells can proliferate and migrate better under the guidance of the BC nanofibrillar patch; thus, we expect that the BC nanofibrillar patch can stimulate wound healing in perforated TMs.

#### **9.4.5. *In vivo* model animal study of TM regeneration by using BC nanofibrillar patch**

To determine whether the BC nanofibrillar patch is a suitable wound-healing platform for TM regeneration, we performed an *in vivo* animal study. Animal models for traumatic TM perforations were prepared using a micropick under a surgical microscope (Fig. 9.5a). BC nanofibrillar patches were applied to the perforated TMs of rats (Figs. 9.1 and 9.5a), and spontaneous TM regeneration was used as a control group. We did not use the paper patch as a control in this study since the paper patch must be detached from the perforated TM to observe the degree of TM regeneration. However, we can observe the degree of TM regeneration when

applying the BC nanofibrillar patch on the perforated TM, which is another advantage of this method. Comparing the ability of the BC patch for TM healing with that of the paper patch is difficult. Therefore, we used rats with spontaneous TM healing as a control group in this study.

Fig. 9.5b shows individual changes in the perforated TMs and the maintenance rate of TM perforations in each group (BC nanofibrillar patch vs. non-BC nanofibrillar patch). The results showed that compared with spontaneous TM healing, the BC nanofibrillar patch accelerated the TM healing time. After 5 days, the TM had not healed perfectly in either group, although we observed a faster healing time in the BC nanofibrillar patch group than in the non-BC nanofibrillar patch group (Fig. 10.5b and c). After 7 days, 3 (27.3%) TMs showed complete healing. In contrast, only 1 (9%) TM showed no perforation in the spontaneous TM healing group; this difference was statistically significant ( $P = 0.045$ ). After 9 d, 6 (54.5%) and 10 (90.9%) TMs had healed perfectly in the BC nanofibrillar patch group and non-BC nanofibrillar patch group, respectively ( $P = 0.082$ ) (Fig. 9c). All the TMs completely healed in 2 weeks. In addition, we observed that there was no discharge in the TMs during healing in the two groups.

Using an auditory brainstem response (ABR) test, we evaluated healing status by using BC nanofibrillar patches for TM healing. As shown in Fig. 9.6, the average auditory threshold of normal TMs was  $12.7 \pm 4.1$  dB. In contrast, the average auditory threshold was  $33.2 \pm 4.0$  dB. After TM healing using BC nanofibrillar patches, the average auditory threshold was  $14.5 \pm 1.5$  dB. There was no significant difference in healing status between normal and regenerated TMs with BC nanofibrillar patches, indicating that TM function had recovered.

These data indicate that the BC nanofibrillar patch promotes faster TM healing as well as aids in the recovery of the functions of TMs, supporting its use as a suitable TM-healing platform.

#### 9.4.6. Evaluation of regenerated TMs by using BC nanofibrillar patch

To evaluate the quality of healed TMs with the BC nanofibrillar patch, we performed hematoxylin and eosin (H&E) staining and transmission electron microscopy (TEM) studies. Fig. 9.7 shows representative H&E-stained histological section images of the normal TM, spontaneously healed TM, and TM healed with the BC nanofibrillar patch. Similar features and structures were observed for all 3; however, the spontaneously healed TM was thinner than the normal TM and the TM healed with the BC nanofibrillar patch. However, the thickness of the TM healed with the BC nanofibrillar patch was similar to that of the normal TM (Fig. 9.7). This finding was also observed on TEM images (Fig. 9.8).

The TEM study showed that TMs healed spontaneously and that those healed with the BC nanofibrillar patch had 3 tissue layers, including an epidermal layer, connective tissue layer, and muscle layer, although the structures observed were more irregular than those in the normal TM (Fig. 9.8). However, the TM healed with the BC nanofibrillar patch was of better quality than those that healed spontaneously; the collagen fibers in the outer radical fibrous layers of TMs healed with the BC nanofibrillar patch were denser than those of spontaneously healed TMs. The histological findings strongly suggested that TMs healed with the BC nanofibrillar patches are more effective for sound conduction and show higher strength than spontaneously healed TMs.

Our study supports the hypothesis that the BC nanofibrillar patch can be used as an efficient strategy for wound healing in cases of TM perforation. The unique characteristics of the BC nanofibrillar patch make it an ideal wound-healing platform for TM regeneration. The *in vitro* and *in vivo* studies clearly demonstrated the potential of the BC nanofibrillar patch for wound healing in traumatic TM perforations. The BC nanofibrillar patch is a good alternative to

the paper patch for eventual clinical applications and has great potential for use in TM regeneration for cases of chronic TM perforation.

## 9.5. Discussion

In this study, we proposed that a BC nanofibrillar patch could be used as a strategy for wound healing of TM perforations. We found that the characteristics of the BC nanofibrillar patch, such as its nanostructured surface, biocompatibility, transparency, and appropriate mechanical properties, satisfy the requirements of an ideal wound-healing platform for TM perforation. We found that the TM cells adhered well and proliferated on the BC nanofibrillar patch and that TM cell growth and migration was promoted under the guidance of the patch. We performed an *in vivo* study that demonstrated the potential of the BC nanofibrillar patch as a useful wound-healing platform for TM perforations. Our *in vivo* study showed that the BC nanofibrillar patch increased the TM healing speed and rate as well as recovered the function of TMs better than spontaneous TM healing. Additionally, using histological analysis, we confirmed that TMs regenerated using the BC nanofibrillar patch had better qualities and structures than TMs showing spontaneous TM healing. We conclude that the BC nanofibrillar patch is a good candidate for eventual clinical applications for traumatic TM regeneration.

## 9.6. References

- [1] L. M. M. Costa, G. M. de Olyveira, P. Basmaji, L. X. Filho, *Journal of Biomaterials and Tissue Engineering* **2012**, 2, 185.
- [2] F. K. Andrade, R. Costa, L. Domingues, R. Soares, M. Gama, *Acta Biomaterialia* **2010**, 6, 4034.

- [3] R. T. Olsson, M. A. S. Azizi Samir, G. Salazar-Alvarez, L. Belova, V. Ström, L. A. Berglund, O. Ikkala, J. Nogués, U. W. Gedde, *Nature Nanotechnology* **2010**, 5, 584.
- [4] A. Svensson, E. Nicklasson, T. Harrah, B. Panilaitis, D. L. Kaplan, M. Brittberg, P. Gatenholm, *Biomaterials* **2005**, 26, 419.
- [5] H. Bäckdahl, G. Helenius, A. Bodin, U. Nannmark, B. R. Johansson, B. Risberg, P. Gatenholm, *Biomaterials* **2006**, 27, 2141.
- [6] C. J. Grande, F. G. Torres, C. M. Gomez, M. C. Bañó, *Acta Biomaterialia* **2009**, 5, 1605.
- [7] J. Kim, P. H. Choung, I. Y. Kim, K. T. Lim, H. M. Son, Y. H. Choung, C. S. Cho, J. H. Chung, *Materials Science and Engineering: C* **2009**, 29, 1725.
- [8] D. H. Kim, P. P. Provenzano, C. L. Smith, A. Levchenko, *The Journal of Cell Biology* **2012**, 197, 351.
- [9] J. Kim, D. H. Kim, K. T. Lim, H. Seonwoo, S. H. Park, Y. R. Kim, Y. Kim, Y. H. Choung, P. H. Choung, J. H. Chung, *Tissue Engineering Part C: Methods* **2012**, 18, 913.
- [10] W. Liu, S. Thomopoulos, Y. Xia, *Advanced Healthcare Materials* **2012**, 1, 10.
- [11] D. H. Kim, K. Han, K. Gupta, K. W. Kwon, K. Y. Suh, A. Levchenko, *Biomaterials* **2009**, 30, 5433.
- [12] H. N. Kim, Y. Hong, M. S. Kim, K. Y. Suh, *Biomaterials* **2012**, 33(34), 8782.
- [13] H. N. Kim, A. Jiao, N. S. Hwang, M. S. Kim, D. H. Kang, D. H. Kim, K. Suh, *Adv. Drug Deliv. Rev.* DOI: <http://dx.doi.org/10.1016/j.addr.2012.07.014> (2013).
- [14] J. Kim, Y. R. Kim, Y. Kim, K. T. Lim, H. Seonwoo, S. Park, S. P. Cho, B. H. Hong, P. H. Choung, T. D. Chung, Y. H. Choung, J. H. Chung, *J. Mater. Chem. B* **2013**, 1, 933.
- [15] P. L. S. Maria, S. L. Redmond, M. D. Atlas, R. Ghassemifar, *The Laryngoscope* **2010**, 120, 2061.



- [16] J. H. Kim, J. H. Bae, K. T. Lim, P. H. Choung, J. S. Park, S. J. Choi, A. L. Im, E. T. Lee, Y. H. Choung, J. H. Chung, *Journal of Biomedical Materials Research Part A* **2009**, 90A, 446.
- [17] J. H. Kim, S. J. Choi, J. S. Park, K. T. Lim, P. H. Choung, S. W. Kim, J. B. Lee, J. H. Chung, Y. H. Choung, *Tissue Engineering Part A* **2010**, 16, 225.
- [18] J. Kim, S. W. Kim, S. J. Choi, K. T. Lim, J. B. Lee, H. Seonwoo, P. H. Choung, K. Park, C. S. Cho, Y. H. Choung, J. H. Chung, *Tissue Engineering Part A* **2011**, 17, 2763.
- [19] B. M. Teh, R. J. Marano, Y. Shen, P. L. Friedland, R. J. Dilley, M. D. Atlas, *Tissue Engineering Part B: Reviews* doi:10.1089/ten.TEB.2012.0389.
- [20] J. Choi, S. Park, J. Cheng, M. Park, J. Hyun, *Colloids and Surfaces B: Biointerfaces* **2012**, 89, 161.
- [21] M. Farhadi, H. Mirzadeh, A. Solouk, A. Asghari, M. Jalessi, H. Ghanbari, P. Yazdanifard, *Journal of Biomedical Materials Research: Part A* **2012**, 100A, 549.
- [22] Y. Shen, S. L. Redmond, B. M. Teh, S. Yan, Y. Wang, L. Zhou, C. A. Budgeon, R. H. Eikelboom, M. D. Atlas, R. J. Dilley, M. Zheng, R. J. Marano, *Tissue Eng Part A* **2012**, 19, 1.
- [23] H. Qin, J. Sun, X. LI, Y. Liu, Z. Jia, *Acta Otolaryngol* **2012**, 132, 1266.
- [24] S. I. Kanemaru, H. Umeda, Y. Kitani, T. Nakamura, S. Hirano, J. Ito, *Otology & Neurotology* **2011**, 32, 1218.

Thickness [ $\mu\text{m}$ ]	Tensile stress [MPa]	Young's modulus [MPa]	Water contact angle [degree]
$10.33 \pm 0.58$	$11.85 \pm 2.43$	$11.90 \pm 0.48$	$31.17 \pm 4.28$

**Table 9.1.** Characteristics of the BC nanofibrillar patch fabricated in this study.

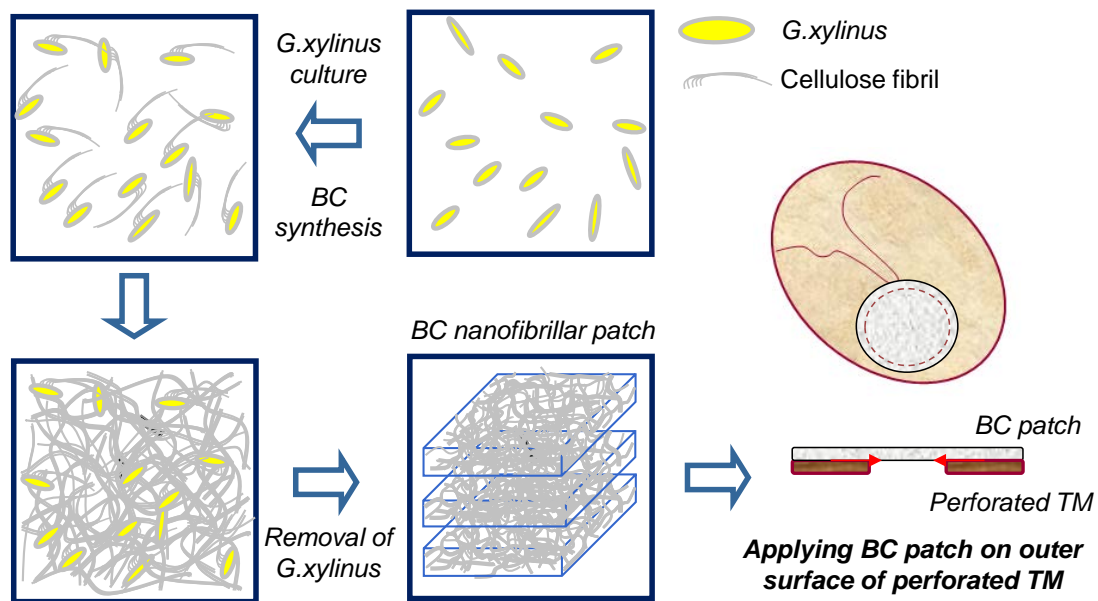


**Figure 9.1. Basic concept of this study for TM regeneration using BC nanofibrillar patch.** The BC nanofibrillar patch is synthesized from *G. xylinus*. The fabricated BC nanofibrillar patch is applied on the perforated TM. The patch guides growth and proliferation of TM cells to promote TM regeneration.

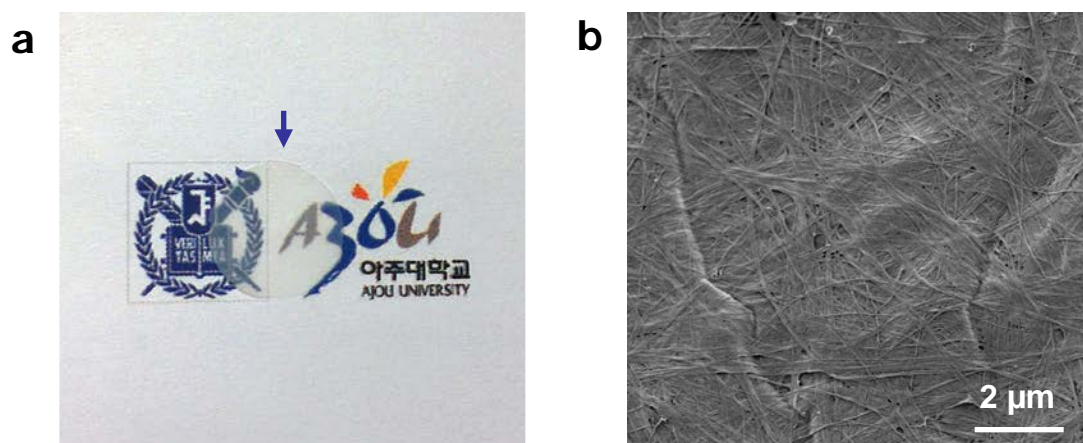


**Figure 9.2. Representative (a) digital camera image and (b) SEM image of the BC nanofibrillar patch.** The digital camera image shows transparent property of the BC nanofibrillar patch. The SEM image shows that the BC nanofibrillar patch had nanoscale fibrous structures. The arrow indicates the BC nanofibrillar patch.

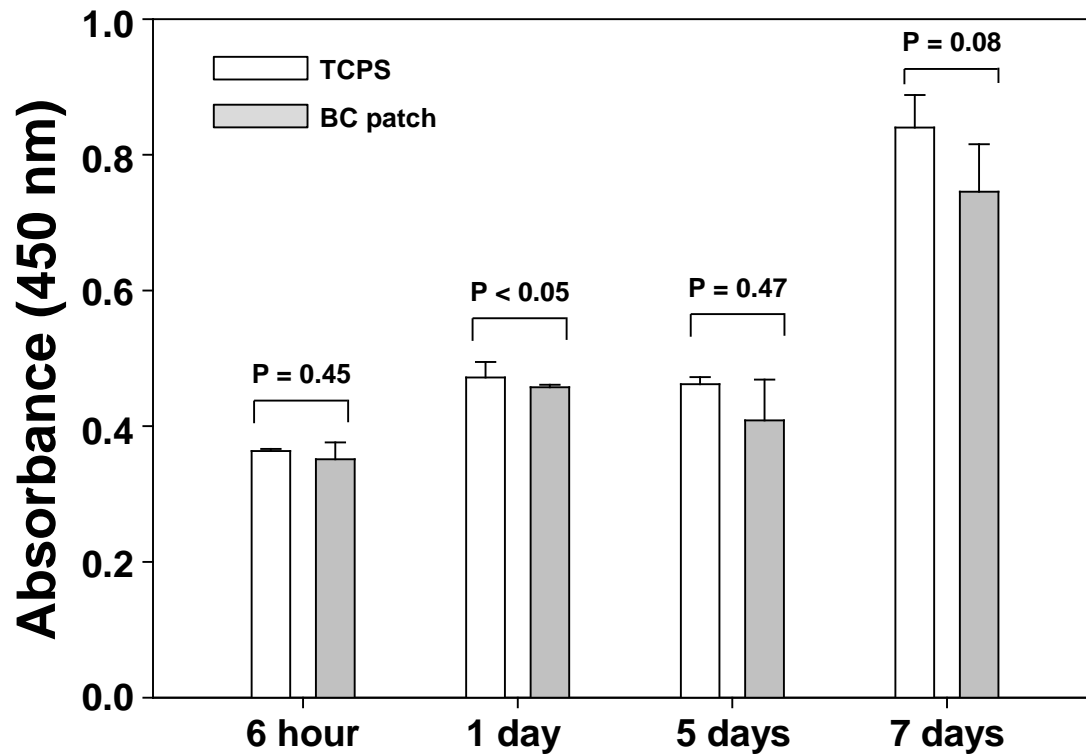


**Figure 9.3.** Time-dependent cell viability of the TM cells on the BC nanofibrillar patch and TCPS as a control at 6 h, 3, 5, and 7 days after seeding of cells, showing a similar time-dependent cell viability of TM cells between the BC nanofibrillar patch and the TCPS group. Three independent experiments were conducted. Error bars represent the SD about mean.

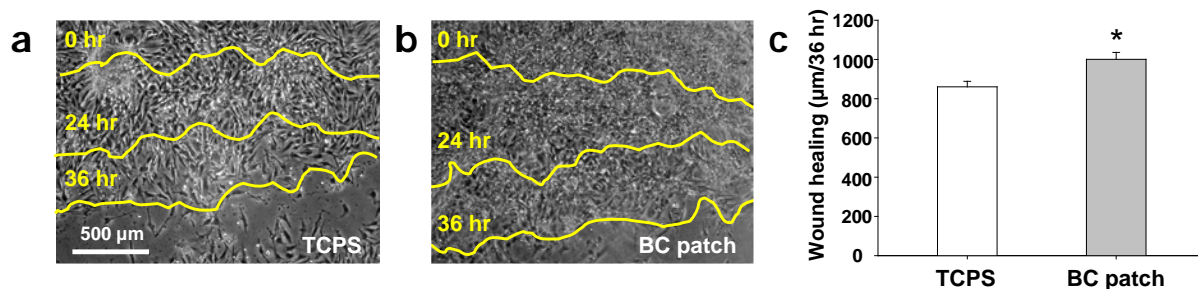


**Figure 9.4. *In vitro* wound healing study for growth and migration of the TM cells under guidance of the BC nanofibrillar patch.** Representative phase contrast micrographs of migration of TM cells (a) without the BC nanofibrillar patch (TCPS alone) and with (b) the BC nanofibrillar patch in the *in vitro* wound healing model of TM perforation. Three independent experiments were conducted. (c) Quantification of wound healing distance for 36 h. To quantify, the wound distance from each image was divided in 20 parts from the representative phase contrast micrograph. Error bars represent the SD about mean. \* $P < 0.05$ .

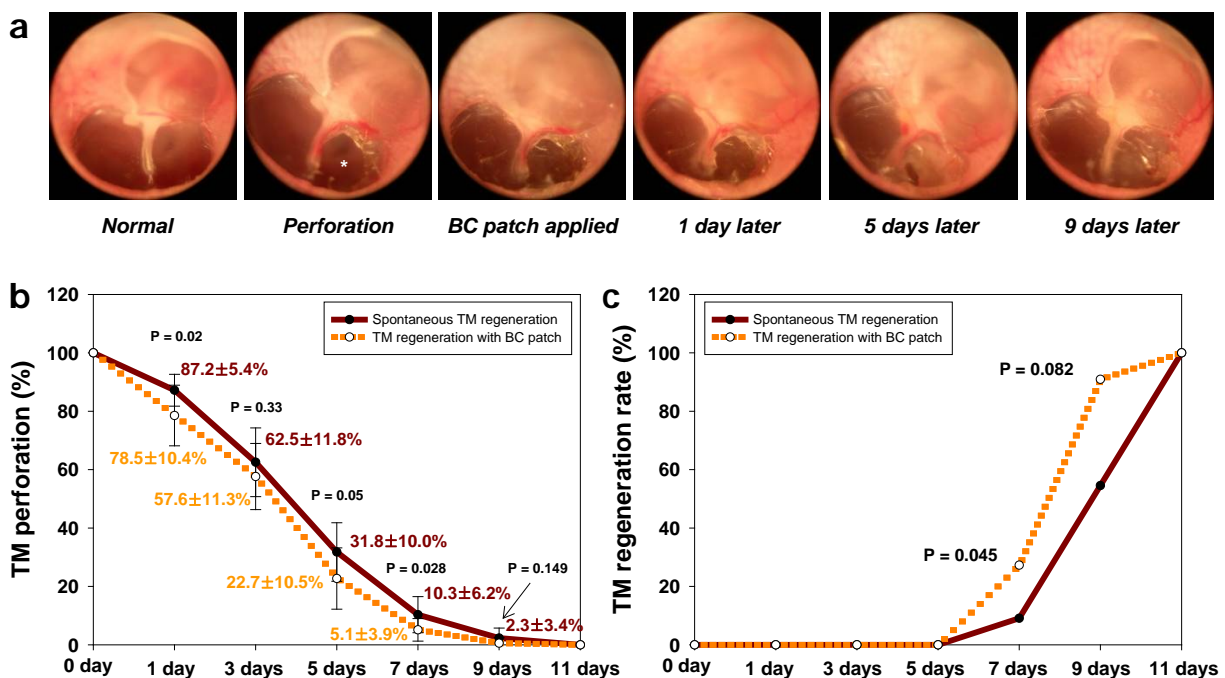


**Figure 9.5. *In vivo* animal study of regeneration of traumatic TM perforation using (a) the BC nanofibrillar patch.** The patch is applied on the perforated TM (\*) to stimulate TM regeneration. (b) The individual changes of perforated TMs in each group (TM regeneration with the BC nanofibrillar patch vs. spontaneous TM regeneration). Student's t-tests were used for statistical analysis. (c) A statistical comparison (chi-square test) of a perforated TM recovery with or without the BC nanofibrillar patch. Eleven independent experiments were conducted. Error bars represent the SD about mean.

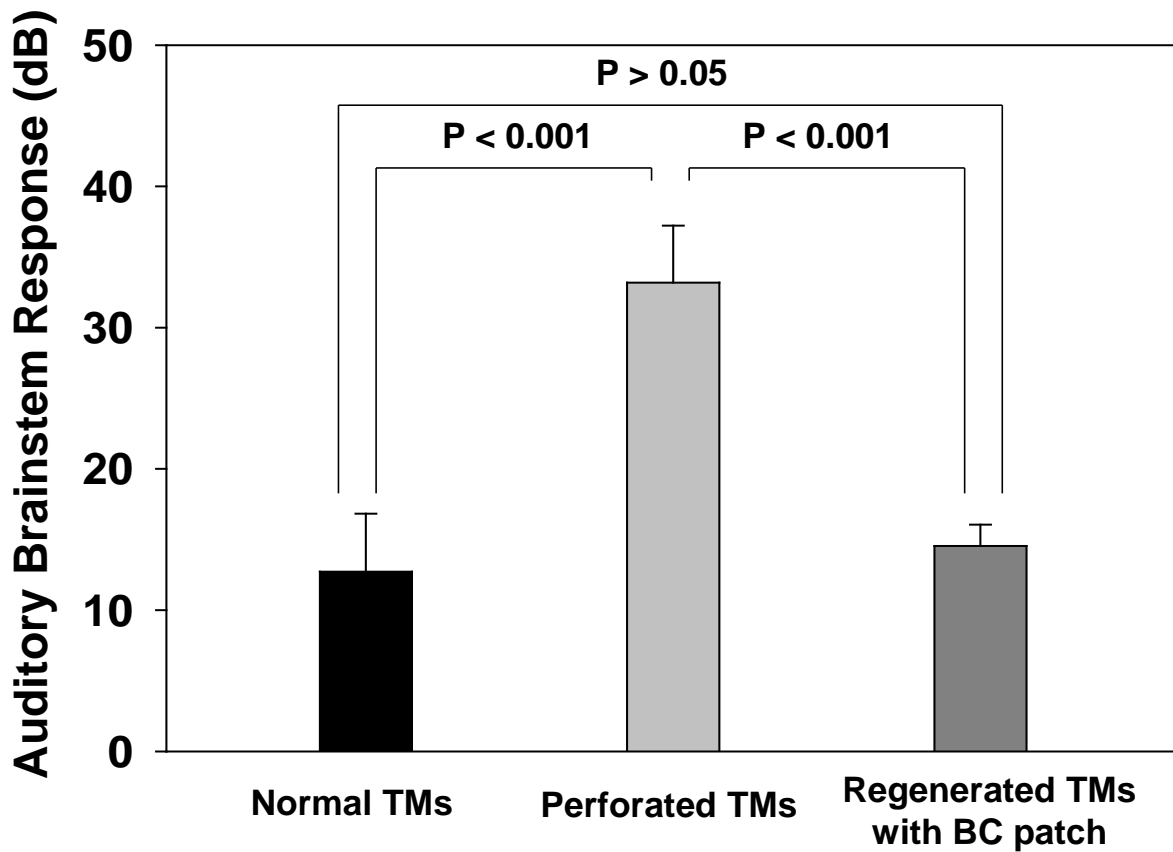


**Figure 9.6.** ABR results of the normal TMs, the perforated TMs, and the regenerated TMs with the BC nanofibrillar patch, indicating that the hearing ability of the TM rats regenerated with the patches was recovered. Eleven independent experiments were conducted. Error bars represent the SD about mean.



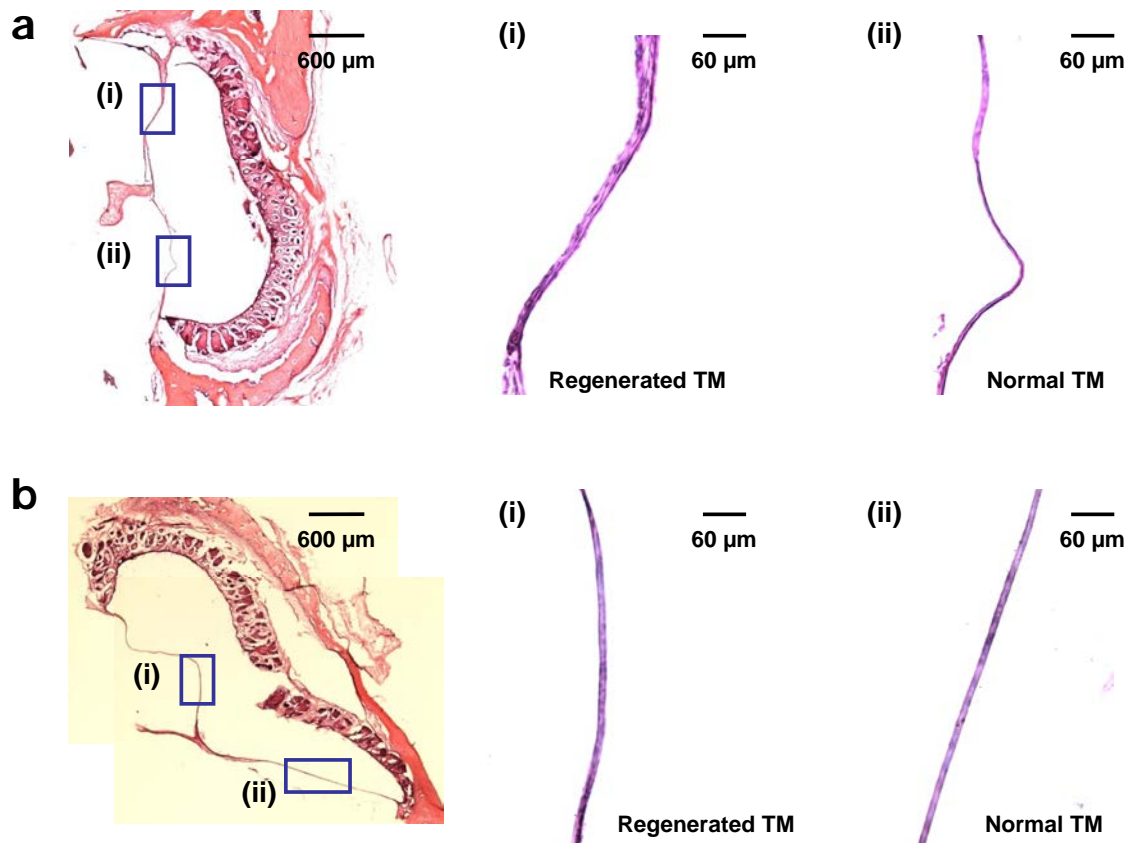


**Figure 9.7. Representative H&E image of (a) the regenerated TM spontaneously and (b) the regenerated TM with the BC nanofibrillar patch.** The (i) and (ii) show the high magnification images. The results indicate that the thickness of the regenerated TM with the BC nanofibrillar patch was similar with that of the normal TM, but the thickness of the regenerated TM spontaneously didn't. Three independent experiments were conducted.

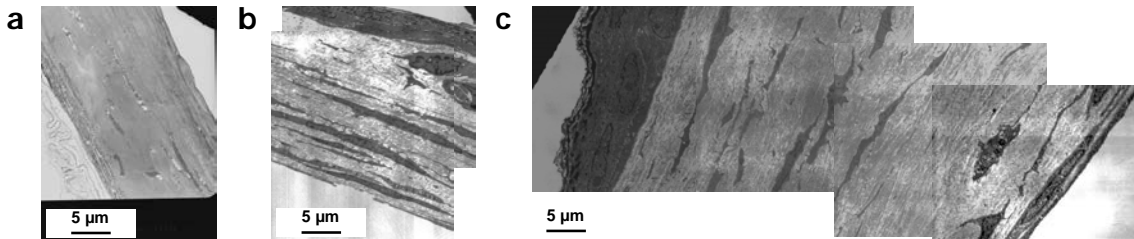


**Figure 9.8. Representative TEM images of the (a) normal TMs, (b) the regenerated TM with the BC nanofibrillar patch, and (c) the regenerated TM spontaneously.** The white arrows indicate epidermal layer and the black arrows indicate mucosal layer of TMs. The (\*) indicates connective layer of TMs. Three independent experiments were conducted.

## Chapter 10. Concluding Remarks

### 10.1. Introduction

My dissertation works try to extend the ‘Biosystems Engineering’ research fields by the multidisciplinary approach involving nanoengineering, biomimetics, biomechanics, and biology with an emphasis on their applications to biomaterial processing, cell mechanics, and tissue engineering. My dissertation works particularly focus on developing the nanotopographically-defined platforms mimicking the *in vivo*-like topographical cell environment such as extracellular matrix (ECM) and specific tissue architectures, and their applications for regulation of cellular and multi-cellular structure and function in the contexts of biological processing such as stem cell differentiation, wound repair, and bone regeneration. Using nanoengineering technology, a series of advanced nanopatterned biomimetic platforms were developed using biomaterials such as polyurethane and poly(lactico-glycolic acid), which allowed us to study the intricate interactions between cell structure and mechanical cues (by nanotopography) in the cell fate and function decisions. Specifically, the nanoengineered biomimetic platforms could be used as a powerful tool for better understanding complex cellular behavior in response to the *in vivo*-like nanotopographical cues, providing a new insight into the control of cellular function and the development of tissue regenerative technologies. In Chapter 10, we introduce the summary of each specific project and discuss how the research works from all these projects can be connected each other to reach the conclusion on this dissertation. Finally, we discuss potential future research directions focused on the nanoengineered biomimetic systems as well as how the major accomplishments from all these thesis projects can be used for broad applications in biological engineering.

## **9.2. Summary of dissertation work**

The major results of my thesis research can be summarized as follows. 1) Inspired by the architectures of native ECMs and tissues, nanotopographically defined platforms with precisely controlled architectures were developed; 2) Using the platforms developed, the detailed roles of nanotopography in cellular structure and function were investigated for developing the methodology for promoting cell function; 3) Nanoengineered biomimetic systems composed ECM-like topographical substrates and cells were proposed as an efficient strategy for tissue regeneration without complex surgical treatments or tissue transplantation.

### **9.2.1. Nanotopographically defined platforms with precisely controlled architectures**

Living cells are exposed to complex and functional microenvironment including soluble macromolecules, biophysical cues, and interactions between cell-cell and cell-ECM. Traditionally, the *in vitro* and *in vivo* experimentations for various biological applications such as fundamental biology, therapeutic and diagnostic research, stem cells and regenerative medicine, and developing *in vitro* disease models have been carried out by using a ‘cocktail’ of chemical factors such as cytokines and hormones, despite of the essential fact that living cells display high sensitivity to the topographical cues such as ECMs composed of complex and well-defined protein fibers with feature sizes ranging from tens to several hundreds of nanometers. The main reasons on this issue are i) traditional biology or clinical scientists are mainly neglected such factors; ii) the current micro- and nanofabrication techniques cannot mimic the complex native physiological architectures; iii) the nanofabrication techniques are complex, time-consuming, and expensive with less control over feature sizes.

To address these issues, in Chapter 3, 4, 5, and 6, we developed a series of advanced

nanopatterned platforms mimicking the *in vivo*-like topographical cell environments. In Chapter 3 and 4 (Part I), we fabricated a series of nanoengineered platforms with defined ridge/groove patterns with precisely controlled sizes using capillary force lithography (CFL) to control the nanotopographical density, inspired by the architectures of native tissues and ECMs revealing the highly oriented grooved structures with various length scales in nanometers. In Chapter 3, anisotropic nanotopographic pattern arrays with variable local sizes in the form of uniformly-spaced ridge/grooved nanosurfaces were designed and fabricated as synthetic ECM. The nanopatterned platforms with the variable ridge width and groove widths (ranged from 300 nm to 800 nm; defined as dense nanotopography (300 - 400 nm), intermediate nanotopography (500 - 600 nm), and sparse nanotopography (700 - 800 nm)) allowed us to characterize the effect topographical density cues of ECM architectures on cellular responses including cell shape, orientation, migration, and function. Throughout the Chapter 3 of this thesis work that the intermediate nanotopography (500 - 600 nm) showed the highest performance compared to other nanotopographical local densities in terms of cell functions, we also designed and fabricated the the matrix nanotopography with controlled density of groove spacing ratio in Chapter 4, allowing us to study the effects of density of nanopatterns for finding an existence of potentially optimized nanotopographical density for functions of cells, especially for stem cells. We fabricated nanogrooves with 1:1, 1:3, and 1:5 spacing ratio (width:spacing, width=550 nm) using CFL with the property that the structures were well-defined with high physical integrity and uniformity.

In Chapter 5 and 6 (Part II), we developed for the first time the methodologies to manipulate topographically hierarchical platforms to fully mimic the topography features of complex ECMs and tissues such as hierarchically organized protein fibers with micro-, nano-, and sub-nano scale sizes. In Chapter 5, we tried to mimic the hierarchically micro and

nanopatterned architecture of ECMs or tissues using the novel method that combines CFL with micro wrinkling technique. Using this methodology, anisotropically multiscale patterned substrata with precisely defined micro- and nanotopography (i.e., micro- and nanopatterned hierarchical platforms) were fabricated, allowing the quantitative analysis on the responses of cell behavior to the variable multiscale topographies. In Chapter 6, we also developed the methodology to manipulate the platforms with nano and sub-nanopatterned hierarchical topographies by using matrix nanotopography and nanomaterials. The graphene was coated on the matrix nanotopography with various nanoscale parallel ridges and grooves (ranged from 300 nm to 800 nm), which showed the nano and sub-nanotopography as well as other functional properties such as controlled stiffness and electrical conductivity. Importantly, we demonstrated that the graphene-matrix nanotopography hybrid platforms greatly promoted the functions of cells compared to the other matrix nanotopography-based platforms developed in this thesis.

### **9.2.2. Role of nanotopography in cellular structure and function decision**

As we previously mentioned, the architecture effects of ECMs have been neglected or minimized as a considering factor for most experimentation for understanding the cell behavior. Namely, the accumulation of the current knowledge of cell-ECM interactions on regulating cell fate and function has relied heavily on *in vitro* studies of cells growing on homogeneously coated flat culture dishes until now. To address these issues, in Chapter 3, 4, and 5, we analyzed the relationships between the *in vivo*-like topographical cell environments and cellular function. In Chapter 3, using biocompatible matrix nanotopography with local density of ridge/groove patterns (i.e., ridge = groove = 300, 400, 500, 600, 700, 800 nm, respectively), we found that the local density of ridges/grooves in nanoscale could control the body and nucleus of cells in single

cell or multi-cells level. In particular, the significantly higher cell migration speed on the topographical local density with 300 nm ridge/groove sizes compared to those on the other topographical local densities and it has cell migration speed was in directly inverse proportion to the topographical sizes. The stress fibers of cells were polarized along the direction of nanotopography, being more polarized with the denser nanotopographical local density as compared to the relatively sparser nanotopographical local density. The larger FA sizes were observed on the sparser nanotopographical local density than on the denser nanotopographical local density. The denser nanotopographical local density showed lower affinity and well-distributed stress fibers of cells on the substrates compared to those on the sparse nanotopographical local density. Our *in vitro* dermal wound healing study demonstrated that the maximum covering rate was observed on the 300 nm ridge/groove sizes on synthetic ECMs. Interestingly, it was found that the denser nanotopographical local density (i.e., 300 and 400 nm ridge/groove sizes) showed highly anisotropically organized cells and synthesized fibronectin fiber bundles, whereas the sparser nanotopographical local density (i.e., 700 and 800 nm ridge/groove sizes) showed less organized cells and synthesized fibronectin fiber bundles.

In Chapter 4, we showed the detailed stem cell-substrate interaction in terms of cell adhesion and function using the matrix nanotopography with controlled density of groove spacing ratio (i.e., matrix nanogrooves with 1:1, 1:3, and 1:5 spacing ratio (width:spacing, width = 550 nm)). In response to the nanotopographical density, the adhesion, migration, and differentiation of stem cells were sensitively controlled. We found that the body and nucleus of human mesenchymal stem cells (hMSCs) with the sparser nanogrooved pattern elongated and orientated more along the direction of nanogrooves than those with the relatively denser nanogroove patterns. In contrast, the perimeter of the cells was lower at the 1:3 pattern as

compared to the 1:1 and 1:5 patterns. We also found that the topographical density-dependent shape of cell body and nucleus, formation of focal adhesions (FAs), and interactions at the cell-substrate and cell-cell interfaces might collectively regulate the functions of hMSCs. In addition, we have investigated the role of nanotopographical density on the function of hMSCs. It was observed that the denser nanogrooved matrices guided faster migration of hMSCs than the sparser nanogrooved matrices. Furthermore, the effect of nanotopographical density on the osteo- or neurogenesis of hMSCs was significant at the 1:1 and 1:3 nanogrooved patterns, but not significant at 1:5 nanogrooved pattern compared to that at the flat substrate. We showed a high positive correlation between the expression of integrin  $\beta 1$  or N-cadherin and the osteo- and neurogenesis. We also found some intriguing correlations between the cell body- or nucleus perimeter/spreading-based shape index and the osteo- and neurogenesis of hMSCs.

In Chapter 5, using hierarchically micro and nanopatterned platforms, various cells including fibroblasts, osteoblast-like cells, endothelial cells, and stem cells are quantitatively analyzed in terms of cellular adhesion and function. It is found that cells could sensitively recognize the nanotopography in multiscale patterned substrates, showing highly aligned and orientated cell shapes as well as enhanced cell functions such as fibronectin synthetics from NIH 3T3 fibroblast cells, bone mineralization from MG-63 cells, and differentiation of hMSCs compared to those on micropatterned substrates. Furthermore, we proposed the possible mechanism on the nanotopography-induced cell function as follows: nanotopography cues in substrate  $\rightarrow$  enhancing cell adhesion on substrata and interactions between cells-substrate  $\rightarrow$  enhancing function of cells.

### **9.2.3. Nanoengineered biomimetic systems for tissue regeneration**



Throughout the Chapter 3-6 of this thesis work, we have learned that the nanoengineered biomimetic platforms showed the great potential for controlling or improving cellular function, which can be used as an efficient tool for repair or regeneration of damaged tissues in a more clinically relevant setting. To this end, we developed the strategy to regenerate the damaged tissues using nanoengineered biomimetic systems composed of ECM-like topographical substrates, chemical molecules, and cells in Chapter 7, 8, and 9 (Part III). In Chapter 7, inspired by the aligned nanostructures and co-existence of vascular cells and stem cells in human cancellous bone, we proposed a biomimetic system composed of nanotopography and co-culture platform for enhancing the osteogenesis of hMSCs for bone regeneration, demonstrating the importance of the synergistic cues (i.e., nanotopography and co-culture) for enhancing cell function. Based on these considerations, we developed the biomimetic systems that integrated the stem cells into the nanopatterned substrates for tissue regeneration (Chapter 8). Inspired from ECMs in a human bone tissue, we developed hierarchically micro and nanopatterned transplantable substrates by employing capillary force lithography in combination with a surface micro-wrinkling method using a Food and Drug Administration (FDA)-approved PLGA polymer. Importantly, we showed that the nanopatterned stem cell patches can guide the bone regeneration without complex surgical treatments or tissue transplantation. This stem cell patch can be utilized for the future engineering of other tissues owing to the high sensitivity of many other cell types to the nanoscale level details of their substrata. Finally, we proposed that a nanofibrillar patch synthesized by bacterial cellulose could be used as a strategy for wound healing of tympanic membrane (TM) perforations (Chapter 9). We have shown that the BC nanofibrillar patch can regenerate the perforated TMs without complex surgical treatments.

Taken together, my dissertation works conclude that nanoengineered biomimetic systems

can hold considerable promise as a cell and tissue culture device, which can be used as valuable tools in a wide variety of biological applications such as fundamental biology, therapeutic and diagnostic research, stem cells and regenerative medicine, and developing *in vitro* disease models.

### **9.3. Broad implications of this dissertation work for biological engineering**

My dissertation researches have the potential to yield fundamental knowledge of i) micro - and nanoscale biomaterial processing technologies and ii) cell and tissue culture devices.

i) Throughout the dissertation works, we have developed the various methodologies to manipulate the micro- and nanoscale platforms with precisely controlled sizes. With this knowledge and additional advanced technology, we will be able to develop the novel platforms using biomaterials for various biological engineering applications. For example, inspired from the functions derived from the specific micro- and nanostructures in the living biosystems such as humans, animals, and plants, we can design and manipulate the biomaterial-based engineering platform with their biocompatibility property for various purposes. Another example is that we can use these micro- and nanoengineering technologies for development of functional food products, which can be a new type of platforms in food processing.

ii) Using various micro- and nanoengineering technologies as well as the knowledge on cellular responses to the biomimetic topographies described here in combination with the traditional technologies such as molecular biology and tissue engineering, we can develop the novel methodologies for the disease treatments, which can directly associate with the health in humans, animals, and plants. Another example is that we can design and manipulate the *in vitro* model platforms mimicking the tissues and organs in humans and animals. These *in vitro* model

platforms will be able to use as a powerful tool to study various diseases in living biosystems or replace the current *in vivo* animal models for evaluating the safety of new medicines or food products.

## 국문초록

살아 있는 세포는 화학 및 물리학적 자극 그리고 주변 세포 혹은 세포외기질간의 상호 관계 등 복잡하고 기능적인 미세 환경에 노출되어 있다. 따라서 이러한 미세 환경과 유사한 혹은 똑같은 조건을 가지고 있는 플랫폼의 개발은 생물학, 치료 및 진단 연구, 줄기세포 및 재생의학, 질병 모델 개발 등 다양한 인간, 동물 및 식물의 생물학적 응용에 있어 매우 중요하다. 세포는 미세 환경 내 콜라겐, 엘라스틴 등의 마이크로 및 나노미터 수준의 고분자 파이버 형태로 구성되어 있는 세포외기질 및 특이적 조직 구조에 둘러 쌓여 있으며 이는 세포의 기능적 조절에 있어 구조적 자극의 중요성을 일러 준다. 하지만 화학 및 물리학적 자극에 따른 세포의 기능적 이해 및 응용에 대한 연구에 비해서 세포외기질 혹은 조직 내 특이적 구조 자극에 따른 세포의 기능적 이해는 거의 되어 있지 않다. 즉, 다양한 생물학적 연구 및 응용에 있어서 세포가 노출되어 있는 구조적 자극은 거의 무시되거나 최소화 되고 있는데 이는 세포 미세 환경 내 나노미터 수준의 매우 미세하고 복잡한 형태의 특이적 구조를 지니는 플랫폼 개발에 있어 기술적 한계가 있기 때문이다.

본 학위논문에서는 이러한 한계점을 극복하고자 생체재료 가공기술을 이용하여 특이적 조직 및 세포외기질의 구조적 특성을 가지고 있는 생체모방형 나노구조 플랫폼을 개발하였다. 모세관력 리소그래피, 나노물질 등을 활용한 다양한 나노기술에 기반하여 살아 있는 세포에게 생체 내 구조적 자극과 유사한 환경을 제공해 줄 수 있는 플랫폼을 개발하고, 이를 응용하여 세포 기능을 조절하거나 촉진 그리고 조직을 재생 시킬 수 있는 기술을 개발하였다. 이에 따른 본 논문의 구체적인 목적은 다음과 같다. (1) 세포 기능

조절 및 촉진을 위한 형태가 정밀하게 컨트롤된 생체모방형 나노구조 플랫폼 개발, (2) 세포 기능 촉진 및 생물학적 현상에 있어 나노구조의 역할 규명, (3) 복잡한 수술적 치료 없이도 조직을 재생 시킬 수 있는 생체모방형 나노구조 시스템 개발. 이를 위해서 본 논문은 3개의 파트 내 7개의 독립적인 연구로 구성되었으며 본 논문의 주요 결과는 다음과 같다.

첫 번째 파트 연구에서 모세관력 리소그래피 기술 기반으로 다양한 나노미터 사이즈와 함께 일렬로 배열되어 있는 특이적 조직 및 세포외기질 구조를 모방한 세포 배양 플랫폼을 개발하였다. 개발한 나노구조 플랫폼을 응용하여 세포의 구조 및 기능이 나노구조의 밀도에 매우 민감하게 반응함을 규명하였고, 플랫폼 내 구성되어 있는 나노구조 밀도의 최적화에 따라 상처 치유, 줄기세포 분화 등 세포 기능을 촉진 시킬 수 있음을 증명하였다. 두 번째 파트 연구에서는 마이크로 및 나노미터 혹은 다양한 나노미터 사이즈를 동시에 가지고 있는 조직 및 세포외기질의 계층 구조를 모방한 세포 배양 플랫폼을 개발하였다. 모세관력 리소그래피 및 마이크로 표면주름 구조 기술을 응용하여 마이크로 및 나노구조가 계층적으로 정밀하게 컨트롤된 플랫폼을 제작하였고, 이를 통하여 나노구조가 세포-지지체 및 세포-세포간 상호 관계를 조절하고 이에 따라 세포의 기능을 촉진 시킬 수 있음을 규명하였다. 또한 모세관력 리소그래피 기술 기반에 나노물질인 그래핀을 이용하여 수백 나노 및 수십 나노미터 구조를 동시에 가지고 있는 플랫폼을 개발하여 구조적 자극에 따라서 세포의 기능을 더욱더 촉진 시킬 수 있음을 증명하였다. 마지막 세 번째 파트 연구에선 생체모방형 나노구조 플랫폼과 세포 미세 환경 내 다양한 화학적 물질과 세포가 시스템으로 구성되었을 때 세포의 기능 촉진을 극대화 시킬 수 있고, 이

러한 시스템적 관점에 따라 손상된 조직의 치료 및 재생을 시킬 수 있음을 제안하였다. 뼈 조직 내 혈관이 함께 존재함에 영감을 얻어 세포외기질을 모방한 세포 배양 플랫폼에 줄기세포와 혈관세포를 동시에 배양하였고, 이에 따라 줄기세포의 골세포로의 분화가 더욱더 촉진 될 수 있음을 보였다. 본 연구에 기반을 두어 생체적합성 물질로 구성되어 있는 생체모방형 나노구조 플랫폼과 줄기세포가 결합되어 있는 줄기세포 패치를 개발하였고, 이를 이용하여 손상된 뼈를 수술적 치료 없이 재생 시킬 수 있음을 동물모델을 통하여 증명하였다. 또한 박테리아를 이용하여 개발한 셀룰로오스 나노구조 패치를 이용하여 천공된 고막 재생을 촉진 시킬 수 있음을 보였다.

결론적으로, 본 학위논문에선 나노공학 및 생체모방학적 접근법을 통하여 생체모방형 나노구조 플랫폼을 개발하였고 이의 세포 기능 조절 및 촉진 그리고 조직 재생을 위한 공학적 도구로서의 가능성을 제시하였다. 본 연구를 통하여 개발된 나노구조 개발 기술은 다양한 생체재료 및 생물재료의 나노 및 마이크로미터 수준의 미세가공 기술 개발에 응용 할 수 있을 것이며, 인간 혹은 동물의 질병 모델, 진단 및 치료 개발 등 다양한 생물학적 응용에 기여할 수 있을 것으로 기대된다.

**주요어:** 나노구조 제작, 생체모방, 생체재료, 세포 역학, 조직 재생

**학 번:** 2012-30997

## **Curriculum Vitae** (July, 2014)

Jangho Kim is working toward the Ph.D. degree in Biosystems Engineering at the Seoul National University (SNU). Prior to joining the current position, he studied as a Research Associate of the Research Institute for Agriculture and Life Sciences and a Senior Researcher of the Biomechanics & Tissue Engineering Laboratory at the SNU from 2010 to 2012. He also studied as a Research Scholar in the Thin Film & Charged Particles Research Laboratory at Department of Electrical and Computer Engineering, University of Illinois at Urbana-Champaign (UIUC) from 2009 to 2010. His research interests include 1) micro/nanofabrication & biologically inspired engineering systems, 2) mechanobiology & stem cell and tissue engineering, and 3) biomaterials & bio-nanotechnology. He has authored and co-authored more than 45 peer-reviewed journal publications, 50 peer reviewed conference proceedings or meeting abstracts, and 1 issued patent in the area of biological engineering focused on the micro- and nanotechnology. Among the awards and honors he received (more than 20), the representatives are as follows. He received the Award for Best or Oral Poster Presentation from the Korean Society for Agricultural Machinery (KSAM) Conference in 2007, 2008, 2012, and 2013 (Biological Engineering section), the Award for Outstanding Oral Presentation (outstanding research award) from the Korea Tissue Engineering and Regenerative Medicine Society in 2012 and 2013, the Best Presentation Award from the Annual Meeting of Korean Society for Stem Cell Research in 2013, the Excellent Researcher from the Research Institute for Agriculture and Life Sciences, SNU in 2011, the National Graduate S&T Scholarship from Korea Science and Engineering Foundation during 2007-2008, the Award for Seoul Science Fellowship in 2008 (selected), the Research Scholarship from the UIUC during 2009-2010, the Young Scientist Award from the Korean Society for Biomaterials and the Japanese Society for Biomaterials in 2012, the Award for Young Plenary Speaker from the Tissue Engineering & Regenerative Medicine International Society Asia-Pacific (TERMIS-AP) Conference, Shanghai, P.R. China in 2013, and the Samsung HumanTech Paper Award from the Samsung Electronics in 2014. In addition, he had been selected the members of the very first Tissue Engineering Young Investigator Council (selected from international young researchers of over 300 qualified candidates in the world) of the Tissue Engineering journals and the Tissue Engineering and Regenerative Medicine International Society (TERMIS) in 2012. He also served as a

professional member such as program committee member as the judge for SYIS best oral and poster competition, TERMIS-AP Conference, Shanghai, P.R. China, 2013, Session Chair, 2013 TERMIS-AP, and theme co-organization for tissue engineering YIC special issue in 2013-2014. He serves as a peer reviewer for high-profiled journal publications such as Scientific Reports, Advanced Functional Materials, Tissue Engineering, Lab on a Chip, Chemical Communications, Biomacromolecules, Materials Science and Engineering C, Materials Letters, Nanoscale, Archives of Medical Research, Journal of Materials Chemistry, Journal of Materials Chemistry B, Integrative Biology, RSC Advances, Energy & Environmental Science, General Physiology and Biophysics and so on.